



Università degli Studi di Napoli “Federico II”

Dottorato di ricerca in “Trasporti”
XVIII° ciclo

INNOVATIVE METHOD FOR DAMAGE IDENTIFICATION
AND STRUCTURAL HEALTH MONITORING BASED ON
VIBRATION MEASUREMENTS

Coordinatore
Ch.^{mo} Prof.
Ing Vincenzo Torrieri

Dottorando
Ing. Igor Bovio

Tutor
Ch.^{mo} Prof.
Ing. Leonardo Lecce

<i>Introduction</i>	page.	1
<i>Chapter I:</i>	page.	3
<i>I.1</i> Frequency changes	page.	3
<i>I.2</i> Mode shape changes	page.	6
<i>I.3</i> Mode shape curvature and Strain mode shape changes	page.	7
<i>I.4</i> Methods based on dynamically measured flexibility	page.	8
<i>I.5</i> Matrix update methods	page.	9
<i>I.6</i> Nonlinear methods	page.	10
<i>I.7</i> Neural network-based methods	page.	11
<i>Chapter II:</i>	page.	13
<i>II.1</i> Frequency Response Function (FRF)	page.	14
<i>II.2</i> Coherence Function	page.	18
<i>II.3</i> Damage Indexes	page.	19
<i>Chapter III:</i>	page.	23
<i>III.1</i> Overview	page.	23
<i>III.1.1</i> The Biological inspiration	page.	23
<i>III.1.2</i> History of the neural network analogy	page.	25
<i>III.2</i> Neural Network application to Health Monitoring	page.	26
<i>III.2.1</i> Implementation of the “auto-associative network”	page.	29
<i>III.2.2</i> Reconstruction index	page.	30
<i>III.2.3</i> Choice of the dispersion measurement	page.	31
<i>III.2.4</i> “Threshold” evaluation	page.	32
<i>III.3</i> Neural Network algorithm	page.	38

<i>III.3.1</i> Training	page. 38
<i>III.3.2</i> Post Process	page. 42
<i>Chapter IV:</i>	page. 45
<i>IV.1</i> Instruments	page. 45
<i>IV.1.1</i> Generators and spectrum analysers	page. 45
<i>IV.1.2</i> Amplifiers	page. 48
<i>IV.1.3</i> Piezoceramic devices	page. 51
<i>IV.1.4</i> Magnetostrictive actuators	page. 55
<i>IV.2</i> Test articles	page. 58
<i>IV.2.1</i> MD-11	page. 58
<i>IV.2.2</i> Aeronautical composite panel	page. 60
<i>IV.2.3</i> ATR-72 aircraft	page. 61
<i>Chapter V:</i>	page. 63
<i>V.1</i> MD-11 fuselage	page. 63
<i>V.1.1</i> First experimental campaign	page. 63
<i>V.1.2</i> Second experimental campaign	page. 95
<i>V.1.3</i> Third experimental campaign	page. 99
<i>V.2</i> Second Test Article	page. 105
<i>V.2.1</i> First Experimental Test	page. 109
<i>V.2.2</i> Second Experimental Test	page. 115
<i>V.2.3</i> Third Experimental Test	page. 121
<i>V.3</i> ATR-72	page. 125
<i>V.3.1</i> Overview	page. 126

<i>V.3.2</i> Frame 29	page. 128
<i>V.3.3</i> Floor Support Zee	page. 150
<i>V.3.4</i> Floor Frame 42	page. 159
<i>V.3.5</i> Main Landing Gear	page. 166
<i>V.3.6</i> Frame 45	page. 176
<i>V.3.7</i> Frame 45	page. 183
<i>Appendix:</i>	page. 185
<i>A.1</i> Subparagraph V.3.3	page. 185
<i>A.2</i> Subparagraph V.3.4	page. 187
<i>A.3</i> Subparagraph V.3.5	page. 209
<i>A.4</i> Subparagraph V.3.6	page. 220
<i>Conclusions:</i>	page. 233
<i>Bibliography:</i>	page. 235

Introduction

*A*eronautics has made great strides since Wilbur and Orville Wright performed the first successful human flight with a means heavier than air, the 17th of December 1903.

Aircraft are faster and faster; the speed of sound has been exceeded by man; intercontinental flights are in the ordinary run of things.

The air freight has become both safe and reliable. For these reasons, nowadays, million of people prefer it to others means of transport either for pleasure or business.

The achievement of high standard of quality and safety needs a continuous scientific and technological research. Above all the safety requires an economical effort, therefore methodologies more and more innovative are demanded in order to reduce maintenance costs preserving the safety.

The purpose of the thesis is to present innovative applications within the Non Destructive Testing field based upon vibration measurements developed by the author at the Department of Aeronautical Engineering of the University of Naples "Federico II" (Italy). The aim of the research has been to develop Non Destructive Tests (NDT) which meet most of the mandatory requirements for effective health monitoring systems while, at the same time, reducing as much as possible the complexity of the data analysis algorithm and the experimental acquisition instrumentation. In fact, classic techniques, which make use, for example, of ultrasonic waves or X ray, have disadvantages like the need to disassemble the part we want to test, expensive equipment and highly qualified operators. With the innovative methods reported in this thesis it is not necessary to disassemble the part, and they can be used even if the part isn't accessible.

The proposed new methods are based upon the acquisition and comparison of the Frequency Response Functions (FRFs) of the monitored structure before and after a damage occurs. Structural damage modifies the dynamic behaviour of a structure affecting its mass, stiffness and damping and consequently the FRFs of a damaged structure, when compared with the FRFs of a sound structure, makes the identification, localization and quantification of structural damage possible.

The activities presented in this thesis focus mainly on a new FRFs processing technique based upon the determination of a representative “Damage Index” for identifying and analysing damage on real-scale aeronautical structural components, such as an MD-11 large-scale fuselage reinforced panel, on an aeronautical composite panel and on a real ATR-72 aircraft.

Furthermore, a dedicated neural network algorithm has been elaborated aimed at obtaining a “recognition-based learning” method. This kind of learning methodology permits us to train the neural network in order to enable it to recognise only “positive” examples and consequently discarding “negative” ones. Within the structural NDT a “positive” example means a “healthy” state of the analysed structural component and, obviously, a “negative” example means a “damaged” or perturbed state. With this objective in mind the neural network has been trained to make use of the same FRFs of the healthy structure used in determining the Damage Index.

Regarding damage, corrosion, failure of linking rivets, simple cracks, impacts on structure and other kind of damage have been induced on the test articles.

From an architectural standpoint, magnetostrictive devices have been tested as actuators, and piezoceramic patches as actuators and sensors. Besides it has been used a laser-scanning vibrometer system to acquire the FRFs. These techniques promise to bring us a step forward in the implementation of an automatic “health monitoring” system which will be able to identify structural damage in real time thereby improving safety and reducing maintenance costs.

Chapter I

State of the Art

*I*n this chapter an overview of the main damage identification and health monitoring methods, based on changes in the measured dynamic properties of structures, and developed all around the world, is reported.

The expounded methods are categorized based on the type of measured data used and the technique used to identify the damage from the measured data:

- ✓ Frequency changes;
- ✓ Mode shape changes;
- ✓ Mode shape curvature and Strain mode shape changes;
- ✓ Methods based on dynamically measured flexibility;
- ✓ Matrix update methods;
- ✓ Nonlinear methods;
- ✓ Neural network-based methods.

I.1 Frequency changes

The amount of literature related to damage detection using shifts in natural frequencies is large. The observation that changes in structural properties cause changes in vibration frequencies was the impetus for using modal methods for damage identification and health monitoring.

It should be noted that frequency shifts have significant practical limitations for applications to the type of structures. The somewhat low sensitivity of frequency shifts to damage requires either very precise measurements or large levels of damage. Currently, using frequency shifts to detect damage appears to be more practical in applications where such shifts can be measured very precisely in a controlled environment, such as for quality control in manufacturing.

Also, because modal frequencies are a global property of the structure, it is not clear that shifts in this parameter can be used to identify more than the mere existence of damage. In other words, the frequencies generally cannot provide spatial information about structural changes. An exception to this limitation occurs at higher modal frequencies, where the modes are associated with local responses. However, the practical limitations involved with the excitation and extraction of these local modes, caused in part by high modal density, can make them difficult to identify. Multiple frequency shifts can provide spatial information about structural damage because changes in the structure at different locations will cause different combinations of changes in the modal frequencies. However, there is often an insufficient number of frequencies with significant enough changes to determine the location of the damage uniquely.

A typical frequency changes method is the forward problem, which consists of calculating frequency shifts from a known type of damage. Typically, the damage is modelled mathematically, then the measured frequencies are compared to the predicted frequencies to determine the damage.

For example, it can be examined the change in the frequencies associated with the first two bending modes and first torsional mode of a structure to identify damage; or it can be used changes in the resonant frequencies, mode shapes, and response spectra to identify damage. The mode shapes are necessary to ensure that the changes in modal frequencies are properly tracked.

Another frequency changes method is the inverse problem, which consists of calculating the damage parameters, e.g., crack length and/or location, from the frequency shifts.

An example is a method whereby damage in a structure that can be represented as one-dimensional can be identified from changes in the resonant frequencies associated with two modes. If the axial vibration modes are looked, the method is based on the relationship between the receptance function on either side of the damage, β and γ , respectively, and the stiffness of a spring representing the damage, k .

The relationship is defined by:

$$\beta + \gamma + \frac{1}{k} = 0$$

An important point is to correct frequency measurements for changes in temperature, which is another possible source of error when frequency changes are used to locate damage.

An inverse problem can be the estimation of modal frequencies and cross-spectral densities to changes in the structural stiffness parameters. The hypothesis is that modal characteristics themselves are not sensitive to damage, but that certain frequency ranges in the structural frequency response are sensitive to damage.

Another method for damage identification can relate changes in the resonant frequencies to changes in member stiffnesses using a sensitivity relation. The relation between the normalized changes in squared frequencies $\{z\}$, the fractional elemental stiffness reductions $\{\alpha\}$, and the fractional elemental mass reductions $\{\beta\}$, is given by:

$$\{z\} = [F]\{\alpha\} - [G]\{\beta\}$$

where $[F]$ and $[G]$ are the sensitivities of the frequency change to changes in elemental stiffness and mass magnitudes, respectively.

Damage is defined as a reduction in the stiffness of one of the elements forming the structure. The stiffness reductions can be located by solving the general inverse problem:

$$\{\alpha\} = [F]^+[\{z\} + [G]\{\beta\}]$$

assuming that $\{z\}$ and $\{\beta\}$ can be measured or assumed. In this equation, $[F]^+$ represents the pseudoinverse of the stiffness sensitivity matrix. The use of the pseudoinverse operator will ensure that the equation holds when is not square, i.e., when the number of measured modes is not equal to the number of structural elements.

I.2 Mode shape changes

An example about a mode shape changes method has been developed to locate a crack and quantify its size from changes in the vibration frequency and mode shape. The crack is located by discretizing the structure and looking at the reduced stiffness in each element. The formulation is based on a first-order Taylor expansion of the modal parameters in terms of the elemental parameters. Once located, the crack length is determined by a formulation based on considering the change in strain energy resulting from the presence of a crack. The Newton-Raphson method is used to solve the resulting equations for the crack parameters.

Another method compares the results of using mode shape relative change and mode shape curvature change to detect damage. The relative difference measure does not typically give a good indication of damage using experimental data. It can point out that the most important factor is the selection of the modes used in the analysis. It is possible to show that the modal assurance criteria (MAC) values can be used to indicate which modes are being affected most by the damage.

Furthermore, it is possible to define a mode shape normalized by the change in natural frequency of another mode as a “damage signature.” The damage signature is a function of crack location but not of crack length. A set of possible signatures by considering all possible damage states can be computed. The measured signatures were matched to a damage state by selecting which of the analytical signatures gave the best match to the measurements using the MAC.

Finally, in the past was proposed a global damage integrity index that is based on a weighted ratio of the damaged natural frequency to the undamaged natural frequency. The weights are used to reflect the relative sensitivity of each mode to the damage event. When damage is indicated, local integrity indices are calculated to locate the defective areas. The local integrity index is calculated from the global integrity index by further weighting the global index by the square of the ratio of damaged mode amplitude to the undamaged mode amplitude for a particular measurement point.

I.3 Mode shape curvature and Strain mode shape changes

An alternative to using mode shapes to obtain spatial information about vibration changes is using mode shape derivatives, such as curvature. It is first noted that for beams, curvature and bending strain are directly related as:

$$\varepsilon = \frac{y}{R} = \kappa y$$

where ε is strain, R is radius of curvature, and κ is curvature or $1/R$.

It was demonstrated that absolute changes in mode shape curvature can be a good indicator of damage for the FEM beam structures they consider. The curvature values are computed from the displacement mode shape using the central difference approximation for mode i and DOF q :

$$\phi_{q,i}'' = \frac{\phi_{q-1,i} - 2\phi_{q,i} + \phi_{q+1,i}}{h^2}$$

where h is the length of each of the two elements between the DOF $(q-1)$ and $(q+1)$. Another method is based on the decrease in modal strain energy between two structural DOF, as defined by the curvature of the measured mode shapes.

Furthermore, it was found that numerically calculating curvature from mode shapes resulted in unacceptable errors. It used measured strains instead to measure curvature directly, which dramatically improved results. Besides, it was found that strain mode shapes facilitated the location of a crack in a cantilever plate using FEM simulation.

Finally, it was defined a method whose mode shape curvature measure was computed using a central difference approximation as defined in the equation $\phi_{q,i}''$. It compares the performance of this relative difference method to a mode shape relative difference method. It can be demonstrated that the curvature change does not typically give a good indication of damage using experimental data. Moreover, the most important factor is the selection of which modes are used in the analysis.

I.4 Methods based on dynamically measured flexibility

Another class of damage identification methods uses the dynamically measured flexibility matrix to estimate changes in the static behaviour of the structure. Because the flexibility matrix is defined as the inverse of the static stiffness matrix, the flexibility matrix relates the applied static force and resulting structural displacement as:

$$\{u\}=[G]\{F\}$$

Thus, each column of the flexibility matrix represents the displacement pattern of the structure associated with a unit force applied at the associated DOF.

The measured flexibility matrix is estimated from the mass-normalized measured mode shapes and frequencies as:

$$[G] \sim [\Phi][\Lambda]^{-1}[\Phi]^T$$

The formulation of the flexibility matrix in that equation is approximate due to the fact that only the first few modes of the structure (typically the lowest-frequency modes) are measured. The synthesis of the complete static flexibility matrix would require the measurement of all of the mode shapes and frequencies.

Typically, damage is detected using flexibility matrices by comparing the flexibility matrix synthesized using the modes of the damaged structure to the flexibility matrix synthesized using the modes of the undamaged structure or the flexibility matrix from a FEM. Because of the inverse relationship to the square of the modal frequencies, the measured flexibility matrix is most sensitive to changes in the lower-frequency modes of the structure.

Several methods are based on dynamically measured flexibility. One, for example, make use of decomposing the measured flexibility matrix into elemental stiffness parameters for an assumed structural connectivity. This decomposition is accomplished by projecting the flexibility matrix onto an assemblage of the element-level static structural eigenvectors. Another method suggests that changes in

curvatures of the uniform load surface (deformed shape of the structure when subjected to a uniform load), calculated using the uniform load flexibilities, are a sensitive indicator of local damage. In fact the changes in the uniform load surface are appropriate to identify uniform deterioration. A uniform load flexibility matrix is constructed by summing the columns of the measured flexibility matrix. The curvature is then calculated from the uniform load flexibilities using a central difference operator $\phi''_{q,i}$.

1.5 Matrix update methods

Another class of damage identification methods is based on the modification of structural model matrices such as mass, stiffness, and damping to reproduce as closely as possible the measured static or dynamic response from the data. These methods solve for the updated matrices (or perturbations to the nominal model that produce the updated matrices) by forming a constrained optimization problem based on the structural equations of motion, the nominal model, and the measured data. Comparisons of the updated matrices to the original correlated matrices provide an indication of damage and can be used to quantify the location and extent of damage.

Methods that use a closed-form, direct solution to compute the damaged model matrices or the perturbation matrices are commonly referred to as optimal matrix update methods. The problem is generally formulated as a Lagrange multiplier or penalty-based optimization, which can be written as:

$$\min_{\Delta M, \Delta C, \Delta K} \{J(\Delta M, \Delta C, \Delta K) + \lambda R(\Delta M, \Delta C, \Delta K)\}$$

where J is the objective function, R is the constraint function, and λ is the Lagrange multiplier or penalty constant.

Another class of matrix update methods is based on the solution of a first-order Taylor series that minimizes an error function of the matrix perturbations.

Such techniques are known as sensitivity-based update methods. The basic theory is the determination of a modified parameter vector:

$$\{p\}^{(n+1)} = \{p\}^{(n)} + \{\delta p\}^{(n+1)}$$

where the parameter perturbation vector is computed from the Newton-Raphson iteration problem for minimizing an error function.

Finally, another matrix update method, known as “eigen-structure assignment,” is based on the design of a fictitious controller which would minimize the modal force error. The controller gains are then interpreted as parameter matrix perturbations to the undamaged structural model.

1.6 Nonlinear methods

A large number of nonlinear methods have been developed. From among them, an interesting method is the one which simulates nonlinear systems using only linear techniques. The motivation for this research is strong because nonlinear elements such as cracks are notoriously difficult to model using finite element analysis. This technique is based on the Volterra series. This technique yields a perturbation series for nonlinear responses based on generalizations of FRFs. The proposed method works by adding auxiliary inputs to model the effects of the nonlinearities. The superposition of the linear response resulting from the actual and auxiliary inputs simulates the true nonlinear response. The strengths of the auxiliary inputs are determined by the form of the nonlinearity and the true input. One problem with this method is that the effective inputs are functions of the entire time histories and must be recomputed if the input changes so the method cannot be used in real time. A second problem is that a different series must be computed for each location where a measured response is desired. A final problem is that to exactly simulate the nonlinear response, one must compute an infinite number of terms.

I.7 Neural network-based methods

In recent years there has been increasing interest in using neural networks to estimate and predict the extent and location of damage in complex structures. Neural networks have been promoted as universal function approximators for functions of arbitrary complexity. The most common neural network in use is the multilayer perceptron (MLP) trained by backpropagation. The commonly used terminology calls a MLP trained by backpropagation a “backpropagation neural network”. The backpropagation neural network is a system of cascaded sigmoid functions where the outputs of one layer, multiplied by weights, summed, then shifted by a bias are used as the inputs to the next layer. Once an architecture for the network is chosen, the actual function represented by the neural network is encoded by the weights and biases. The backpropagation learning algorithm is a way of adjusting the weights and biases by minimizing the error between the predicted and measured outputs. Typically, more adjustable weights than experiments are present in neural network-based methods, and the body of data was repeatedly run through the training algorithm until a criterion for the error between the data and the neural network was satisfied. Each error-generating run is called an epoch.

The identification of damage using neural networks is still in its infancy. Backpropagation neural network are largely used, but in literature it is very difficult to find a paper which compares the performance of two different neural network types. The damage identification is often attempted from information related to modal frequencies. All damage are modelled by linear processes, and they are often used changing member shapes and/or cross-sectional areas. Besides, most of the papers assume detailed knowledge of the mechanical structure including mass and stiffness matrices. A few performed the identification of system parameters based on measured data so that no detailed knowledge of the structure was assumed.

Intentionally blank

Chapter II

Damage Index Method

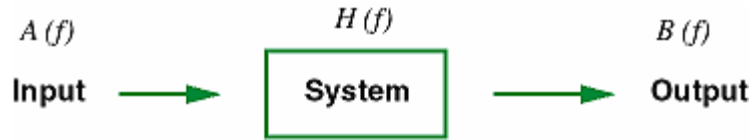
The proposed new method is based on the acquisition and comparison of Frequency Response Functions (FRFs) of the monitored structure before and after an occurred damage. Structural damage modify the dynamical behaviour of the structure such as mass, stiffened and damping, and consequently the FRFs of the damaged structure in comparison with the FRFs of the sound structure, making possible to identify, to localize and quantify a structural damage.

In order to make use of those techniques, the system must satisfy the following hypotheses:

- ✓ stability: in consequence of an excitation which is present in a definite frequency range, the response of the structure has to be defined into the same range;
- ✓ causality: the response of the structure is the only consequence of the presence of the signal excitation;
- ✓ stationariness: the dynamical characteristics of the structure do not change during the executions of the experimental tests.

II.1 Frequency Response Function (FRF)

The frequency response function represents the relationship between the input and output of electrical systems or structural vibration transmission systems, and is represented by the ratio of the Fourier spectrum of the input $A(f)$ to the Fourier spectrum of the output $B(f)$.



Frequency response function $H(f)$ can be represented by the following expression.

$$H(f) = \frac{B(f)}{A(f)}$$

Each of the denominator and numerator at the right side is multiplied by $A^*(f)$ (complex conjugate of $A(f)$), and $H(f)$ can be represented by expression below.

$$H1(f) = \frac{B(f) * A^*(f)}{A(f) * A^*(f)} = \frac{G_{ab}}{G_{aa}}$$

The denominator is the power spectrum of $A(f)$ and the numerator is the cross spectrum of $A(f)$ and $B(f)$. Therefore, the frequency response function $H(f)$ can be obtained by dividing the cross spectrum for input and output by the power spectrum for input.

The frequency response function can also be obtained by expression below.

$$H2(f) = \frac{B(f) * B^*(f)}{A(f) * B^*(f)} = \frac{G_{bb}}{G_{ab}}$$

Each function has the following characteristic:

✓ H1

If the output signal $b(t)$ contains much external noise, random error can be minimized by averaging. Using a random signal as an input signal, a non-linear system can be linearized by averaging (approximation with method of least squares).

✓ H2

If output signal $b(t)$ contains much external noise, random error can be minimized by averaging. If leakage error is assumed at the resonance point, bias error can be reduced.

When the true frequency response function is $Ht(f)$, if both input and output contain much noise, the following relationship results (when a linear system is assumed).

$$H1(f) \leq Ht(f) \leq H2(f)$$

The phase of $H1(f)$, $H2(f)$ is equal to the phase of cross spectrum G_{ab} .

The relationship with the coherence function is represented by:

$$\gamma^2 = \frac{|G_{ab}|^2}{G_{aa} G_{bb}} = \frac{H1(f)}{H2(f)}$$

which is the ratio of $H1$ to $H2$.

When the ratio of the power spectrum for input and output (transfer characteristic) is $|Ha(f)|^2$,

$$|H(f)|^2 = \frac{G_{bb}}{G_{aa}}$$

Therefore:

$$|H(f)|^2 = |H1| * |H2|$$

If you apply logarithm to both sides of expression:

$$10 \log |H(f)|^2 = \frac{1}{2} (10 \log |H1|^2 + 10 \log |H2|^2)$$

the expression indicates that the average of logarithmic value of the gain of $H1$ and $H2$ is equal to the logarithmic value of the true frequency response function H_a .

The frequency response function can be represented by the gain and phase characteristics. The gain characteristic indicates the amplitude variation when a signal passes through the system. The X-axis denotes the frequency and the Y-axis decibel based on $10 \log_{10} |H(f)|^2$.

The phase characteristic leading or lagging of the phase between the input and output signals. The X-axis denotes the frequency and the Y-axis the angle in degree or radian.

All the calculations executed and reported in this thesis are related to the H1 Frequency Response Functions.

Furthermore, the unit of measurement of the y-axis of all the FRF graphs is Volt/Volt when the piezoceramic patches are used as sensor, and it is $\frac{m/s}{V}$ when the Laser Vibrometer is used as sensor system.

The following graphs show an example of FRF drawing to both linear and logarithmic scale.

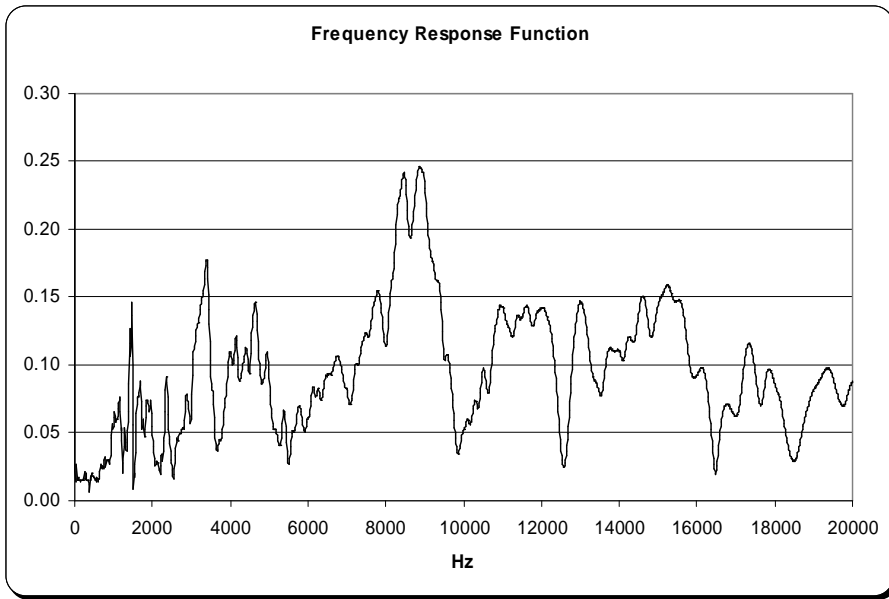


Fig. 2.1.1 – Frequency Response Function – linear

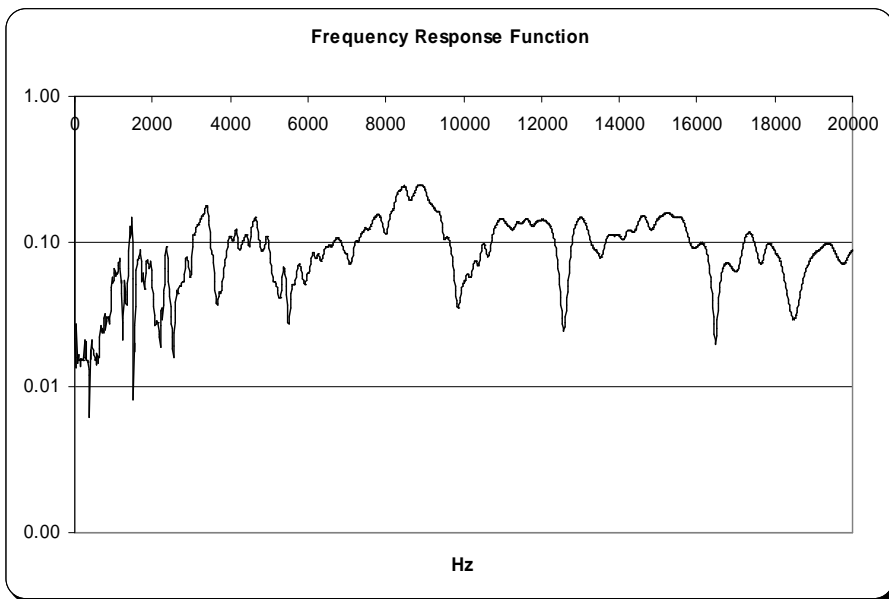


Fig. 2.1.2 – Frequency Response Function – logarithm

II.2 Coherence Function

The coherence function (*coh*) indicates the degree of the correlation between the input and output of a system. It gives a value from 0 to 1 for each frequency. This function, if evaluated between the response and the actuation patch signal presents values very close to 1 if the input and output signal are correlated; those values become much lower at frequencies where the sensor measurements are not correlated with the excitation, or, in other words, where the input mechanical energy does not reach anymore the sensors.

This function is very important to determine if the FRFs acquired are suffering from environmental disturbance as unwanted vibrations, since, when $0 < coh < 1$, presence of noise occurred inside the system or non-linearity or time delay of the system can be assumed.

The coherence function is obtained by the following expression.

$$coh^2(f) = \frac{|G_{ab}(f)|^2}{G_{aa} * G_{bb}}$$

where G_{ab} is the cross spectrum and G_{aa} and G_{bb} are the power spectrum of a and b respectively. The coherence function *coh* is the square of the absolute value of the cross spectrum divided by each power spectrum of the input and output of the system.

The inequality:

$$|G_{ab}(f)|^2 \leq G_{aa}(f) * G_{bb}(f)$$

indicates that if a cross spectrum includes a non-coherent noise, the square of the absolute value of the cross spectrum is lower than the product of the auto spectrum functions.

The coherence function, in its nature, is not meaningful unless averaging is performed.

Practically the coherence function is a quality index of the FRF acquired.

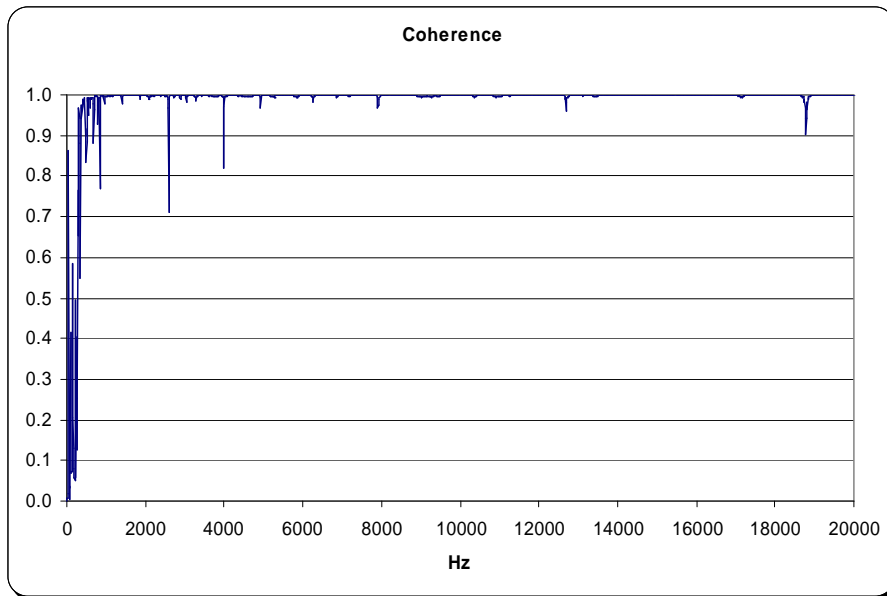


Fig. 2.2.1 – Coherence function

II.3 Damage Indexes

It is common knowledge that structural damages modify the dynamical behaviour of the structure such as mass, stiffened and damping. It has evaluated the variations occurred by means of FRF, which is the ratio between the Fourier transform of the signal used to excite the structure in a point and the Fourier transform of the signal response acquired by a sensor in another point. In fact the FRFs of the sound structure are different from FRFs of the damaged structure. They have determined two damage indexes to evaluate the variations of FRFs of the monitored structure owing to an occurred damage. The indexes give, directly, the measurements of the damage.

The indexes are shown by means of “1” and “2” symbols:

$$Index 1 = \frac{\sum_{i=1}^n |FI_i - FD_i|}{\sum_{i=1}^n FI_i}$$

$$Index 2 = \sum_{i=1}^n \left(\frac{|FI_i - FD_i|}{FI_i} \right) / n$$

FI_i and FD_i are the amplitude of the FRFs of the sound and damaged structure at the “ i ” frequency. “ n ” is the number of the spectral lines we have acquired.

The first index is the ratio between the absolute value of the arithmetic mean of the deviation between FRFs of the sound and damaged structure and the arithmetic mean of the FRFs of the sound structure. The second index is the ratio between the absolute value of the FRFs deviation of the sound and damaged structure and the FRFs of the sound one.

The variable “ n ” is of use of making the second index order of magnitude the same as the first index, so it can be compared the first index with the second.

It can be noted that only the FRF amplitude, and not its phase, is used to calculate the Damage Indexes.

Furthermore, a particular Damage Index has to be mentioned: the sensitivity index, which is determined using FRFs of the healthy structure acquired at different times to measure the experimental error and the environmental noise and vibrations which can influence the FRFs. The following graphs show the possible difference between two FRFs acquired at different times by the same actuator-sensor couple, and referred at the same damaging configuration of a structure.

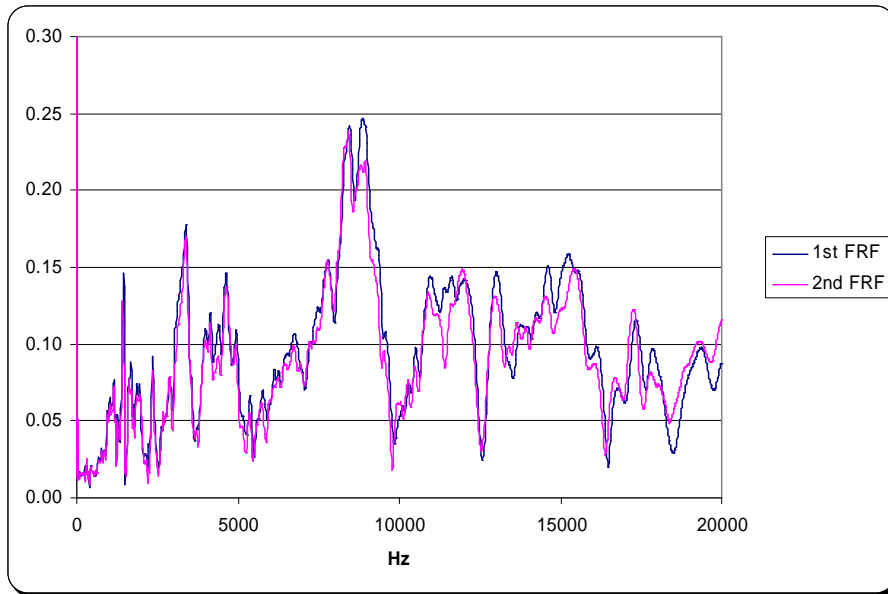


Fig. 2.3.1 – FRFs deviation – linear

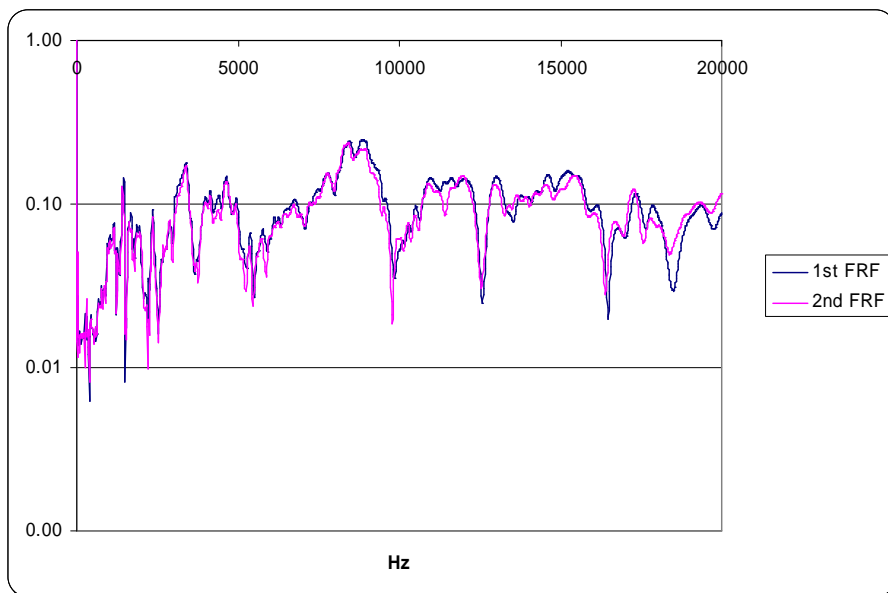


Fig. 2.3.2 – FRFs deviation – logarithmic

Intentionally blank

Chapter III

Neural Network

The Department of Aeronautical Engineering has developed during the last ten years a damage analysis approach based on the comparison of the amplitudes of Frequency Response Functions (FRFs). Differences between healthy and damaged configuration' FRFs represent the basis for the assessment of the health status of the selected structural component; obviously a critical point for the validation of the developed approach consists in a "statistical test" assessing the confidence level relatively to the mentioned amplitude differences in order to verify that FRFs variations were effectively due to structural perturbations instead of environmental influences (noise, temperature, humidity, vibrations, etc...) which excite not linear behaviour of the experimental set-up. That statistical test permits to identify the threshold dividing healthy configurations from damaged ones. Furthermore, to quantify the amplitudes of FRFs differences, it has been developed a dedicated Neural Network algorithm.

III.1 Overview

III.1.1 The Biological inspiration

Neural networks grew out of research in Artificial Intelligence; specifically, attempts to mimic the fault-tolerance and capacity to learn of biological neural systems by modeling the low-level structure of the brain (see Patterson, 1996). The main branch of Artificial Intelligence research in the 1960s -1980s produced Expert Systems. These are based upon a high-level model of reasoning processes (specifically, the concept that our reasoning processes are built upon manipulation of symbols). It became rapidly apparent that these systems, although very useful in some domains, failed to capture certain key aspects of human intelligence. According to one line of speculation, this was due to their failure to mimic the

underlying structure of the brain. In order to reproduce intelligence, it would be necessary to build systems with a similar architecture.

The brain is principally composed of a very large number (circa 10,000,000,000) of *neurons*, massively interconnected (with an average of several thousand interconnects per neuron, although this varies enormously). Each neuron is a specialized cell which can propagate an electrochemical signal. The neuron has a branching input structure (the dendrites), a cell body, and a branching output structure (the axon). The axons of one cell connect to the dendrites of another via a synapse. When a neuron is activated, it *fires* an electrochemical signal along the axon. This signal crosses the synapses to other neurons, which may in turn fire. A neuron fires only if the total signal received at the cell body from the dendrites exceeds a certain level (the firing threshold).

The strength of the signal received by a neuron (and therefore its chances of firing) critically depends on the efficacy of the synapses. Each synapse actually contains a gap, with neurotransmitter chemicals poised to transmit a signal across the gap. One of the most influential researchers into neurological systems (Donald Hebb) postulated that learning consisted principally in altering the "strength" of synaptic connections. For example, in the classic Pavlovian conditioning experiment, where a bell is rung just before dinner is delivered to a dog, the dog rapidly learns to associate the ringing of a bell with the eating of food. The synaptic connections between the appropriate part of the auditory cortex and the salivation glands are strengthened, so that when the auditory cortex is stimulated by the sound of the bell the dog starts to salivate. Recent research in cognitive science, in particular in the area of nonconscious information processing, have further demonstrated the enormous capacity of the human mind to infer ("learn") simple input-output covariations from extremely complex stimuli (e.g., see Lewicki, Hill, and Czyzewska, 1992).

Thus, from a very large number of extremely simple processing units (each performing a weighted sum of its inputs, and then firing a binary signal if the total input exceeds a certain level) the brain manages to perform extremely complex tasks. Of course, there is a great deal of complexity in the brain which has not been

discussed here, but it is interesting that artificial neural networks can achieve some remarkable results using a model not much more complex than this.

III.1.2 History of the neural network analogy

The concept of neural networks started in the late-1800s as an effort to describe how the human mind performed. These ideas started being applied to computational models with the Perceptron.

In early 1950s Friedrich Hayek was one of the first to posit the idea of spontaneous order in the brain arising out of decentralized networks of simple units (neurons). A design issue in cognitive modeling, also relating to neural networks, is additionally a decision between holistic and atomism, or (more concrete) modular in structure.

The Perceptron learning algorithm incrementally refines the weight vector with training data to improve the decision space. The Perceptron's main problem is the requirement for the input vectors to be linearly independent for proper classification to occur.

The Cognitron (1975) was the first multilayered neural network. The actual structure of the network and the methods used to set the interconnection weights change from one neural strategy to another, each with its advantages and disadvantages. Networks can propagate information in one direction only, or they can bounce back and forth until self-activation at a node occurs and the network settles on a final state. The ability for bi-directional flow of inputs between neurons/nodes was produced with the Hopfield's network (1982), and specialization of these node layers for specific purposes was introduced through the first hybrid network.

The parallel distributed processing of the mid-1980s became popular under the name connectionism.

The backpropagation network (1986) is a commonly used neural network. It often uses a sigmoid activation function and adjustments to the weight vector as a learning rate, depends upon error propagation in a backwards method. The problem with backpropagation is its susceptibility to over-determination of the decision space.

Cross-validation is one means of addressing this problem, but recent improvements address this problem with Bayesian neural networks. This combines the field of statistics with neural networks to lower the importance of redundant training sets.

III.2 Neural Network application to Health Monitoring

The damage identification problem can be classified as a typical example of binary learning (“healthy” or “damaged”). A neural network able to implement binary learning can be modelled following two approaches: the “discrimination-based learning” and the “recognition-based learning”. In the first approach the network is trained using both “positive” and “negative” samples in order to learn how to discriminate among them; in the second one the network is trained using only “positive” samples and it is able to recognise only these.

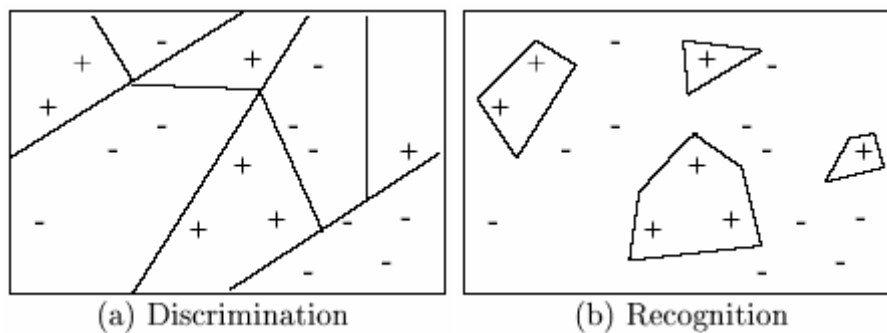


Fig. 3.2.1 – Binary learning approaches

Within this research has been implemented a system based on the latter approach; the damage analysis represents, actually, a typical engineering problem for which it is almost impossible to forecast all the “negative” events, since this would mean to be able to discover all the possible perturbations that a structural component would suffer as damage.

The engine of the damage analysis system is represented by an “autoassociative” neural network (or “auto-encoder”) made of three layers: an input one, an hidden one and obviously the output one, fully connected one each other [3].

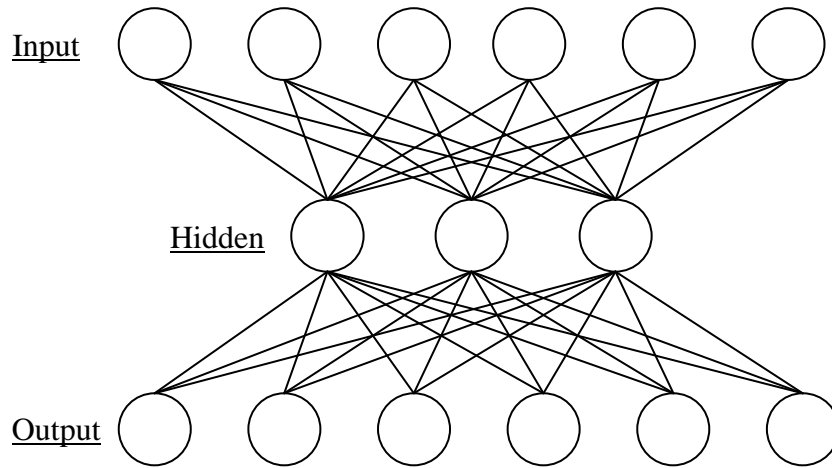


Fig. 3.2.2 – Neural Network layers

An auto-associative neural network is a feed forward type network trained only by positive samples in order to rebuild the input on the output layer.

A typical feed-forward network has neurons arranged in a distinct layered topology. The input layer is not really neural at all: these units simply serve to introduce the values of the input variables. The hidden and output layer neurons are each connected to all of the units in the preceding layer. Again, it is possible to define networks that are partially-connected to only some units in the preceding layer; however, for most applications fully-connected networks are better.

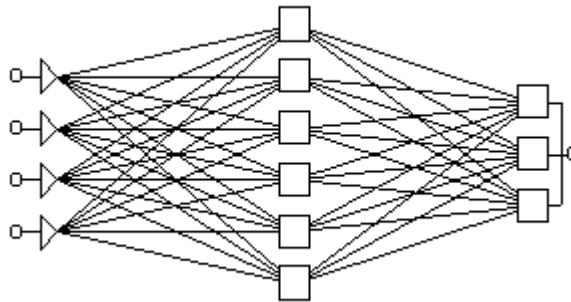


Fig. 3.2.3 – Feed-forward scheme

When the network is executed (used), the input variable values are placed in the input units, and then the hidden and output layer units are progressively executed. Each of them calculates its activation value by taking the weighted sum of the outputs of the units in the preceding layer, and subtracting the threshold. The activation value is passed through the activation function to produce the output of the neuron. When the entire network has been executed, the outputs of the output layer act as the output of the entire network.

If the training phase is successful the network is able to find the common features that samples present in order to extract few general laws permitting to recognise positive unknown examples. This learning technique is therefore called “Redundancy Compression and Non-Redundancy Differentiation”. In that case the positive samples are represented by the “healthy” configuration’ FRFs. Following the training phase, the auto-encoder will be able to reconstruct more or less accurately on the output layer the positive samples, while it will always reconstruct wrongly the negative samples. That implies that a bad reconstruction of the input layer on the output one is a clear symptom of an anomalous dynamic behaviour of the monitored structure.

Once the auto-encoder has been implemented and trained, in order to use it as a “classifier” for the health status of a structural component, it is necessary to complete the system by an other component permitting the determination of a threshold for dividing operatively the two samples classes (positive or “healthy” and negative or “damaged”). To do so it will be preliminary necessary to create an index quantifying the reconstruction level of the input layer on the output one; it is obviously directly related to the reconstruction error that the network presents when trying to recreate the input on its output layer. The error, on its side, will be bigger about negative samples then positive ones [4]. For the training technique we used an error back-propagation technique. Training algorithm make the error, which is present on the output layer, follow the opposite route across the links between output and hidden layers. In back propagation, the gradient vector of the error surface is calculated. This vector points along the line of steepest descent from the current point, so we know that if we move along it a "short" distance, we will decrease the error. A sequence of such moves (slowing as we near the bottom) will eventually

find a minimum of some sort. The difficult part is to decide how large the steps should be.

Large steps may converge more quickly, but may also overstep the solution or (if the error surface is very eccentric) go off in the wrong direction. A classic example of this in neural network training is where the algorithm progresses very slowly along a steep, narrow, valley, bouncing from one side across to the other. In contrast, very small steps may go in the correct direction, but they also require a large number of iterations. In practice, the step size is proportional to the slope (so that the algorithm settles down in a minimum) and to a special constant: the learning rate. The correct setting for the learning rate is application-dependent, and is typically chosen by experiment; it may also be time-varying, getting smaller as the algorithm progresses.

The algorithm is also usually modified by inclusion of a momentum term: this encourages movement in a fixed direction, so that if several steps are taken in the same direction, the algorithm "picks up speed", which gives it the ability to (sometimes) escape local minimum, and also to move rapidly over flat spots and plateaus.

The algorithm therefore progresses iteratively, through a number of epochs. On each epoch, the training cases are each submitted in turn to the network, and target and actual outputs compared and the error calculated. This error, together with the error surface gradient, is used to adjust the weights, and then the process repeats. The initial network configuration is random, and training stops when a given number of epochs elapses, or when the error reaches an acceptable level, or when the error stops improving (you can select which of these stopping conditions to use).

III.2.1 Implementation of the “auto-associative network”

If we have x actuators and y sensors on a generic monitored structure, after a test campaign, xy FRFs (x actuators * y sensors) are available. Note that we are interested in using only the FRFs amplitude and not their phase.

It had avoided to implement a single neural network including all the FRFs due to the high number of neurones needed (if we have, for example, $x = 10$ and $y =$

10 and n (number of spectral lines) = 1600, we have $xy * n = 160000$ neurones). Also considering to implement a single network where neurones were associated with FRFs, some problems were forecasted: in such case in fact it could have been possible that for distinct experimental campaigns two FRFs related to different sensor-actuator couples resulted very similar; this would be a symptom of structural modifications but the network could deduce the opposite situation if the actuator-sensor couple is not explicitly declared. In the end it has employed only one kind of network which is trained separately for each actuator-sensor couple. That has resulted in $(x * y)$ neural networks equal from an architectural point of view but each one trained by FRFs referred to the healthy configuration and measured by a specific actuator-sensor couple. The neural net algorithm was implemented in MATLAB environment by using Neural Networks Toolbox.

III.2.2 Reconstruction index

Once completed the training phase it raised up the problem on how to concretely employ the networks for identifying damage. The idea was to develop a “reconstruction” index representing the ability of the networks in rebuilding (and as a consequence, recognise) the input FRFs received. A good recognition level would have been connected with a “healthy” status of our structure. It has been defined for each network the individual reconstruction error between input I and output O:

$$E_n = (O_n - I_n)^2 \quad n=1, \dots, N$$

where n represents the number of neurones (or acquired FRFs spectral lines). Following it has been defined an overall index of reconstruction of the input vector as:

$$R = \text{mean}(E_n) + \text{spread}(E_n)$$

where “mean” is the individual error mean and “spread” represents a measurement of their dispersion in a statistic sense. It is possible to plot a graph S(R) of the output of the neural network obtained. That graph shows, for each value of R, the ratio

between the FRFs (used for the post process), which have a reconstruction R value higher than the fixed one, and the total number of FRFs acquired during a single test campaign. The range of S is from 0 to 1. Practically, the curve $S(R)$ is an estimator of the healthy status of the panel.

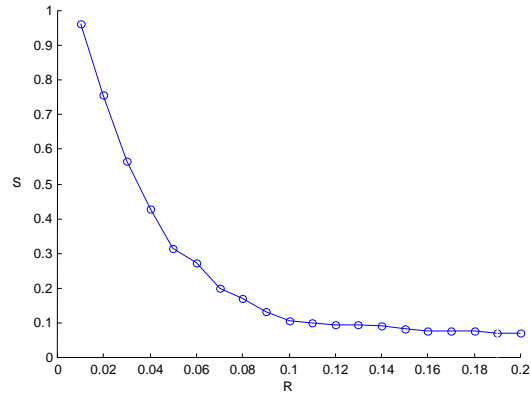


Fig. 3.2.4 – Reconstruction curve

III.2.3 Choice of the dispersion measurement

In order to obtain the best statistical dispersion measurement index an evaluation of the probability distribution of E_n has been carried on: firstly, supposing the probability distribution of errors as a normal distribution the “standard deviation” was considered as “spread” index. To confirm this choice a simple test was considered: the FRFs acquired during a single campaign were perturbed using a “variable” normal distribution. After the reconstruction curve was evaluated considering as “spread” both the standard deviation (std) and the “interquartile range” (iqr).

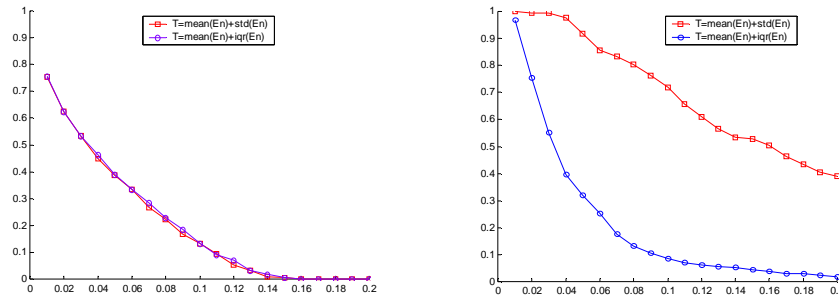


Fig. 3.2.5 – Reconstruction. curves for perturbation normally distributed and for “real” perturbation distribution

After this test the probability distribution of disturbances in experimental data was estimated and assigned to the same reference FRFs of the previous case. Figure 5 shows that estimating the dispersion measurement through the standard deviation the curve’s shape becomes different from that obtained by experimental data. Employing the interquartile range the experimental curve shape is well fitted. For this reason interquartile range was chosen as dispersion measurement.

III.2.4 “Threshold” evaluation

This subparagraph reports how the threshold was evaluated by means of several acquisition campaigns of FRFs of the undamaged aeronautical composite panel.

Even if no damage has occurred, FRFs, which have been acquired for each actuator-sensor couple on different times, could be not equal between them because of environmental disturbance. Once the FRFs of the sound structure are settled, the more different FRFs are the higher reconstruction error is, even if the damage is not present. For that reason is very important to consider the FRF maximum discrepancy of an actuator-sensor couple such that the neural network is able to reconstruct the input correctly. To do this the $(x * y)$ FRFs of the sound structure have been perturbed by means of increasing disturbance so much that it has been possible to specify the limit. In order to perturb the reference FRFs it has summed to each FRF a vector having the same dimension. Random values, whose probability distribution

is normal with a variable mean and standard deviation, form the vector. Those random values have the same order of magnitude as FRF; to make the number of generated negative values negligible, since FRFs magnitudes are positive quantities, the mean has been restricted to be greater or, at least, equal to the standard deviation. The measurement noise modifies the probability distribution (as well the FRFs). Therefore the real probability distribution does not agree with the common normal distribution.

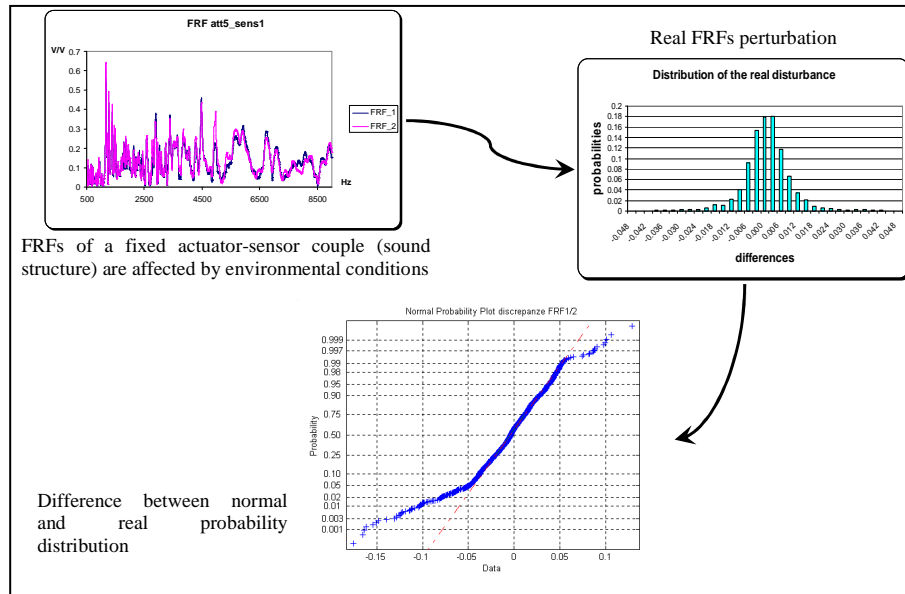


Fig. 3.2.6 – FRFs perturbation

If we consider this difference acceptable, we can generate vectors with random values, which have a normal probability distribution, by means of the following MATLAB command:

✓ Random numbers from the normal distribution

$R = \text{normrnd}(\text{MU}, \text{SIGMA}, m, n)$

That expression generates normal random numbers with parameters MU and SIGMA, where scalars m and n are the row and column dimensions of R.

After estimating the order of magnitude of the reference FRFs, we have generated perturbing vectors whose values have a mean and a standard deviation,

whose range is, for example, from 0,005 to 0,4. Therefore, this kind of analytically perturbed vector is characterised by normal probability distribution values (mean plus standard deviation).

Then, such vectors have been added to the reference FRFs so as to generate two various families of perturbed FRFs. First family (figure 3.2.7) has been determined assuming the same disturbance, having a mean greater or, at least, equal to the standard deviation, for all reference FRFs. The relevant curves are characterised by a quick descent of the parameter S from 1 to 0.

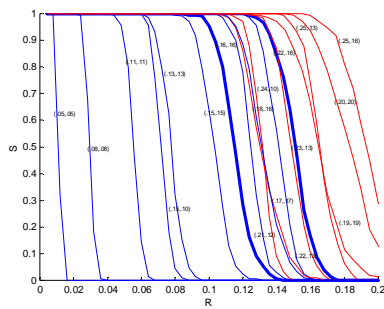


Fig. 3.2.7 – First family

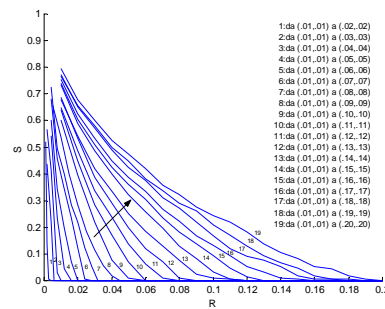


Fig. 3.2.8 – Second family

Second family (figure 3.2.8) has arisen from considering that a real disturb modify the 36 FRFs acquired during a campaign, which represent the healthy status of the panel in a particular instant, with several quantities; with this object in view perturbations having several intensities (mean and standard deviation which vary from (0,005;0,001) to (0,4;0,4)) have been imposed randomly to the reference FRFs. If we take in account the output of the neural network whose input data are the gradually increasing perturbations of the second family FRFs, we note that the reconstruction error increase and the estimator curves shift coherently toward the right.

After having trained a neural network it is possible to estimate the error which is in its output by means of the analysis of the linear regression between the network output and the corresponding target (during the training we assume that

target coincides with input data). In order to do this analysis, MATLAB places the postreg routine at our disposal.

```
a = sim(net,p)
[m,b,r] = postreg (a,t)
```

That routine gives three parameter: m, b and r. The parameter m and b represent, respectively, the slope and the intercept (with ordinate axes) of the straight line, which is the best interpolation curve of the point which correspond to the output-target couple. It is obvious that the reconstruction curve of the neural network would be perfect if the best fit line coincided with the line $A = T$ (output = target): in that case $m = 1$ and $b = 0$. The third parameter r represents the correlation coefficient between output and target; its optimal value is 1. That routine can be used to estimate the deviation of the correlation parameter r from its optimal value when it inputs into the network the reference 36 FRFs which are perturbed with the same increasing disturbance whose mean is equal to the standard deviation.

On the base of experimental experiences a maximum 20% error of the correlation parameter r has been fixed (maximum acceptable disturbance having mean = standard deviation = 0,065).

According to the above defined maximum error the correlation coefficient r can be evaluated with reference to the first family FRFs. These FRFs have been perturbed using disturbances whose mean value is different from the standard deviation.

That FRFs can give rise to the maximum value of r with several mean-standard deviation couple. Besides it can be evaluated the relevant estimating curves $S(R)$.

Then we can identify two boundary curves R_{lim1} and R_{lim2} .

- if there is an analytic disturbance whose mean is less or equal to 0,0099, independently from the standard deviation (whose value is equal to the mean, at most), the reconstruction curve of the perturbed FRFs is correct;

- if there is an analytic disturbance whose mean is less or equal to 0,1, independently from the standard deviation, the reconstruction curve is wrong and represents a damage;
- if there is an analytic disturbance whose mean is included between 0,0099 and 0,1, the reconstruction curve is correct or wrong depending on the standard deviation.

Therefore all sound structure estimator curves are placed on the left of the R_{lim1} curve, while all damaged structure estimator curves are placed on the right of the R_{lim2} one.

Between R_{lim1} and R_{lim2} there are all the other estimator curves whose position, with regard to the threshold, need to rate for estimating the state of health of the monitored panel. As regards the panel we have considered, the boundary curve R_{lim1} is the estimator curve of the reference FRFs which have been perturbed using the disturbance (0,0099 ; 0,0099), while the boundary curve R_{lim2} is the estimator curve of the reference FRFs which have been perturbed using the disturbance (0,1;0,1). Therefore it is possible to identify two bound values of the reconstruction index R which practically coincide with the values of R which are determined by the intersection between R_{lim1} , R_{lim2} and the x axes. The lower value is equal to 0,0025.

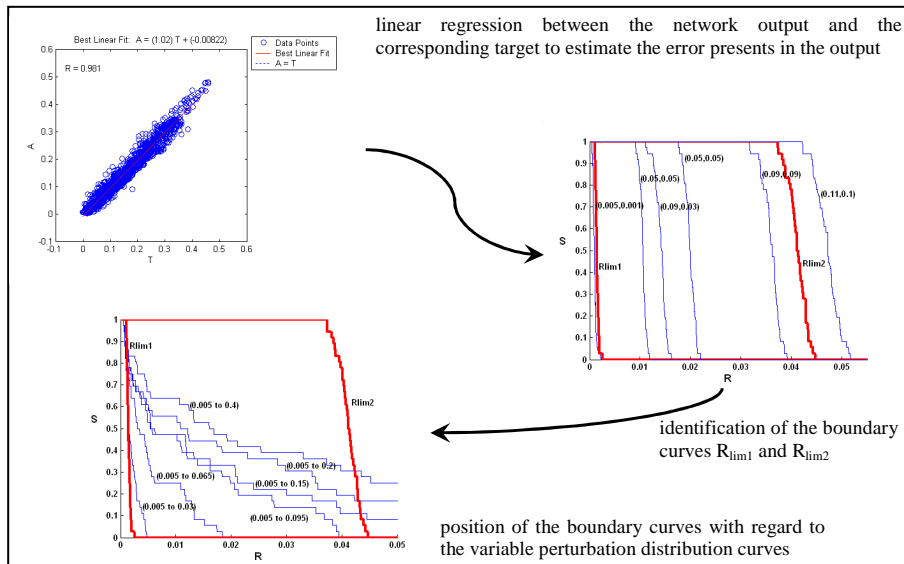


Fig. 3.2.9 – Boundary curves of R index

As subsequent step the estimator curves of the perturbed FRFs of the second family have been drawn, and their position with regard to the boundary curves has been estimated.

To evaluate the threshold, first of all, it has identified the estimator curve of the second family which intercept the R_{lim1} and the x axes. The interception between that curve of the second family and the vertical line, which starts from the intersection between the x axes and the R_{lim1} curve, fixes the healthy status threshold.

If an estimator curve of the healthy status of the panel passes under the threshold, the panel is considered to be sound. If that curve passes over the threshold, a damage has occurred. In that case the damage size is proportional to the gap between the threshold value and the value of S, which has been determined by the intersection between the estimator curve at issue and the vertical line going through the threshold value (threshold line).

III.3 Neural Network algorithm

III.3.1 Training

The list of the training algorithm is reported in this subparagraph. The training of all the test articles was carried out by means of the Matlab Neural Network Toolbox. Then, the algorithm has been adapted for each experimental configuration.

For meaning of the algorithm' instructions please refer to a Matlab user's manual.

```
% Neural Network training;
% firstly load the FRF of the sound structure;
% the vectors used for the network training must be identified as
% Pd=Atti-Senj, with d=1..30;
% Pd is a matrix since there are more acquisition for each actuator-sensor couple;
% each neural network is called FRFdnet, with d=1..30;

P1=[Train02(:,1) Train03(:,1) ..... Train08(:,1)];
P2=[Train02(:,2) Train03(:,2) ..... Train08(:,2)];
...
...
...
P30=[Train02(:,30) Train03(:,30) ..... Train08(:,30)];
for i=1:681
    R(i,:)=[0 0.01];
end
% the reduced frequency range is 90 (number of hidden neurones);
for i=1:56
    d=num2str(i)
    istr=strcat('FRF',d,'net=network;');
    eval(istr);
```

```
istr=strcat('FRF',d,'net.numInputs=1;');
eval(istr);
istr=strcat('FRF',d,'net.inputs{1}.size=281;');
eval(istr);
istr=strcat('FRF',d,'net.inputs{1}.range=R;');
eval(istr);
istr=strcat('FRF',d,'net.numLayers=2;');
eval(istr);
istr=strcat('FRF',d,'net.layers{1}.size=40;');
eval(istr);
istr=strcat('FRF',d,'net.layers{2}.size=281;');
eval(istr);
istr=strcat('FRF',d,'net.biasConnect=[1;1];');
eval(istr);
istr=strcat('FRF',d,'net.inputConnect=[1;0];');
eval(istr);
istr=strcat('FRF',d,'net.layerConnect=[0 0;1 0];');
eval(istr);
istr=strcat('FRF',d,'net.outputConnect=[0 1];');
eval(istr);
istr=strcat('FRF',d,'net.targetConnect=[0 1];');
eval(istr);
istr=strcat('FRF',d,'net.layers{1}.transferFcn='tansig');');
eval(istr);
istr=strcat('FRF',d,'net.layers{2}.transferFcn='purelin');');
eval(istr);
istr=strcat('FRF',d,'net.initFcn='initlay');');
eval(istr);
istr=strcat('FRF',d,'net.performFcn='mse');');
eval(istr);
istr=strcat('FRF',d,'net.trainFcn='traingdx');');
eval(istr);
```

```
istr=strcat('FRF',d,'net.layers{1}.initFcn='initnw');  
eval(istr);  
istr=strcat('FRF',d,'net.layers{2}.initFcn='initwb');  
eval(istr);  
istr=strcat('FRF',d,'net.biases{2}.initFcn='initzero');  
eval(istr);  
istr=strcat('FRF',d,'net.biases{1}.learn=1;');  
eval(istr);  
istr=strcat('FRF',d,'net.biases{2}.learn=1;');  
eval(istr);  
istr=strcat('FRF',d,'net.inputWeights{1,1}.learn=1;');  
eval(istr);  
istr=strcat('FRF',d,'net.layerWeights{2,1}.initFcn='initzero');  
eval(istr);  
istr=strcat('FRF',d,'net.layerWeights{2,1}.learn=1;');  
eval(istr);  
istr=strcat('FRF',d,'net.trainParam.show=10;');  
eval(istr);  
istr=strcat('FRF',d,'net.trainParam.lr=0.05;');  
eval(istr);  
istr=strcat('FRF',d,'net.trainParam.lr_inc=1.05;');  
eval(istr);  
istr=strcat('FRF',d,'net.trainParam.lr_dec=0.7;');  
eval(istr);  
istr=strcat('FRF',d,'net.trainParam.mc=0.9;');  
eval(istr);  
istr=strcat('FRF',d,'net.trainParam.min_grad=1e-10;');  
eval(istr);  
istr=strcat('FRF',d,'net.trainParam.epochs=300;');  
eval(istr);  
istr=strcat('FRF',d,'net.trainParam.goal=1.0e-6;');  
eval(istr);
```

```
istr=strcat('T=P',d,','');
eval(istr);
% initialization;
istr=strcat('FRF',d,'net=init(FRF',d,'net)');
eval(istr);
% training;
istr=strcat('[FRF',d,'net,tr]=train(FRF',d,'net,P',d,',T)');
eval(istr);
% simulation;
istr=strcat('A',d,'=sim(FRF',d,'net,P',d,','');
eval(istr);
end
```

The following curve represents a typical graphic output of the training phase.

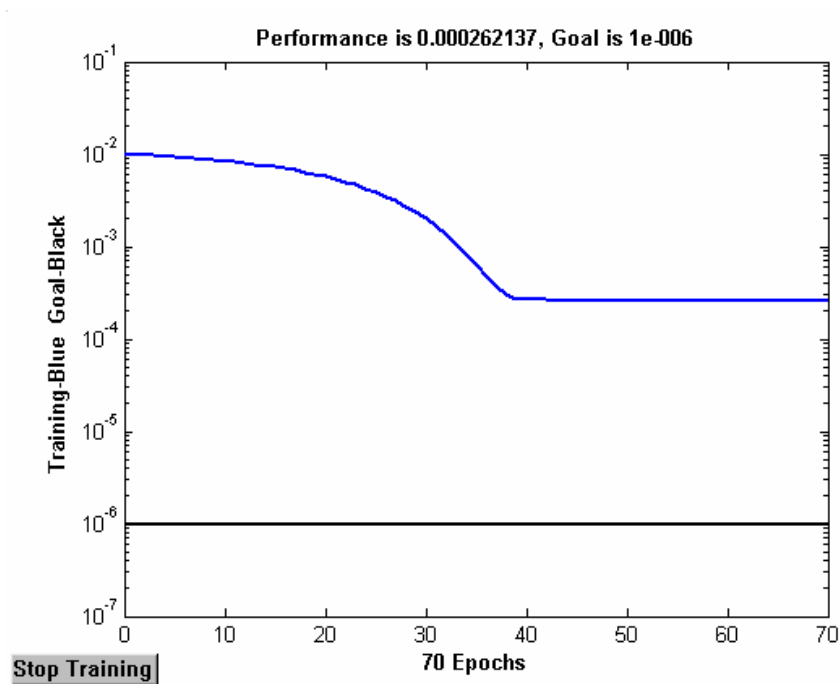


Fig. 3.3.1 – Training output curve

III.3.2 Post Process

Once the training phase has been executed, the post process phase serves to recognize the unknown samples, furnished by FRFs, as representatives of a sound or damaged configuration of the structure. In this subparagraph the list of the post process algorithm is reported.

```

% Postprocessing to calculate the matrix reconstruction index R;
% firstly load the workspace with all the training variables;
% select the file with data to be post-processed (damage condition = FRFdam.dat);

istrmat=strcat('Mathr=[]');
% acquisition;
for i=1:30
    d=num2str(i);
    istr=strcat('v',d,'=[FRFdam(:,',d,')]');
    eval(istr);
    istr=strcat('a',d,'=sim(FRF',d,',net,v',d,')');
    eval(istr);
    istr=strcat('at',d,'=a',d,',''');
    eval(istr);
    istr=strcat('pt',d,'=v',d,',''');
    eval(istr);
    istr=strcat('med',d,'=mean(FRFdam(:,',d,')-P',d,',(:,1)));');
    eval(istr);
    istr=strcat('medabs',d,'=mean(abs(FRFdam(:,',d,')-P',d,',(:,1)));');
    eval(istr);
    istr=strcat('diqr',d,'=iqr(FRFdam(:,',d,')-P',d,',(:,1)));');
    eval(istr);
    istr=strcat('devst',d,'=std(FRFdam(:,',d,')-P',d,',(:,1)));');
    eval(istr);

```

```

istr=strcat('Med',d,'=mean((at',d,'-pt',d,').^2);');
eval(istr);
istr=strcat('Diqr',d,'=iqr((at',d,'-pt',d,').^2);');
eval(istr);
istr=strcat('Devst',d,'=std((at',d,'-pt',d,').^2);');
eval(istr);
istr=strcat('R1',d,'=Med',d,'+Diqr',d,');');
eval(istr);
istr=strcat('R2',d,'=Med',d,'+Devst',d,');');
eval(istr);
istrmat=strcat(istrmat,'med',d,',medabs',d,',diqr',d,',devst',d,',Med',d,',Diqr',d,
',Devst',d,',R1',d,',R2',d,');');

end

istrmat=strcat(istrmat,'];');
eval(istrmat);

% S(R) curve;
E=Mathr(:,9);
istr=strcat('e=[');
for n=1:2000
    Th=n*0.00005;
    nc=0;
    for i=1:30
        if E(i)<=Th
            nc=nc+1;
        end
    end
    nc=30-nc;
    pr=nc/30;
    dt=num2str(Th);
    dn=num2str(nc);
    dp=num2str(pr);

```

```
    istr=strcat(istr,dt,',' ,dn,',' ,dp,',' );  
end  
istr=strcat(istr,dt,',' ,dn,',' ,dp,']');  
eval(istr);  
hold on  
plot(e(:,1),e(:,3));  
end
```

Chapter IV

Experimental Set-up

In this chapter both the instruments and the test-articles, which have been used for the execution of the experimental tests itemized in the next chapter, are reported. About the first and the second test articles the place where the experimental tests have been executed is the Acoustics and Vibrations Laboratory of the Department of Aeronautical Engineering of the University of Naples “Federico II”, while the place where experimental tests on the ATR-72 aircraft have been executed is the Toulouse airport (France).

IV.1 Instruments

Several signal generators and spectrum analysers have been used to execute the experimental tests. Moreover a piezoceramic amplifier and current amplifiers for magnetostrictive actuators and, of course, either piezoceramic patches, which can work both as actuators and sensors, or magnetostrictive actuators have been used.

IV.1.1 Generators and spectrum analysers

Two generators and spectrum analyser made by the ONO SOKKI company have been used. The models are the CF-350 and the DS-2100.



Fig. 4.1.1 – ONO SOKKI CF-350



Fig. 4.1.2 – ONO SOKKI DS-2100

The ONO SOKKI CF-350 has two input channels, one output channel and an input and output frequency range up to 40 kHz.

The ONO SOKKI DS-2100 has four input channels, one output channel, an input frequency range up to 40 kHz and an output frequency range up to 20 kHz.

Furthermore the Scanning Laser Vibrometer PSV-400 by the Polytec company has been used as well. It has three input channels more an input channel reserved to the laser data output, three output channels, an input frequency range up to 1 MHz and an output frequency range up to 512 kHz.

The Scanning Laser Vibrometer is a velocity sensor system. It is able to measure the distribution of vibration velocities of an object, on the basis of laser interferometry, orthogonally to the laser beam. It can quickly acquire from a large number of points of the object, since it is able to deflect the direction of the beam by means of two mirrors driven by fast piezoelectrical motors.

The light source of the vibrometer is a helium neon laser. It is a Class 2 product.



Fig. 4.1.3 – Polytec PSV-400



Fig. 4.1.4 – Laser head

A generator can furnish several kind of signals, as:

- Sine;
- Swept sine;
- Impulse;
- Random.

From among all these signals, the swept sine has been chosen. The swept sine is a sinusoidal signal whose amplitude is constant in the selected frequency range. So it is possible to excite a structure with the same intensity at all frequencies.

About the frequency range the experimental tests have been carried out from 0 Hz to 10 kHz. Sometimes from 0 Hz to 20 kHz. Moreover, the voltage output of generators can vary from 0 Volt to 2, 5 or 10 Volt depending on the device. In any test the maximum possible voltage for the used device has been chosen.

All the generators devices are able to work as spectrum analyzer.

The following graph represents a swept sine signal generated from 0 Hz to 20 kHz. It can be observed that at the highest frequencies the spectrum shows an higher amplitude since it is feeling the impedance of a piezoceramic patch which was working, at that time, as actuator, and it was receiving the signal by the generator.

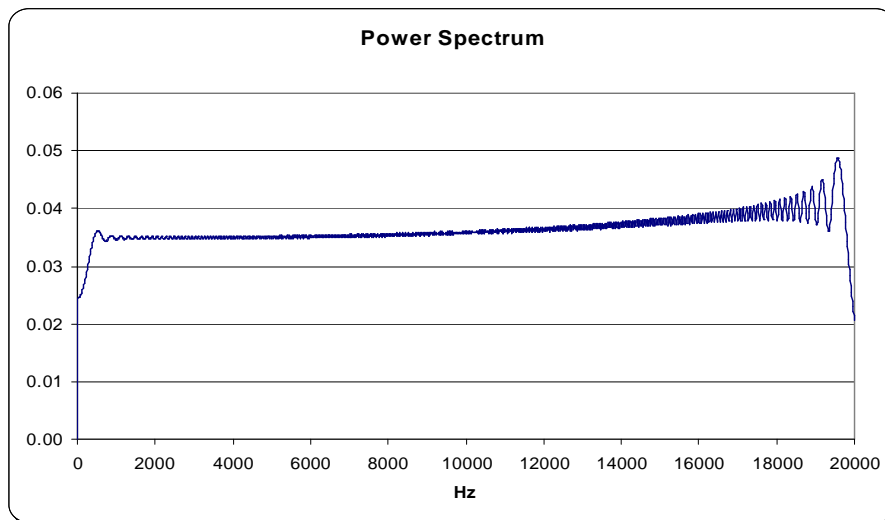


Fig. 4.1.5 – Swept sine signal

IV.1.2 Amplifiers

An amplifier is a device which amplifies the amplitude of the signal produced by the generator.

Three different amplifiers have been used:

- Audio amplifier UP2301;
- LDS amplifier PA500;
- TREK amplifier.

The first one is a current amplifier which has been used to amplify the excitation signal for the magnetostrictive actuators. It has an adjustable gain.



Fig. 4.1.6 – Audio amplifier

The second one is another current amplifier which has been used to amplify the excitation signal for the magnetostrictive actuators. It also has an adjustable gain.



Fig. 4.1.7 – LDS amplifier

The third one is a voltage amplifier which has been used to amplify the excitation signal for the piezoceramic patches. It has a fixed gain which multiplies the signal voltage amplitude 25 times.



Fig. 4.1.8 – TREK amplifier

IV.1.3 Piezoceramic devices

Several piezoceramic patches Stetner PPK23 have been used as actuators and sensors, having a square and rectangular shape whose dimension is 30 x 30 mm or 20 x 30 mm and a thickness equal to mm.0,5 or mm.1.

The piezoceramic patches have been bonded on the structures by means of a bicomponent epoxy adhesive.

The piezoceramic patches are made of piezoelectric material. The piezoelectricity is the ability of certain crystals to generate a voltage in response to applied mechanical stress. The word is derived from the Greek “*piezein*”, which means to squeeze or press. The piezoelectric effect is reversible; piezoelectric crystals, subject to an externally applied voltage, can change shape by a small amount. The deformation, about 0.1% of the original dimension in PZT, is of the order of nanometers. The lead zirconium titanate (PZT, also Lead zirconate titanate) is a ceramic perovskite material that shows a marked piezoelectric effect - that is, it develops a voltage difference across two of its faces when compressed, and ferroelectric effect. It also features an extremely large dielectric constant.

Of the thirty-two crystal classes, twenty-one are non-centrosymmetric (not having a centre of symmetry), and of these, twenty exhibit direct piezoelectricity the remaining one being the cubic class 432. Ten of these are polar (i.e. spontaneously polarize), having a dipole in their unit cell, and exhibit pyroelectricity. If this dipole can be reversed by the application of an electric field, the material is said to be ferroelectric.

- Piezoelectric Crystal Classes: 1, 2, m, 222, mm2, 4, -4, 422, 4mm, -42m, 3, 32, 3m, 6, -6, 622, 6mm, -62m, 23, -43m;
- Pyroelectric: 1, 2, m, mm2, 4, 4mm, 3, 3m, 6, 6mm.

In a piezoelectric crystal, the positive and negative electrical charges are separated, but symmetrically distributed, so that the crystal overall is electrically neutral. Each of these sites forms an electric dipole and dipoles near each other tend to be aligned in regions called Weiss domains. The domains are usually randomly oriented, but can be aligned during poling, a process by which a strong electric field is applied across the material, usually at elevated temperatures.

When a stress is applied, this symmetry is disturbed, and the charge asymmetry generates a voltage across the material. For example, a 1 cm cube of quartz with 500 lbf (2 kN) of correctly applied force upon it, can produce 12.500 V of electricity.

Piezoelectric materials also show the opposite effect, called converse piezoelectricity, where the application of an electrical field creates mechanical deformation in the crystal.

Piezoelectricity is the combined effect of the electrical behavior of the material:

- Charge Density, $D = \text{Permittivity} \times \text{Electric Field, } E$

and Hooke's Law:

- Strain, $S = \text{Compliance, } s \times \text{Stress, } T$

This may be expressed as:

$$\{S\} = [s^E]\{T\} + [d]\{E\}$$

$$\{D\} = [d]^t + [\epsilon^T]\{E\}$$

The bending forces generated by converse piezoelectricity are extremely high, of the order of tens of millions of pounds (tens of meganewtons), and usually cannot be constrained. The only reason the force is usually not noticed is because it causes a displacement of the order of few nanometers.

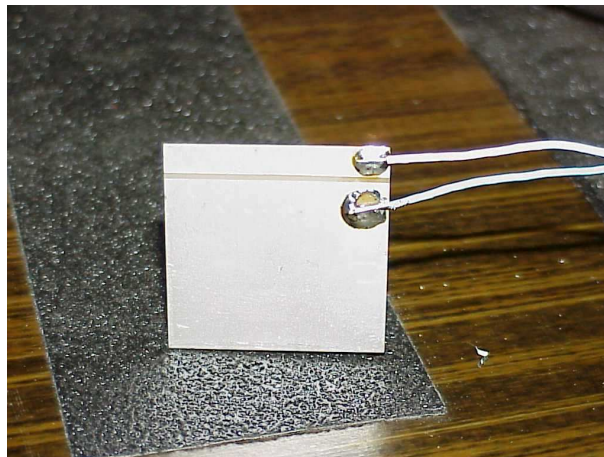


Fig. 4.1.9 – Piezoceramic patch

During a test, in consequence of an irregular behaviour of a piezoceramic patch bonded on the aeronautical composite panel, it has been necessary to verify if that patch had been working properly or not. The use of the Laser Vibrometer has permitted to analyze the behaviour of the patch which had been used as sensor. The surface of two patches during a FRF acquisition have been scanned by the laser. The patch located in the centre of the panel had been working as actuator.

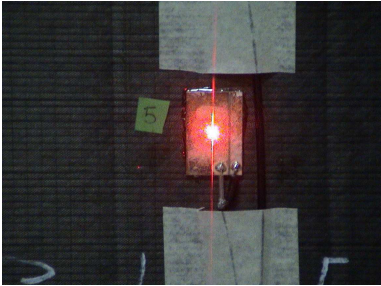


Fig. 4.1.10 – Laser beam

The output of the vibrometer is reported in the next figure:

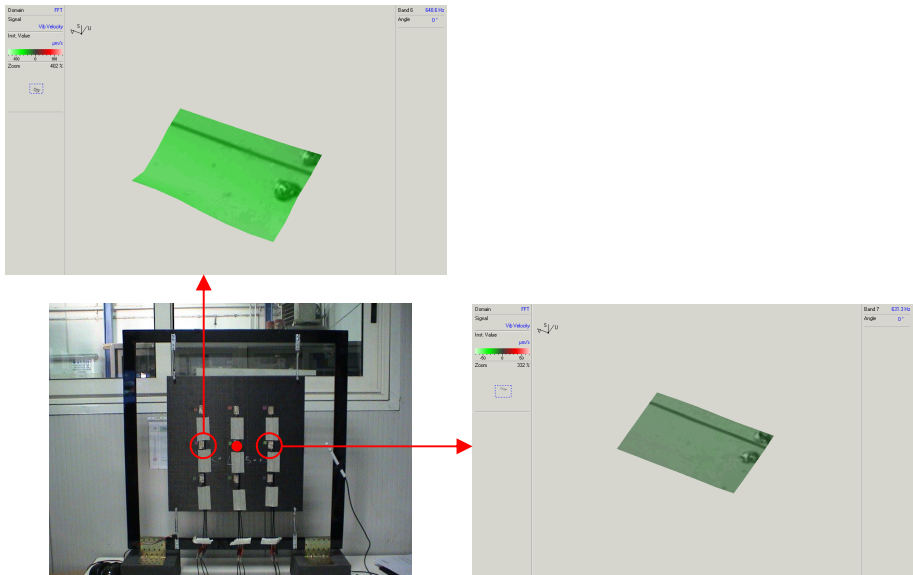


Fig. 4.1.11 – Piezoceramic patch failure

It can be observed that the Vibrometer is able to identify a piezoceramic patch failure. The upper picture shows that the left patch presents a discontinuity line during the deformation motion resulting from the vibration of the panel. That motion is impossible if a piezoceramic patch has no crack, because of the high stiffness. In fact, the right patch, which was working properly, does not present that discontinuity line.

IV.1.4 Magnetostrictive actuators

Two magnetostrictive actuators AMA50 have been used as actuators for the experimental tests executed on the MD-11 test article.

Those actuators are made of magnetostrictive material TERFENOL-D, whose meaning is:

- TER = Terbium;
- FE = Iron;
- NOL = Naval Ordnance Laboratory;
- D = Dysprosium.



Fig. 4.1.12 – Magnetostrictive actuators

Magnetostriction is a property of ferromagnetic materials to undergo a change of their physical dimensions when subjected to a magnetic field. This effect was first identified in 1842 by James Joule when observing a sample of nickel. This property, which allow magnetostrictive materials to convert magnetic energy into kinetic energy and conversely, is used for the building of both actuation and sensing devices. It is often quantified by the magnetostrictive coefficient, L , which is the fractional change in length as the magnetization of the material increases from zero to the saturation value. The effect is responsible for the familiar "electric hum"

which can be heard near transformers and high power electrical devices (depending on country, either 100 or 120Hz, plus harmonics).

The reciprocal effect, the change of the susceptibility of a material when subjected to a mechanical stress, is called the Villari effect. Two other effects are related to magnetostriction: the Matteucci effect is the creation of a helical anisotropy of the susceptibility of a magnetostrictive material when subjected to a torque and the Wiedemann effect is the twisting of these materials when an helical magnetic field is applied to them.

The Villari Reversal is the change in sign of the magnetostriction of iron from positive to negative when exposed to magnetic fields of approximately 500 oersteds.

Most ferromagnetic materials exhibit some measurable magnetostriction. The highest room temperature magnetostriction of a pure element is that of Co which saturates at 60 microstrain. Fortunately, by alloying elements one can achieve "giant" magnetostriction under relatively small fields. The highest known magnetostriction are those of cubic laves phase iron alloys containing the rare earth elements Dysprosium, Dy, or Terbium, Tb; DyFe_2 , and TbFe_2 . However, these materials have tremendous magnetic anisotropy which necessitates a very large magnetic field to drive the magnetostriction. Noting that these materials have anisotropies in opposite directions, Clark and his co-workers at NSWC-Carderock, prepared alloys containing Fe, Dy, and Tb. These alloys are generally stoichiometric, of the form $\text{Tb}_x\text{Dy}_{1-x}\text{Fe}_2$ and have been coined Terfenol-D. Terfenol-D, operated under a mechanical-bias, strains to about 2000 microstrain in a field of 2 kOe at room temperatures. For typical transducer and actuator applications, Terfenol-D is the most commonly used engineering magnetostrictive material.

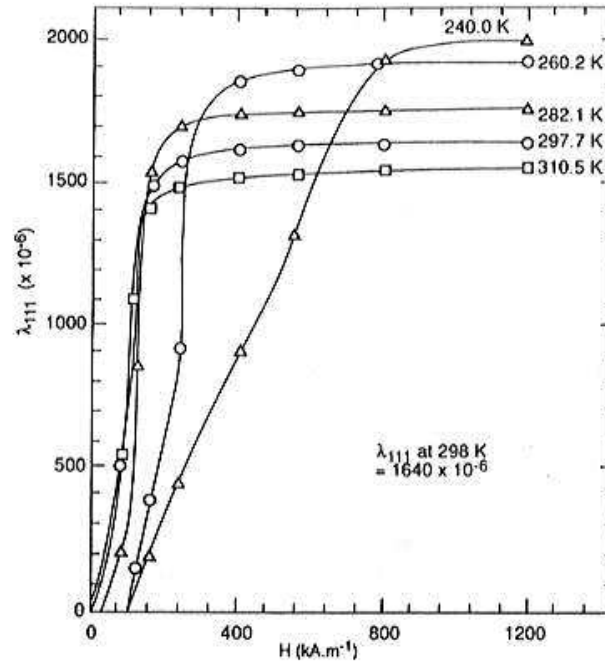


Fig. 4.1.13 – Terfenol-D response around room temperature, from Clark

The mechanism of magnetostriction at an atomic level is relatively complex subject matter but on a macroscopic level may be segregated into two distinct processes. The first process is dominated by the migration of domain walls within the material in response to external magnetic fields. Second, is the rotation of the domains. These two mechanisms allow the material to change the domain orientation which in turn causes a dimensional change. Since the deformation is isochoric there is an opposite dimensional change in the orthogonal direction. Although there may be many mechanism to the reorientation of the domains, the basic idea, represented in the figure, remains that the rotation and movement of magnetic domains causes a physical length change in the material.

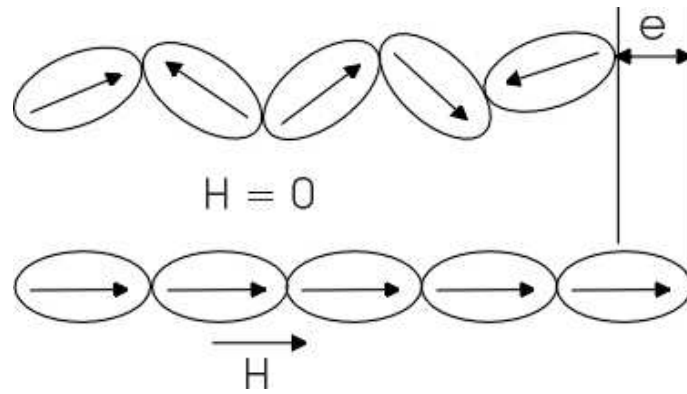


Fig. 4.1.14 – Movement of magnetic domains

Magnetostrictive materials are typically mechanically biased in normal operation. A compressive load is applied to the material, which, due to the magneto-elastic coupling, forces the domain structure to orient perpendicular to the applied force. Then, as a magnetic field is introduced, the domain structure rotates producing the maximum possible strain in the material. A tensile preload should orient the domain structure parallel to the applied force though this has not yet been observed due to the brittleness of the material in tension

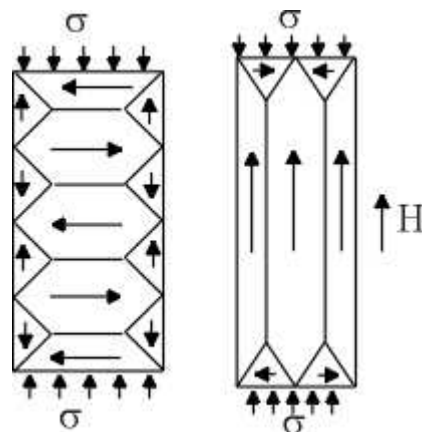


Fig. 4.1.15 – Orientation of the domain structure

IV.2 Test articles

Three different structures have been used in order to verify the capabilities of both Damage Index and Neural Network methods in identifying, localizing and quantifying a structural damage:

- MD-11 fuselage;
- Aeronautical composite panel;
- ATR-72 aircraft.

IV.2.1 MD-11

A typical fuselage stiffened panel available in the labs of the Department of Aeronautical Engineering has been chosen as first test-article. It is an MD11 fuselage panel made of:

- ✓ a 2024 aluminium alloy skin (1350mm x 1700mm);
- ✓ a 7075 aluminium alloy for the remainder of the structure;
- ✓ aluminium alloy rivets and titanium alloy hi-lock rivets;
- ✓ an alodyne 1200 protective coating on both faces of the panel;
- ✓ a primer protective coating on the inner surface (green colour).

That panel is a part of the MD-11 aircraft, which has been removed from the forward left zone of the fuselage, during the conversion of the aircraft from passenger to freighter, where a larger cargo door replaces the smaller passenger door.

The panel has been constraint to the wall by means of stiffeners.

On the test-article eight piezoelectric patches have been bonded in order to create an array of actuators-sensors. Following several tests which have been carried out in order to set up the frequency range, only four piezoelectric patches have been used, since four are enough to demonstrate the capability of the techniques to identify and quantify the damage.



Fig. 4.2.1 – MD-11 fuselage panel



Fig. 4.2.2 – MD-11 Constraint

IV.2.2 Aeronautical composite panel

A typical aeronautical composite panel made by means of RFI technology, available in the labs of the Department of Aeronautical Engineering, has been chosen as second test-article.

The panel has been constrained to a frame by means of four iron springs.

On the test-article 9 piezoelectric patches have been bonded in order to create an array of actuators-sensors.

The main characteristics of the panel are:

- ✓ 14 plies made of multi-axial HTA 3/6 K (520mm x 520mm x 2mm);
- ✓ panel lay-up: [(90/0/+/-)(+0/-)]s;
- ✓ fibre: multiaxial HTA-6K;
- ✓ resin: epoxy film 977-2 by Cytec;
- ✓ technical data:
 - $E1 = 1.352e11 \text{ N/m}^2$;
 - $E2 = 9.3e9 \text{ N/m}^2$;
 - $\nu12 = 0.34$;
 - $G12 = 4.87e9 \text{ N/m}^2$;
 - $\rho = 1600 \text{ Kg/m}^3$.



Fig. 4.2.3 – Composite panel



Fig. 4.2.4 – Composite panel set-up

IV.2.3 ATR-72 aircraft

Thanks to the ATR company it has been possible to execute experimental tests on a real ATR-72 aircraft. It is a prototype which serial number is MSN-098.



Fig. 4.2.5 – ATR-72

On the aircraft five different areas have been chosen in order to carry out the tests, and twenty-five piezoceramic patches have been bonded to create an array of actuators-sensors. For all the details it refers back to the chapter 5.

The fuselage of ATR 72 aircraft is of semimonocoque construction, and it is manufactured in structural sections as follows :

- ✓ Section 11 : Fuselage Nose Section;
- ✓ Section 13 : Fuselage FWD Center Section;
- ✓ Section 15 : Fuselage Center Section;
- ✓ Section 16 : Fuselage Rear Center Section;
- ✓ Section 18 : Fuselage Tail Section;
- ✓ Aerodynamic fairings.

The monocoque structure consists of frames and panels. The fuselage frames are generally built in 7075-T6 with a Z-profile.

The load introduction frames (main frames at wing and MLG attachment) are made in 7050-T74 52. The main frames to support the vertical tail are made in 7075-T6 "Z" shaped on the lateral and lower lobe.

The fuselage panels are made of 2024-T3 skin stiffened by 7076-T6 riveted stringers, except on some parts where they are hot bonded.

The stringers are made mainly of 7075 material.

A crease beam runs along the pressurized fuselage at the intersection of the two fuselage lobes to take the kink loads coming from pressurization and to transfer the floor shear loads to the fuselage skin.

The skin panels of ATR 72 aircraft fuselage are made mainly of 2024 material. They are reinforced by a system of riveted or hot bonded stringers and bonded doublers.



Fig. 4.2.6 – Piezoceramic patches installation examples

Chapter V

Experimental tests and Results

The core of the research is formed by experimental tests, and the results obtained, executed on the test articles which are described in the chapter IV. The object of this chapter is to explain the analysis of the results which will be treated with regard to each test article, not in a chronological way.

V.1 MD-11 fuselage

V.1.1 First experimental campaign

On that structure either magnetostrictive or piezoelectric patches has been used as actuators, while seven piezoelectric patches have been used as sensors.

First, it has been used two magnetostrictive actuators, and two different amplifiers: the audio power amplifier and the LDS amplifier. First it has been used the audio one. In order to define their right position on the structure a perturbation has been simulated to not change for ever the structure characteristics, to test several position for the actuators. Firstly, the magnetostrictive actuators have been installed on the right frame of the structure, far from the structure constraints.



Fig. 5.1.1 – Magnetostrictive actuators

The perturbation has been carried out by means of a mass of gr.500, rested on the structure without fasteners, so that it could be easily moved everyway, with no problem. That kind of perturbation, even if it leads to good damage identifications (see after), is not a real damage simulation, since it is a damage unfaithful to realities. In fact 500 grams added on a structure causes a redistribution of the mass of the structure.



Fig. 5.1.2 – 500 grams mass

To test how could change the behaviour of the system structure-magnetostrictive actuators when these ones are installed on other places, the left frame of the structure was drilled before moving the actuators from the right frame to the left one. So, it was possible to check if the piezoceramic array sensors were able to identify the holes (two which diameter is equal to mm. 4) as a damage.

Both holes are out from the sensors array, on the left frame which is a very stiff element, so the identification of the holes was not so evident.

It can be noted that both the Damage Global Index, which is determined summing all sensitivity indexes and all damage indexes, and the damage indexes obtained for each sensor, are able to identify the damage, but all damage indexes are not so high with regard to the sensitivity indexes.

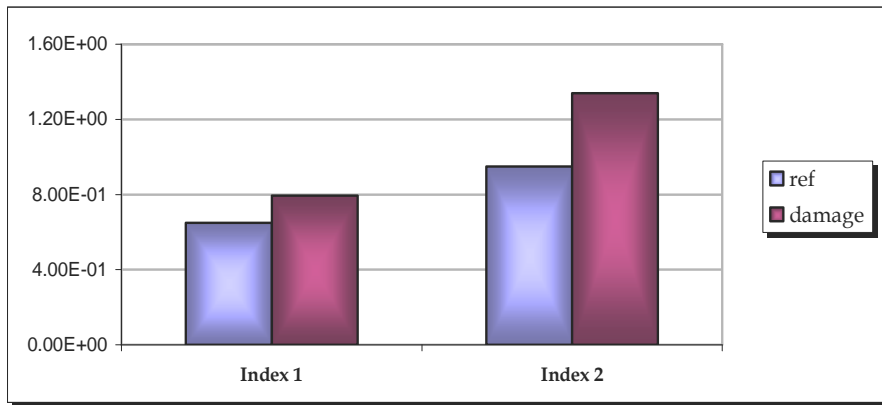


Fig. 5.1.3 – Global Damage Index

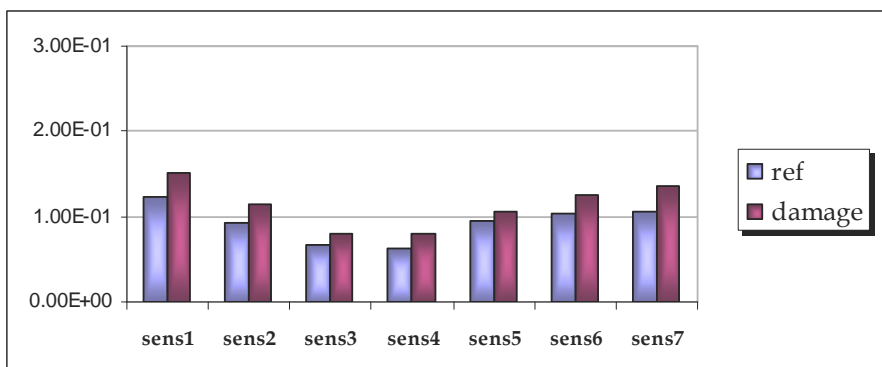


Fig. 5.1.4 – Damage Index "1"

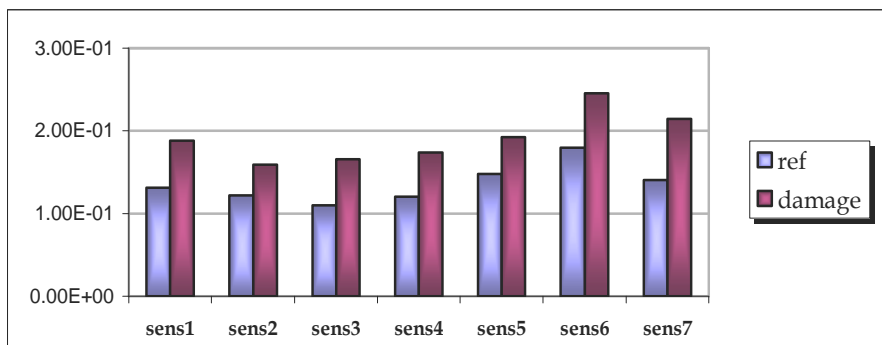


Fig. 5.1.5 – Damage Index "2"

Then both magnetostrictive actuators have been installed on the left frame, at the same height of the right frame actuators position.

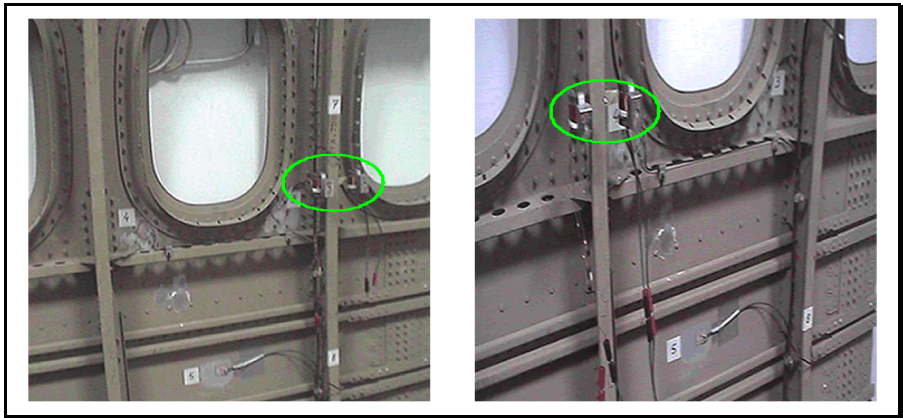


Fig. 5.1.6 – Magnetostrictive moving

In the end it has been tested a configuration where one actuator is on the left frame and the other is on the right one.

The analysis of the Frequency Response Functions pertinent to the three actuators configurations shows the different dynamical behaviour of the structure, since the different location of the actuators gives rise a redistribution of the mass of the structure. In theory this is not a problem, if the three different excitation configurations are related to three different structure.

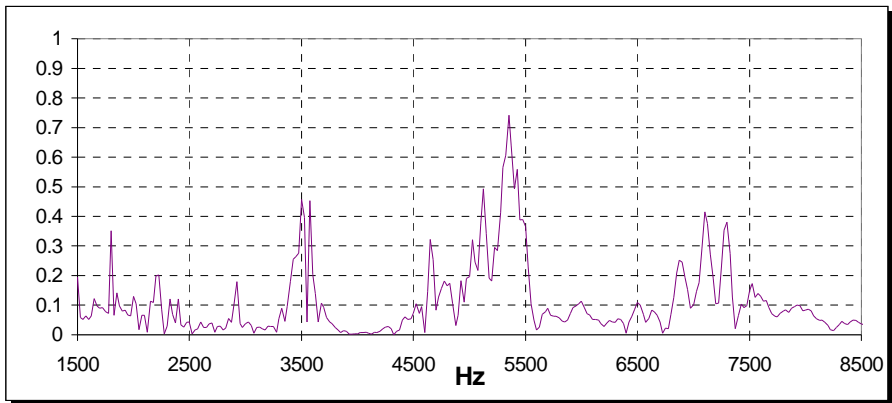


Fig. 5.1.7 – FRFs of sound structure – sens #5 – actuators left and right

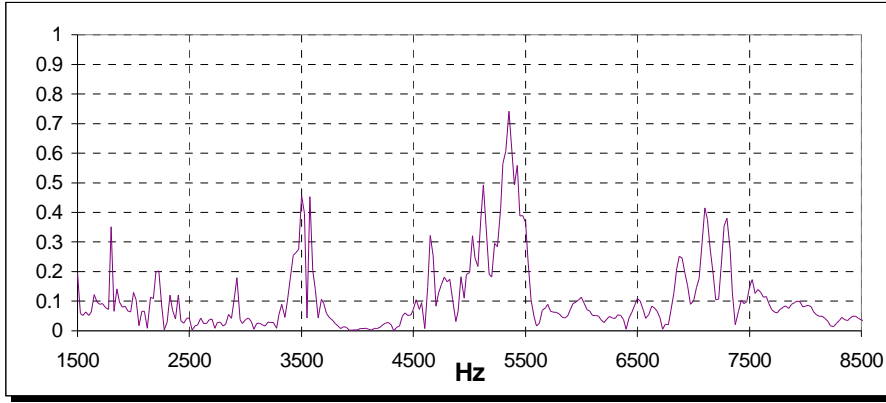


Fig. 5.1.8 – FRFs of sound structure – sens #5 – actuators right

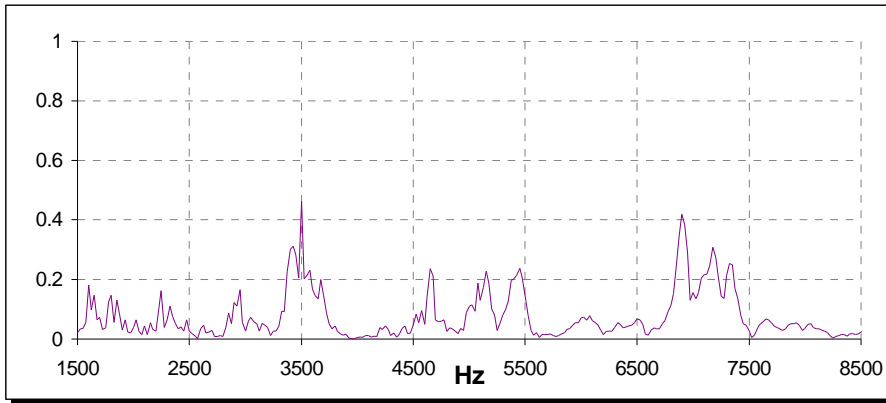
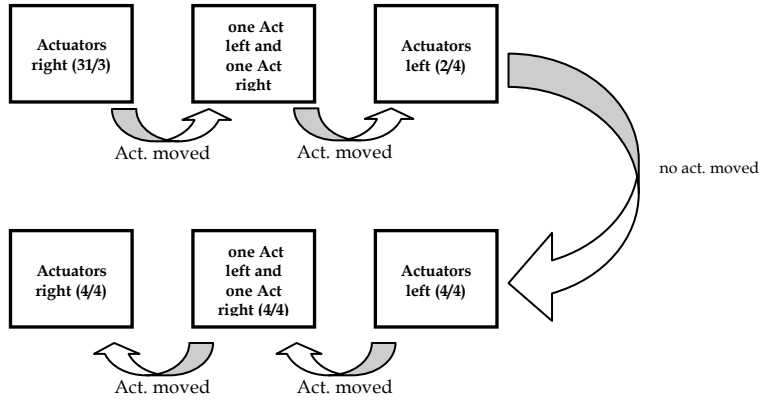


Fig. 5.1.9 – FRFs of sound structure – sens #5 – actuators left

In the following figure it is shown a typical temporal cycle test to determine reference and damage indexes for each excitation scheme.



It can be noted that the structure having both the magnetostrictive actuators on the left frame has given good results. In fact all sensors, especially #5 and #6 well identify and localize the presence of the mass.

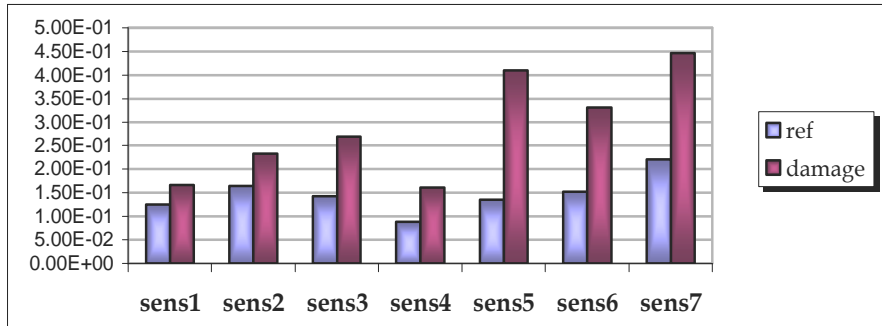


Fig. 5.1.10 – Damage Index “1” – actuators left

The other two actuators configurations (both on the right frame and each of them on a different frame) have not lead a good identification of the perturbation because of very high sensitivity indexes. The structure has not changed, and the environmental disturbance cannot be the cause why the reference indexes determined with regard to the second and third configurations are so high. When the magnetostrictive actuators are moved, the clamping of the bolts changes. Since the acquisition of the first configuration was the only one which has been executed without disassembling the actuators, probably, this fact is the cause of the different reference indexes calculated with regard to the second and third configuration. It can be noted that the FRFs definitely change.

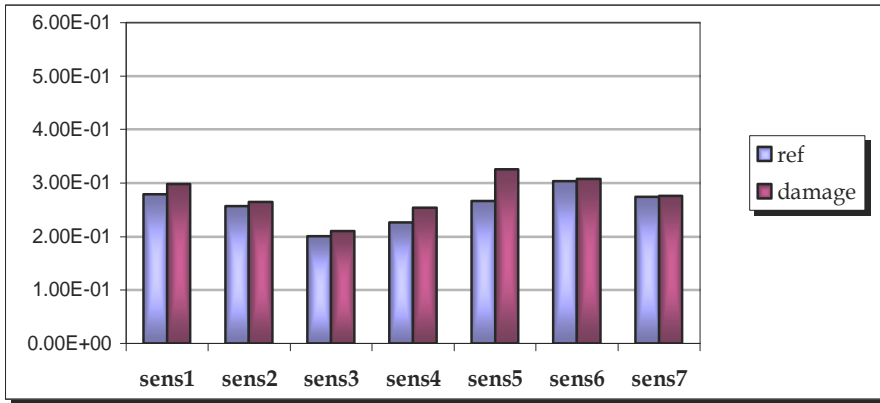


Fig. 5.1.11 – Damage Index “1” – actuators left and right

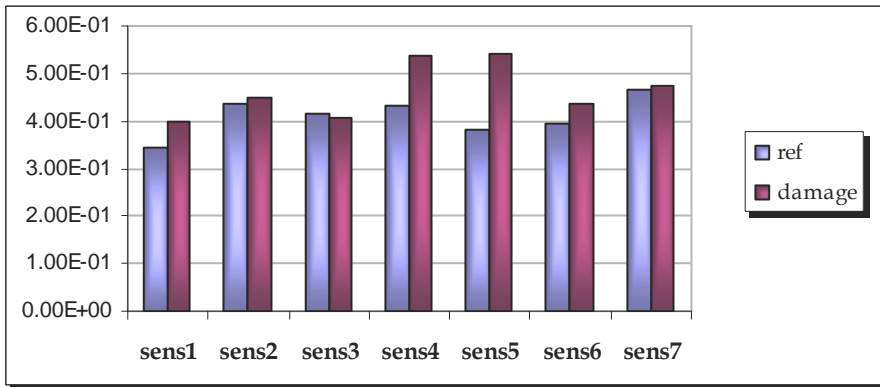


Fig. 5.1.12 – Damage Index “1” – actuators right

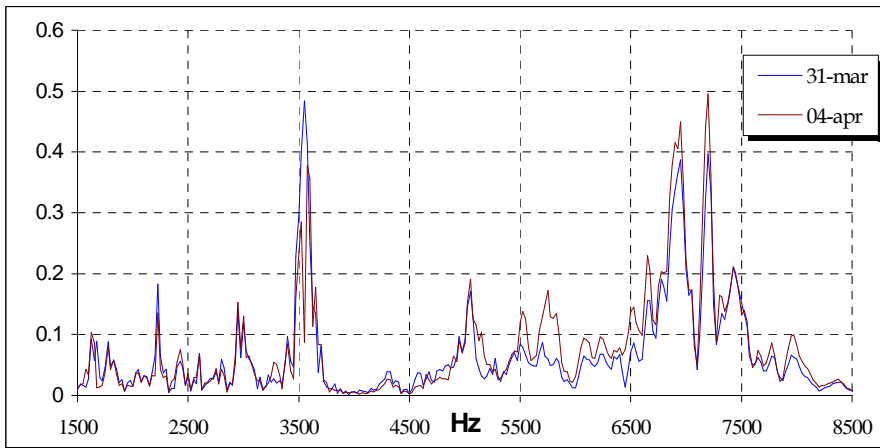


Fig. 5.1.13 – FRFs sensor #6

In the end only the configuration having an actuator on a frame and the second actuator on the other frame has been chosen, to avoid moving the actuators. Besides they have been used either together or one at a time.

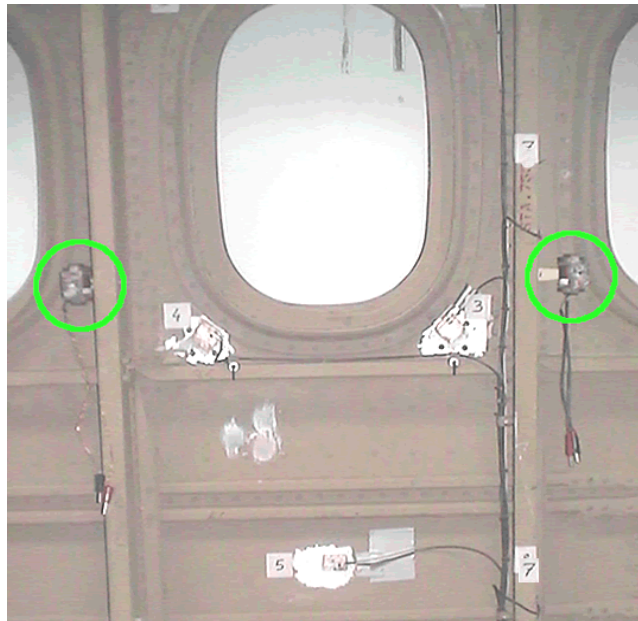


Fig. 5.1.14 – Magnetostrictive final configuration

In order to avoid that the excitation signal was cut by the amplifier, when both actuators have been used at the same time, each one was supplied by means of 1,1 Ampere current (2,2 total Ampere current), while when one actuator only has been used, it was supplied by 1,5 Ampere current. So, to have the maximum vibration energy, both actuators have been used at the same time. Note that each magnetostrictive actuator can be supplied by 3,0 Ampere current. Anyway, damage indexes determined using one actuator only at a time have given good results about the identification of the presence of the mass close to the piezo patches #5 and #6.

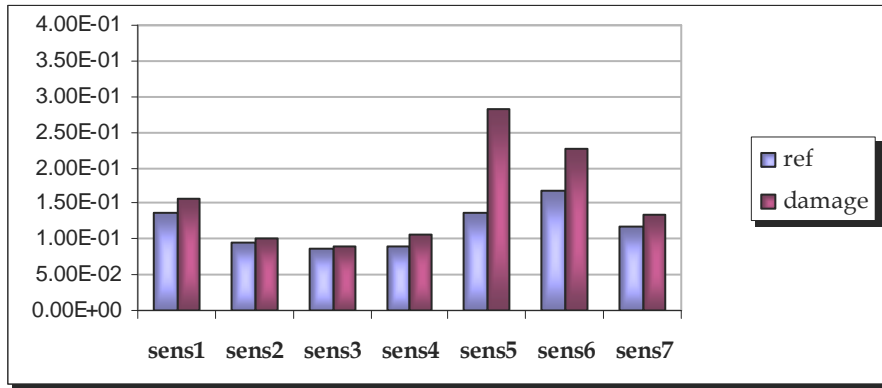


Fig. 5.1.15 – Damage Index – one actuator right

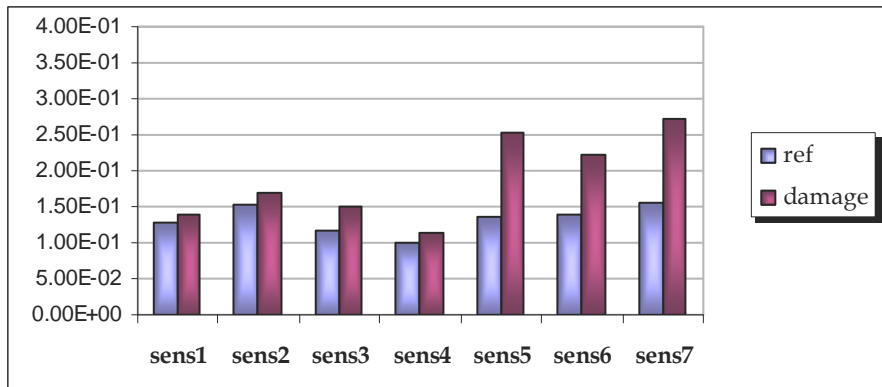


Fig. 5.1.16 – Damage Index – one actuator left

Localization

Once the actuators configuration has been fixed, the capability of the Damage Index method in localize the presence of a damage has been tested. So, the mass of gr.500 has been put on different positions on the structure.



Fig. 5.1.17 – Masses locations

Mass position A:

all Damage Indexes are higher than the sensitivity ones, so the presence of the mass has been identified. About the localization it can be noted that the sensors #5, #6 and #7 have given the highest indexes. Because of the route of vibrations from the actuators to the sensors, it is obvious that sensors #5 and #6 have localized the presence of the mass, while, about the sensor #7, it has to take into account that the sensor #7 is on the frame, which has a high stiffness, so the vibration waves prefer to travel through it.

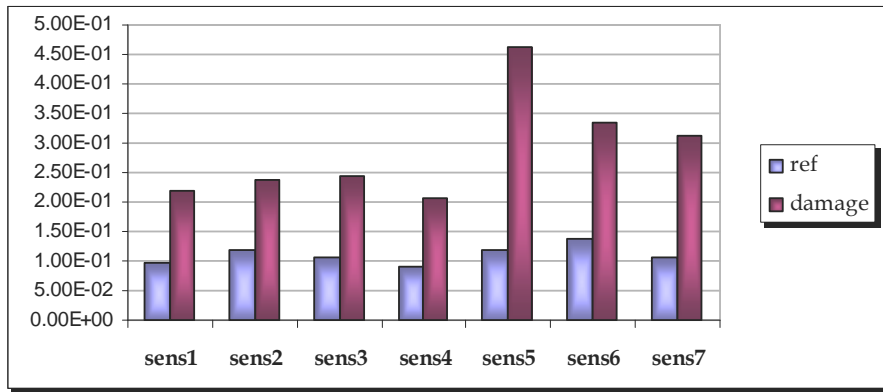


Fig. 5.1.18 – Damage Index “2” damage “A”

Mass position B and C:

In those cases it is not possible to localize the presence of the mass because of all indexes have similar values. It is noted that the mass put on position C was equal to kg.1. Maybe the problem is the stiffness of the structure in that region. There, in fact, the skin has a thickness equal to cm.1, and there are a lot of hi-lock rivets. Furthermore, the sensor #4 is less sensitive than the other sensors.

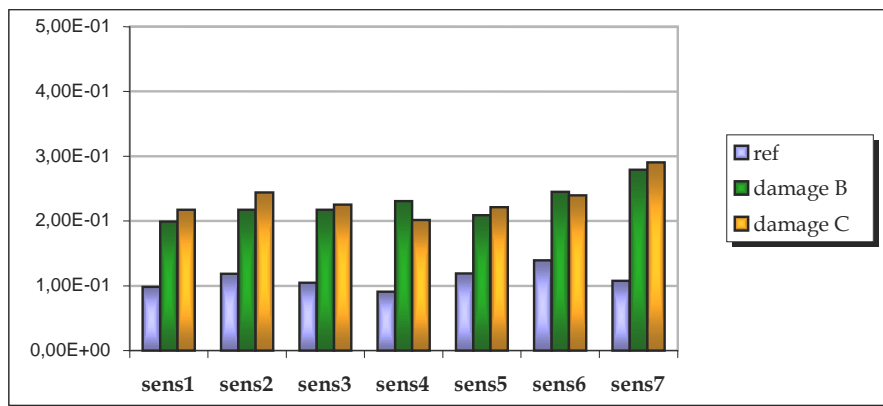


Fig. 5.1.19 – Damage Index “2” damage “B and C”

Mass position D:

all sensors identify the presence of the mass, and the sensor #3 localize it. It can be noted that the position D is symmetric to the position B, but, evidently, the sensor #3 is more sensitive than the sensor #4.

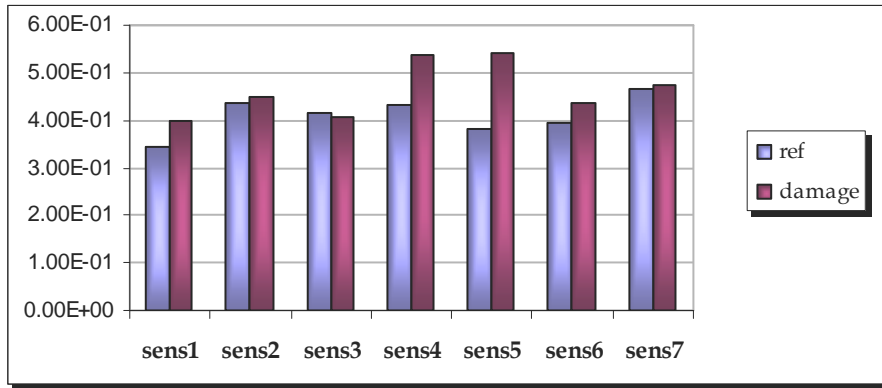


Fig. 5.1.20 – Damage Index “2” damage “D”

Mass position E:

also in that case the sensors identify the mass, and sensors #5 and #6 localize it. Besides, it can be observed the sensor #5 has noted that the mass is far from the position A, in fact it has give a lower index.

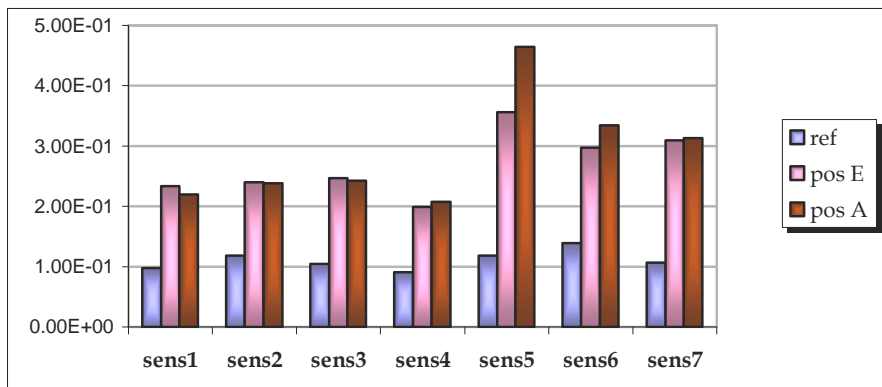


Fig. 5.1.21 – Damage Index “2” damage “E and A”

In all the cases the sensor #7, put on the frame, identify the presence of the mass independently from its position, because of the high stiffness of the frame with regard to the rest of the structure.

LDS amplifier

In order to use the magnetostrictive actuators at their peak the LDS power amplifier has been used. It can be observed how the increased energy level has modified the transfer function, especially at low frequencies.

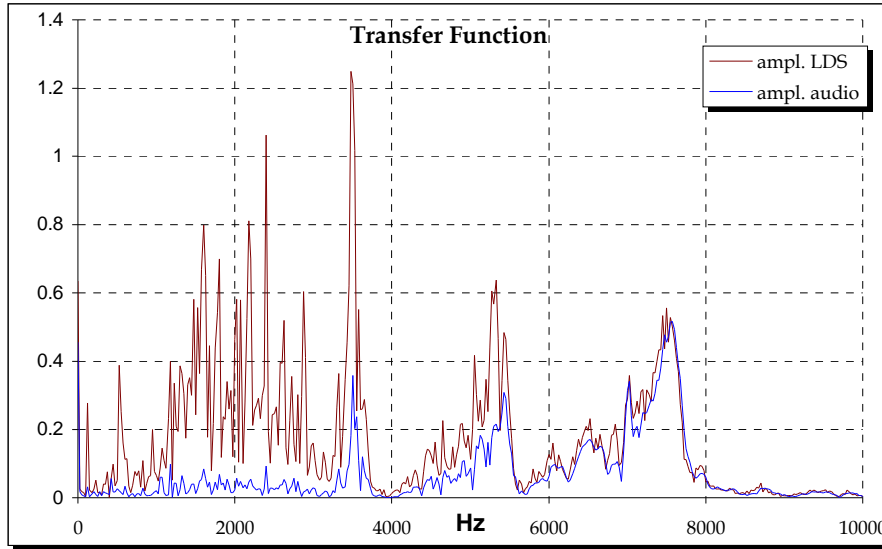


Fig. 5.1.22 – FRFs comparison – LDS amplifier – sensor #3

At the same time the coherence function which has been calculated using the new amplifier is worse than using the audio amplifier. Even if there are an higher energy level, the signal is noisy, and, consequently, the sensitivity indexes will be higher.

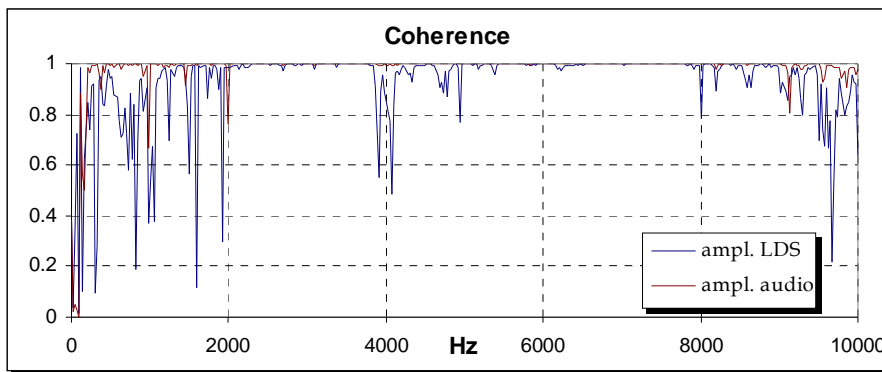


Fig. 5.1.23 – Coherence comparison between audio and LDS amplifiers – sens #3

To show the differences between the two amplifiers behaviour, the mass of gr. 500 has been put on the position A, B and D again, and they have been compared the results obtained by using the LDS amplifier with the results obtained by using the audio power amplifier.

About the following graphs, each slice of pie chart represents the percentage of the difference between the damage index and the reference index calculated for each sensor, with regard to the global reference index:

$$\%sensor_i = \frac{DI_i - RI_i}{\sum_i DI_i - \sum_i RI_i} * 100$$

while each bar represents the increment of a damage index with regard to the associate sensitivity index.

The deviation between the indexes of the sensors placed close to the mass and the indexes of the sensors located far from it shows that the LDS amplifier improve the capability of the Damage Index method in identify and localize a structure perturbation.

Mass position A:

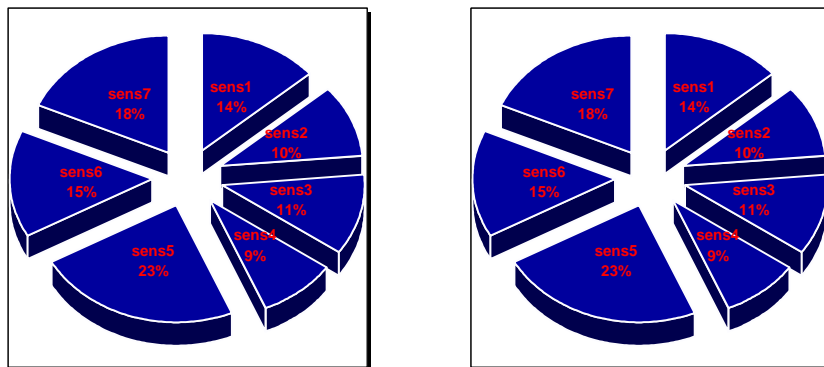


Fig. 5.1.24 – Pie charts comparison between audio and LDS amplifiers

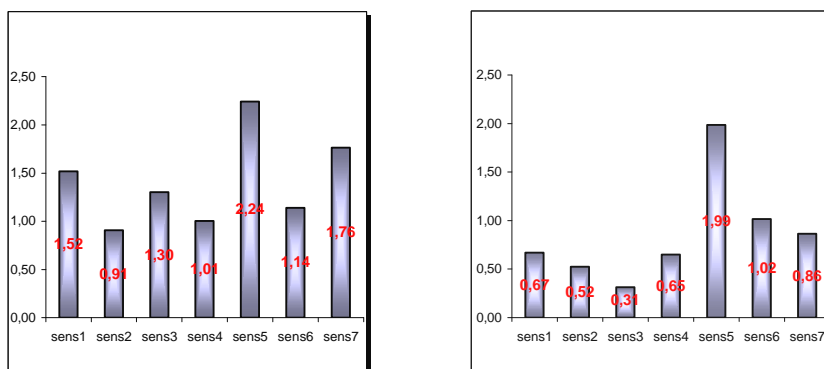


Fig. 5.1.25 – Bar charts comparison between audio and LDS amplifiers

Mass position B:

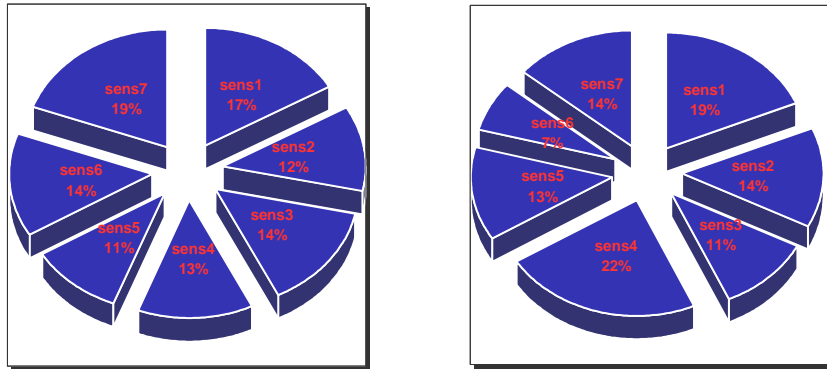


Fig. 5.1.26 – Pie charts comparison between audio and LDS amplifiers

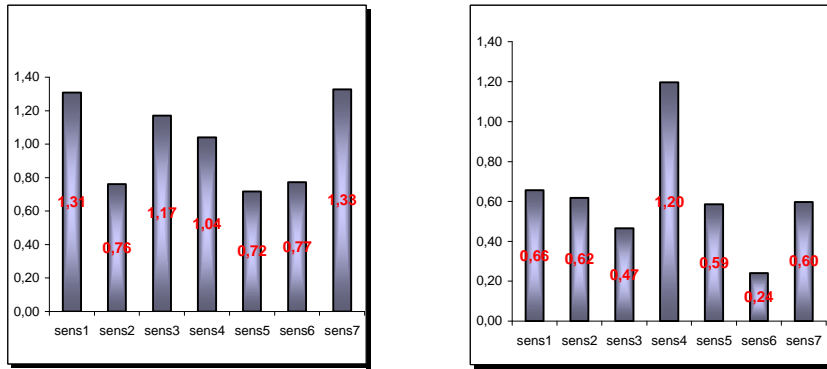


Fig. 5.1.27 – Bar charts comparison between audio and LDS amplifiers

Mass position D:

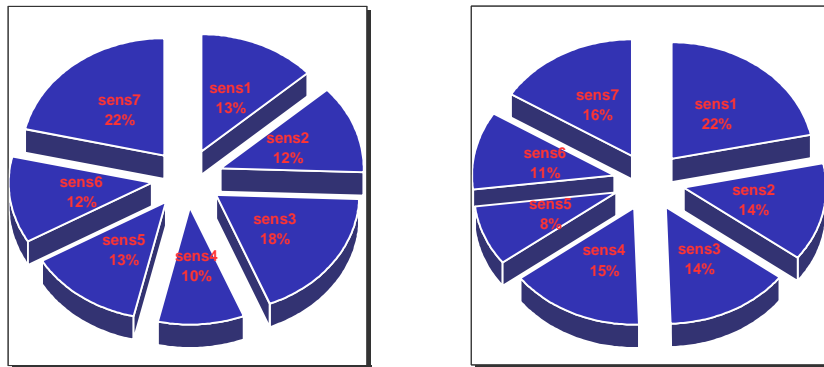


Fig. 5.1.28 – Pie charts comparison between audio and LDS amplifiers

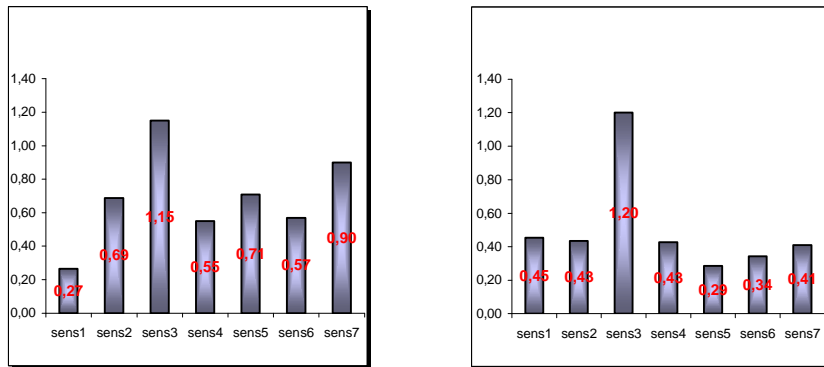


Fig. 5.1.29 – Bar charts comparison between audio and LDS amplifiers

A Neural Network was trained by means of five FRFs acquisition campaign of the sound structure to verify the capability in identifying the mass added.

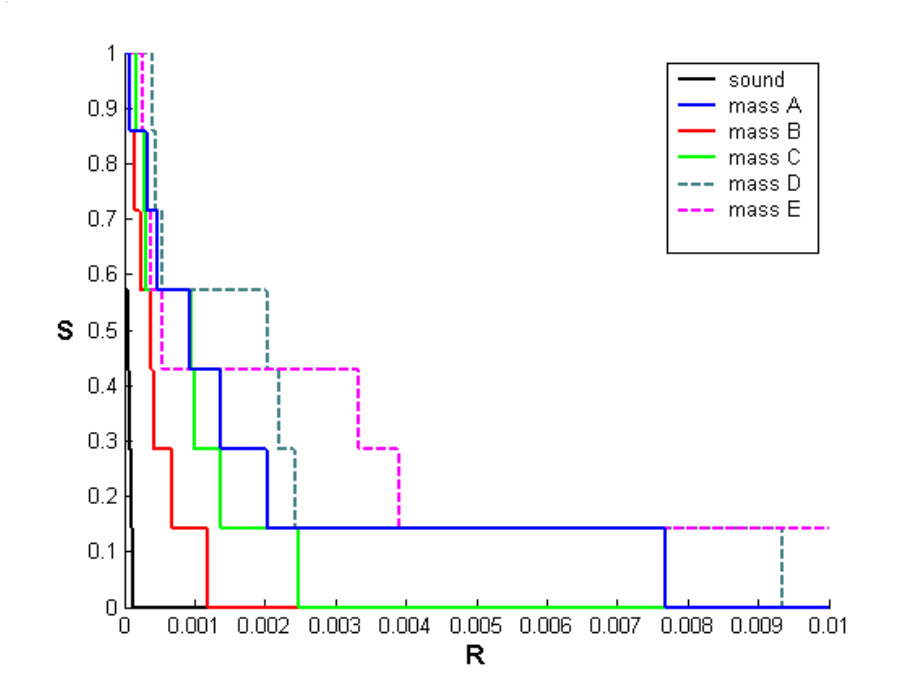


Fig. 5.1.30 – Neural Network output

The Neural Network output show that the presence of the mass has been identified, independently by the position. In fact the undamaged structure curve is very close to the x-axis, while the other are far from it. Moreover, it seems that the Neural Network is more sensitive about some locations.

Even if there is no threshold, the mass, located in the “E” position, has been clearly identified, while the mass put on the “A” position gives a bit doubt about its identification.

Real damage

After having perturbed the structure, as shown in the previous paragraph, some real damage have been carried out on the structure in order to test the Damage Index technique. Besides, either the amplifiers audio or LDS have been used, so it is possible to highlight the importance of the power of the energy used and the signal coherence (noise produced by the equipment).

First experimental test

The first experimental test has consisted of a subsequent removal of two hi-lock rivets, made of titanium alloy, connecting the window stiffening to the skin, to test the capability of the Damage Index method in identify a damage on very stiff region of structures.

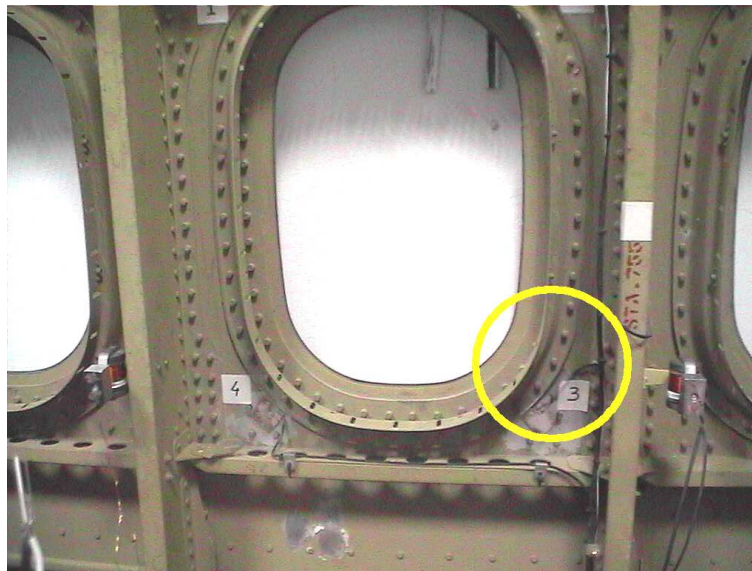


Fig. 5.1.31 – First Damage location

Before removing the two rivets, the nuts which clamp the rivets have been removed, to verify if it is possible to identify a little damage, too. In next figures the obtained results are reported:

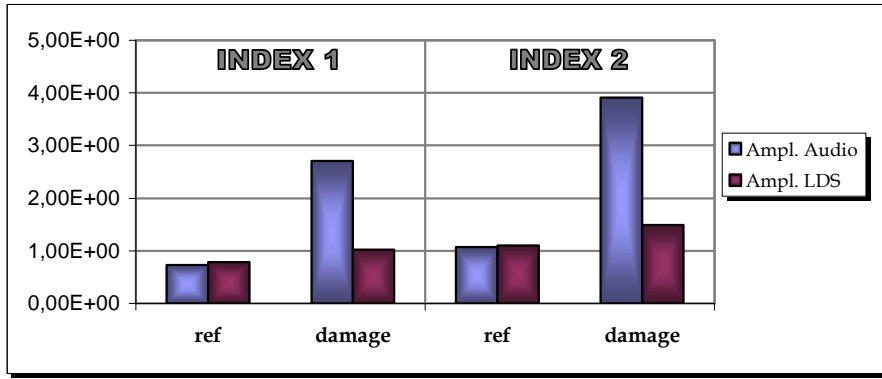


Fig. 5.1.32 – Global Damage Index – both amplifiers

the figure above represents the global damage indexes which shows that the highest coherence is the better identification is, even if the energy power is low. In the following figures there are the details of the indexes for each sensors, obtained by means of the LDS amplifier and, then, by the audio amplifier.

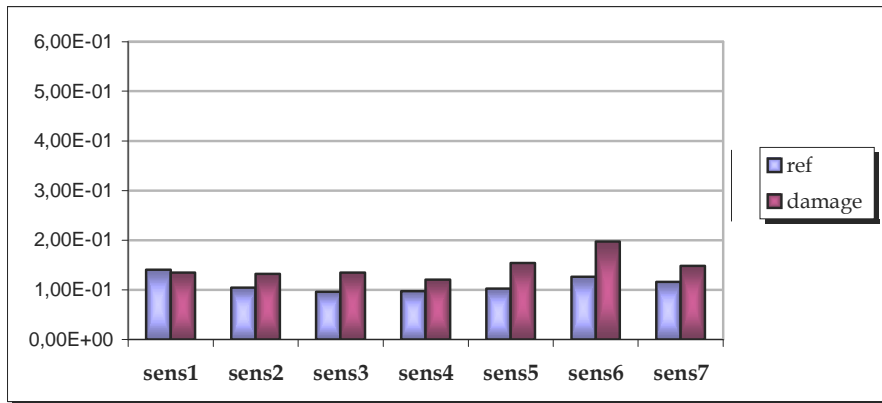


Fig. 5.1.33 – Damage Index “1” LDS amplifier

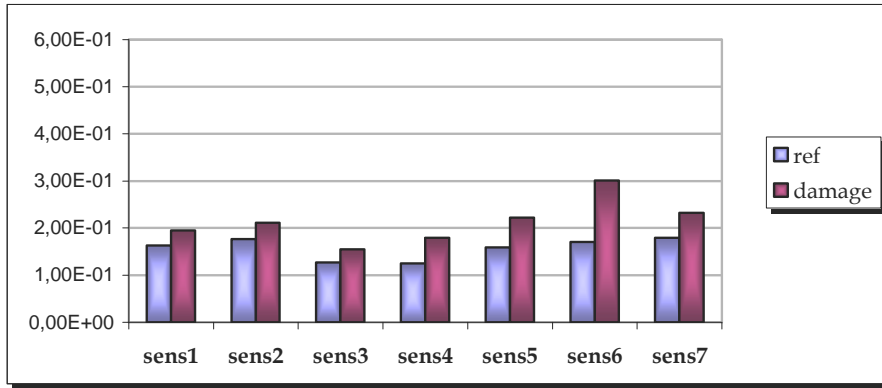


Fig. 5.1.34 – Damage Index “2” LDS amplifier

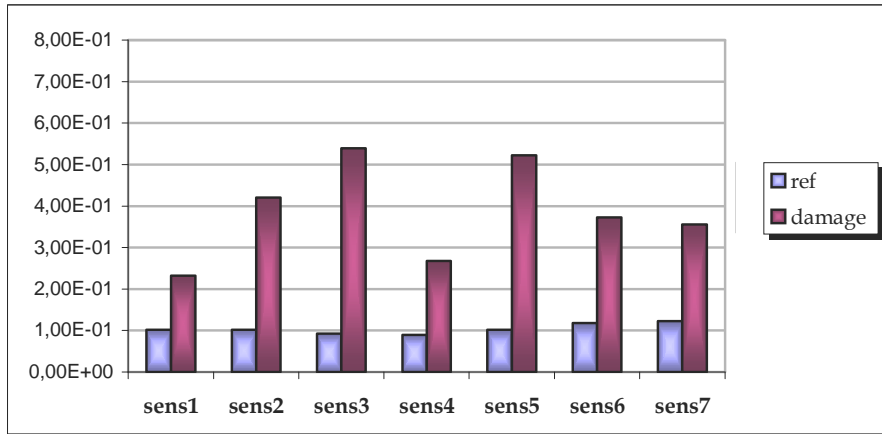


Fig. 5.1.35 – Damage Index “1” audio amplifier

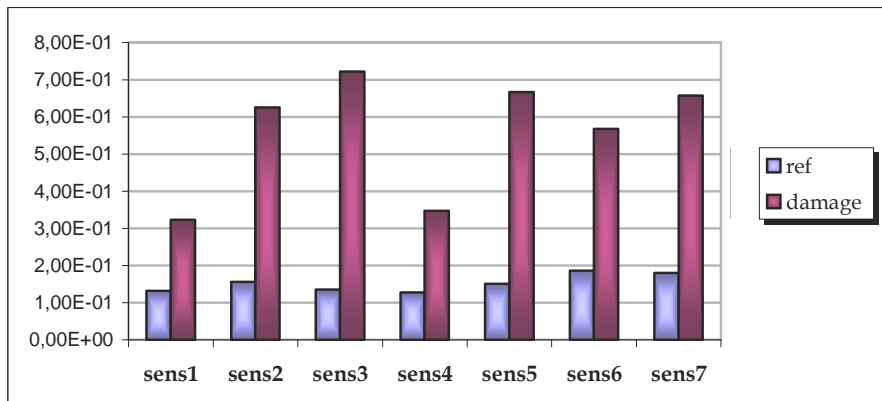


Fig. 5.1.36 – Damage Index “2” audio amplifier

The charts show that the audio power amplifier gives the best results. Using the LDS amplifier it is not possible to identify the damage clearly. The sensor #3 has localize the damage. Taking into account the route of the vibrations, it is possible to explain why other sensors localize the damage too, for example the sensor #5. It can be noted that the sensors #1 and #4, out of the vibration route, do not localize the damage. The following figures show the same results by means of pie charts and percentage bar graphs.

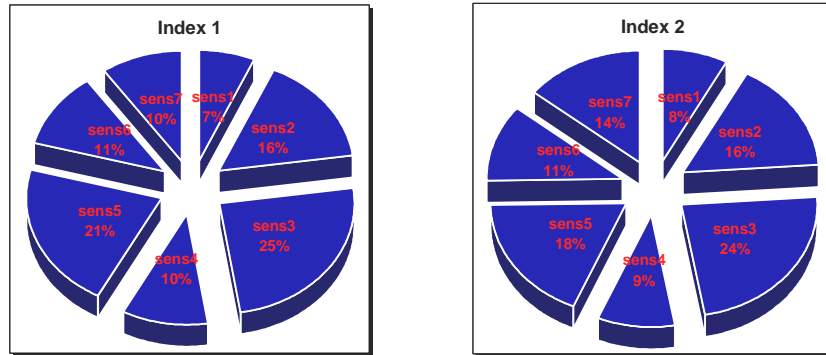


Fig. 5.1.37 – Pie charts Index “1” and Index “2” audio amplifier

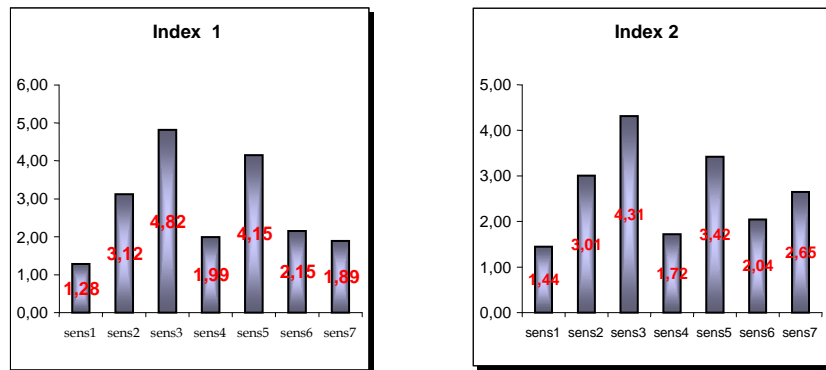


Fig. 5.1.38 – Pie charts Index “1” and Index “2” audio amplifier

Since both Index “1” and “2” give good results in identification, to show the next results it will be used the first only, in order to make the treatment of the work lighter.

The removal of the first rivet is shown in the next figures:



Fig. 5.1.39 – First rivet removal

Also for the removal of the first rivet the results will be shown using the same charts which have been used to show the damage of the nuts:

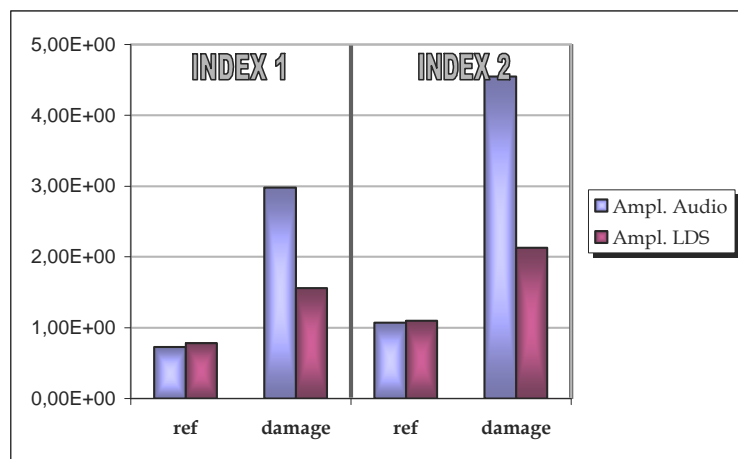


Fig. 5.1.40 – Global Damage Index First rivet removal

It can be observed that the removal of the rivet has been identified.

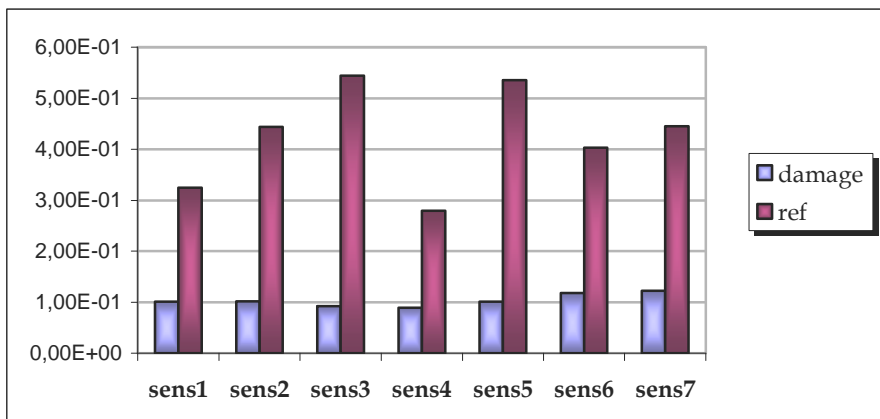


Fig. 5.1.41 – Damage Index “1” audio amplifier

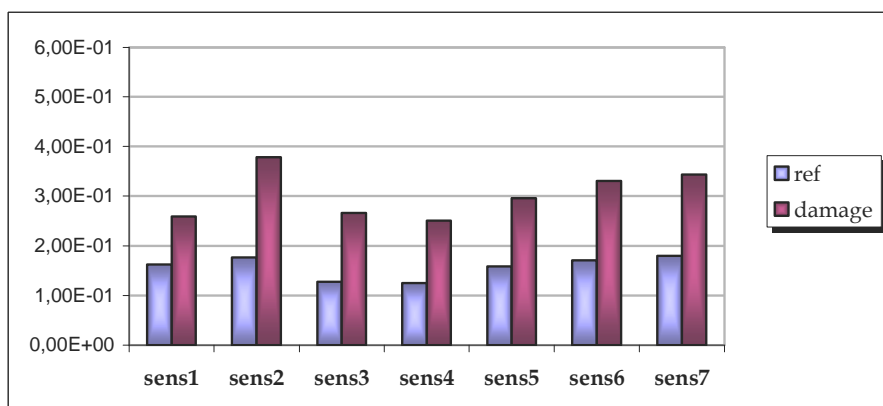


Fig. 5.1.42 – Damage Index “1” LDS amplifier

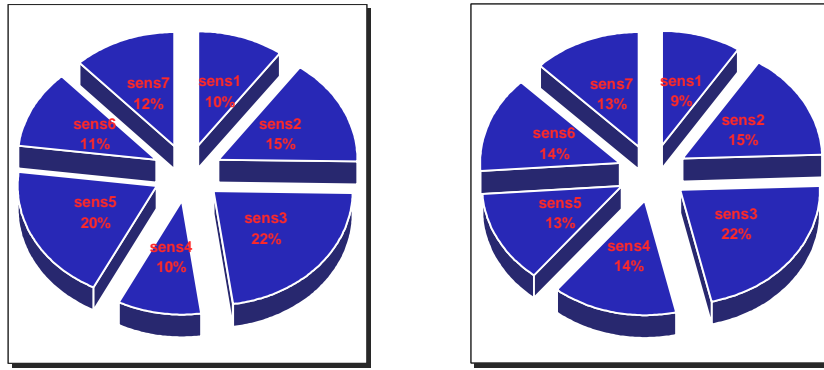


Fig. 5.1.43 – Pie charts Index “1” comparison between audio and LDS amplifiers

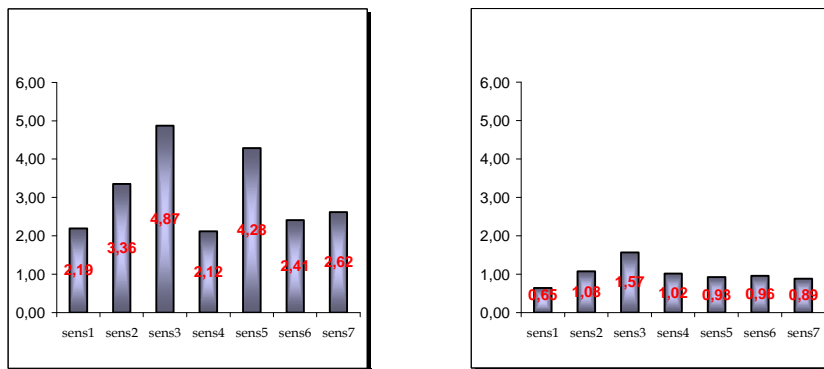


Fig. 5.1.44 – Bar charts Index “1” comparison between audio and LDS amplifiers

Also in that case the use of the audio power amplifier has given the best results in identification and localization of the damage.

Second rivet removed

The removal of another rivet, close to the first, has been the following step.



Fig. 5.1.45 – Second rivet removal

Next figures show all the results obtained by means of the Damage Index “1” only, and both the amplifiers.

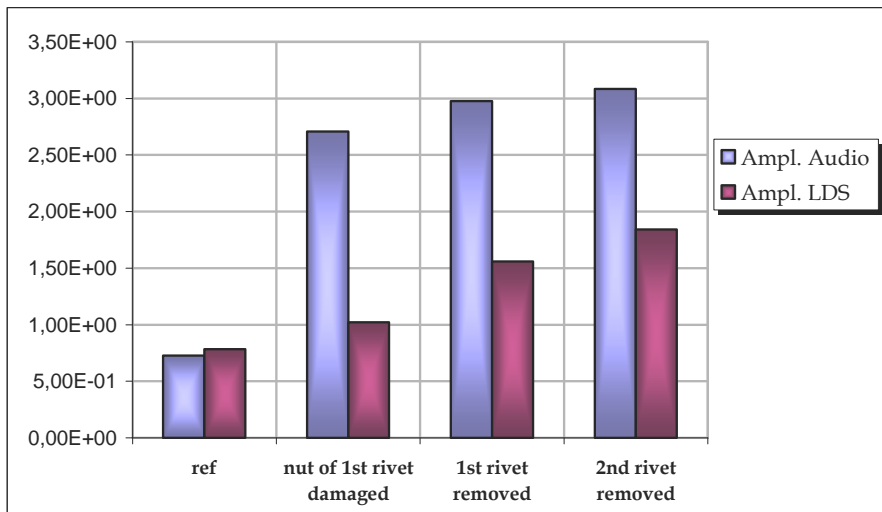


Fig. 5.1.46 – Global Damage Index “1” both amplifiers

It can be observed that the damage have been identified, but using a more clean signal, even if the level of the energy is low (using the audio amplifier), the identification is better.

About the localization, the following charts report the indexes for each sensor.

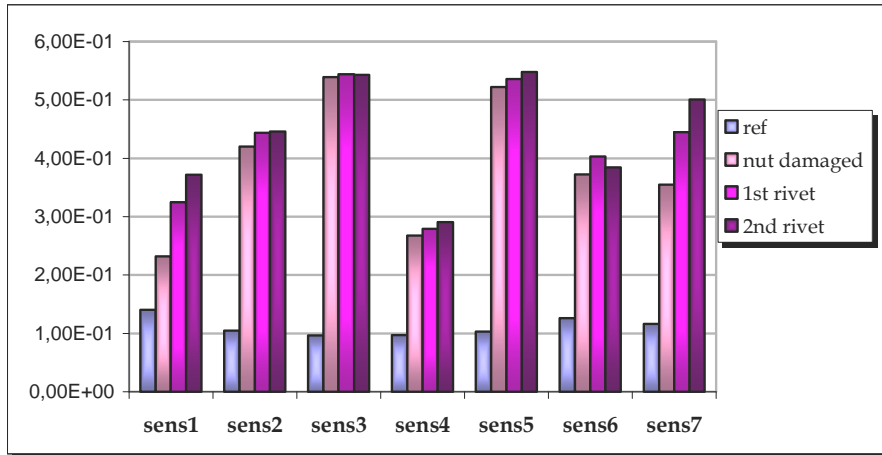


Fig. 5.1.47 – Damage Index “1” audio amplifier

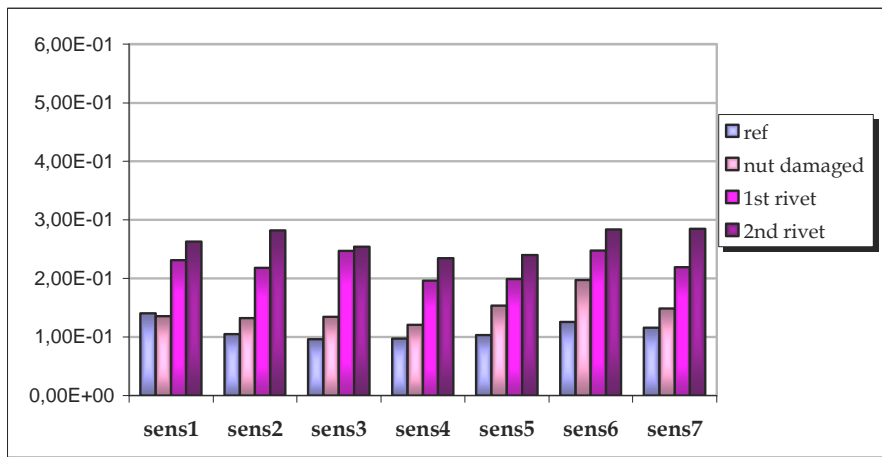


Fig. 5.1.48 – Damage Index “1” LDS amplifier

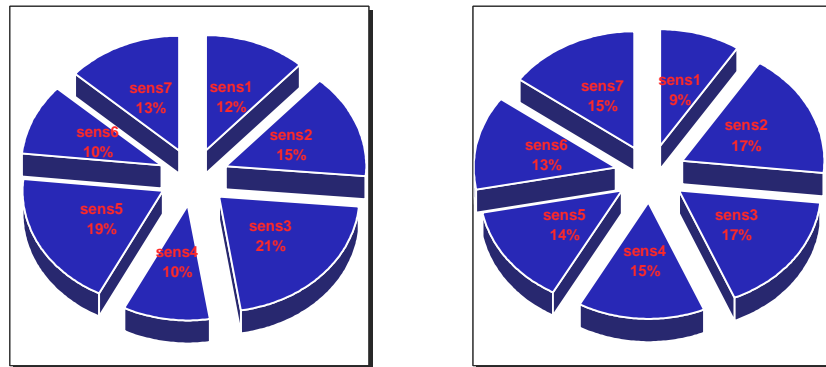


Fig. 5.1.49 – Damage Index “1” audio and LDS amplifiers

The following bar charts show the increments percentage of the indexes with regard to the reference ones, starting from the damage of the nut of the first rivet removed.

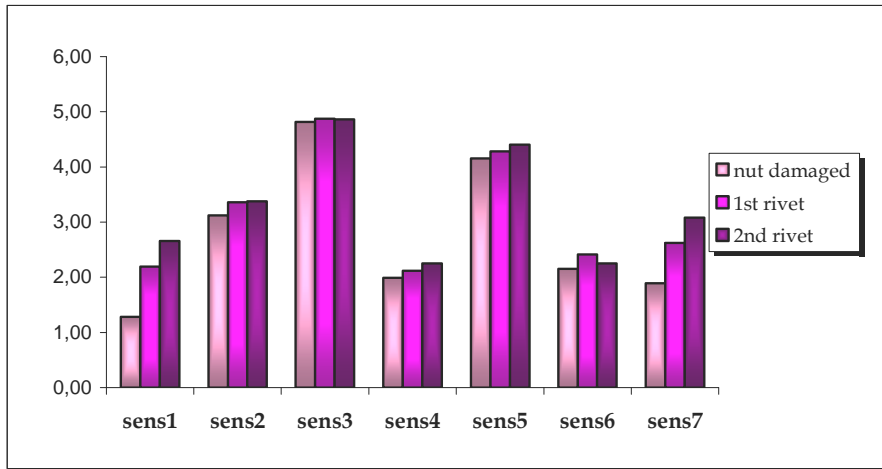


Fig. 5.1.50 – Damage Index “1” percentage increments – audio amplifiers

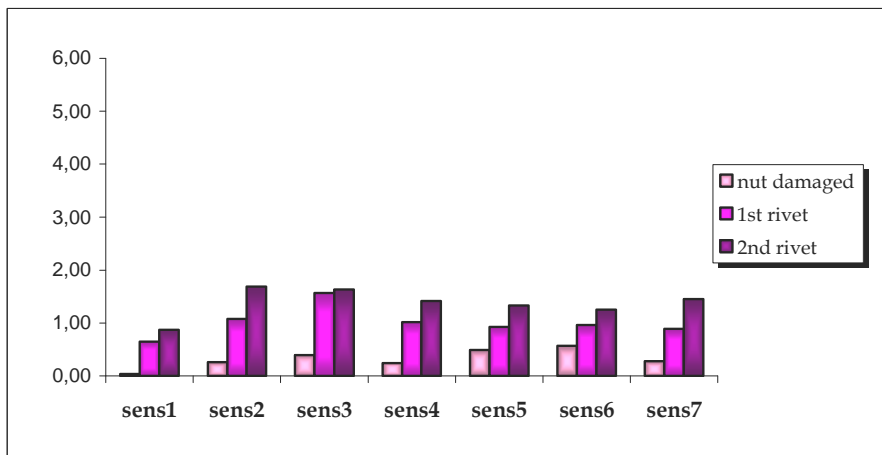


Fig. 5.1.51 – Damage Index “1” percentage increments – LDS amplifiers

Second experimental test

The next step has been the removal of another rivet, after having damaged its nut, using one magnetostrictive at a time, and the audio power amplifier only.

The region of the structure which has been damaged is the one close to the sensor #4.

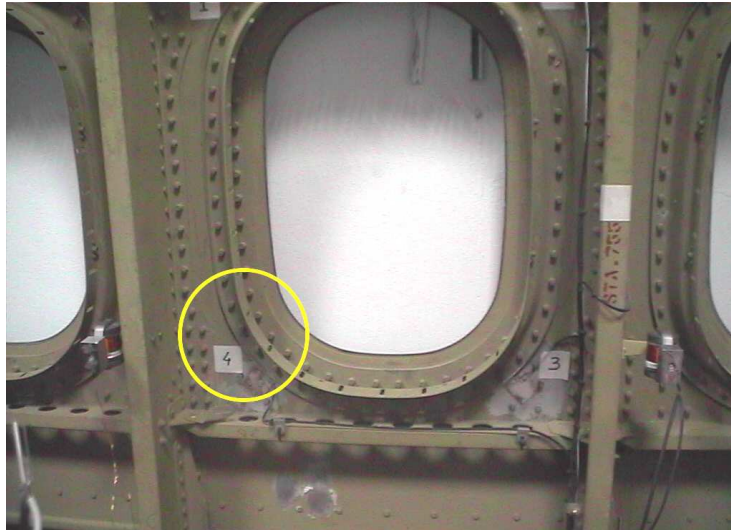


Fig. 5.1.52 – Second Damage location

Firstly the nut of the rivet has been damaged. That damage has been identified, even if one only actuator has been used at a time (less energy than before).

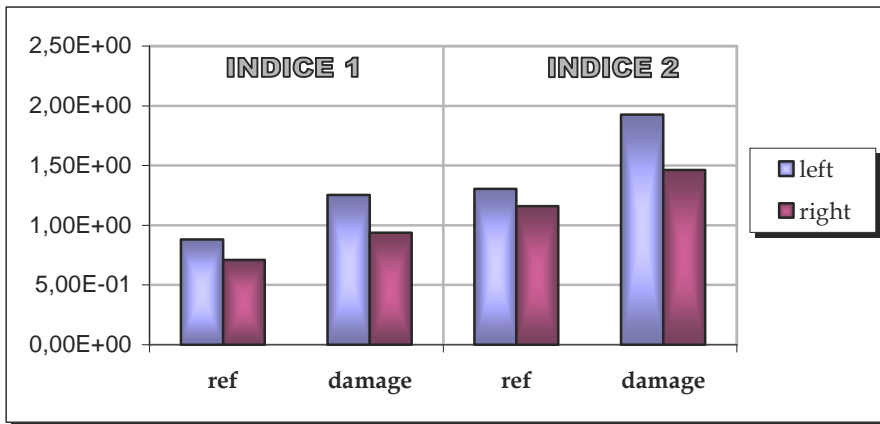


Fig. 5.1.53 – Global Damage Index – both actuators

Besides, the actuator put on the left frame, close to the damaged area, gives the highest indexes, because of the shortest run from the actuator to the damaged area. Furthermore, it can be observed from the increments percentage bar charts, that the Damage Index “2” localize the damage better the index “1”.

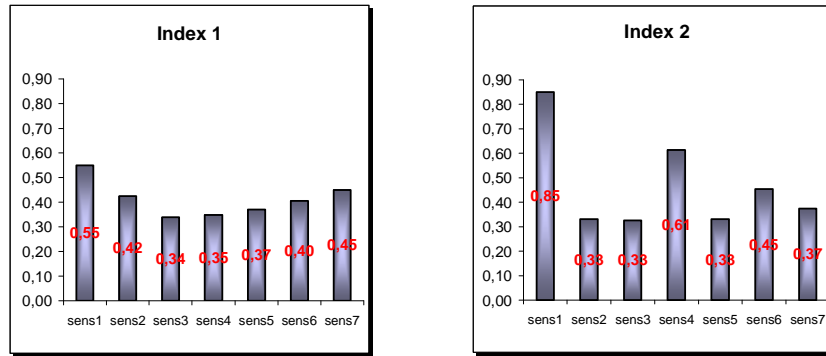


Fig. 5.1.54 – Damage Index “1” and “2” – left actuator

Next figures show the results obtained from the Index “2”:

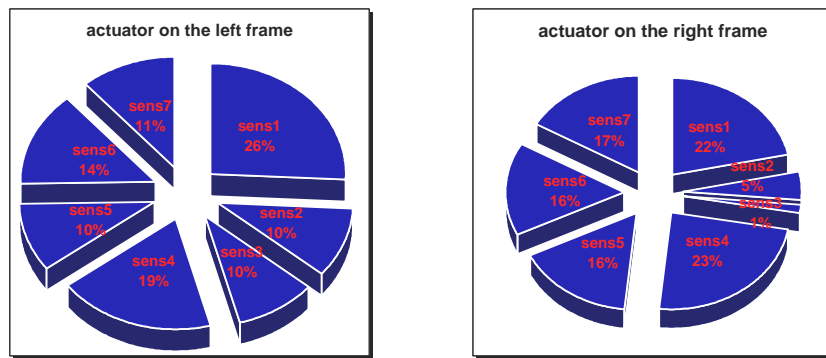


Fig. 5.1.55 – Damage Index “2” left and right actuators

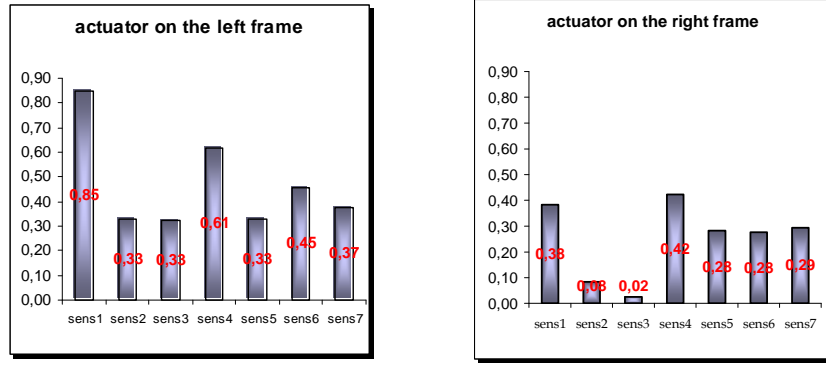


Fig. 5.1.56 – Damage Index “2” left and right actuators

It can be affirmed that the damage is between sensors #1 and #4, on the left side of the structure.

After having removed the rivet, the method has quantified the damage, giving indexes higher than the indexes pertinent to the nut damaged.

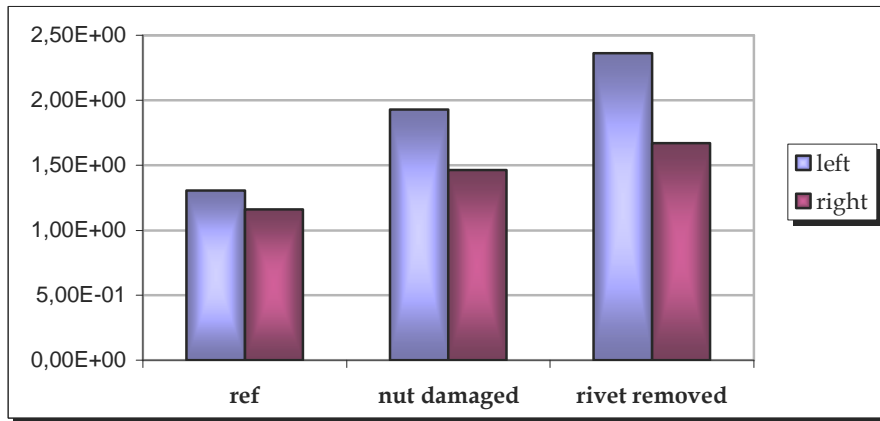


Fig. 5.1.57 – Global Damage Index “2” left and right actuators

About the localization the following charts show the Damage Index “2” determined using either the left or the right actuator. Also for the localization of the rivet removed the actuator installed on the left frame has given the best results.

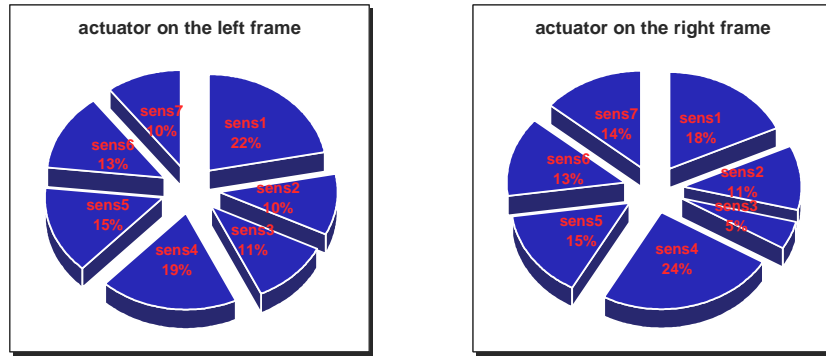


Fig. 5.1.58 – Damage Index “2” left and right actuators

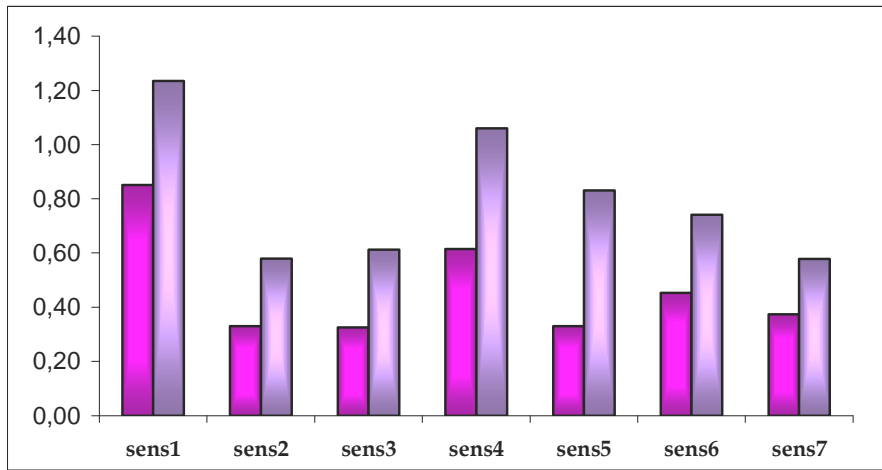


Fig. 5.1.59 – Damage Index “2” percentage increments – left actuator

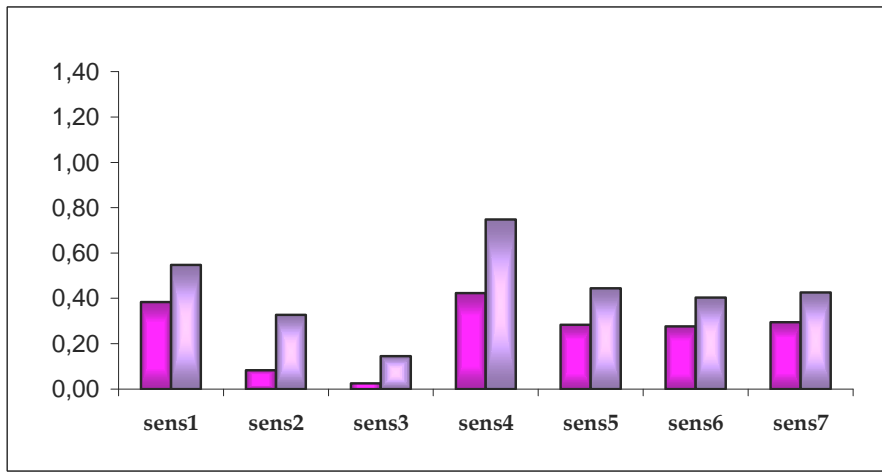


Fig. 5.1.60 – Damage Index “2” percentage increments – right actuator

V.1.2 Second experimental campaign

The second damage imposed on the test-article has consisted in a chemical corrosion. It was carried out by means of the hydrochloric acid with a 15% title, whose pH is -0,65. The corroded region measures 8,5 cm². The corrosion was carried out two times on that region, removing about 0,67 grams at a time.

On the test-article 8 piezoelectric patches have been bonded in order to create an array of actuators-sensors. Following several tests which have been carried out in order to set up the frequency range, only 4 piezoelectric patches have been used, since 4 are enough to demonstrate the capability of the techniques to identify and quantify the damage.



Fig. 5.1.61 – Second experimental test set-up

The FRFs of the monitored structure have been acquired from the points where piezoceramic patches have been glued. Employing alternately the piezoceramic patches as sensors and as actuators it was possible to acquire 12 Frequency Response Functions (4 actuators x 3 sensors).

The operative frequency range was fixed at 1,0 and 19,0 kHz measured through 1422 spectral lines.



Fig. 5.1.62 – Damage location



Fig. 5.1.63 – Corrosion detail

About the Damage Index method, it is possible to show a graph for each couple of actuator-sensor. To sum up the results, they have been gathered in a graph which contains four groups of bars. Every group represents the sum of indexes of the couple actuator-sensor, in which the actuator is fixed. Moreover each group consists of three bars: the first represent the sensitivity index, which is determined using FRFs of the healthy structure acquired at different times to measure the experimental error and the environmental noise and vibrations which can influence the FRFs; the second and third bars are the indexes obtained after the two corrosion steps.

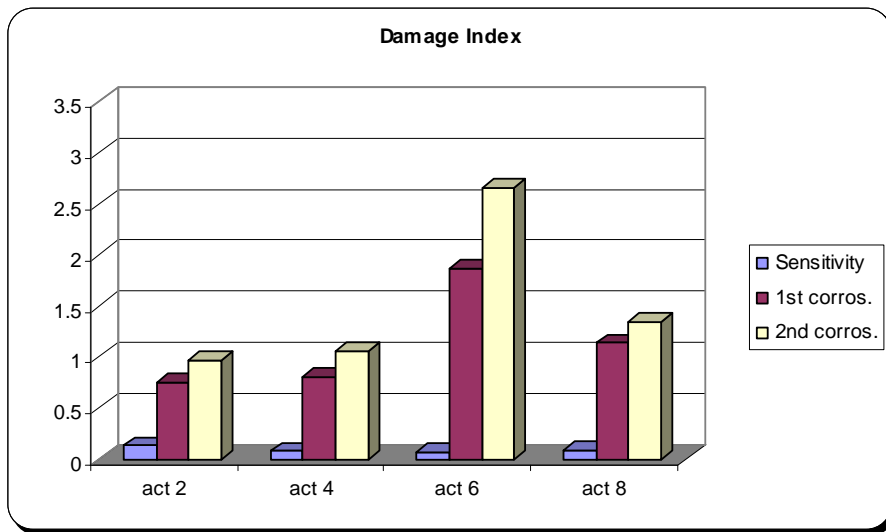


Fig. 5.1.64 – Corrosion Damage Index “2”

It can be noted that the index has identified the damage. In fact DIs are higher than the sensitivity indexes. Besides, the piezoceramic patch #6, which is close to the damaged area, has given the highest index, so it is possible to assert that the damage has been localised. About the quantification it can be noted that the second corrosion step has increased all the indexes.

A Neural Network was trained by means of eight FRFs acquisition campaign of the sound structure.

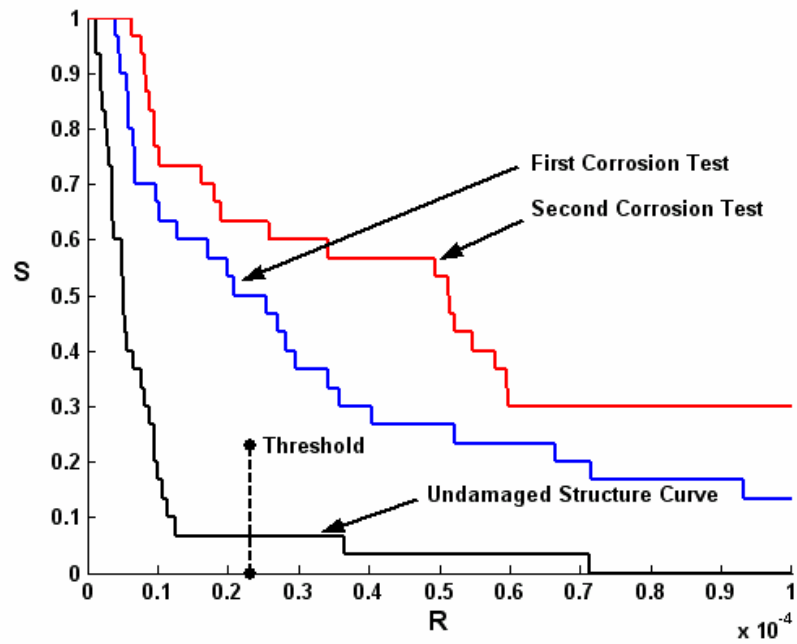


Fig. 5.1.65 – Neural Network output

About the Neural Network technique, it is possible to notice that the healthy configuration do not exceed the threshold, determined using the procedure which has been explained in the chapter 3, while the corrosion curves exceed the value itself.

It can be noted that the network was able to quantify the increasing of the corrosion.

V.1.3 Third experimental campaign

In order to execute the third experimental tests, the Vibrometer Scanning Laser and three only piezoceramic patches have been used.

The excitation signal was the swept sine, generated from 0 to 5 kHz. Taking into account the coherence function behaviour, the frequency range was fixed from 1,0 to 5,0 kHz. The excitation voltage was equal to 125 Volt.



Fig. 5.1.66 – Third experimental tests set-up

The piezoceramic patch #1 was used as actuator, while the other two patches as sensors. Furthermore, by means of the Laser Vibrometer, twenty-two acquisition points on the structure have been defined.

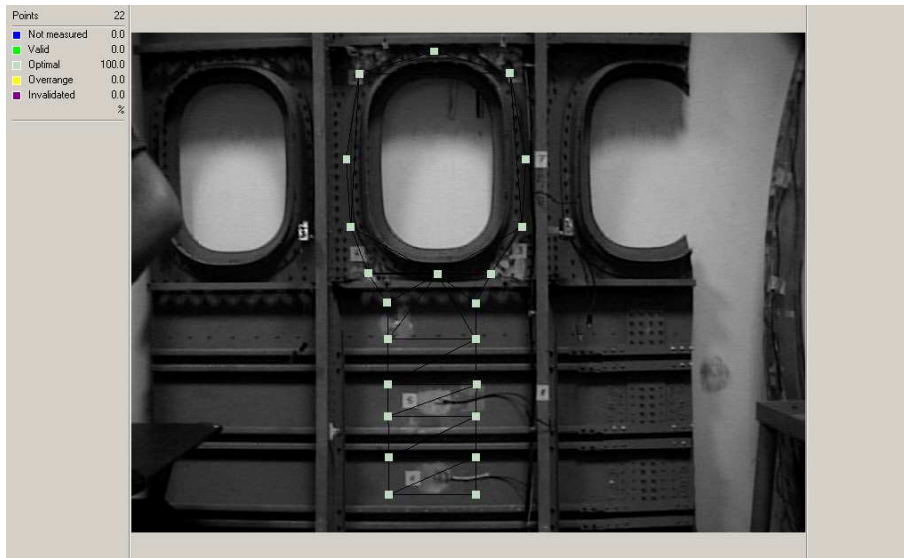


Fig. 5.1.67 – Laser Scanning Vibrometer scan points

Three experimental tests have been executed. One has regarded an addition of a mass of 50 grams only; the second regarded a hole made on the structure, having a diameter of mm.3, increased up to mm.4 to verify the capability of the method in quantifying the damage; the third regarded a crack whose length was equal to mm.6, enlarged up to perforate the structure. All those damage were execute in proximity of the patch #3.

The following pictures and graphs show the damage and the results obtained by means of the Damage Index “1” technique.

The bar charts show the results obtained using the piezoceramic patches #2 and #3 as sensors. The first bar of each group of bars represents the sensitivity index, while the second one represents the damage index.

Next, graphs which represent the results obtained by means of the twenty-two points acquired by the Laser Vibrometer are reported.



Fig. 5.1.68 – Mass addition

The mass of 50 grams was located in two different positions, a little far and close to the piezoelectric patch #3.



Fig. 5.1.69 – Drilling damage



Fig. 5.1.70 – Crack damage

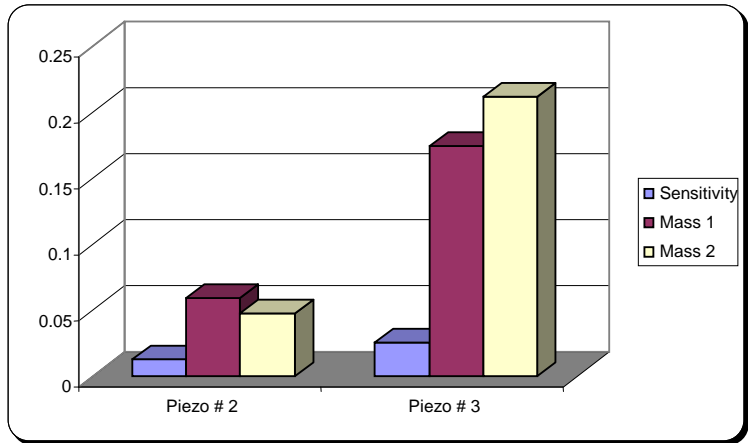


Fig. 5.1.71 – Mass Damage Index – piezoceramic patches

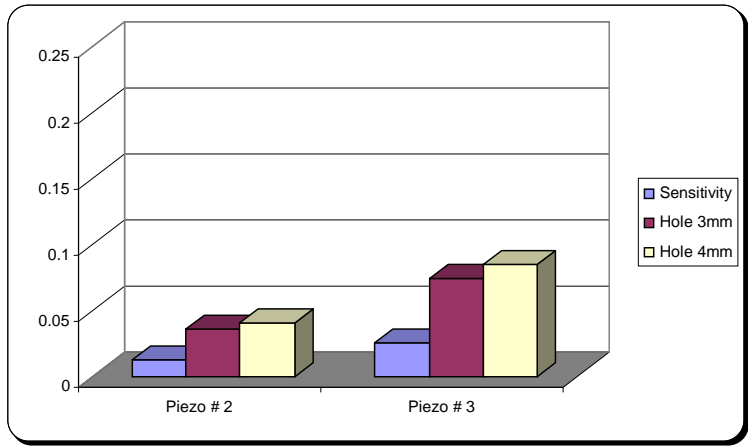


Fig. 5.1.72 – Hole Damage Index – piezoceramic patches

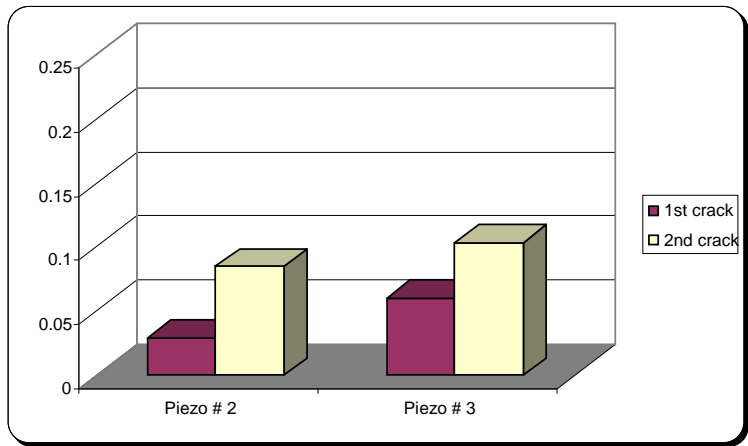


Fig. 5.1.73 – Crack Damage Index – piezoceramic patches

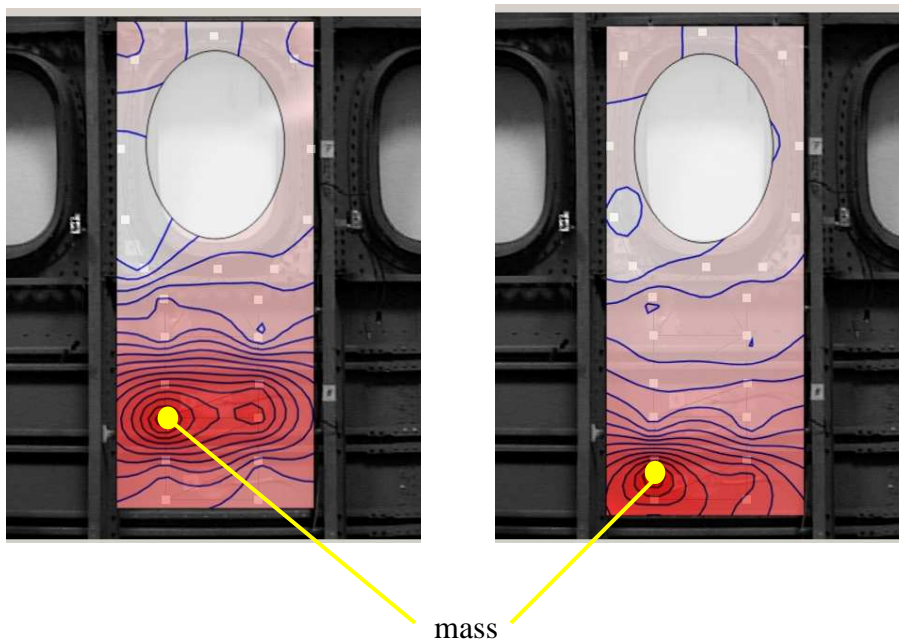


Fig. 5.1.74 – Mass Damage Index – Laser Vibrometer



Fig. 5.1.75 – Hole Damage Index – Laser Vibrometer



Fig. 5.1.76 – Crack Damage Index – Laser Vibrometer

It can be observed that:

- ✓ the presence of the mass has been identified and localized. Observing the piezoceramic results, it can be noted that the piezo #3 was able to define with precision the position of the mass, which is close to that piezo more and more;
- ✓ the hole has been also identified and localized. Furthermore, the Damage Index method was able to quantify its increase;
- ✓ the increasing crack was identified and localized as well. Besides, the quantification of the crack propagation up to perforate the structure has been clearly shown.

V.2 Second Test Article

The second test article which was used in order to verify the capability of the Damage Index and the Neural Network methods in identifying an localizing a damage was an aeronautical composite panel.

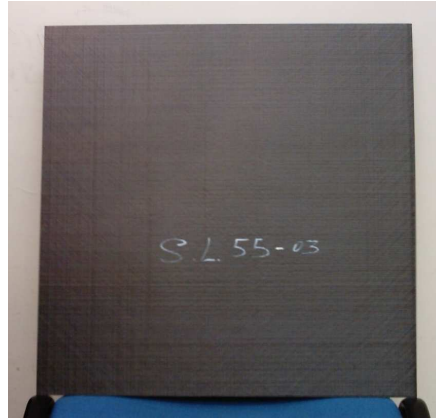


Fig. 5.2.1 – Composite panel

On that test article nine piezoelectrical patches have been bonded to create a symmetrical array of actuators and sensors. Several kind of signal generators, spectrum analyser, piezoceramic amplifiers have been used. Furthermore, as sensors system, a vibrometer scanning laser have been used.

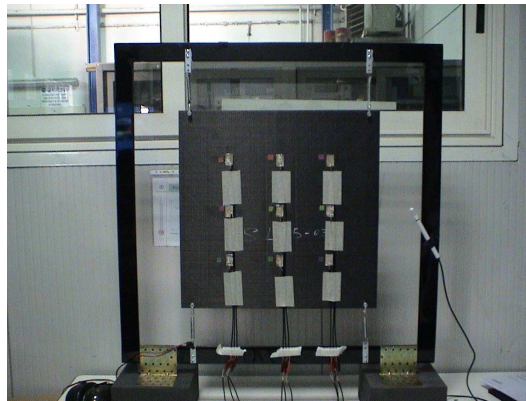


Fig. 5.2.2 – Composite panel set-up

Three experimental tests was executed on that panel. Before carrying out those experiments, a long time has been spent to define the right set-up. In fact, after an acquisition campaign of FRFs of the sound configuration of the panel, large variations of the sensitivity indexes were measured. Several kind of constraint, rubber or iron springs have been tested to discover why those variations are so large.

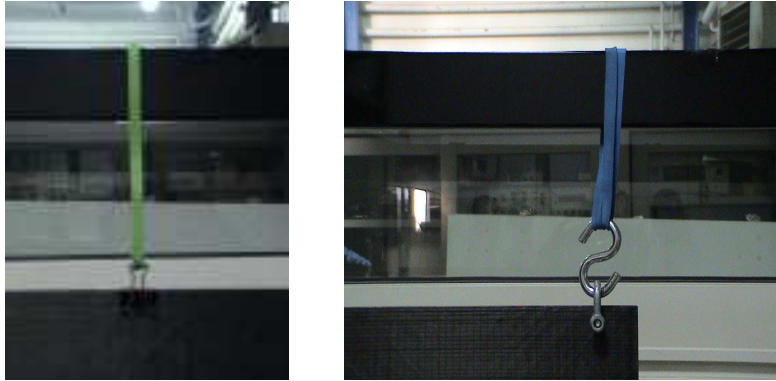


Fig. 5.2.3 – Suspension springs

In the end the panel has been constraint by means of four iron springs, since no explanation was found. The next step was to verify the environmental behaviour of the system formed by the panel, the piezoceramic patches and the glue which has been used to bond the patches on the panel.

The environmental parameters have been modified by means of an air conditioner and a vaporiser. In such a way it was possible to monitor the parameters, measuring temperature and humidity, not to control them, since an environmental room was not available.

First, the temperature and the humidity were decreased, then increased. It can be observed in the figure 5.2.5, and table 5.2.1, that an equal temperature, but a different relative humidity gives different sensitivity indexes.



Fig. 5.2.4 – Environmental set-up

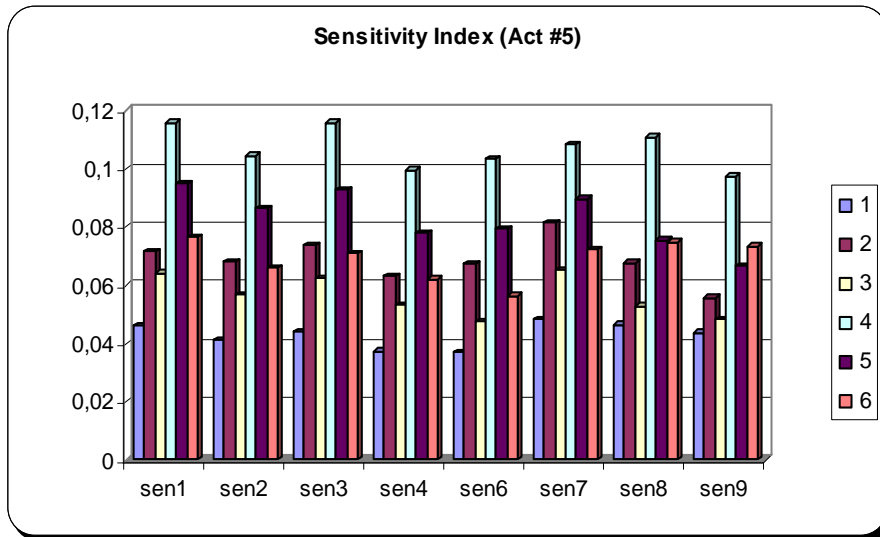


Fig. 5.2.5 – Sensitivity Index (Act #5 – central)

	T (°C)	p (mb)	rel hum %
1)	25.71	1013.3	54.7
2)	25.97	1013.3	55.9
3)	25.96	1013.2	56.4
4)	23.99	1013.1	48.8
5)	25.05	1013.1	54.0
6)	25.71	1013.1	57.1

table 5.2.1

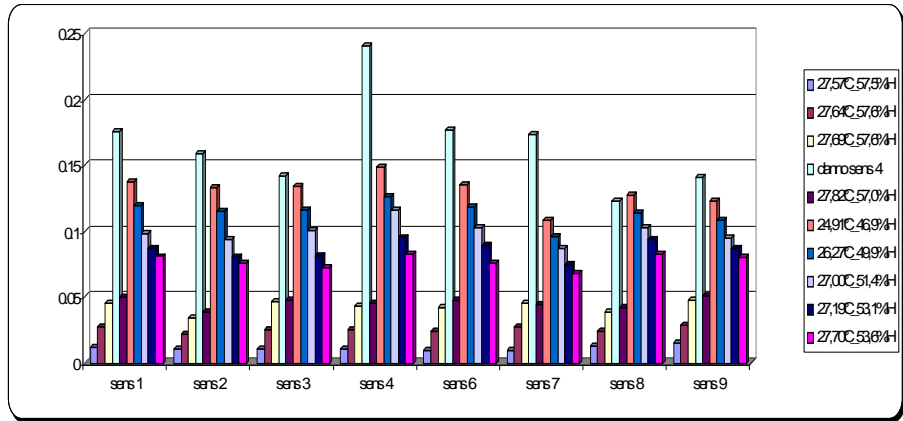


Fig. 5.2.6 – Sensitivity and Damage Index (Act #5 – central)

The figure 5.2.6 show then differences between the sensitivity indexes obtained modifying the environmental parameter, and the damage index determined adding a little mass close to the piezo patch #4. It can be noted that the damage can be identified, even if the sensitivity indexes show large variations (see the fourth cyan bar).

Three experimental tests have been carried out in order to test the “Damage Index” method, the neural network and the discrimination approach.

Employing alternately the piezoceramic patches as sensors and actuators it has been possible to acquire 72 Frequency Response Functions (9 actuators x 8 sensors). Moreover the frequency range of the acquisitions was fixed by taking in account the “coherence function”. Following that analysis the operative frequency range was fixed from 0,5 to 9,0 kHz measured through 1361 spectral lines (this last number is related to the signal acquisition device).

In the following subparagraphs the experimental tests executed on that panel are reported.

V.2.1 First Experimental Test

The first experimental test has consisted of an addition of a mass of 4 grams close to the piezoceramic patch #1 and, then, close to the patch #6. Imposing that kind of simulated perturbation it has been possible to test the capability of the neural network in identifying structural changes independently by their location. Besides, at the end of the tests, it has been possible to restore the composite panel to the initial configuration.

About the Damage Index method, it is possible to show a graph for each couple of actuator-sensor. To sum up the results, they have been gathered in two graphs. One about the first index and the other about the second index. Both graphs contain nine groups of bars. In the first graph every group represent the sum of indexes of the couple actuator-sensor, in which the sensor is fixed. In the second graph every group represent the sum of indexes of the couple actuator-sensor, in which the actuator is fixed.

Each group consists of three bars: the first represents the sensitivity index, which is determined using FRFs of the healthy structure acquired at different times to measure the experimental error and the environmental noise and vibrations which can influence the FRFs; the second and third bar are the indexes obtained after the addition of the masses.

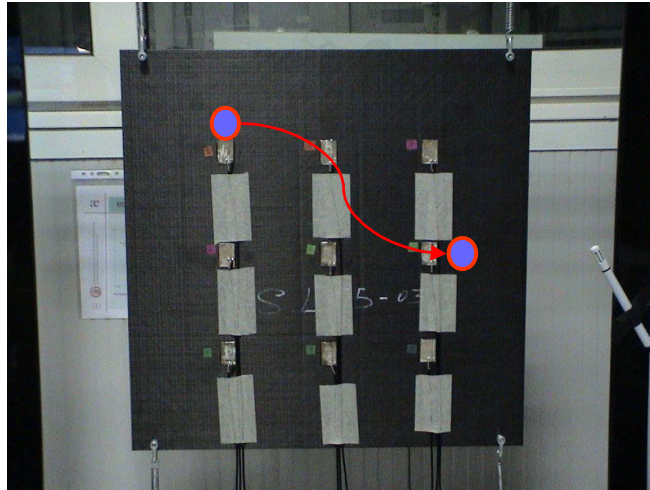


Fig. 5.2.7 – Mass locations

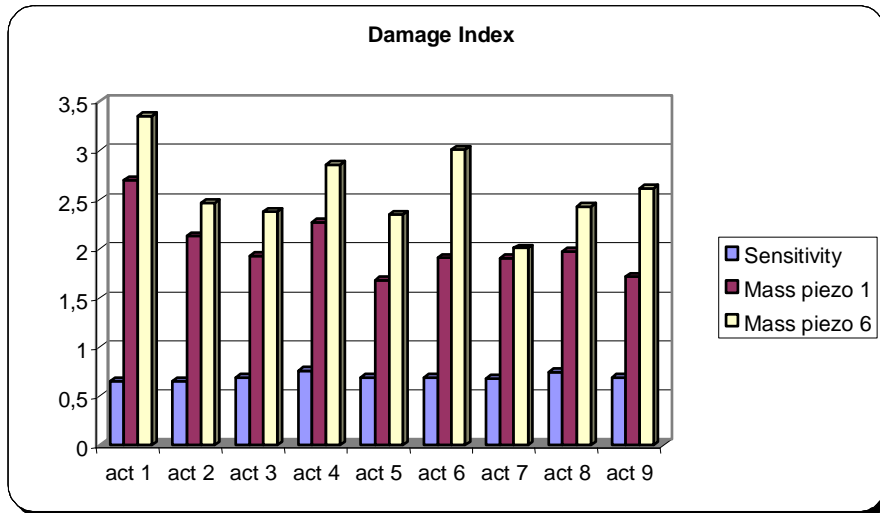


Fig. 5.2.8 – Actuators Damage Index “2”

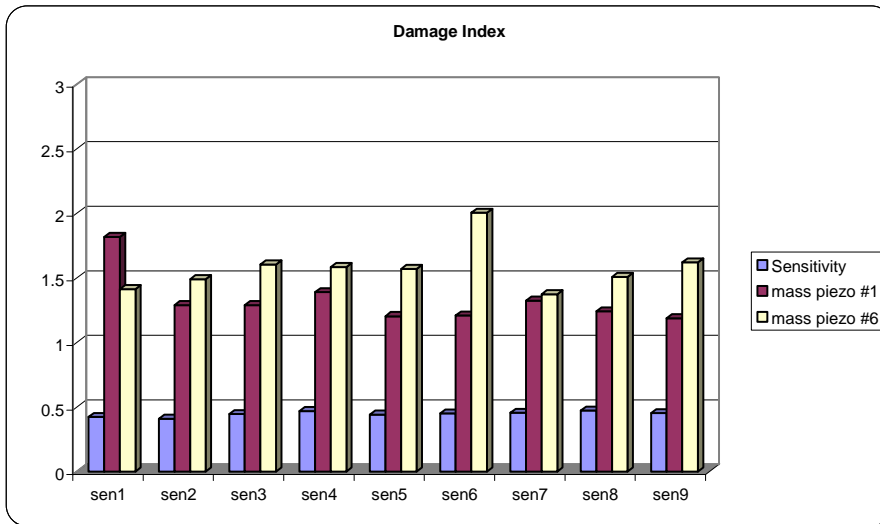


Fig. 5.2.9 – Sensors Damage Index “1”

It can be noted that the index has recognized the reference structure and identified and localized the perturbation. All patches have given higher DIs than the sensitivity indexes and it can be noted that the piezoceramic patches which are close to the added mass have the highest indexes, so it is possible to assert that the damage

has been localised. There is not the quantification because of the masses were no added in the same time.

Furthermore, to test the capability of the DI method in quantifying an increasing damage, three masses of 3, 5 and 10 grams have been added close to the piezo patch #1. For that test the piezoceramic patch #1 was the only one which was used as actuator.

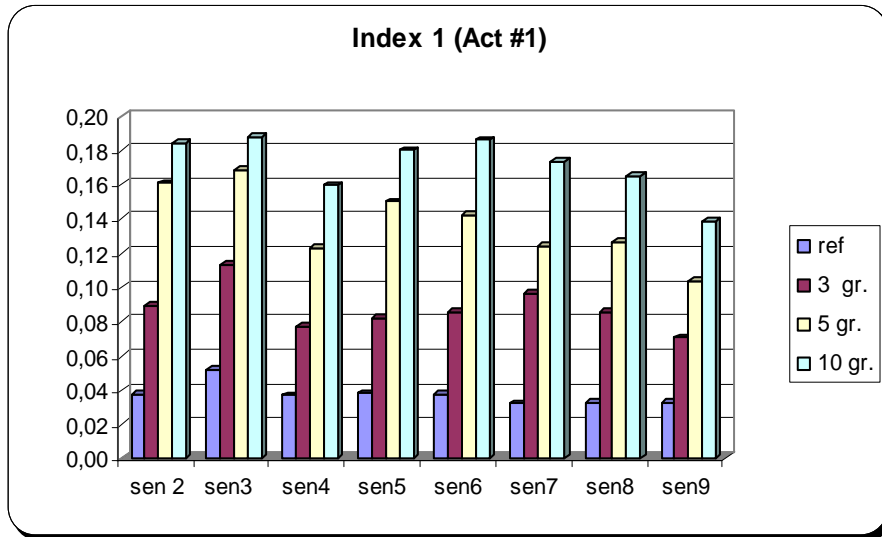


Fig. 5.2.10 – Quantification DI

It can be observed that the increasing of the mass added to the panel has been clearly quantified.

Both to summarize the results and to verify its capabilities, the vibrometer scanning laser was used. It is able to furnish global FRFs of the panel, since it acquires the FRFs in x points, then it calculates the average. The following graphs show a global Sensitivity and Damage Indexes obtained by the global FRFs acquired (fig. 5.2.10), and the differences between the DIs determined by means of the piezoceramic patches, and the laser vibrometer set to acquire in the same points where the piezoceramic patches have been bonded (fig. 5.2.11 and 5.2.12). The patch #5 worked as actuator; the mass was put close to the patch #1.

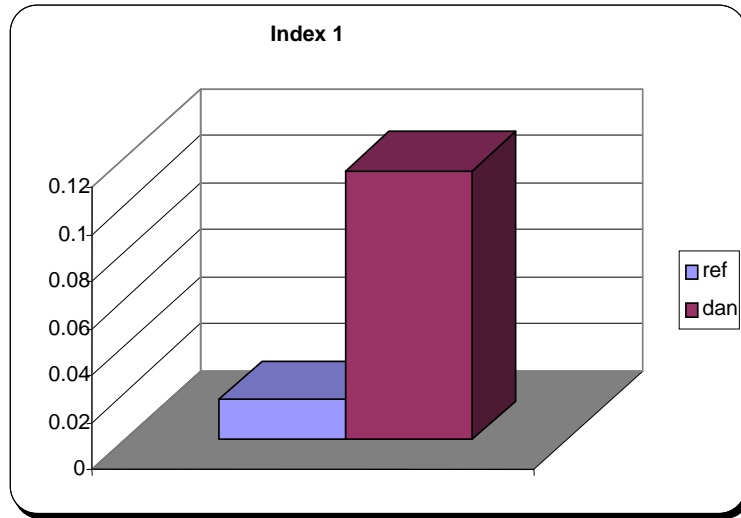


Fig. 5.2.11 – Global Damage Index

It is obvious that the damage has been identified by the laser system, since the Damage Index is much higher than the Sensitivity one.

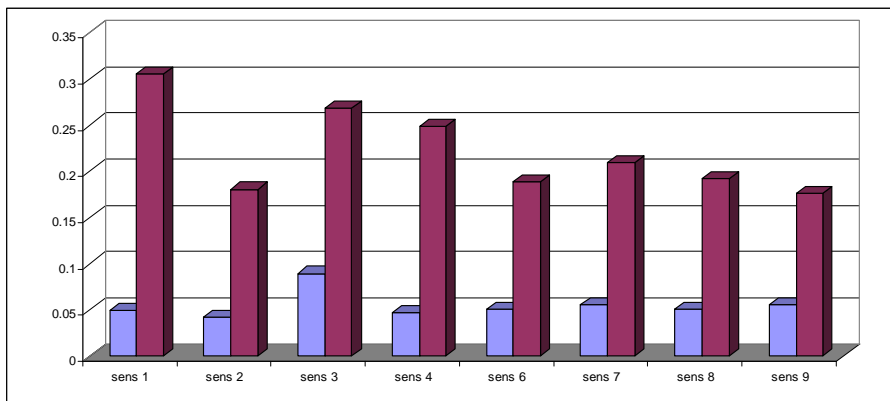


Fig. 5.2.12 – Piezo patches indexes

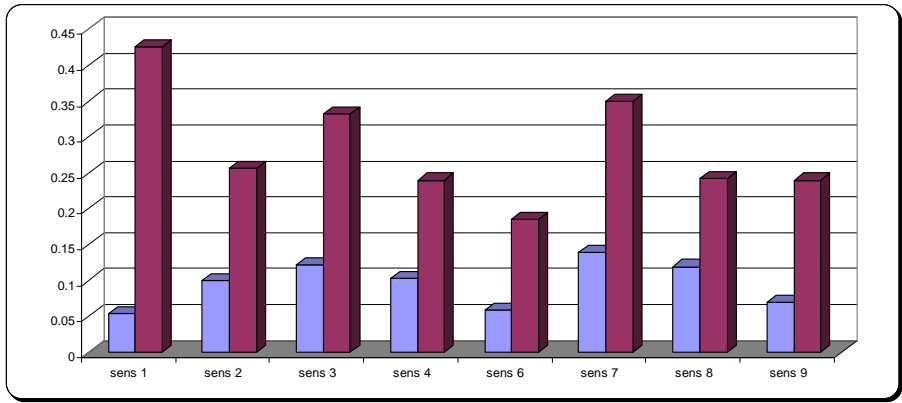


Fig. 5.2.13 – Laser Vibrometer indexes

Both sensors system were able to identify and localize the presence of the mass which is close to the piezo patch #1.

The last chart shows what happen when the frequency range is higher. In fact a Damage Index has been determined either from 0,5 to 9,0 kHz or from 10,5 to 19 kHz.

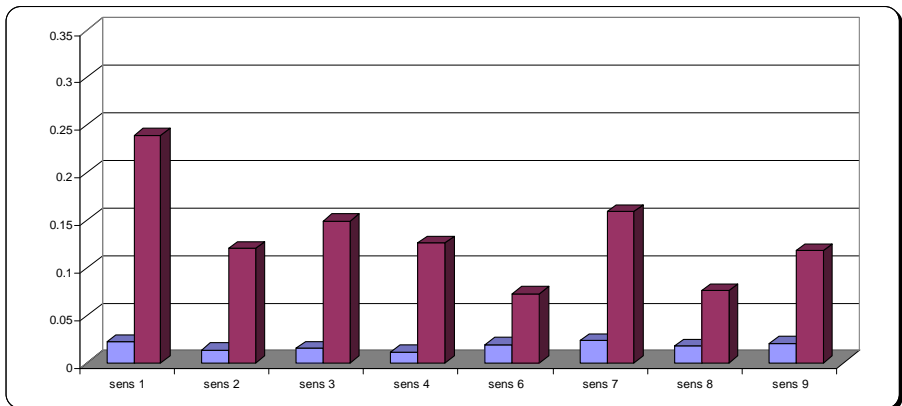


Fig. 5.2.14 – Laser Vibrometer indexes

It can be noted, comparing the figures 5.2.11 and 5.2.13, that the highest frequency is the more evident the localization of the damage is.

About the neural network, once the threshold representing the health status of the structure was identified (see Chapter 3), thirteen campaigns of acquisition, each of them consists of 72 FRFs, have been acquired for the training.

The neural network has been trained making use of the same FRFs of the healthy structure used for the determining of the Damage Index, as positive examples. Owing to reciprocity, since the system is linear, we have now used 36 FRFs only, reducing the redundancy of the information, so the network was lighter.

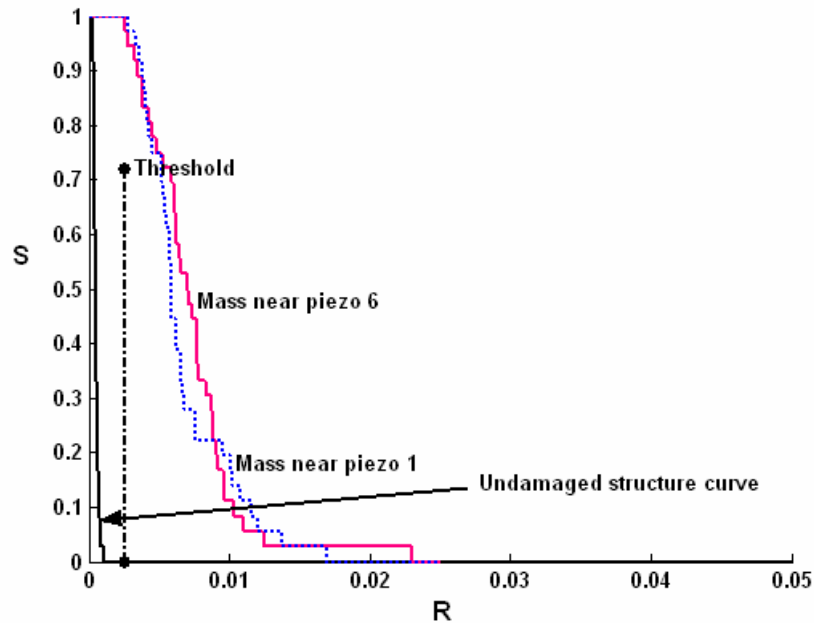


Fig. 5.2.15 – Neural Network output

As for the experimental test, it is possible to assert that the neural network has recognized the reference structure and has identified the perturbation. It is possible to notice from the output graph reported in figure 5.2.13 that the reference structure curve, which has been obtained by means of the acquisition of FRFs of the sound structure, is very close the x-axis, while the addition masses curves are over the threshold.

Furthermore the position of the mass is irrelevant for the identification, in fact the curves are practically super imposable.

V.2.2 Second Experimental Test

The second experimental test has consisted in three impact tests. A sphere made by steel, whose mass is 146,4 grams and the diameter is equal to 4 centimetres, has been used for the impact. The edges of the composite panel have been stiffened, and the panel has been placed horizontally.



Fig. 5.2.16 – Impact set-up

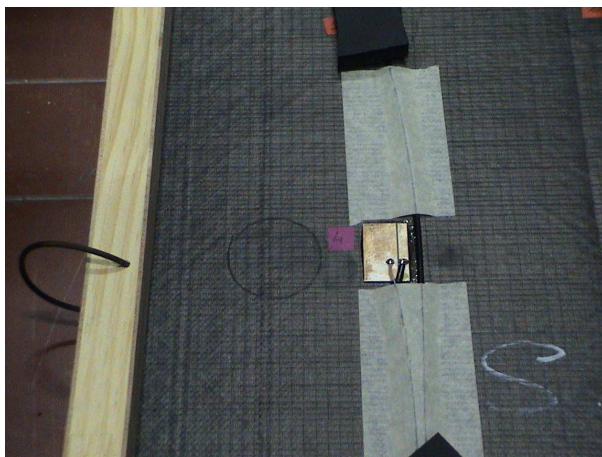


Fig. 5.2.17 – First Impact location

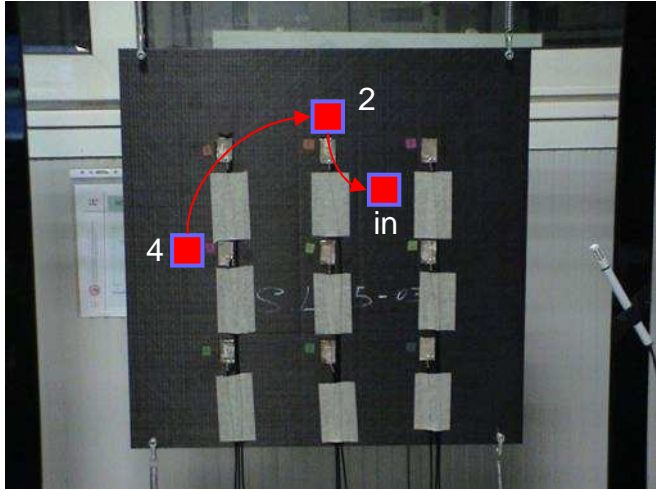


Fig. 5.2.18 – Impact tests locations

For the first impact test that sphere has been dropped from a height of 2 metres, so the impact energy has been equal to 2,87 Joule, close to the piezoceramic patch #4, outside of the patches array; for the second impact test the sphere has been dropped from a height of 2,80 metres, so the impact energy has been equal to 4,02 Joule, close to the patch #2, and, for the third impact test, the height was equal to 3,30 metres, and the impact energy has been equal to 4,74 Joule, internal to the array. The next chart represents the global index obtained by means of the Vibrometer.

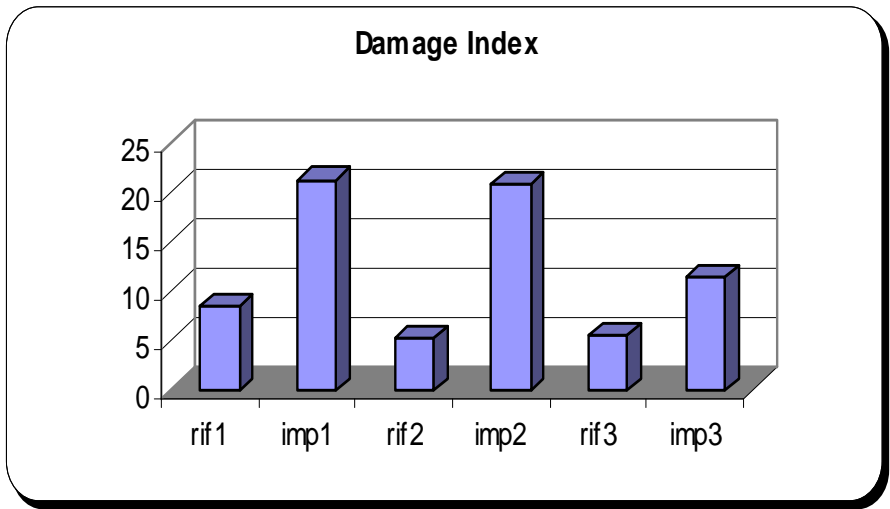


Fig. 5.2.19 – Global impacts indexes

It can be observed, from the chart 5.2.17, that all the impacts have been identified by the Laser Scanner.

About the Damage Index method, it is possible to show a graph for each couple of actuator-sensor. To sum up the results, they have been gathered in two graphs. One about the first index and the other about the second index. Both graphs contain nine groups of bars. In the first graph every group represent the sum of indexes of the couple actuator-sensor, in which the sensor is fixed. In the second graph every group represent the sum of indexes of the couple actuator-sensor, in which the actuator is fixed.

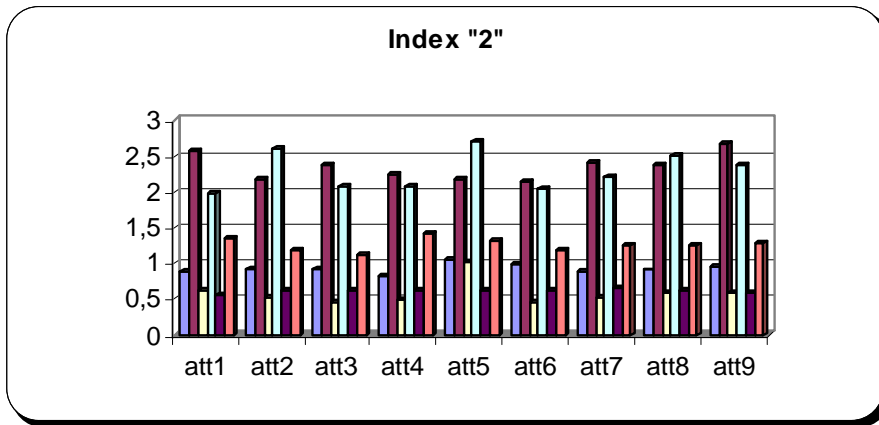


Fig. 5.2.20 – Actuators DI “2”

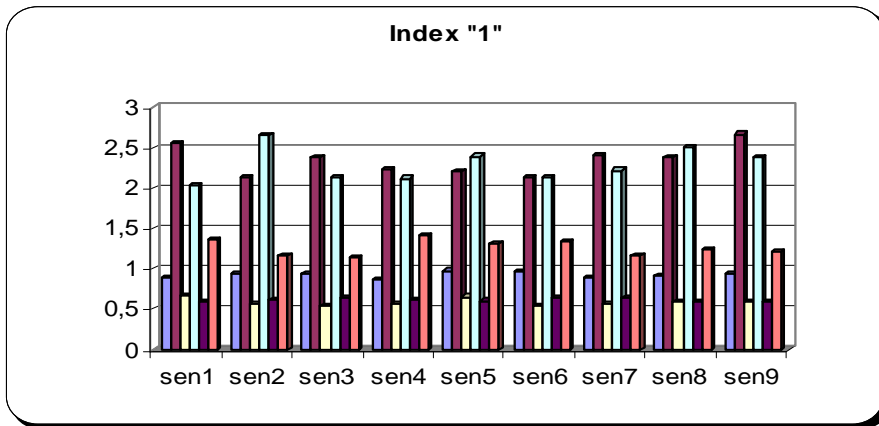


Fig. 5.2.21 – Sensors DI “1”

The first, the third and the fifth bars represent the sensitivity indexes determined before each impact; the second, the fourth and the sixth bars are the indexes determined after the subsequent impacts.

All the indexes have identified the damage, in fact all damage indexes are higher than the sensitivity ones, but only the second impact has been localized by the Index “1”. Probably the first impact had too low energy, while the third, induced internally to the patches array, leads to a sort of shadow effect since the patches are located in a narrow array.

The last two charts show what happen when the frequency range is higher. A Damage Index has been determined either from 0,5 to 9,0 kHz or from 10,5 to 19,0 kHz for the second impact test close to the piezoceramic patch #2.

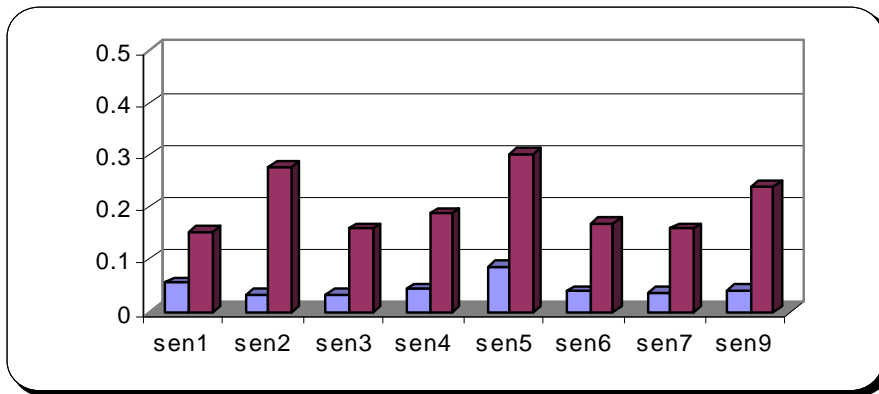


Fig. 5.2.22 – Damage Index (0,5 – 9,0kHz)

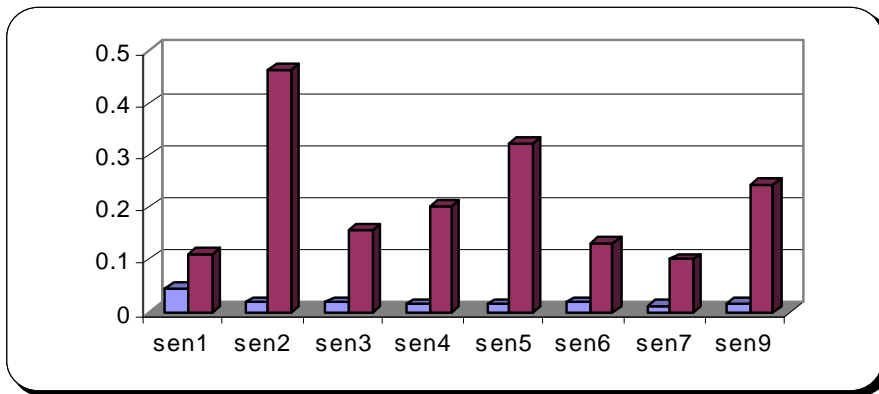


Fig. 5.2.23 – Damage Index (10,5 – 19,0kHz)

The previous charts show how the frequency can improve the localization of the damage, in fact at higher frequencies the localization is better.

About the Neural Network, as for the second experimental tests, the impacts by means of the iron sphere, probably a damage has occurred. The neural network has confirmed it, in fact its output puts the impact curves far from the undamaged structure curve.

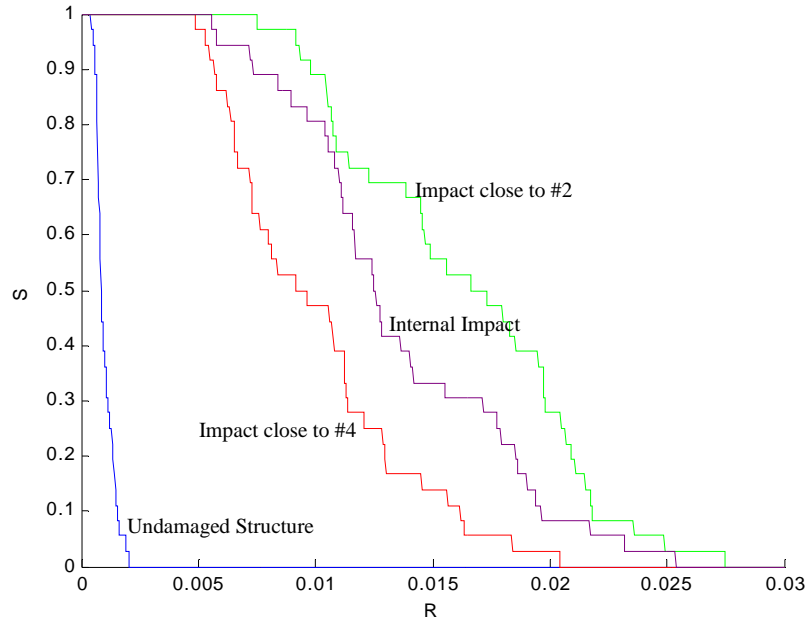


Fig. 5.2.24 – Neural Network impacts output

The FRFs, which have been acquired after the impact test, are definitely changed. That damage could be a delamination.

Next graph represents the neural Network output about the second impact, after that the threshold was determined as in Chapter 3.

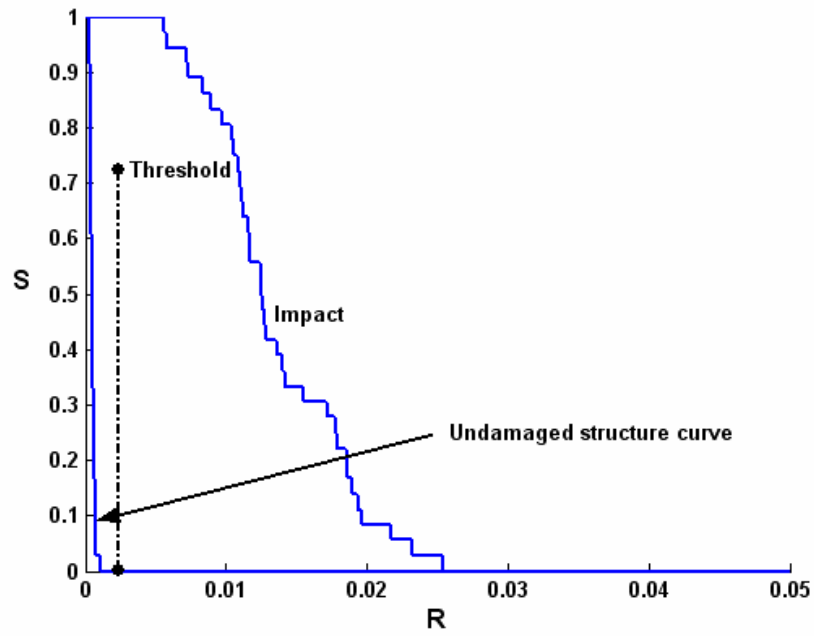


Fig. 5.2.25 – Neural Network impact #2 output

It is clear that the impact has been identified. The neural network has confirmed it, in fact its output puts the impact curve far from the threshold, and very far from the undamaged structure curve.

The FRFs, which have been acquired after the impact tests, are definitely changed. That damage could be a delamination.

V.2.3 Third Experimental Test

About the third experimental test, the panel has been drilled. Two holes were made close to the patches #2 and #3, having a diameter equal to mm.5. Besides, the hole close to the patch #2 was increased up to mm.7.

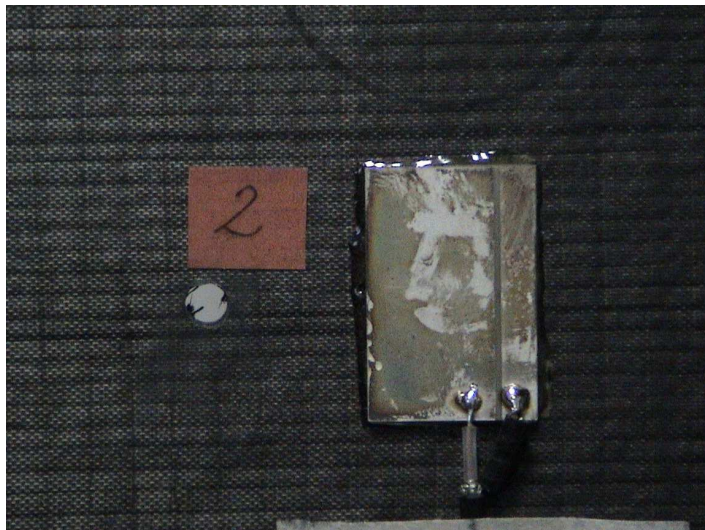


Fig. 5.2.26 – Hole mm.5 location #2

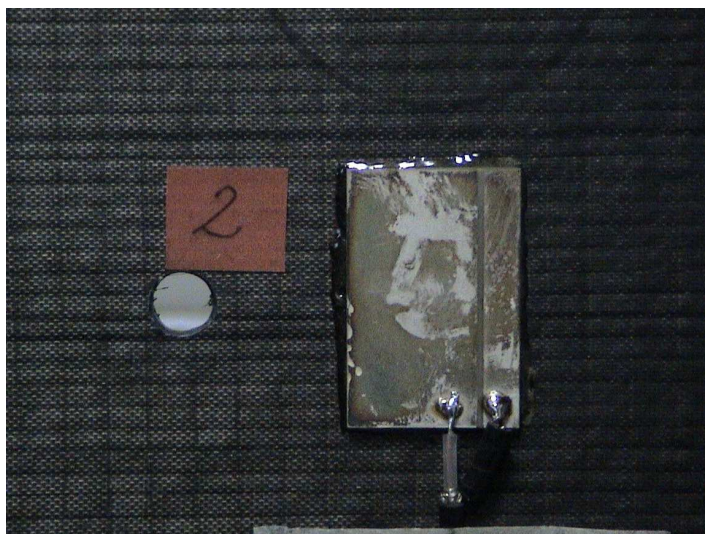


Fig. 5.2.27 – Hole mm.7 location #2



Fig. 5.2.28 – Hole mm.5 location #3

As well as the previous experimental tests, a global Damage Index has been calculated by means of the Vibrometer Scanning Laser for the hole close to the patch #3. The following chart show that result. It can be noted that the hole has been identified.

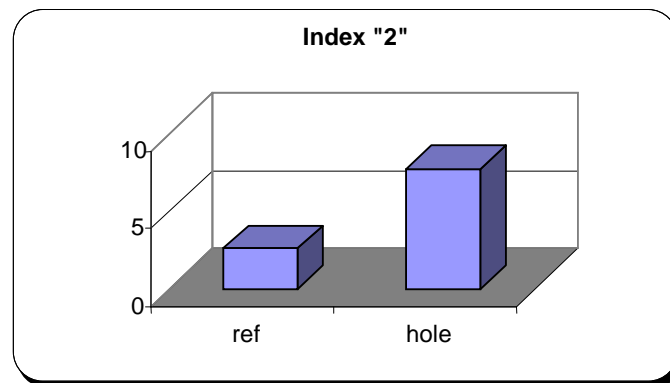


Fig. 5.2.29 – Global Damage Index “2”

Moreover, the Damage Index results are shown for each couple of actuator-sensor. They have been gathered in two graphs. One for each Damage Index. Both graphs contain nine groups of bars. In the first graph every group represent the sum

of indexes of the couple actuator-sensor, in which the sensor is fixed. In the second graph every group represent the sum of indexes of the couple actuator-sensor, in which the actuator is fixed.

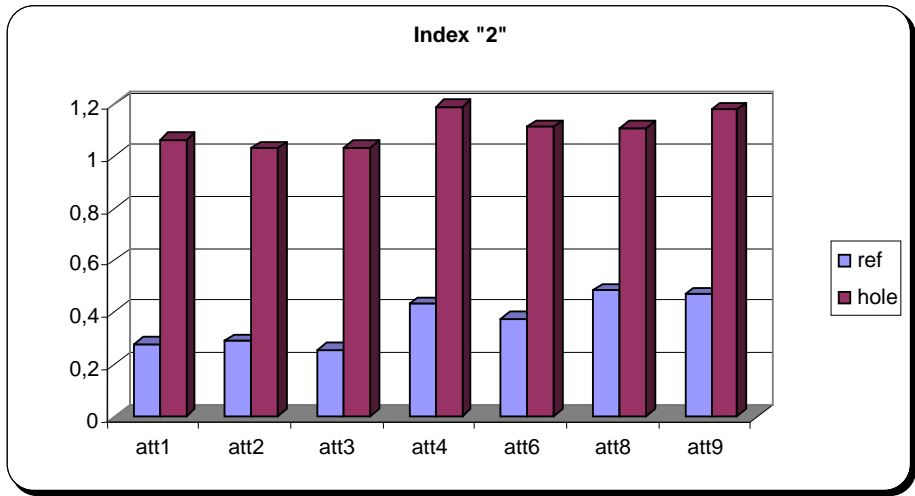


Fig. 5.2.30 – Actuator DI “2”

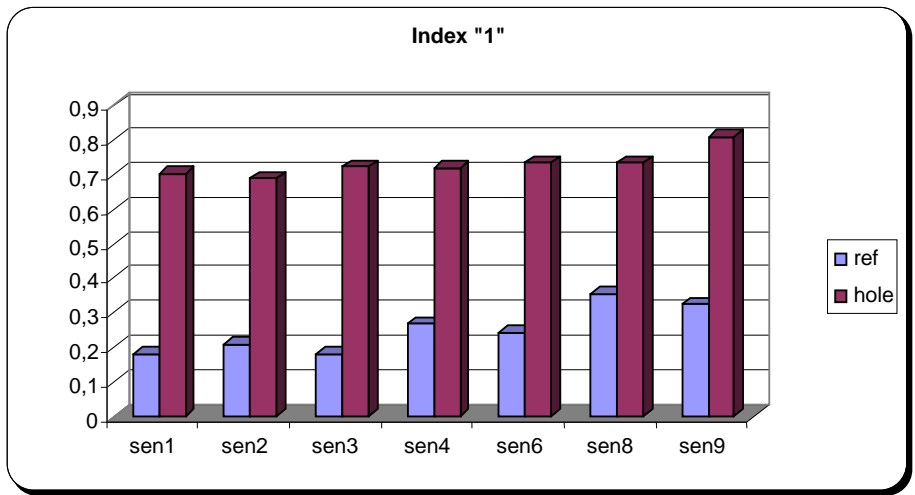


Fig. 5.2.31 – Sensors DI “1”

Both indexes have identified the damage, in fact the damage indexes all higher than the sensitivity ones, but they have not localized it, probably because the hole was realized internally at the patches array. Note that the same kind of problem has been discussed in the previous subparagraph.

About the hole close to the piezoceramic patch #2, the next charts show the results.

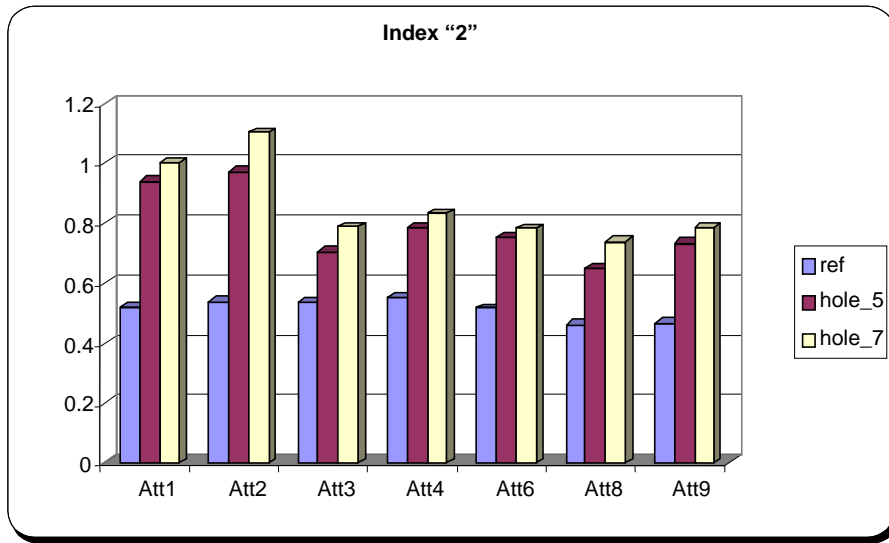


Fig. 5.2.32 – Actuator DI "2"

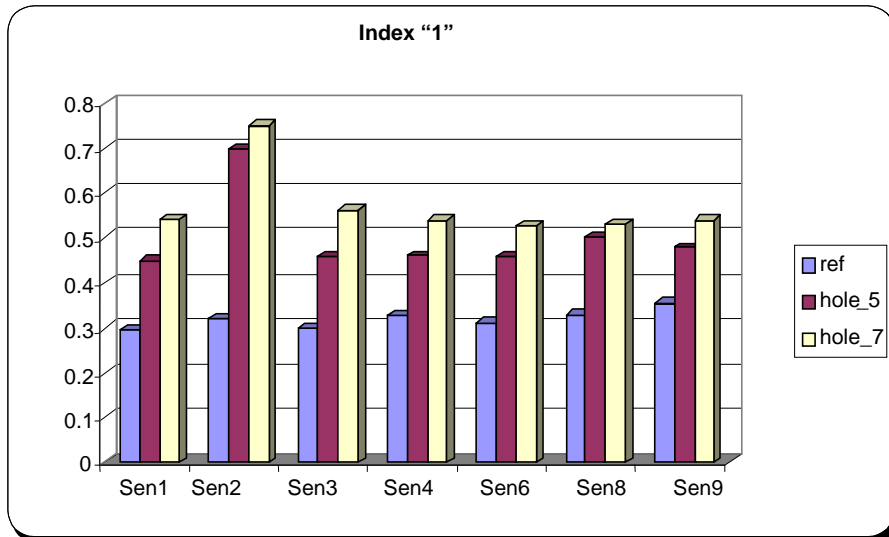


Fig. 5.2.33 – Sensors DI "1"

In that case the damage has been identified, localized and quantified. All indexes are higher than the sensitivity ones, especially the index related to the patch #2. Furthermore, all the bars which represent the hole increased up to mm.7, have values higher than the bars which represent the hole equal to mm.5.

V.3 ATR-72

The last test article which has been used to execute experimental tests in order to verify the capabilities of both methods, the Damage Index and the Neural Network, has been an ATR-72 aircraft.



Fig. 5.3.1 – ATR-72 MSN 098



Fig. 5.3.2 – ATR-72 internal views

V.3.1 Overview

Five different areas of the aircraft have been monitored. Those areas have been defined in collaboration with engineers of the Department of Structural Engineering of the ATR Toulouse division. Three areas are internal to the fuselage, and two out of that:

- A part where the frame 29 is linked to the stringer 13, on the right side of fuselage;
- A floor support zee close to the passenger door;
- A floor frame located in the rear of the fuselage, where the frame 42 is;
- The Main Landing Gear (MLG) truss shear on the right side of the aircraft;
- The frame 45 located in the tail cone.

The used instrumentation has been formed by the Ono Sokki DS2100 spectrum analyzer which has generated the excitation signal and acquired the FRFs; the TREK piezoceramic amplifier; a laptop and the interface device to connect the aircraft cables to the instrumentation.



Fig. 5.3.3 – Instrumentation



Fig. 5.3.4 – Interface device

The excitation signal used is the swept sine from 0 Hz to 20 kHz. The output voltage of the generator has been fixed to 2 Volt, amplified 25 times by the amplifier, up to 50 Volt only.

About the Damage Index method they have been determined the indexes “1” and “2” with regard to two frequency ranges, from 1,5 kHz to 10 kHz and from 10 kHz to 18,5 kHz, for each monitored part of the aircraft, taking into account both the coherence function, which has given bad values from 0 Hz to 1,5 kHz, and the Brigg effect which has influenced the frequencies close to 20 kHz. The number of spectral lines used is equal to 681 for each frequency range.

Furthermore, they have been trained Neural Networks for each part of the fuselage and for each frequency range.

About the identification of damage it has not been possible waiting for a natural damaging of the structure, since it would have need much more time we had. So, for example, rivets have been removed, simulating a typical aeronautical damage in those areas, changing the stiffness of the structure.

In the following paragraphs all the results are explained for each monitored area.

V.3.2 Frame 29

The first area tested is an internal region of the fuselage, close to the interception point between the frame #29 and the stringer #13, on the right side of the aircraft. Six piezoceramic patches have been bonded on the structure: five, which have a square shape, on the fuselage skin, and one, which has a rectangular shape, on the stringer #13. the piezoceramic patches #1, #2, #3 and #4 have a thickness equal to mm.1, while the patches #5 and #6 have a thickness equal to mm.0,5.

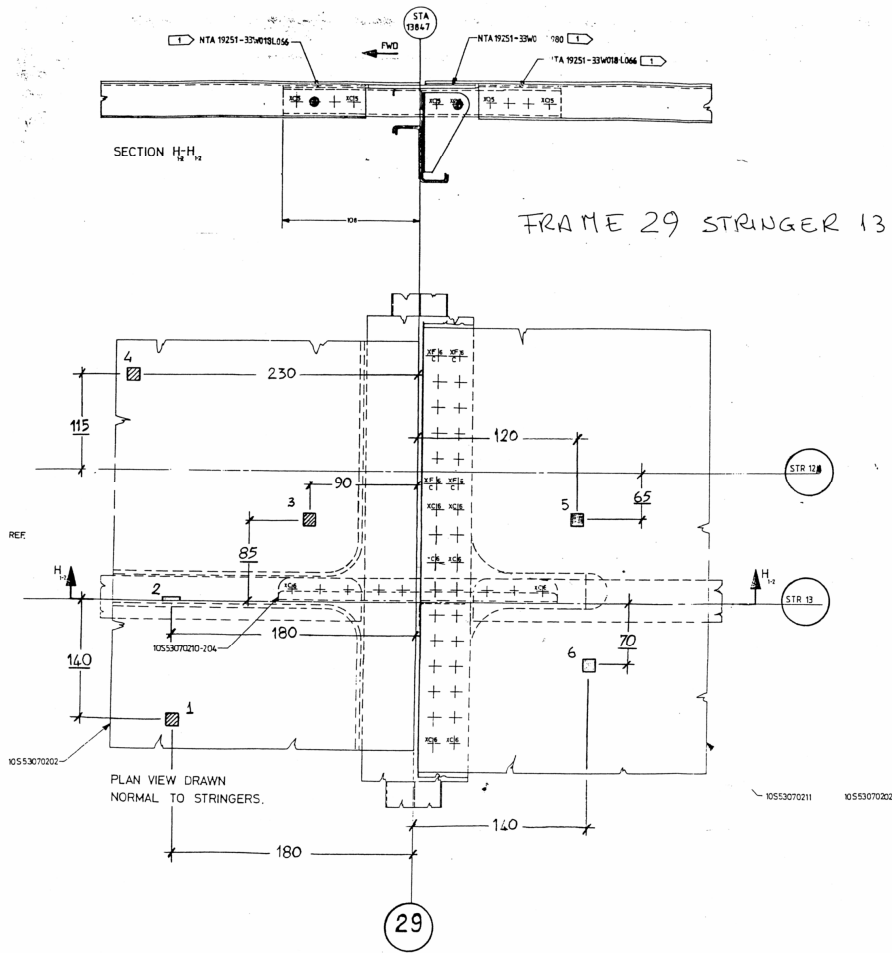


Fig. 5.3.5 – First monitored area scheme



Fig. 5.3.6 – First monitored area



Fig. 5.3.7 – First monitored area



Fig. 5.3.8 – First monitored area (zoom)

Firstly, an acquisition campaign of the sound structure has been executed both to define the right sensitivity index and to be able to train a dedicated Neural Network. They have been carried out eight FRF' acquisitions at different times for each actuator-sensor couple, which are thirty. In the end there are seven sensitivity indexes, since an FRFs acquisition is for the reference, for each actuator-sensor couple, for each frequency range and for each Damage Index. Furthermore, two Neural Networks have been trained, one for each frequency range.

In the following charts each group of bars show the indexes for a specific actuator-sensor couple: act. #1 – sens. # 2 ... act. #1 – sens. #3 act. #6 sens. #5.

The following step has been a simulation of a damage, consisting of a removal of a rivet connecting the stringer #13 to the joint stringer, which have the Part Number 10S53070210, and it has made of 7075-T73511 aluminium alloy, derived by an extruded piece NTA 44256 (Alenia Technical Standard).

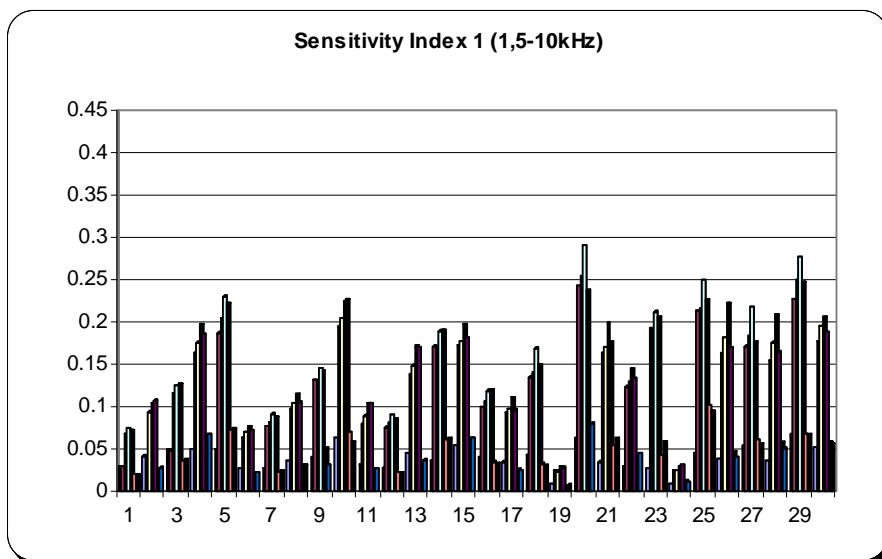


Fig. 5.3.9 – Sensitivity Index

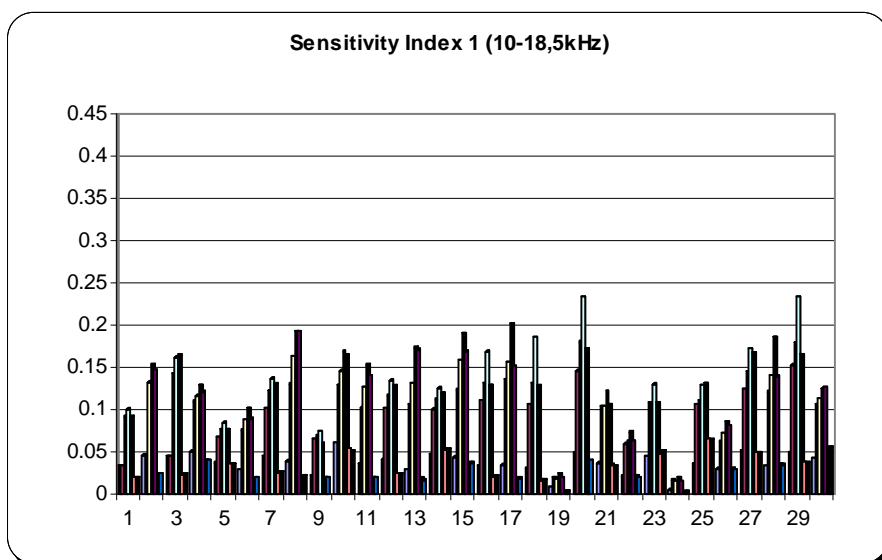


Fig. 5.3.10 – Sensitivity Index

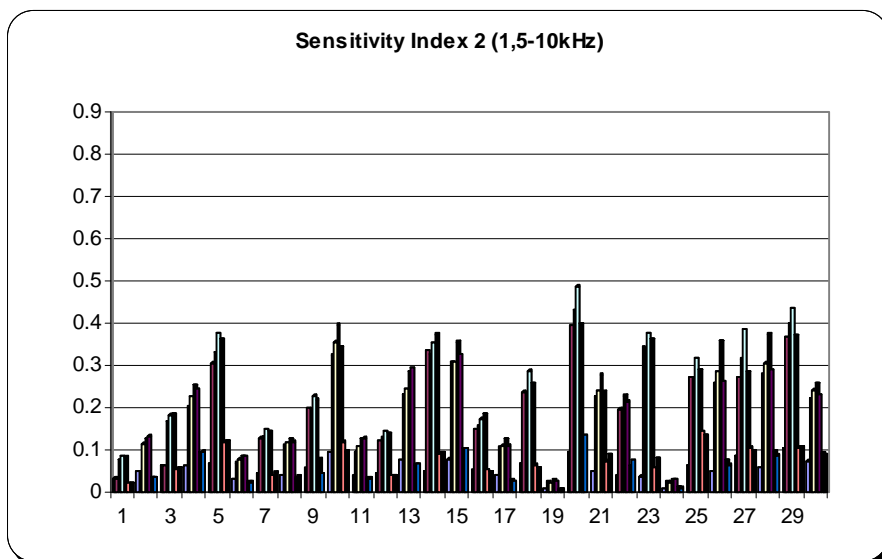


Fig. 5.3.11 – Sensitivity Index

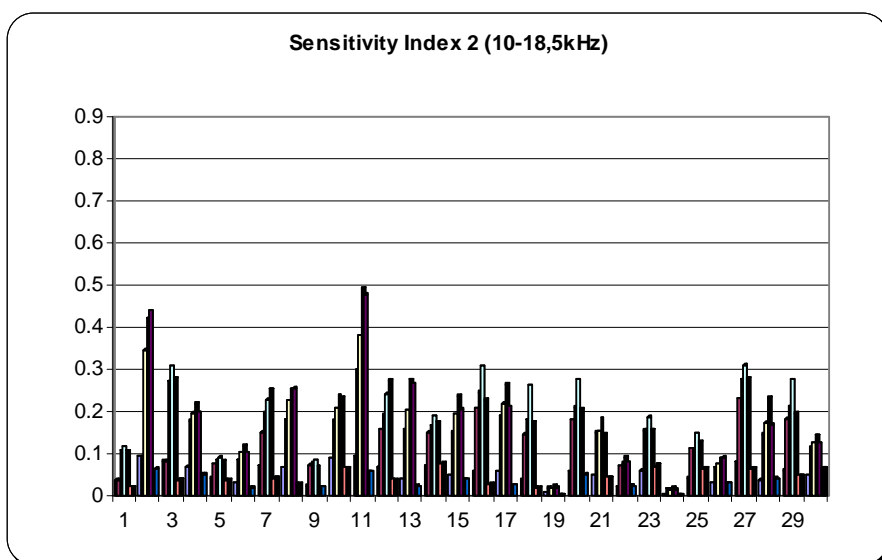


Fig. 5.3.12 – Sensitivity Index



Fig. 5.3.13 – Rivet removal

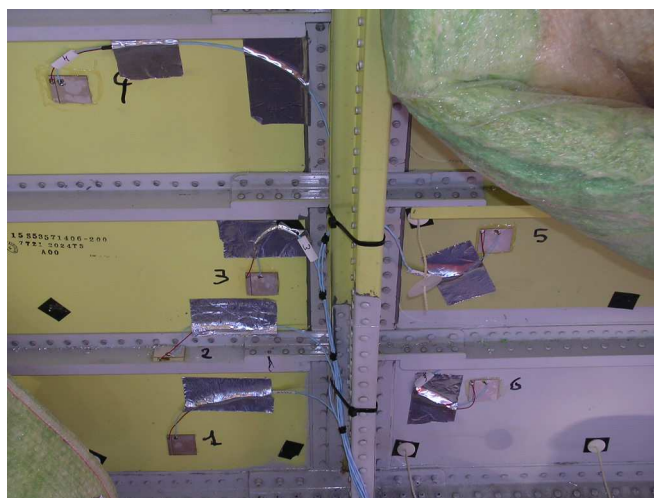


Fig. 5.3.14 – Area after the “damage”

Lastly, an acquisition campaign of the damaged structure has been executed. They have been carried out six FRF’ acquisitions at different times for each actuator-sensor couple. In the end there are six damage indexes for each actuator-sensor couple, for each frequency range and for each Damage Index.

The following charts show the damage indexes as same as the sensitivity ones.

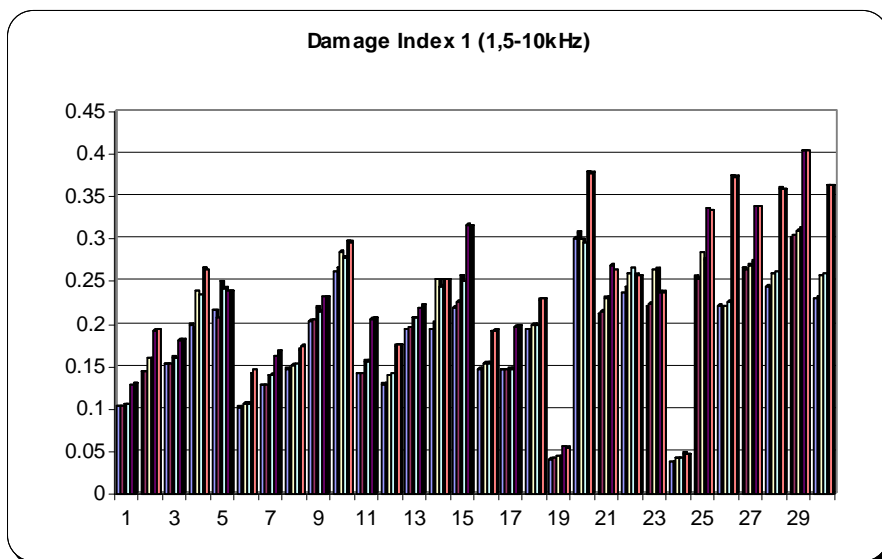


Fig. 5.3.15 – Damage Index

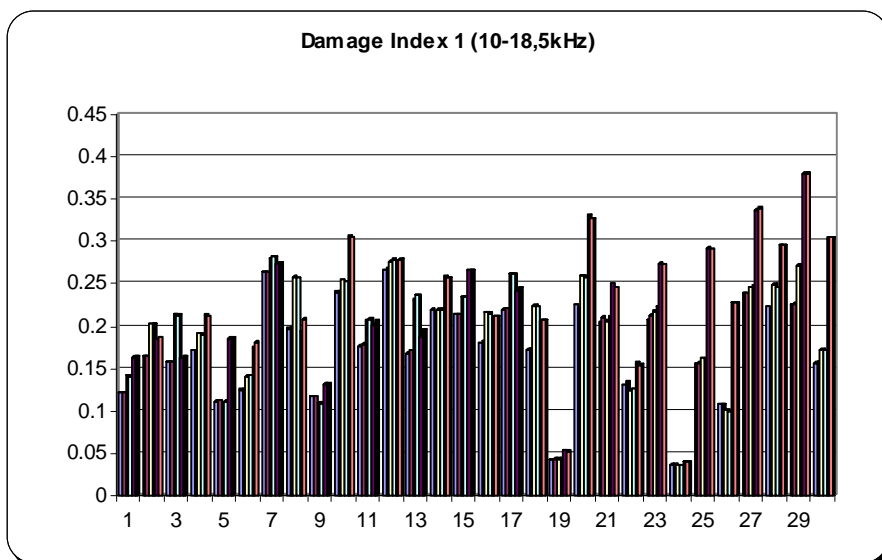


Fig. 5.3.16 – Damage Index

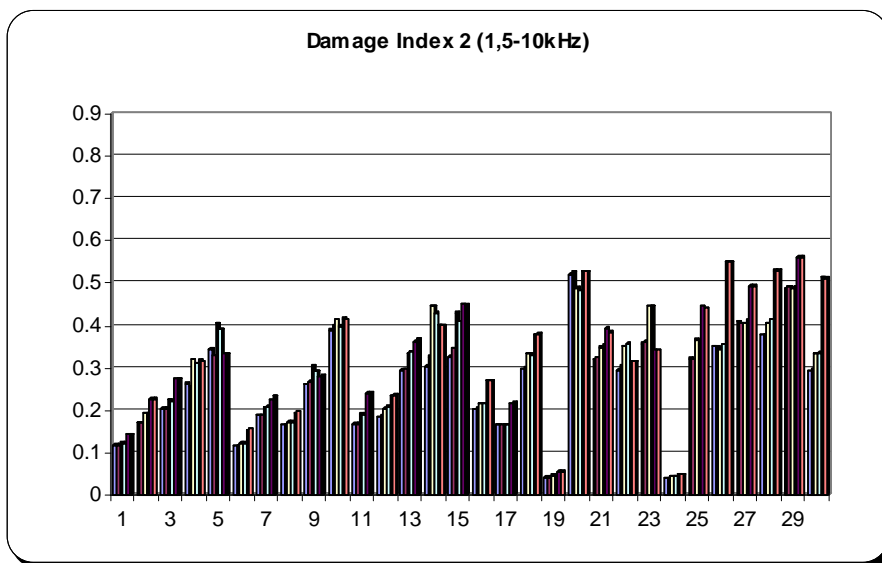


Fig. 5.3.17 – Damage Index

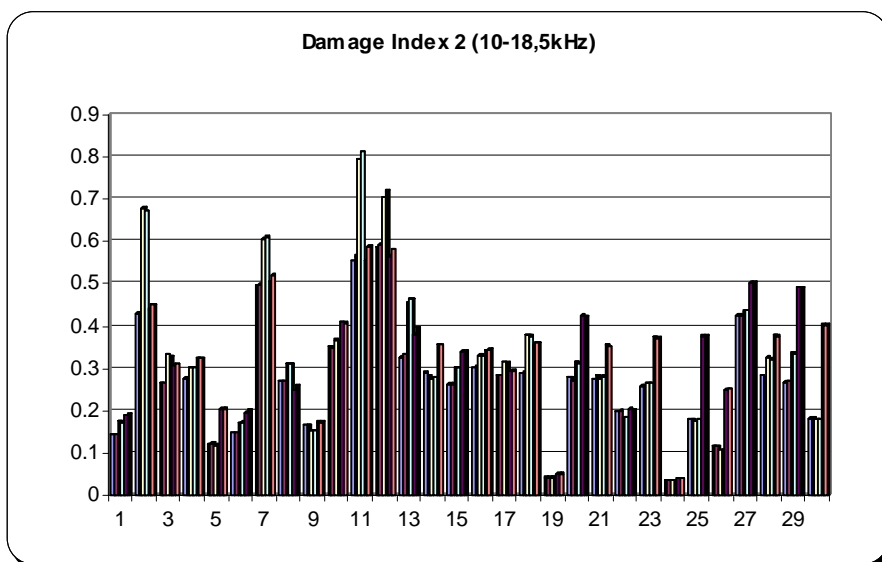


Fig. 5.3.18 – Damage Index

It can be observed that the removal of the rivet has been identified and localized. In order to make all the results more evident, some data manipulations have been done.

First, to sum up the results, they have been gathered in eight graphs. Four about the first index and the others about the second one; about each index, two about the low frequency range (1,5 – 10kHz) and two about the high frequency range (10 – 18,5kHz); about each frequency range, one chart represents the sum of indexes of the actuator-sensor couples, in which the actuators are fixed, while the second one represents the sum of indexes of the actuator-sensor couples, in which the sensor are fixed.

It can be observed that every index has identified the damage. In fact all DIs are higher than the sensitivity indexes. The localization is not so evident: maybe the point is that the system is very sensitive, in fact all the sensors have felt the presence of the damage, and, furthermore, that representation method is not the best. The piezoelectric patch #2, put on the stringer, does not give a good localization of the rivet failure. The Damage Index “2” works better than the Index “1”., and working at the highest range frequency gives the best localization. In fact, to localize the damage, it is necessary to calculate the Index “2” at the high frequency. In that case, the graphs show that the piezoceramic patch #3 localizes the rivet failure, helped by the piezoceramic patch #2.

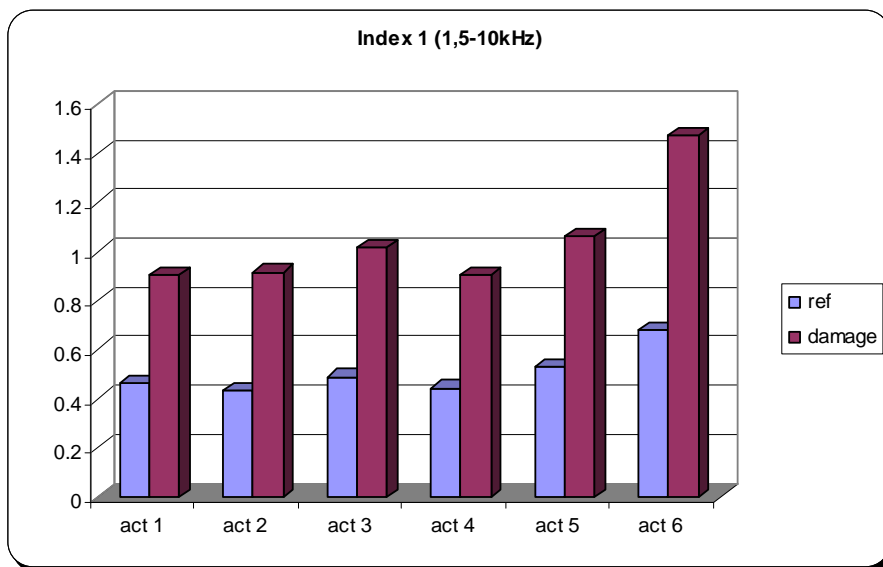


Fig. 5.3.18 – Actuators DI

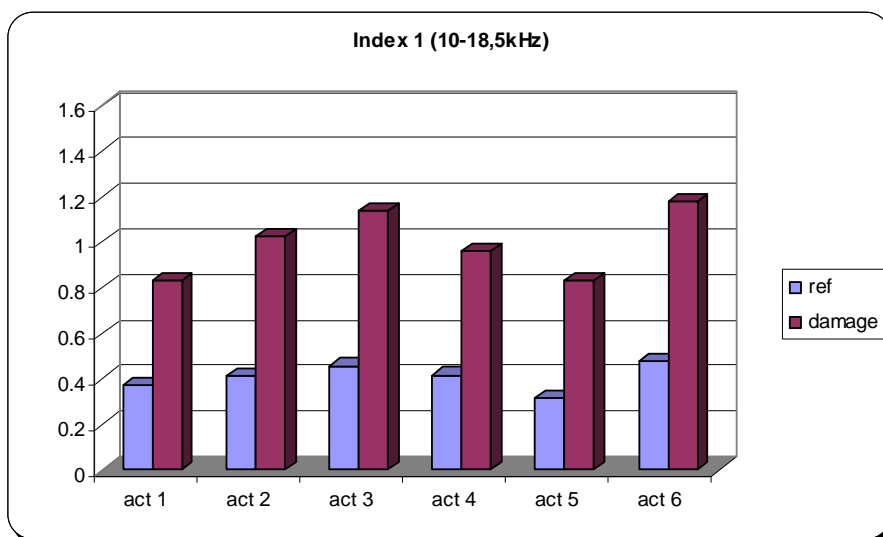


Fig. 5.3.19 – Actuators DI

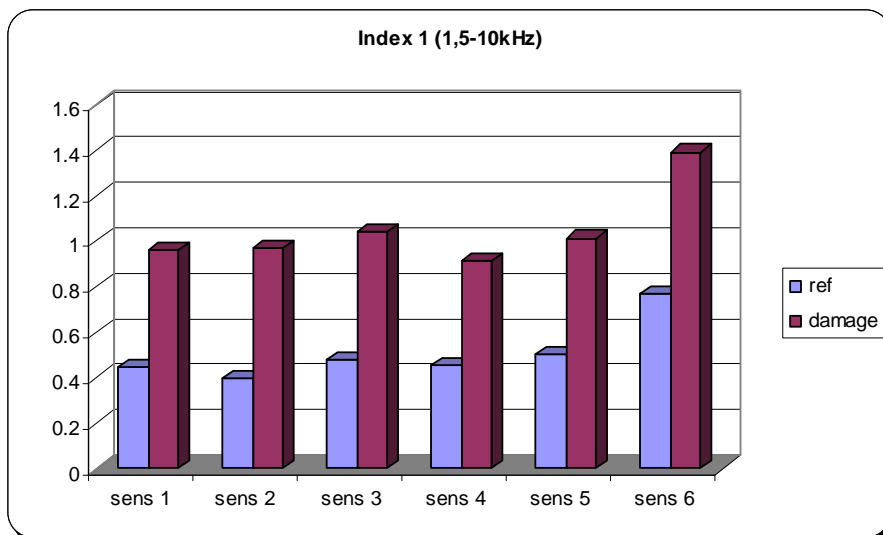


Fig. 5.3.20 – Sensors DI

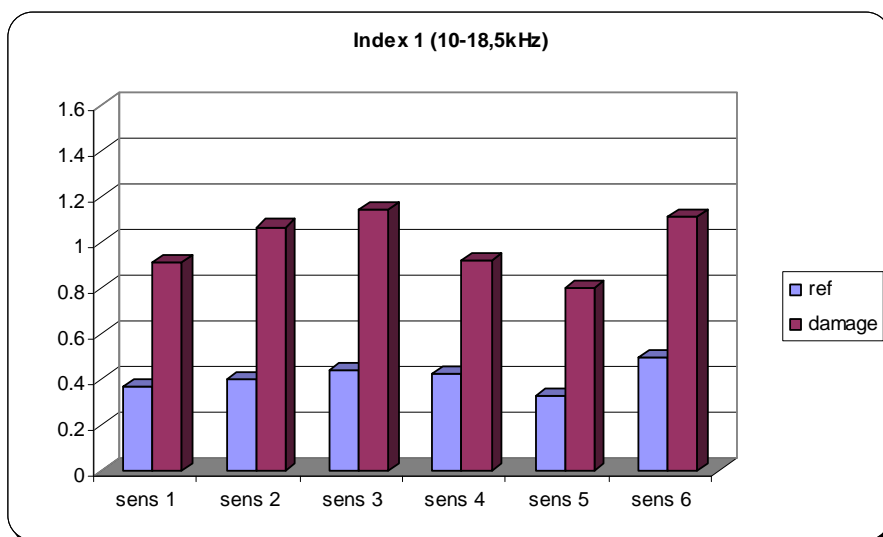


Fig. 5.3.21 – Sensors DI

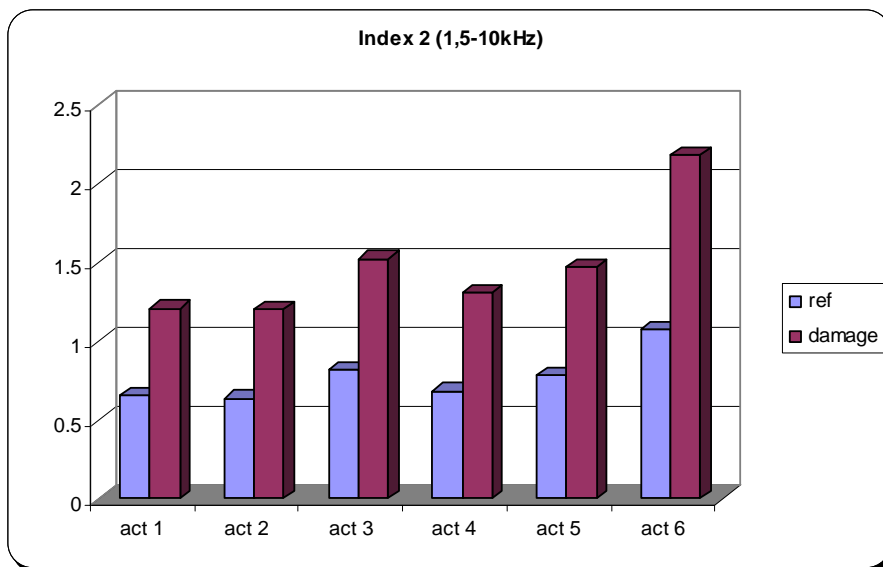


Fig. 5.3.22 – Actuators DI

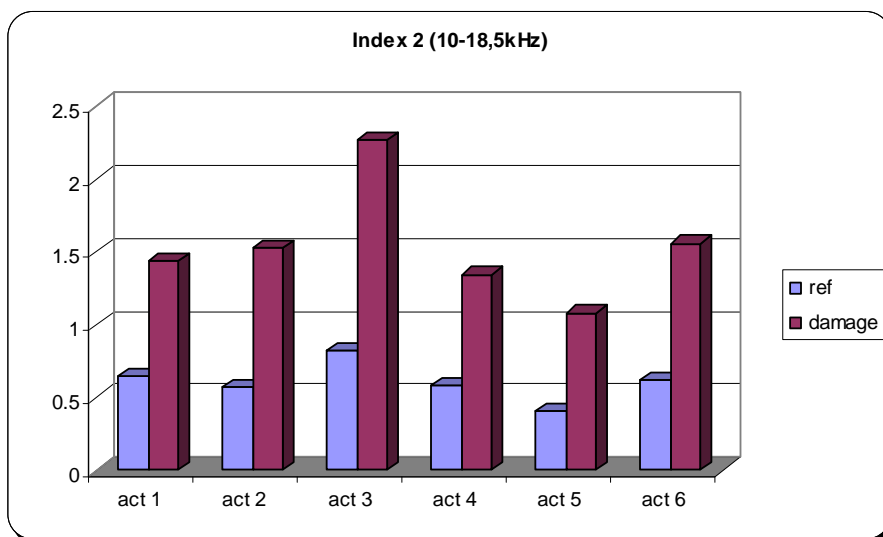


Fig. 5.3.23 – Actuators DI

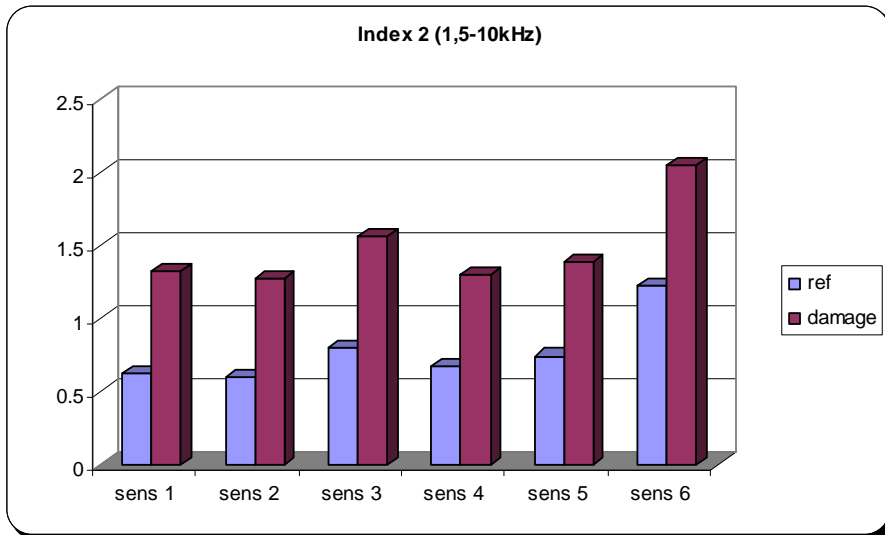


Fig. 5.3.24 – Sensors DI

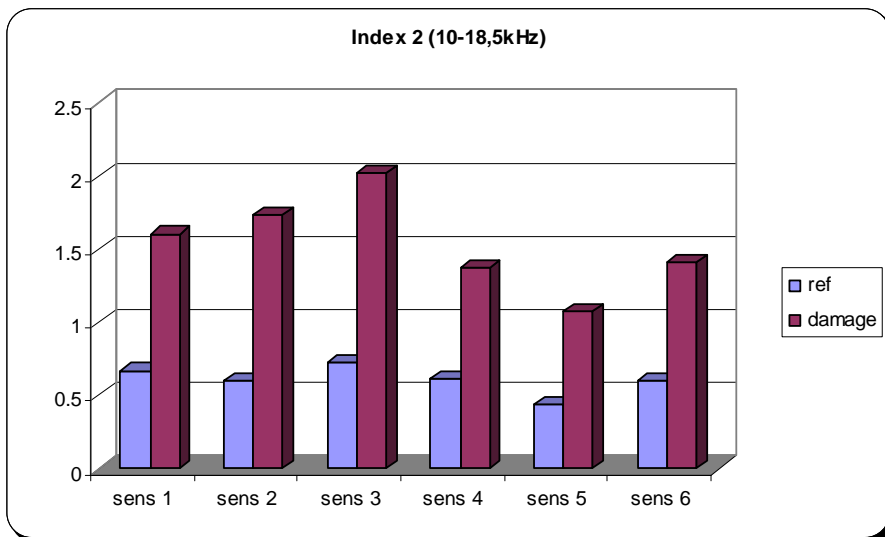


Fig. 5.3.24 – Sensors DI

In order to better localize a damage, a Student t test has been used by means of the Matlab software. All t values obtained by the Matlab have been gathered in four bar charts, two for each index and for each frequency range. The degree of freedom (DOF) is equal to 11.

Bearing in mind that the damage is located close to the piezo patch #2, it can be observed that using the t test the localization is improved, but it is not good enough, in fact the piezoelectric patch #5 localizes the rivet failure too.

In the end, a recalculation of the indexes has been done. The last graphs represent the ratio between the absolute deviation of the damage indexes with regard to the sensitivity ones, and the sensitivity indexes.

Those charts show a good localization when the sensors are fixed. Besides, a little more clear result has been given by the index "2" calculated at the highest frequency range.

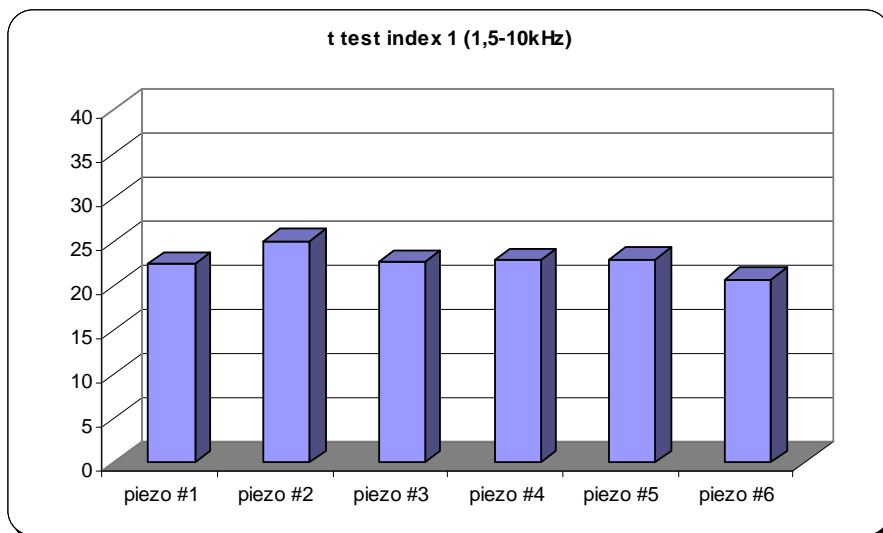


Fig. 5.3.25 – T_test

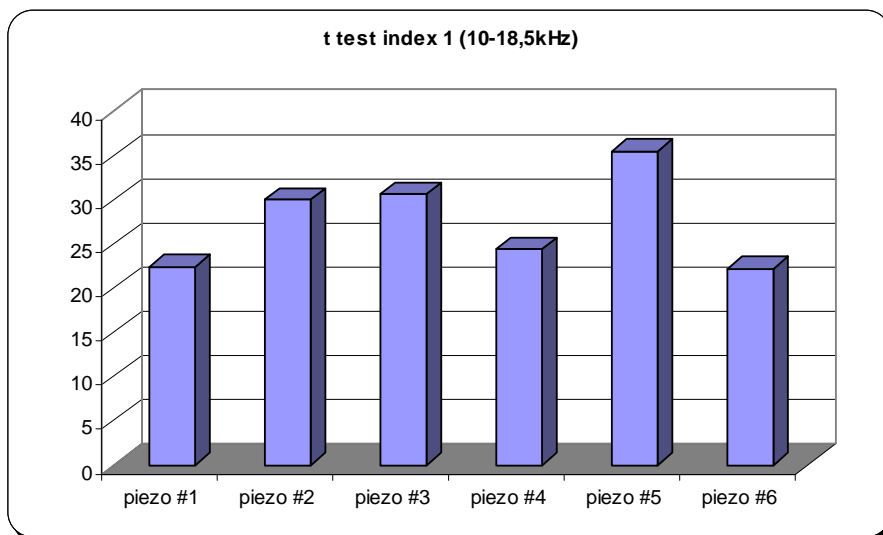


Fig. 5.3.26 – T_test

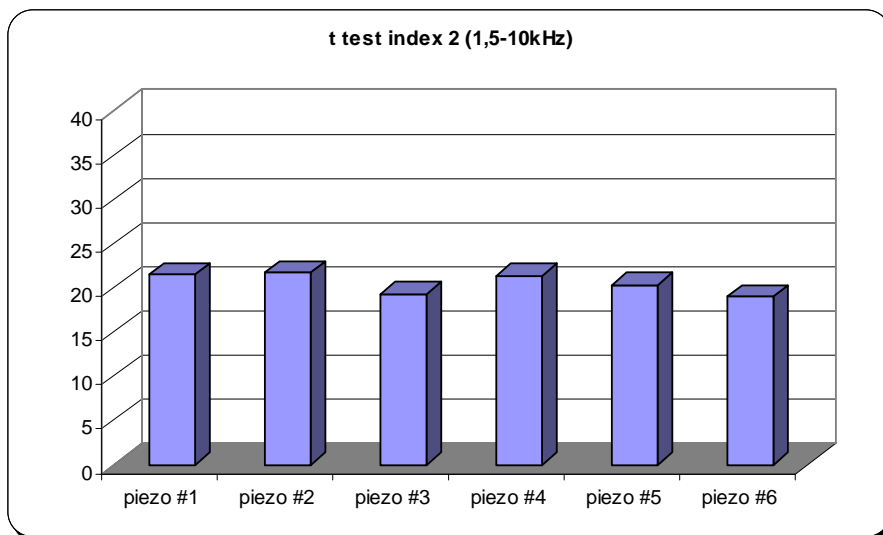


Fig. 5.3.27 – T_test

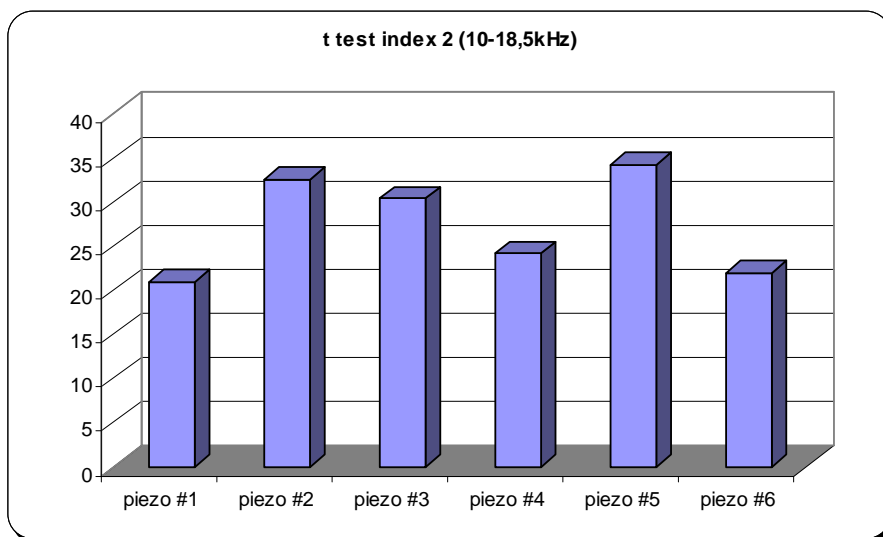


Fig. 5.3.28 – T_test

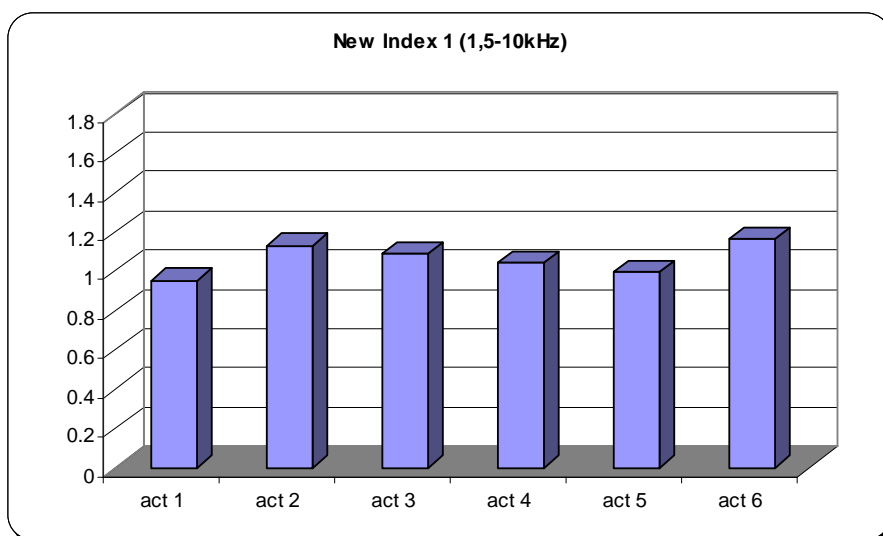


Fig. 5.3.29 – Actuators new DI

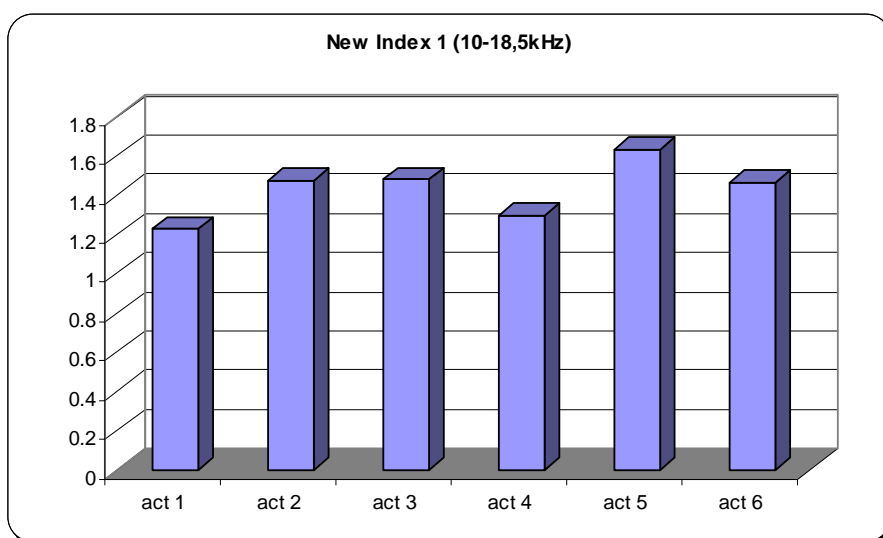


Fig. 5.3.30 – Actuators new DI

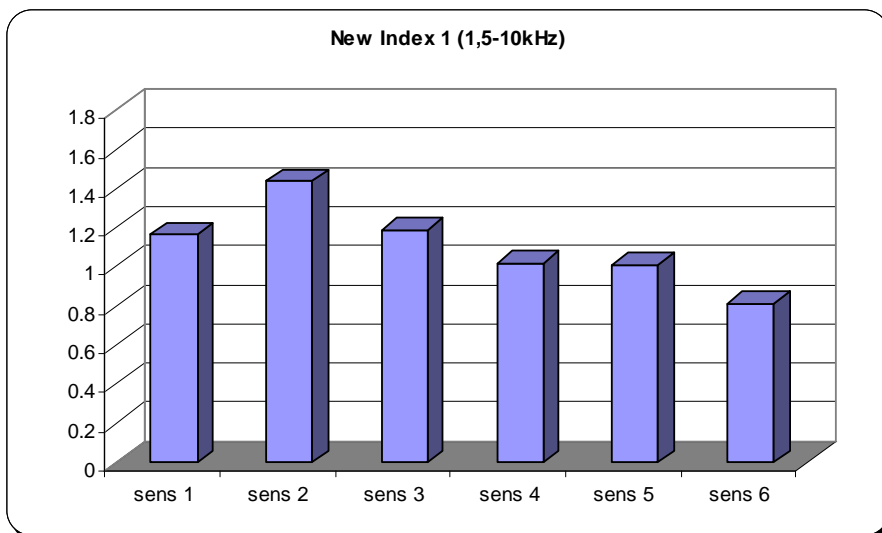


Fig. 5.3.31 – Sensors new DI

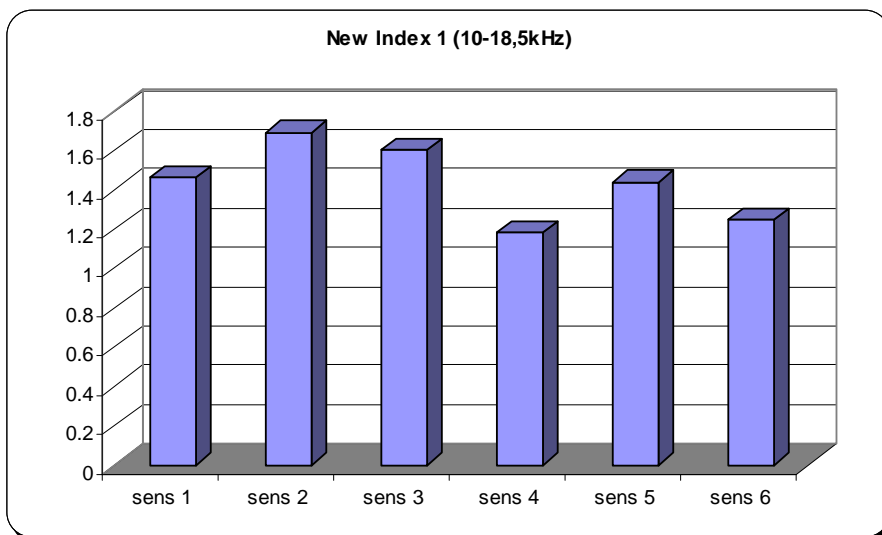


Fig. 5.3.32 – Sensors new DI

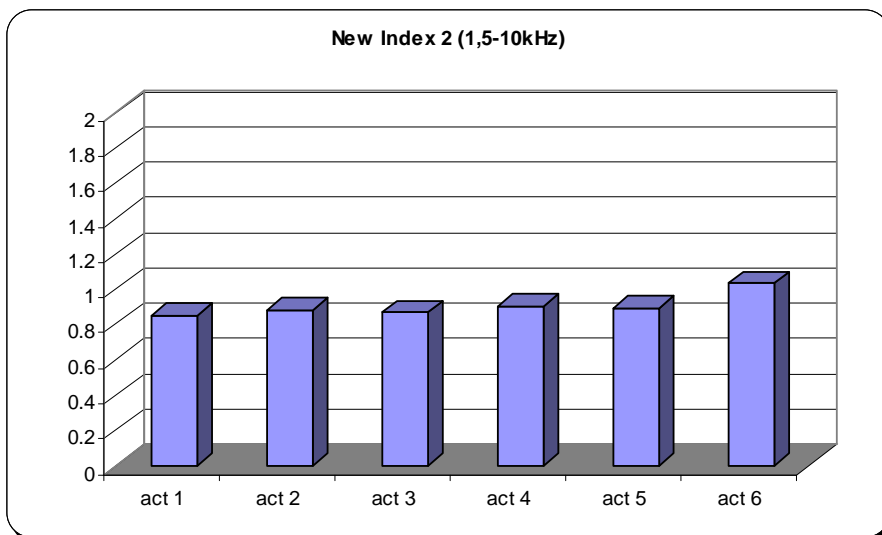


Fig. 5.3.33 – Actuators new DI

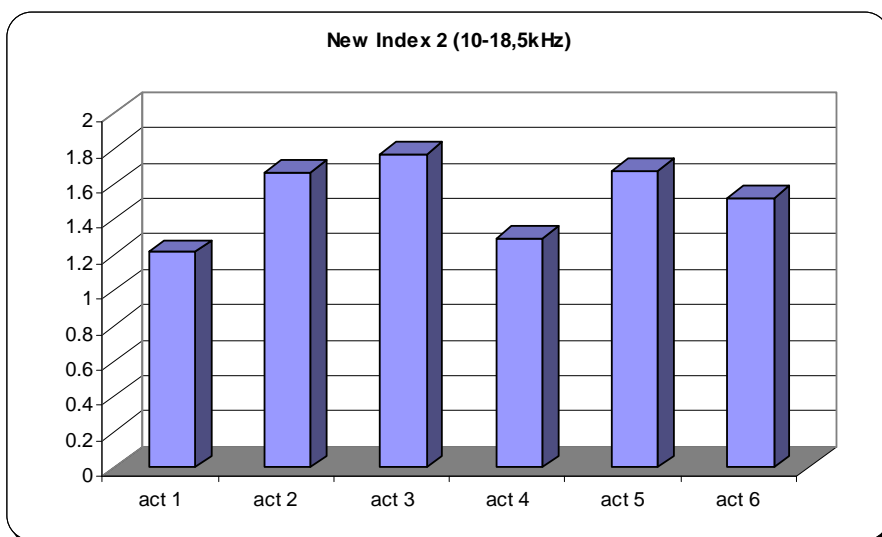


Fig. 5.3.34 – Actuators new DI

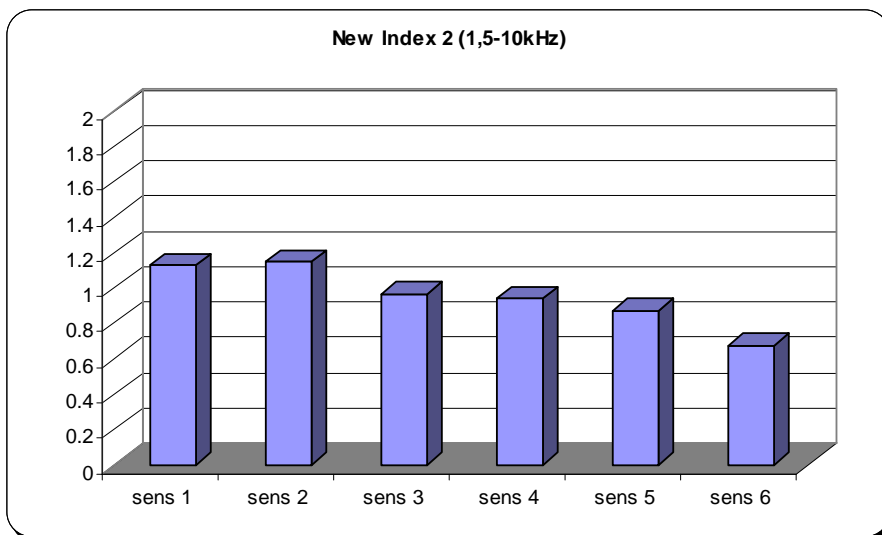


Fig. 5.3.35 – Sensors new DI

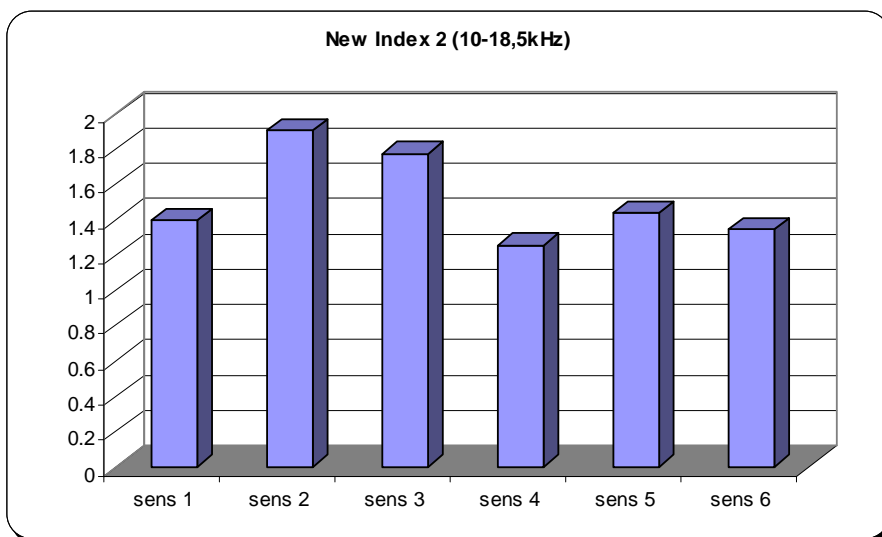


Fig. 5.3.36 – Sensors new DI

The neural network has been trained making use of the same FRFs of the healthy structure used for the determining of the Damage Index, as positive examples. Training and post-processing algorithms are reported in the chapter 3.

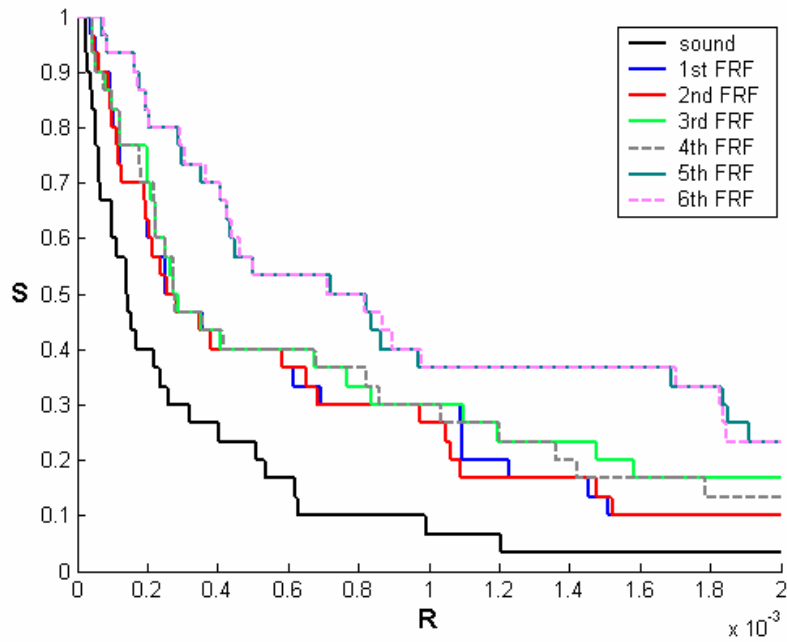


Fig. 5.3.37 – Neural Network output (range 1,5-10kHz)

It can be observed that all the curves obtained by the six acquisition of the FRFs of the damaged structure are located far from the x-axis, and far from the undamaged structure curve. The rivet failure has been identified. In that case the FRFs acquired do not give the same output curves, since the fifth and the sixth curves are located a bit farther.

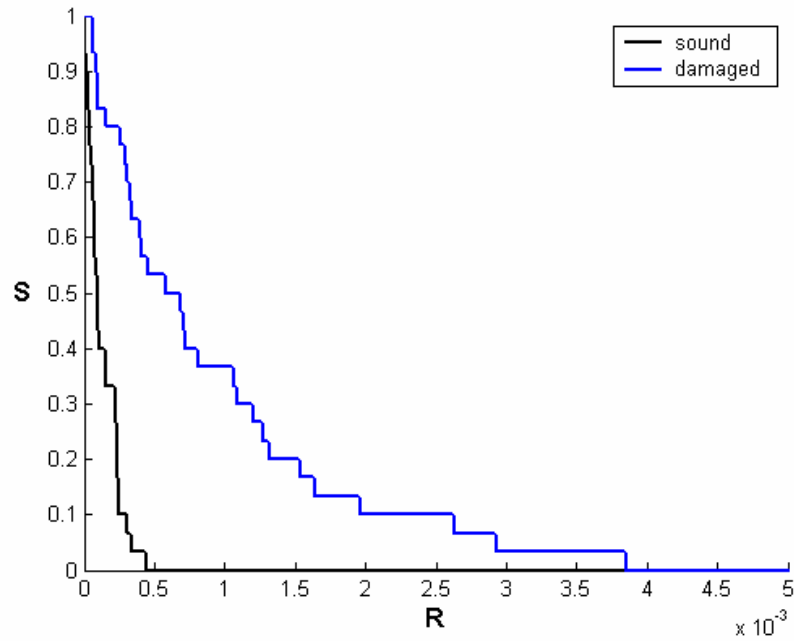


Fig. 5.3.38 – Neural Network output (range 10-18,5kHz)

Considering one only FRFs acquisition of the damaged structure for the neural network, it can be observed that the network, trained with FRFs acquired from 10 to 18,5 kHz, is able to identify better than at the lowest frequency range, since the distance between the undamaged and damaged curves is greater than the respective curves obtained at the lowest frequency range.

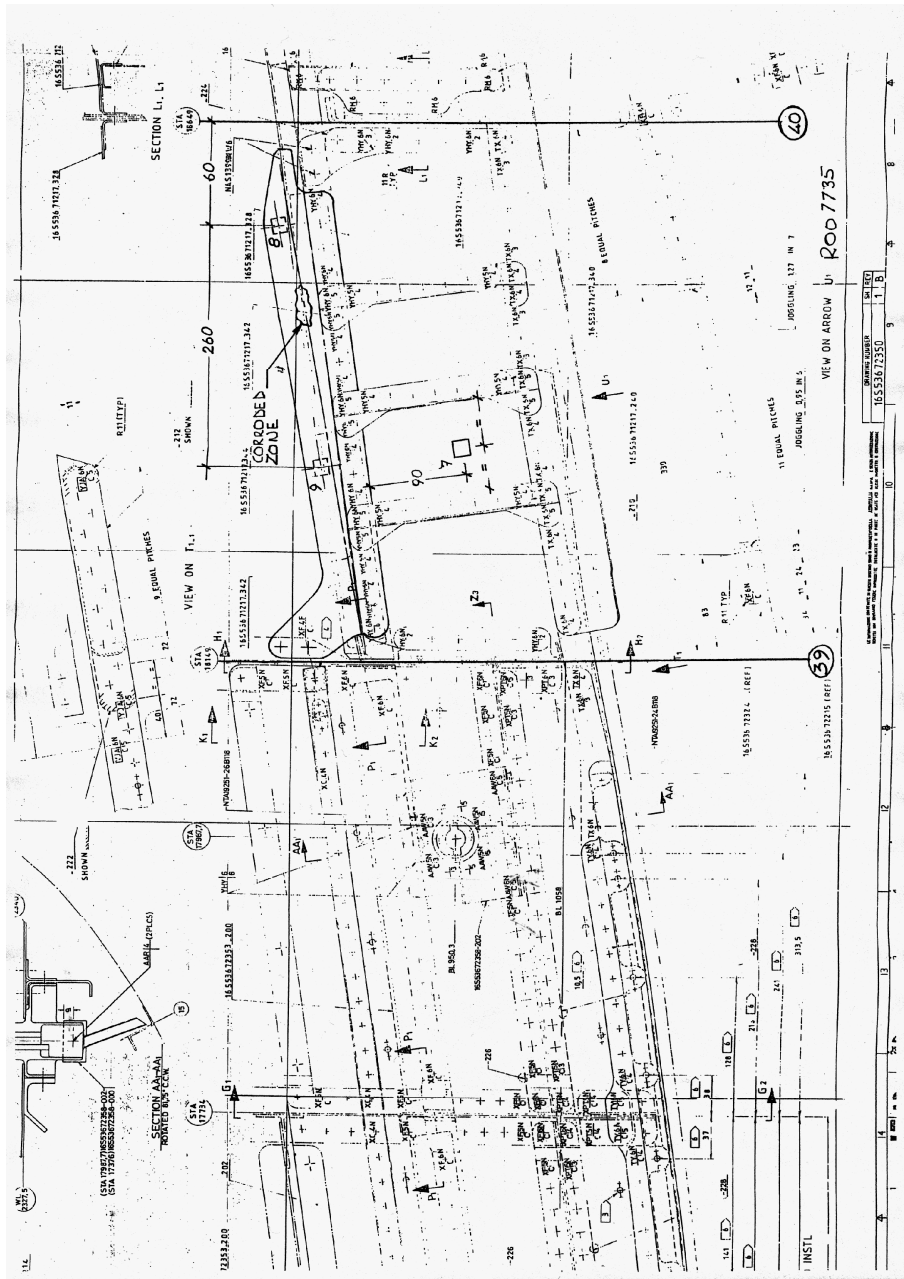


Fig. 5.3.40 – Second monitored area scheme



Fig. 5.3.41 – Second monitored area



Fig. 5.3.42 – Second monitored area



Fig. 5.3.43 – Second monitored area (zoom)

Three only piezoceramic patches have been bonded on the floor support zee, so the actuator-sensor couples are only six. An acquisition campaign, similar to that executed for the first area, has been carried out to define the sensitivity threshold of the structure and to train a Neural Network, formed by six FRF' acquisitions.

Also in this case a damage has been imposed on the structure. Since, on that support, there was a little corroded region just before the first acquisition campaign, which defines the “our” sound configuration (even if a damage is on), a mechanical cleaning of that region has been executed.

The experimental tests executed on this area and the results obtained are similar to those carried out on the first area. Therefore, in order to make the exposition lighter, some graphs only and a brief description of the main results obtained for this area are reported in the next pages. About all the others charts it refers back to the appendix.

The progressive numbering of the figures is kept to make faster the searching of the chart wanted.



Fig. 5.3.44 – Damage simulated



Fig. 5.3.45 – Area mechanical cleaned

The pictures show the damage imposed on the floor support zee. It is a light damage located between the piezoceramic patches #8 and #9. A campaign formed by four FRF' acquisitions has been executed. The following charts show an example of both Sensitivity and Damage Indexes obtained.

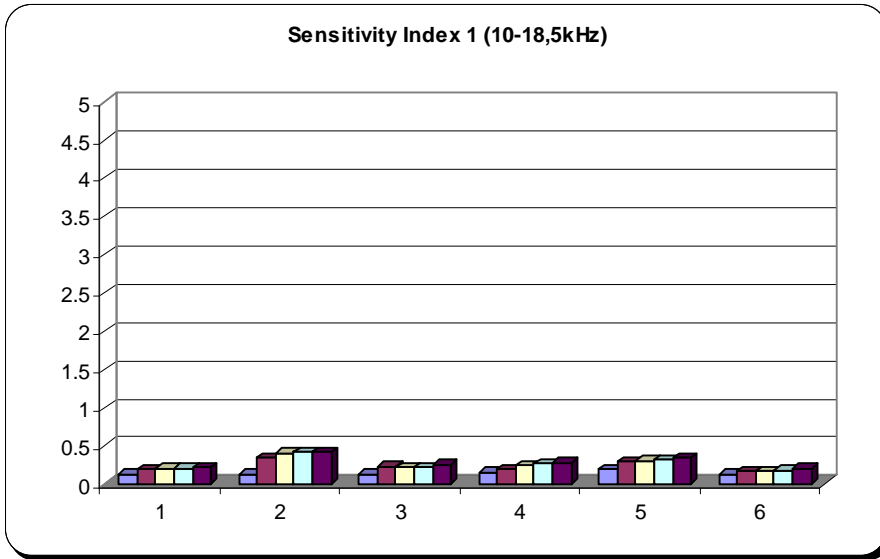


Fig. 5.3.47 – Sensitivity Index

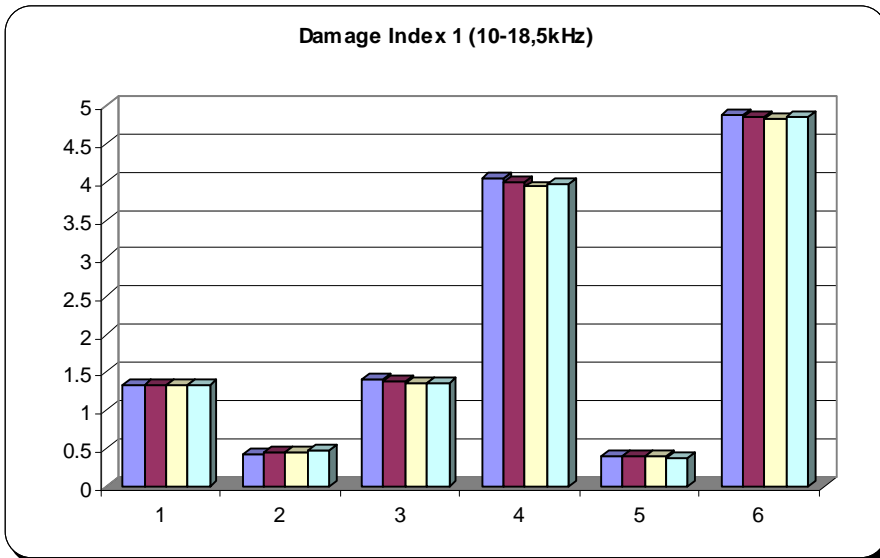


Fig. 5.3.51 – Damage Index

Most of the actuator-sensor couples have identified the damage, in fact the damage indexes are higher than the sensitivity ones. The damage has been also localized. In fact the fourth and the sixth group of bars represent the couples formed by actuator #8 – sensor #9 and actuator #9 – sensor #8 respectively.

The next graphs summarize the results. The piezo patches #7, #8 and #9 are reported as actuators and sensors #1, #2 and #3 in order to make the explanation of the results clearer. Therefore, the damage is located between #2 and #3.

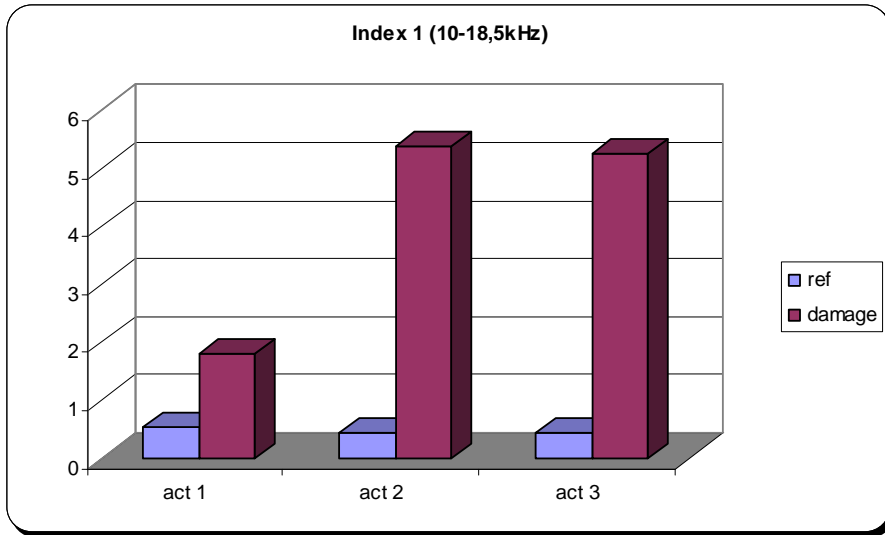


Fig. 5.3.55 – Actuators DI

It can be observed that the damage is clearly identified and localized. In fact, the index “1” (as well the index “2”) calculated at the highest frequency range, undoubtedly localize the damage.

A T_test chart reported in the next page, unfortunately, shows that the Student T_test gives a not so clear localization of the damage, since the bars #2 and #3 have not the same value.

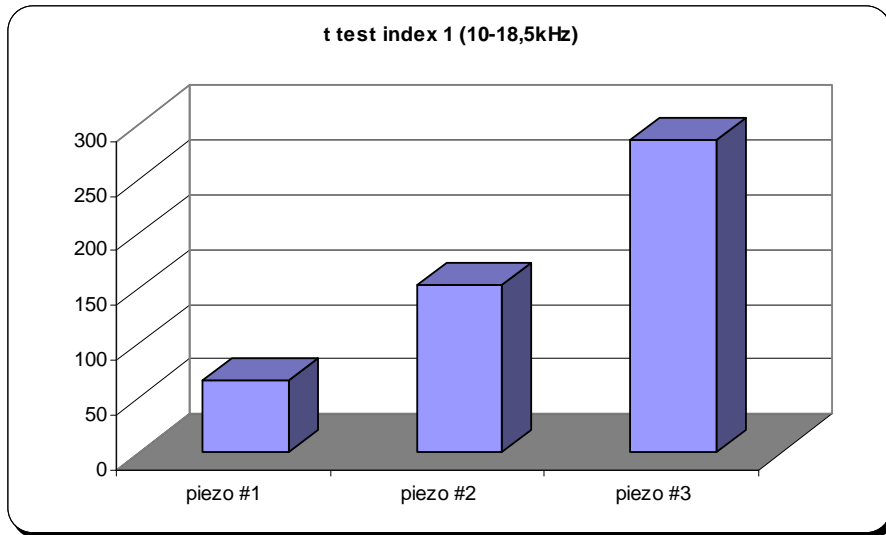


Fig. 5.3.63 – T_test

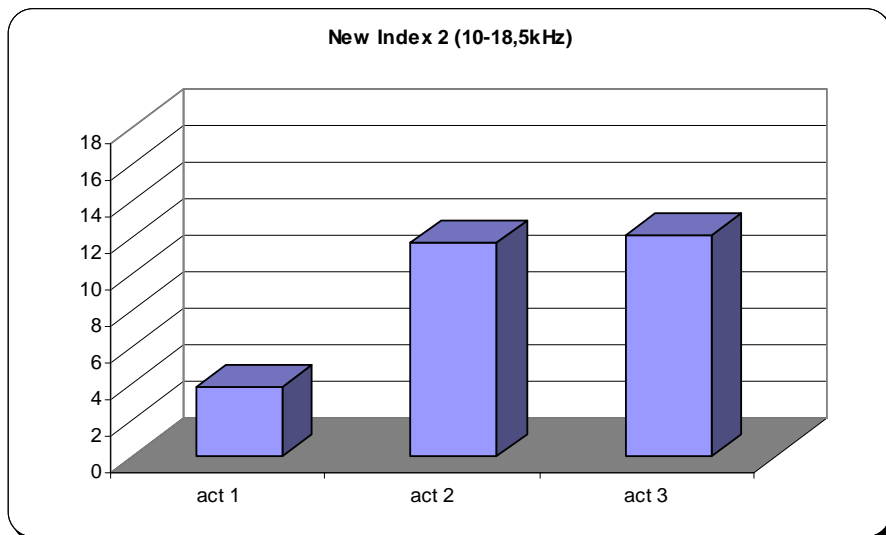


Fig. 5.3.71 – Actuators new DI

The new Indexes perfectly localize the damage (very similar #2 and #3 bars values), especially if they are calculated at the highest frequency range.

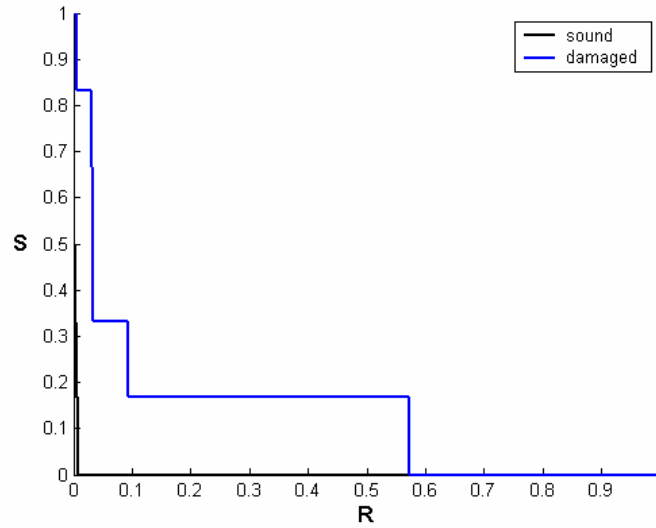


Fig. 5.3.74 – Neural Network output (range 1,5-10kHz)

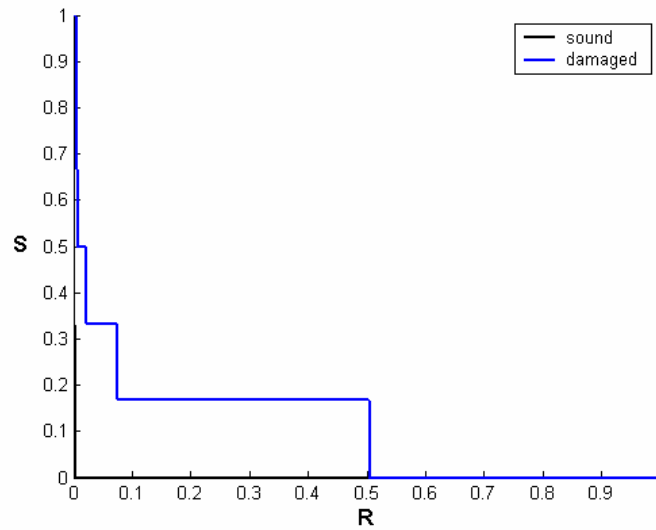


Fig. 5.3.75 – Neural Network output (range 10-18,5kHz)

Even if there is no threshold line, it is obvious that the damage has been identified by the neural network, since, in both graphs, the damaged curves are located far from the sensitivity ones.

V.3.4 Floor Frame 42

The third area is a floor support where the frame 42 is, on the station 19557, internal to the aircraft, close to the bulkhead. Its P/N is 16S53672412. On that part five piezoceramic patches have been symmetrically bonded. All patches have a square shape; the piezoelectrical patches #10, #12 and #14 have a thickness equal to mm.0,5, while the patches #11 and #13 have a thickness equal to mm.1. In that case the actuator-sensor couples are twenty.



Fig. 5.3.76 – Floor frame



Fig. 5.3.77 – Third monitored area



Fig. 5.3.79 – Rivets removed

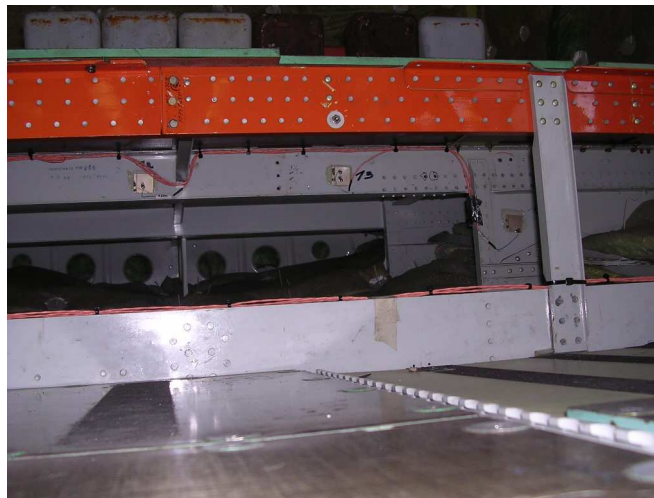


Fig. 5.3.80 – Damaged area

In order to simulate a damage, two rivets connecting the floor frame to stiffener element have been removed, reducing the stiffness of the region between the piezoceramic patches #13 and #14.

Eight FRFs have been acquired for each actuator-sensor couple, obtaining seven sensitivity indexes for each couple, and six FRFs have been acquired to determine the damage indexes. It is possible to observe, by means of the comparison between the next graphs, that, also in this case, the damage has been identified and localized. In fact the groups #4, #8, #12 and #16 represent the couples formed by the actuators #10, #11, #12, #13 and the sensor #14 respectively; besides, the groups

from #17 to #20 represent the couples actuator-sensor in which the patch #14 is the actuator. The vibrations which go from an actuator to a sensor of each couple pass through the damaged zone.

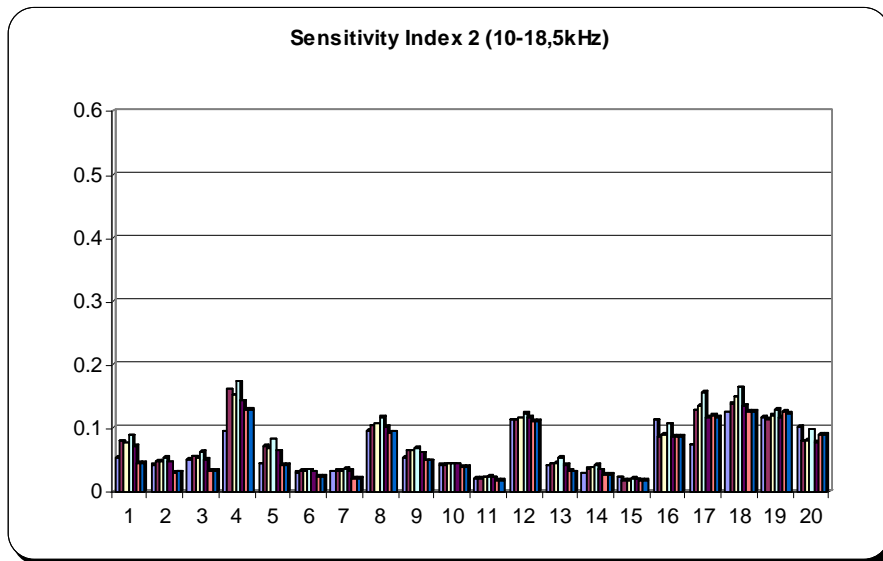


Fig. 5.3.84 – Sensitivity Index

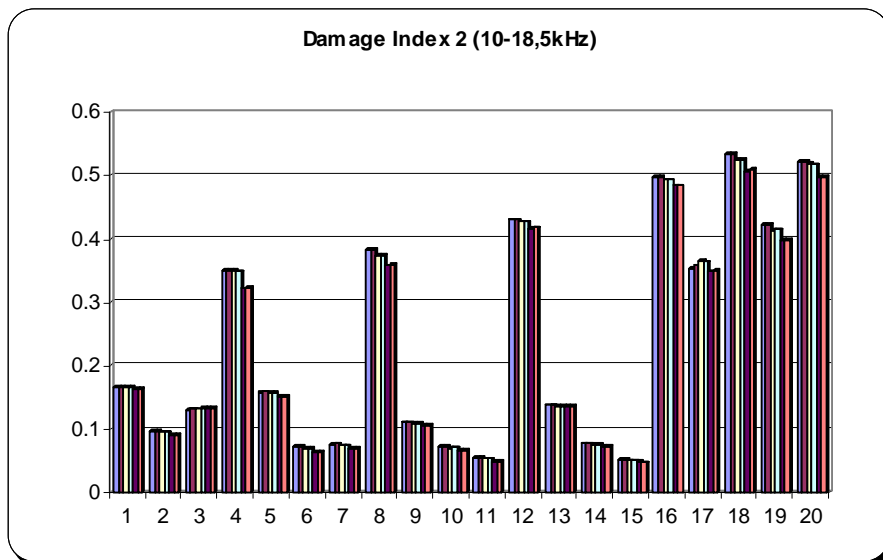


Fig. 5.3.88 – Damage Index

In order to extend the discussion about the damage localization, the following summarizing charts are shown, where the patches from #10 to #14 are reported as #1, #2, #3, #4 and #5. Therefore the damage is now located between the patches #4 and #5.

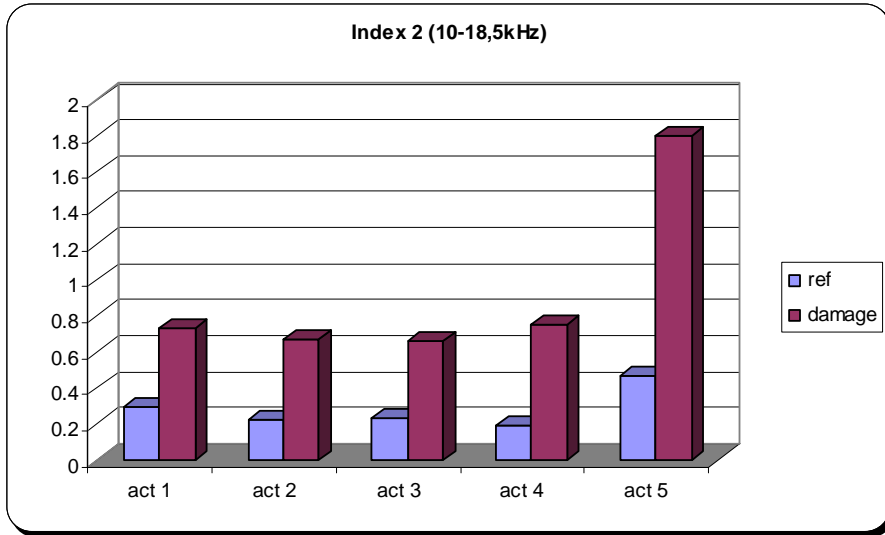


Fig. 5.3.94 – Actuators DI

The Damage Indexes calculated at the highest frequency range have clearly identified and localized where the rivets have been removed. Evidently, the removal of two rivets represents a substantial damage.

The T_test chart reported in the next page, as well as the Damage Index one, shows a good localization of the damage, even if in a not so evident way.

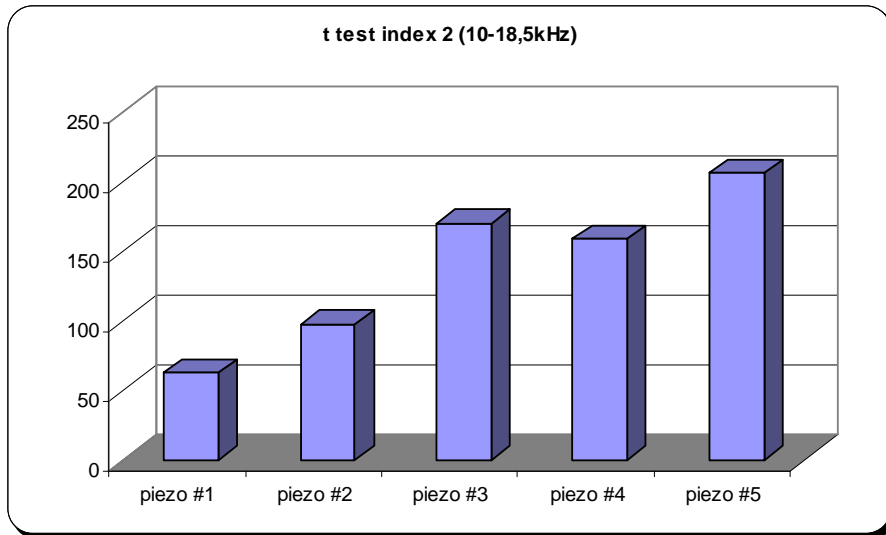


Fig. 5.3.100 – T_test

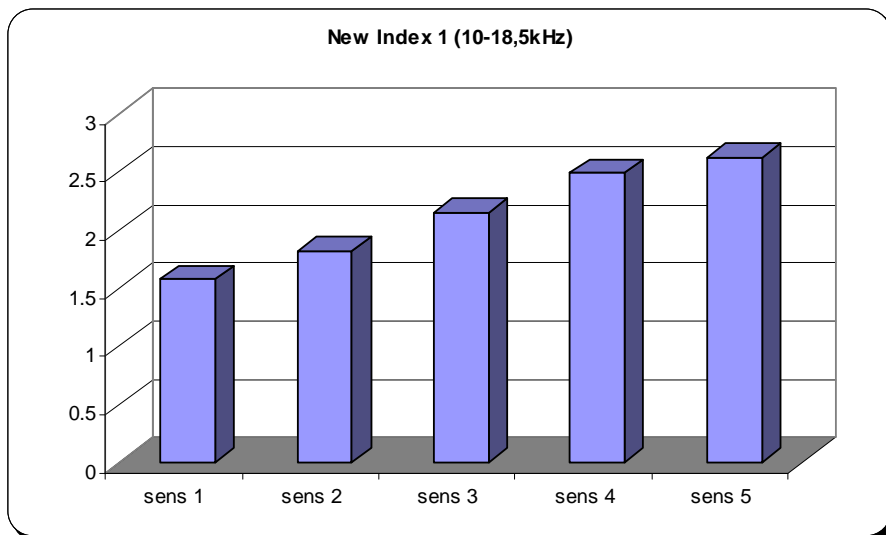


Fig. 5.3.104 – Sensors new DI

Also about the new indexes the localization of the damage is more evident if it analyzes the results obtained at the highest frequency range.

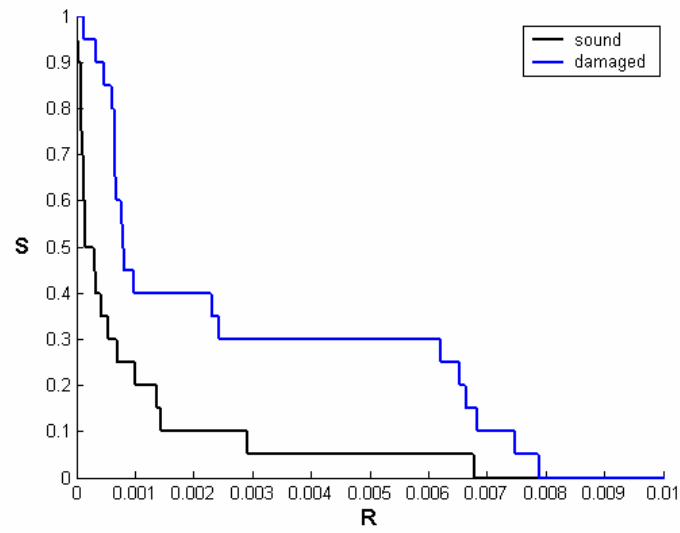


Fig. 5.3.109 – Neural Network output (range 1,5-10kHz)

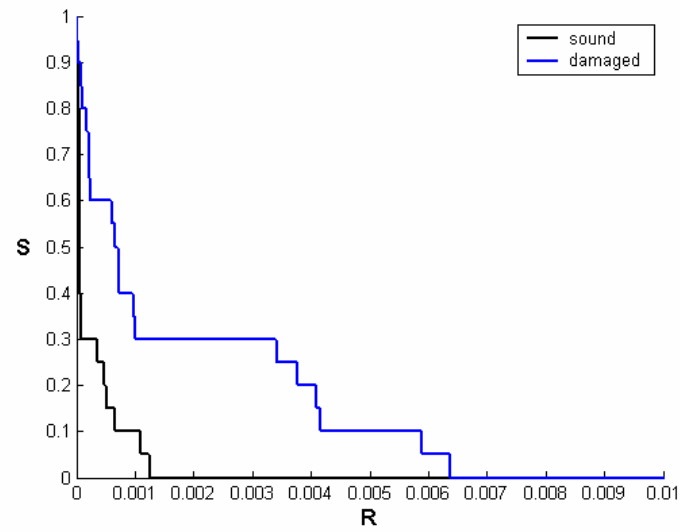


Fig. 5.3.110 – Neural Network output (range 10-18,5kHz)

The Neural Network identifies the damage, and there is no particular differences between the low and high frequency range outputs.

V.3.5 Main Landing Gear

The fourth area is located out of the aircraft, under the fairing. The structure monitored is formed by the Main Landing Gear (MLG) truss shear and the MLG fairing support. On the truss shear four piezoceramic patches have been bonded. Those patches have a rectangular shape; the patch #15 has a thickness equal to mm.1, while the patches #16, #17 and #20 have a thickness equal to mm.0.5. Besides, two patches have been glued on the fairing support, whose P/N is 14S53973301-201. One has a square shape, while the other has a rectangular shape; both of them have a thickness equal to mm.1.

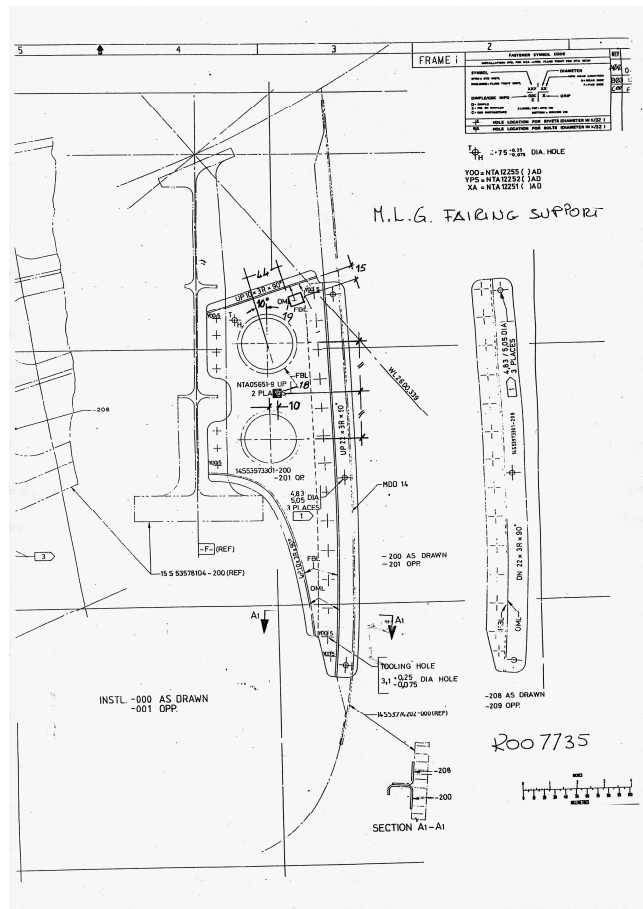


Fig. 5.3.111 – Fairing support scheme



Fig. 5.3.113 – MLG without the fairing



Fig. 5.3.114 – MLG without the fairing



Fig. 5.3.115 – MLG truss shear

The six piezoceramic patches have been able to monitor both the MLG truss shear and the fairing support. This area is critical because of the very high loads which are transmitted from the landing gear to the aircraft structure during the aircraft landing.

Besides, a problem reported by the ATR Structural Engineering Department regards the vibrations which are present during the flight on the fairing and cause cracks on the fairing support. It would be useful to have a system which indicates a possible crack on that support. Therefore a fairing support damaging has been simulated.

A rivet has been removed to simulate a damage of the conjunction between the MLG truss shear and the fairing support, close to the patches #18 and #19.

Eight FRFs have been acquired for each actuator-sensor couple, obtaining seven sensitivity indexes for each actuator-sensor couple. Besides, six FRFs have been acquired to calculate six damage indexes.



Fig. 5.3.116 – Damaged area

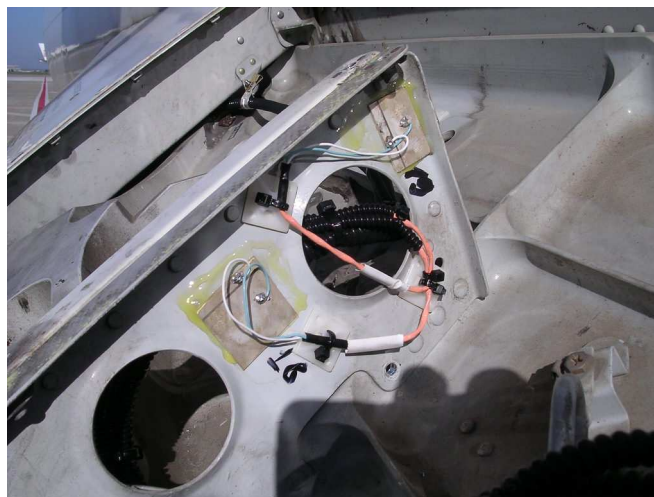


Fig. 5.3.117 – Rivet failure

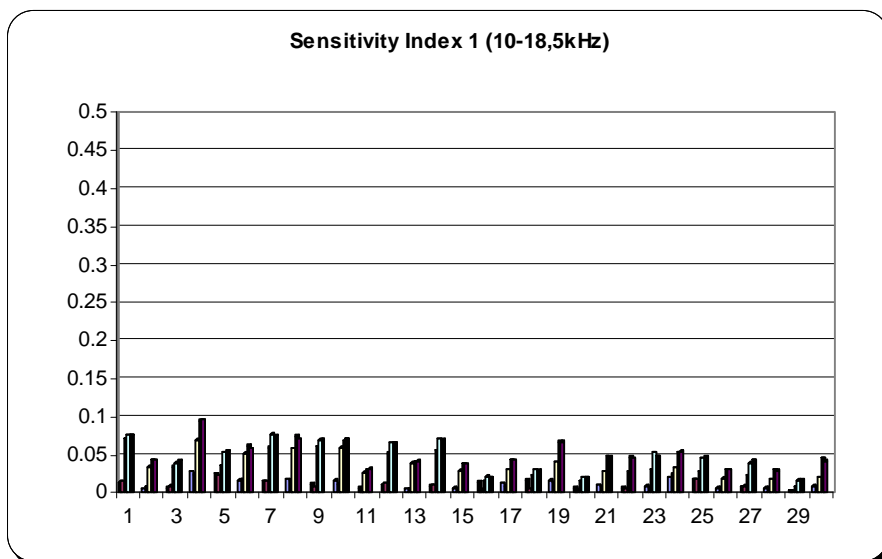


Fig. 5.3.119 – Sensitivity Index

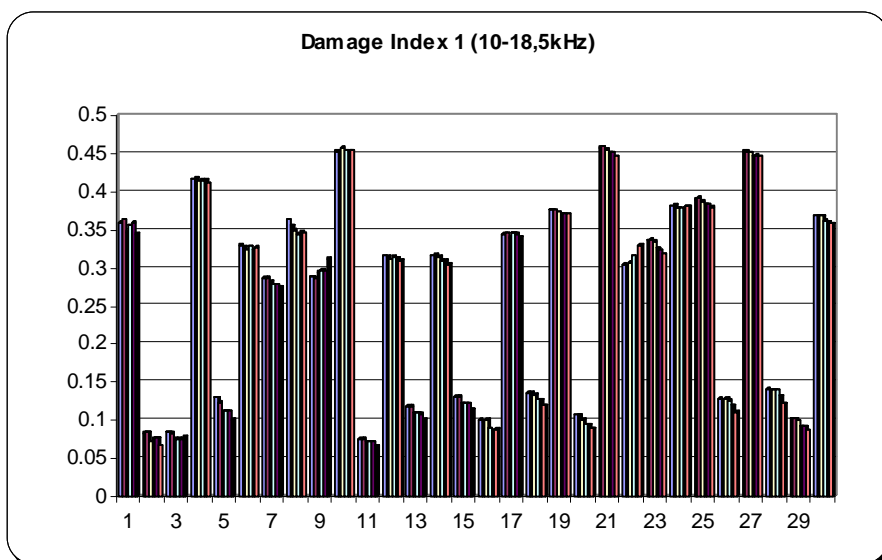


Fig. 5.3.123 – Damage Index

It can be observed that all the indexes exceed the sensitivity ones: the damage has been identified.

As usual, to better define the localization capabilities of the technique, the following summarizing charts are shown, where the patches from #15 to #20 are reported as #1, #2, #3, #4, #5 and #6. Therefore the damage is located between the piezoceramic patches #4 and #5.

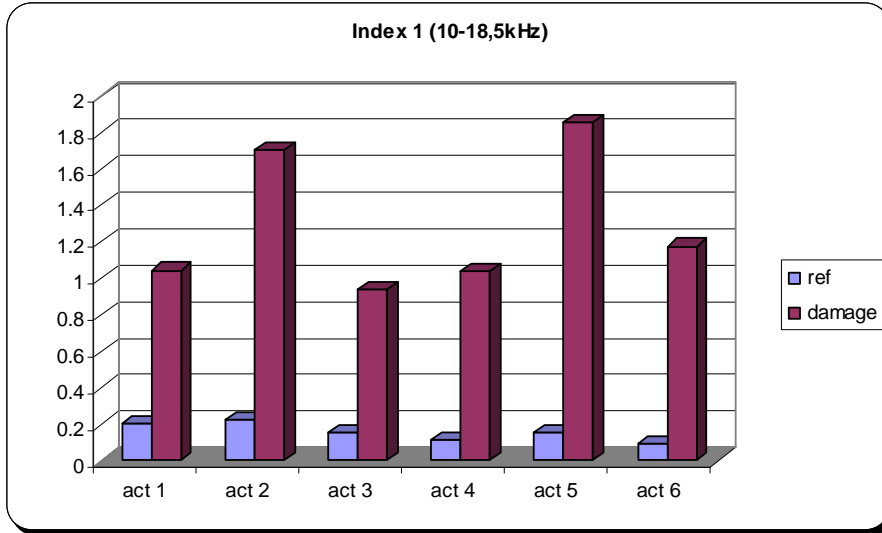


Fig. 5.3.127 – Actuators DI

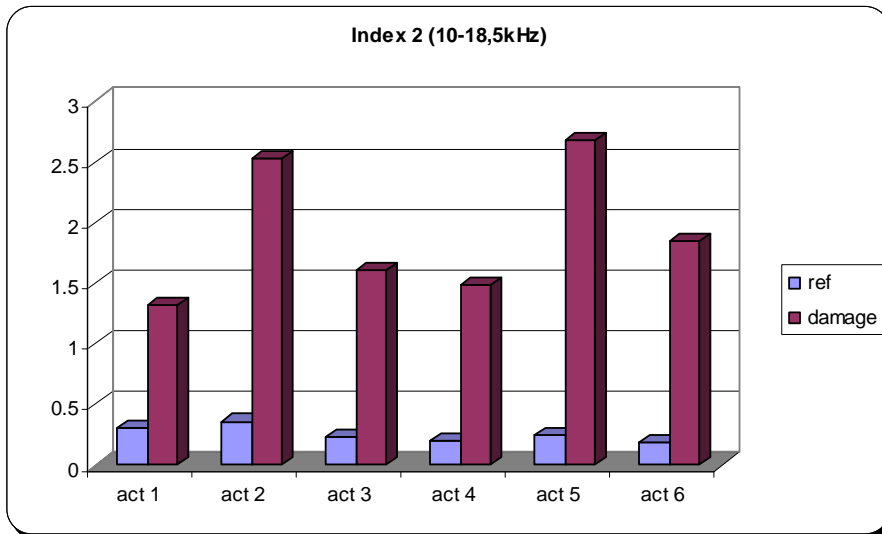


Fig. 5.3.131 – Actuators DI

From a point of view the indexes have identified the damage, even if the patch #2, identifies the rivet failure too.

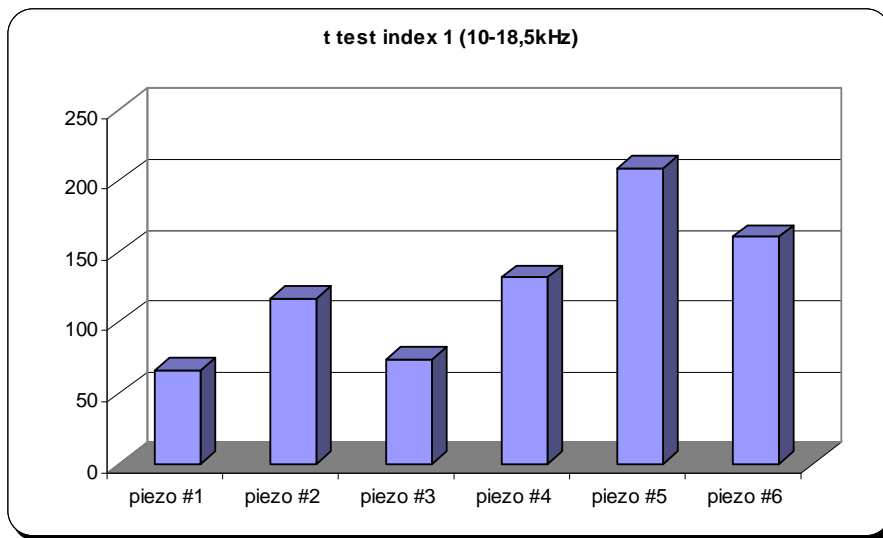


Fig. 5.3.135 – T_test

The T_test indexes have been able to refine the capability of the DI method in localizing the damage, in fact it is clear that the damage is close to the patch #5, i.e. the piezo #19 put on the fairing support.

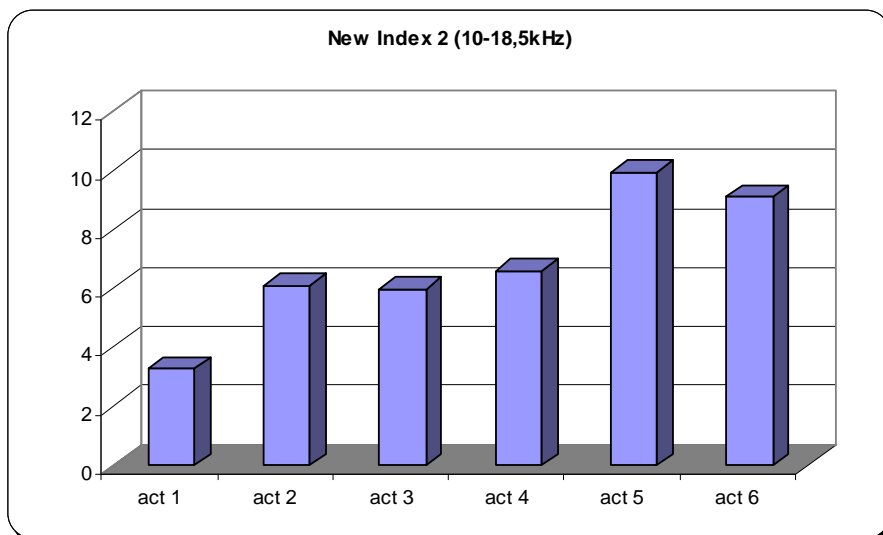


Fig. 5.3.143 – Actuators new DI

The new Damage Indexes do not give the localization of the rivet failure clearly, since the piezoceramic patch #6 gives an high index. Probably the problem is the high stiffness of the truss shear, and, consequently, the generated vibrational energy is too low.

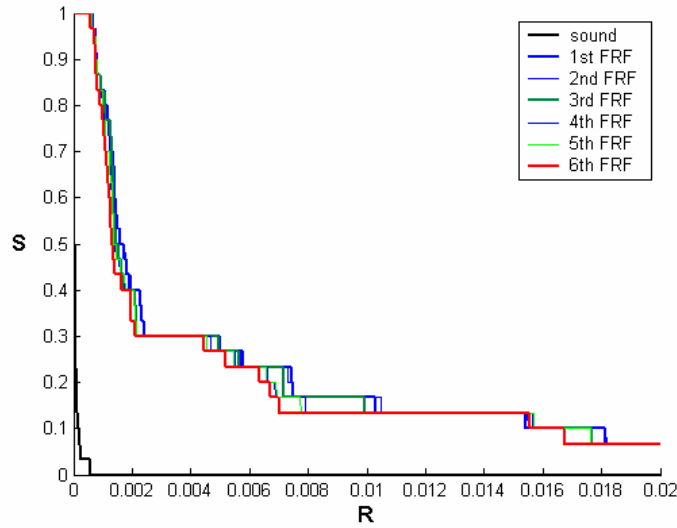


Fig. 5.3.146 – Neural Network output (range 1,5-10kHz)

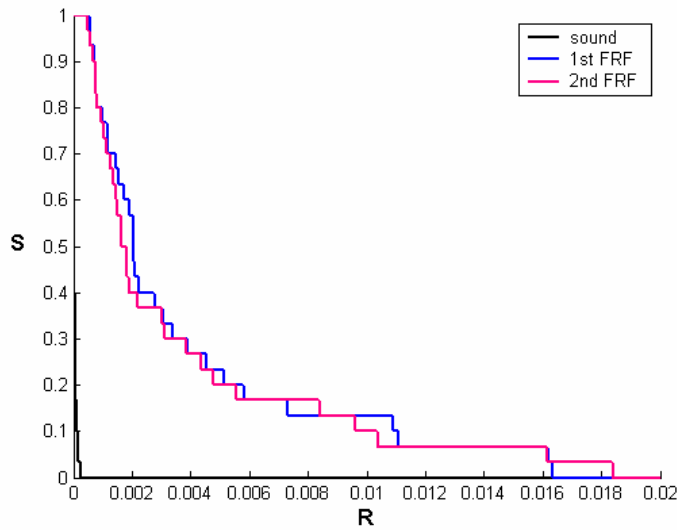


Fig. 5.3.147 – Neural Network output (range 10-18,5kHz)

The identification of the rivets failure is evident, since all the damaged curve are very far from the undamaged ones. Moreover, the damaged structure FRFs curves are practically superimposables, in fact they represent the same damage configuration of the structure.

V.3.6 Frame 45

The fifth and last area which has been monitored is located into the tail cone, it is the lowest zone of the frame 45, whose P/N is 18S53871100. On that frame five piezoceramic patches have been glued, from piezo #21 to #25. They have a square shape; the patches #21, #23 and #25 have a thickness equal to mm.1, while the others have a thickness equal to mm.0,5. The patches have been bonded on the lowest part of the frame, therefore, only that region has been monitored.



Fig. 5.3.148 – Tail cone



Fig. 5.3.149 – Frame 45

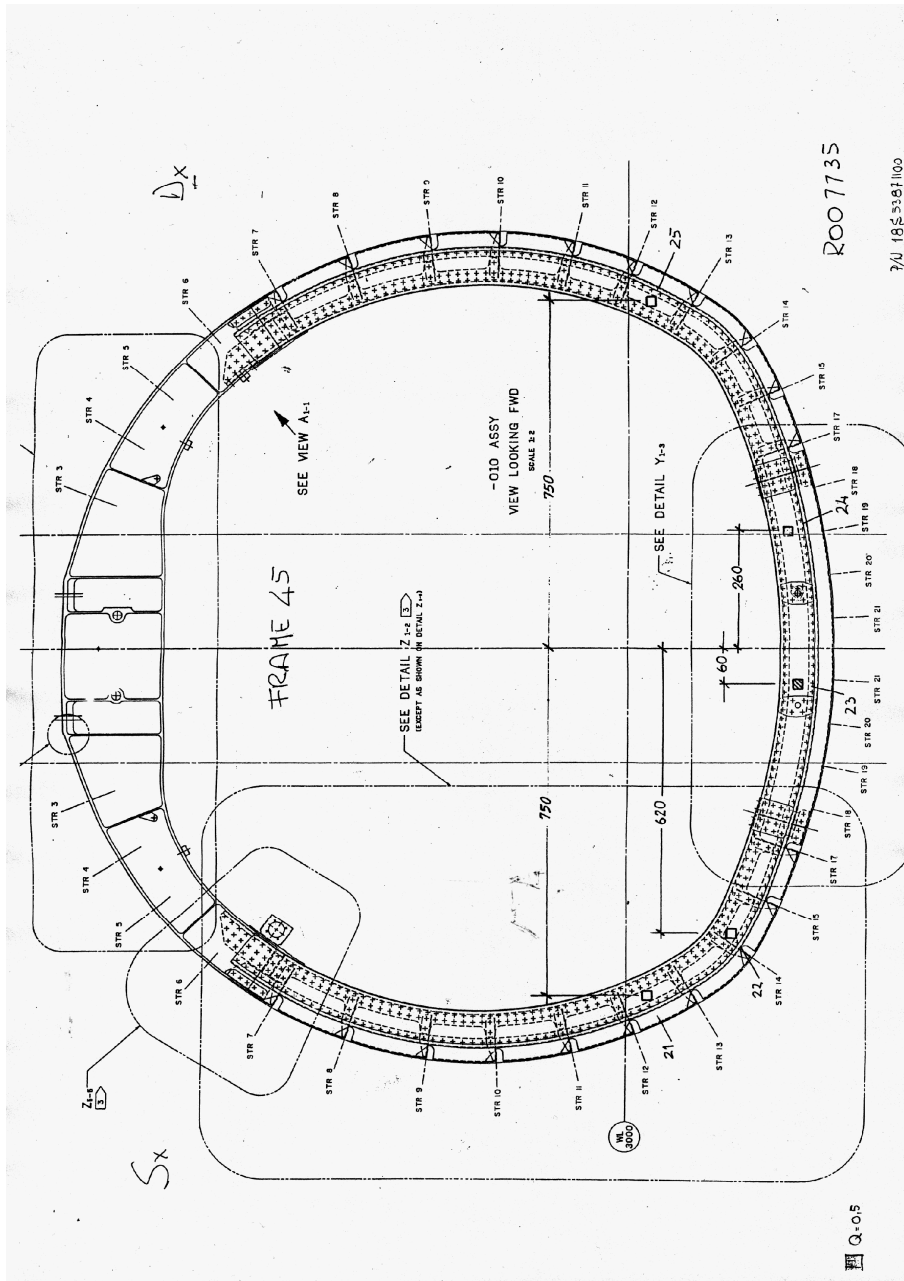


Fig. 5.3.150 – Frame 45 scheme



Fig. 5.3.151 – Area damaged



Fig. 5.3.152 – Rivets failure

On that area the damage has been executed by means of a removal of two rivets which connect the frame 45 with a stiffener, between the piezoceramic patches #23 and #24.

Eight FRFs have been acquired for each actuator-sensor couple, obtaining seven sensitivity indexes for each actuator-sensor couple, and six FRFs to obtain six Damage Indexes.

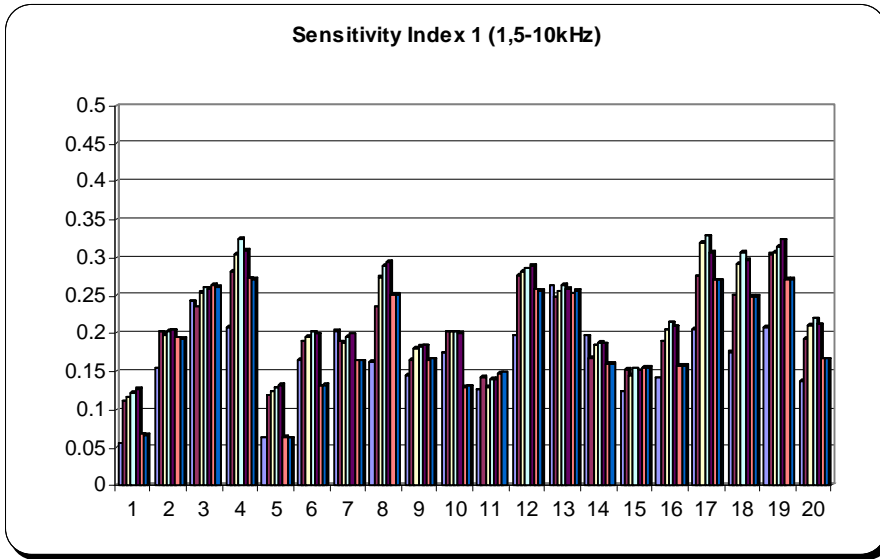


Fig. 5.3.153 – Sensitivity Index

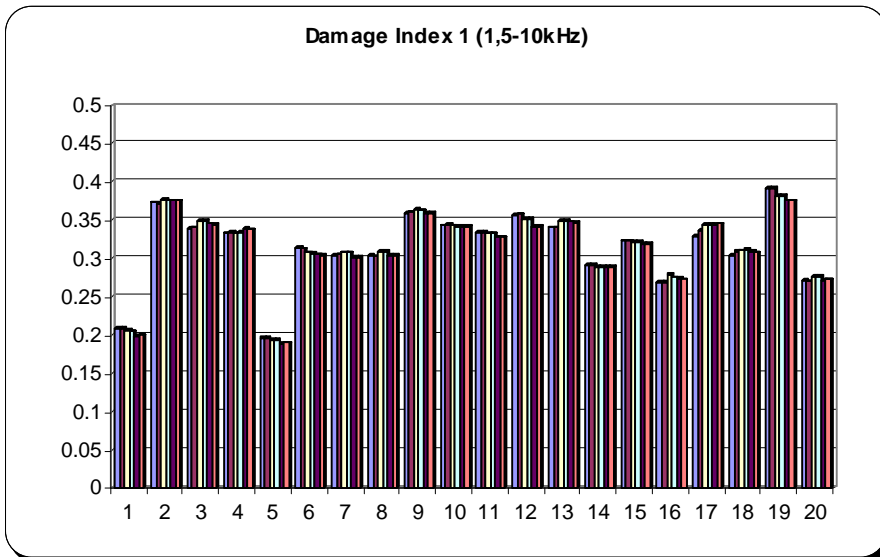


Fig. 5.3.157 – Damage Index

Comparing the Damage Index chart and the Sensitivity ones it can be observed that the rivets failure has been identified as well as the previous monitored area, since all damage indexes are higher than the sensitivity ones.

About the following charts, where the indexes are gathered fixing either the actuators or the sensors, the patches from #1 to #5 represent the piezoceramic patches from #21 to #25. Therefore the damage is located between #3 and #4.

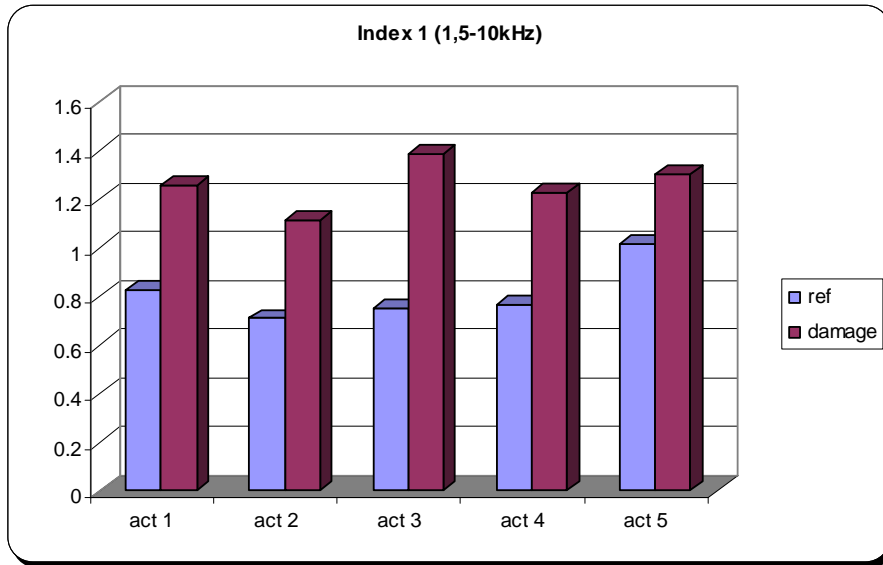


Fig. 5.3.161 – Actuators DI

All the piezoceramic patches have identified the rivets failure, but the localization is not so evident.

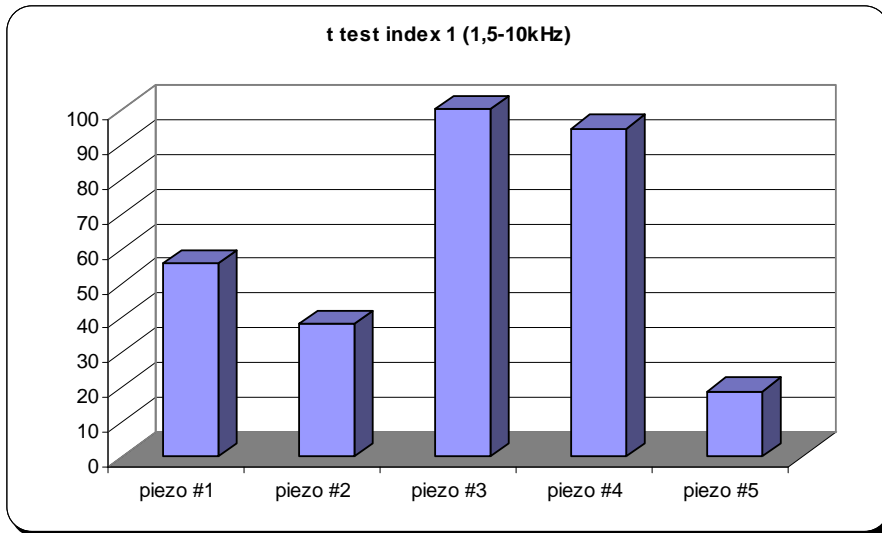


Fig. 5.3.169 – T_test

The T_test indexes localize the presence of the damage as well as in previous areas, since it is able to refine the data.

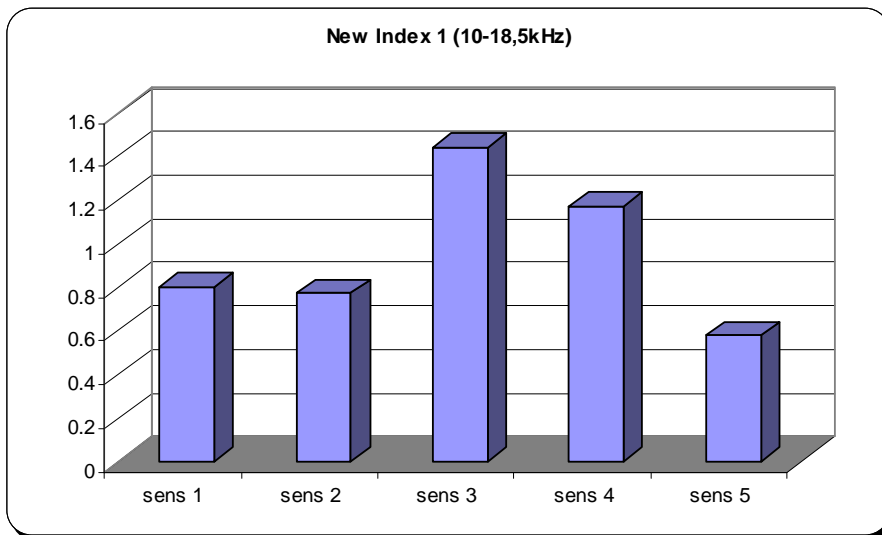


Fig. 5.3.176 – Sensors new DI

About the new Indexes representation the index "1" localizes undoubtedly where the rivets have been removed, especially considering the results determined at the highest frequency range.

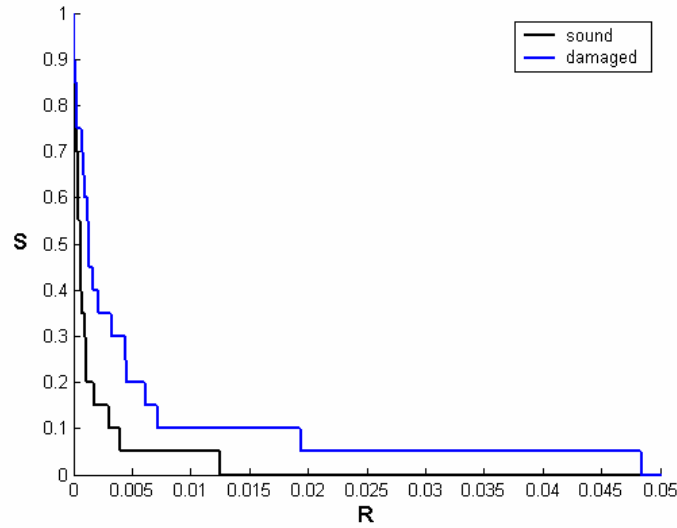


Fig. 5.3.181 – Neural Network output (range 1,5-10kHz)

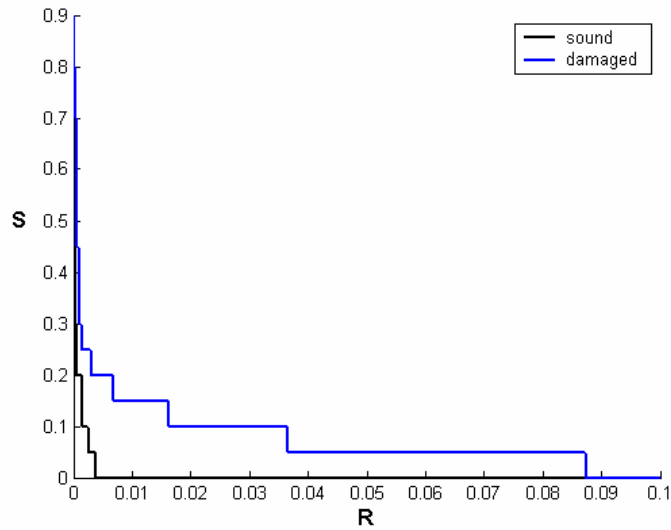


Fig. 5.3.182 – Neural Network output (range 10-18,5kHz)

In that case the Neural Network output determined at the highest frequency range identifies the damage better than the output obtained at the lowest range. In fact the distance between the damaged and undamaged curves at the highest range is greater than the distance of the corresponding curves at the lowest range.

182

V.3.7 Frame 45

A resume of the main results which have been expounded in this paragraph is following reported.

Both the Damage Index and the Neural Network methods have identified all the damage which have been executed on the ATR-72 aircraft.

✓ About the first monitored area, where the frame 29 is linked to the stringer 13, on the right side of fuselage, the best damage localization has been furnished by the damage indexes “2” obtained at the highest frequency range, in which the sensors are fixed, and by the new indexes “1” and “2” if they are calculated fixing the sensors, independently by the frequency range;

✓ About the second monitored area, the floor support zee close to the passenger door, the best damage localization has been furnished by the damage indexes “1” obtained at the highest frequency range, in which the actuators are fixed, by the T_test indexes “1” calculated at the highest frequency range, and by the new indexes “2” calculated fixing the actuators, at the highest frequency range;

✓ About the third monitored area, the floor frame located in the rear of the fuselage, where the frame 42 is, the best damage localization has been furnished by the damage indexes “2” obtained at the highest frequency range, in which the actuators are fixed, by the T_test indexes “2” calculated at the highest frequency range, and by the new indexes “2” calculated fixing the sensors, at the highest frequency range;

✓ About the fourth monitored area, the Main Landing Gear truss shear on the right side of the aircraft, the best damage localization has been furnished by the T_test indexes “1” calculated at the highest frequency range, and by the new indexes “2” calculated fixing the actuators, at the highest frequency range;

✓ About the fifth monitored area, the frame 45 located in the tail cone, the best damage localization has been furnished by the T_test indexes “1” calculated at the lowest frequency range, and by the new indexes “1” calculated fixing the sensors, at the highest frequency range;

In conclusion it appears that, generally, the higher frequency range is the better damage localization can be obtained.

Intentionally blank

Appendix

All the figures which have been removed from the paragraph V.3 are following gathered and reported for each subparagraph. The progressive numbering of the figures is kept to make faster the searching of the chart wanted.

A.1 Subparagraph V.3.3

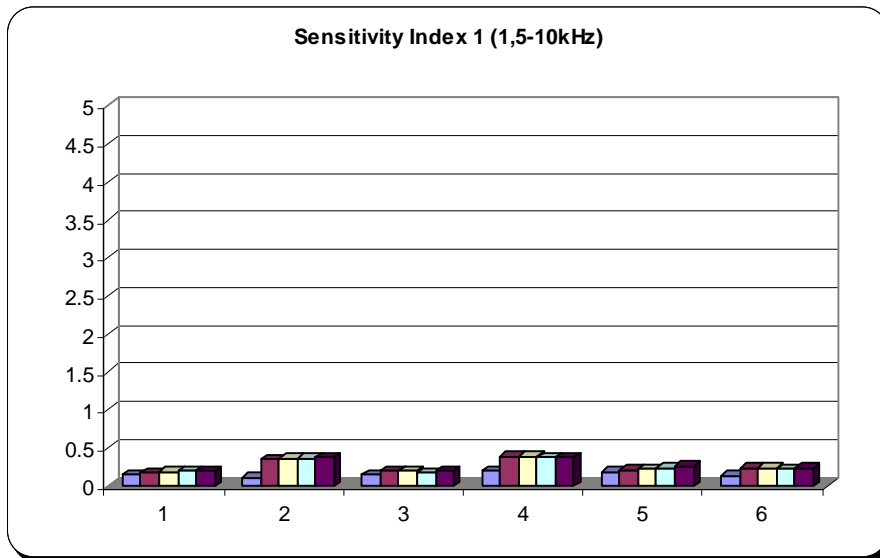


Fig. 5.3.46 – Sensitivity Index

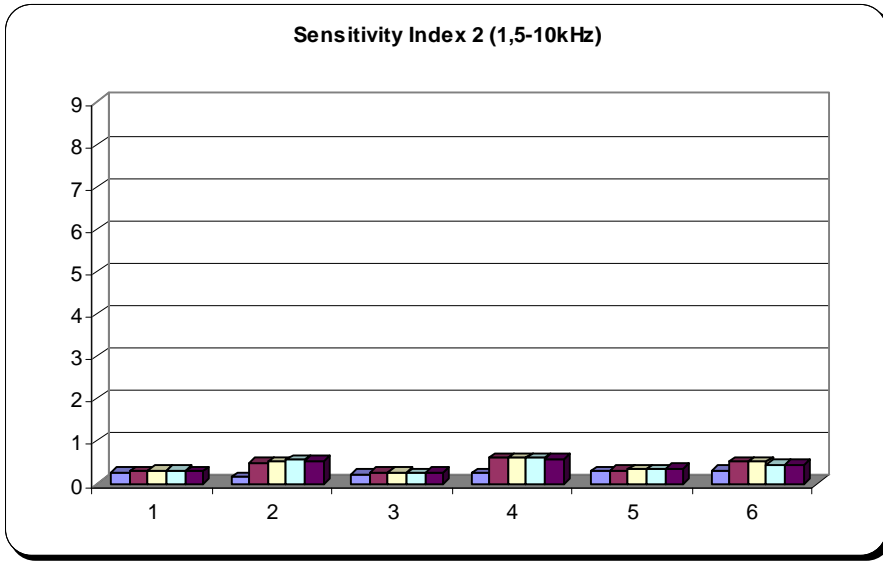


Fig. 5.3.48 – Sensitivity Index

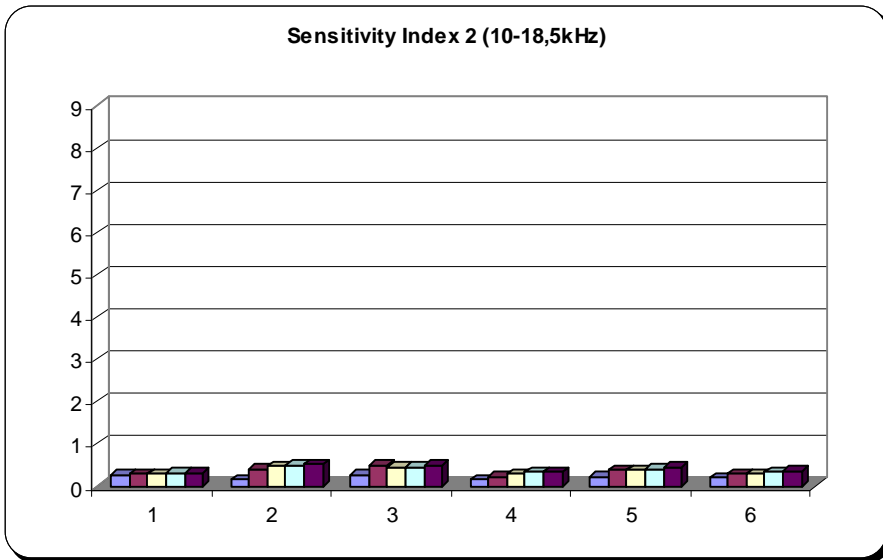


Fig. 5.3.49 – Sensitivity Index

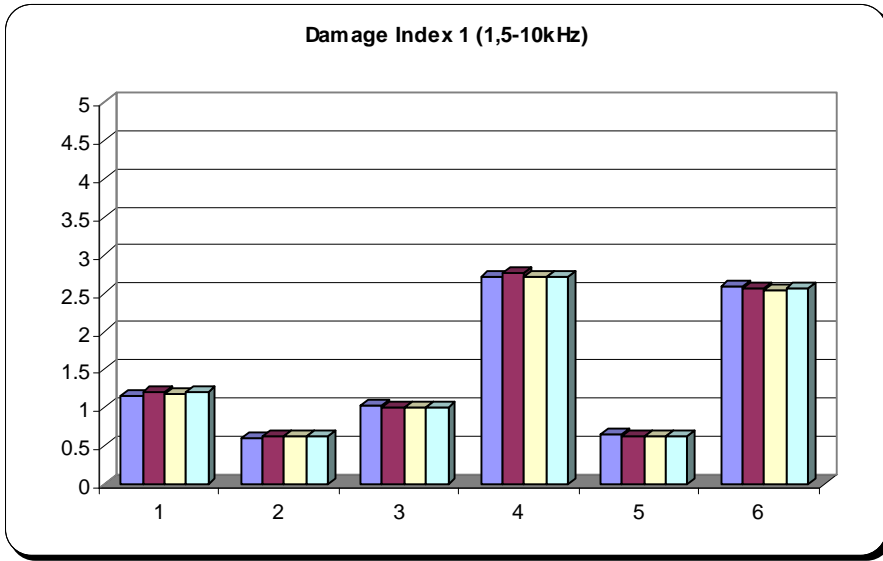


Fig. 5.3.50 – Damage Index

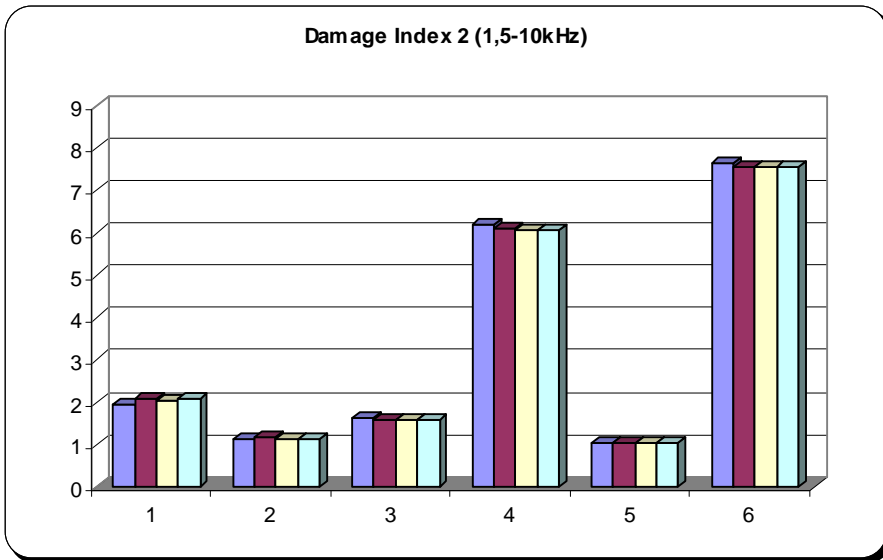


Fig. 5.3.52 – Damage Index

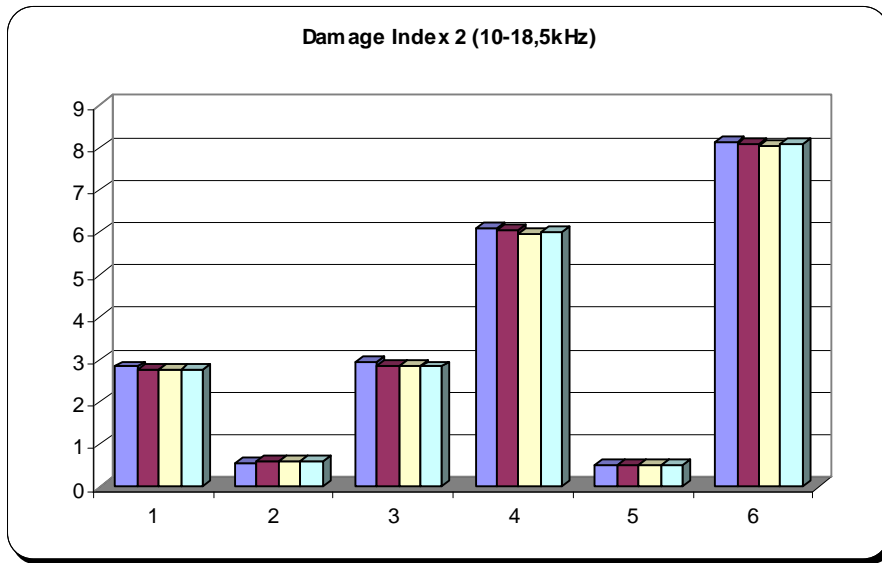


Fig. 5.3.53 – Damage Index

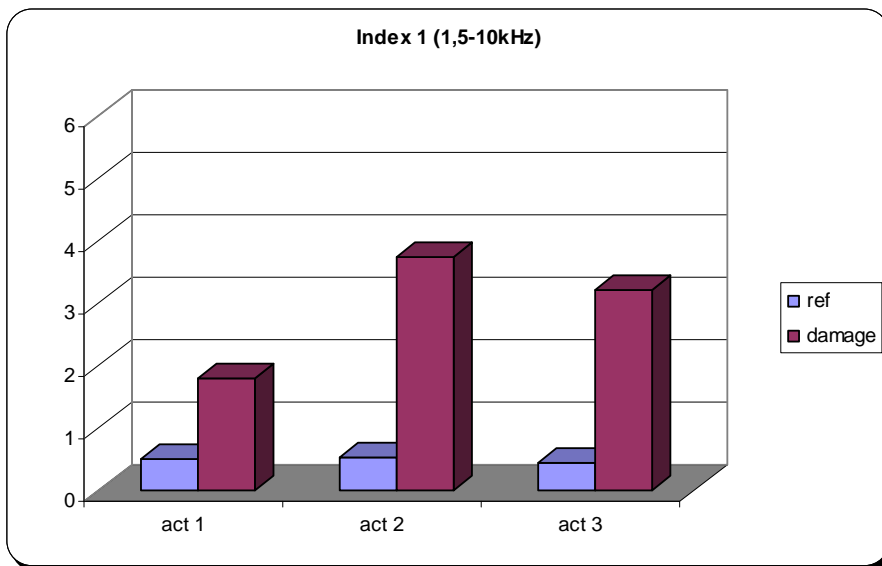


Fig. 5.3.54 – Actuators DI

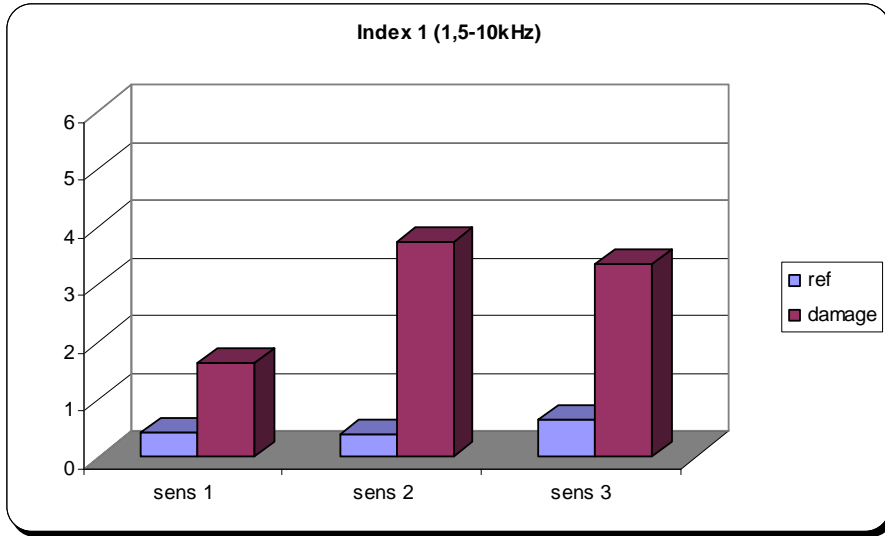


Fig. 5.3.56 – Sensors DI

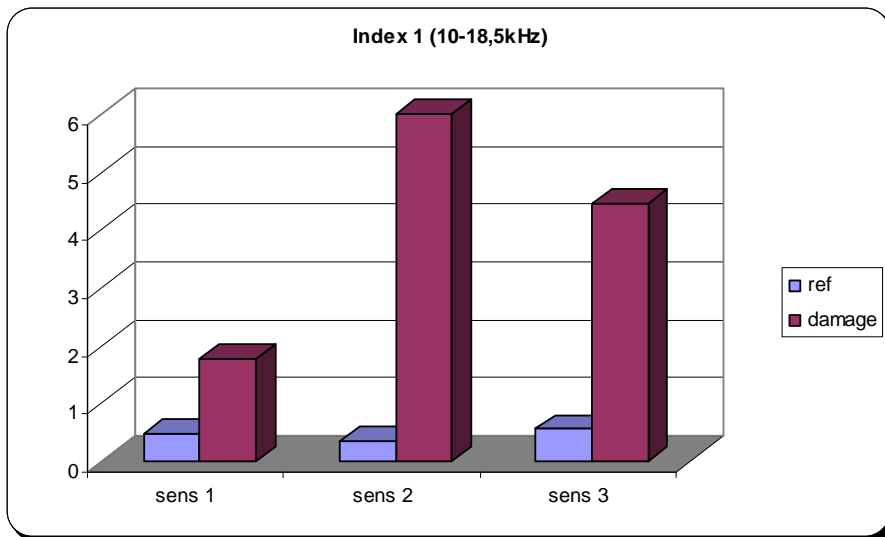


Fig. 5.3.57 – Sensors DI

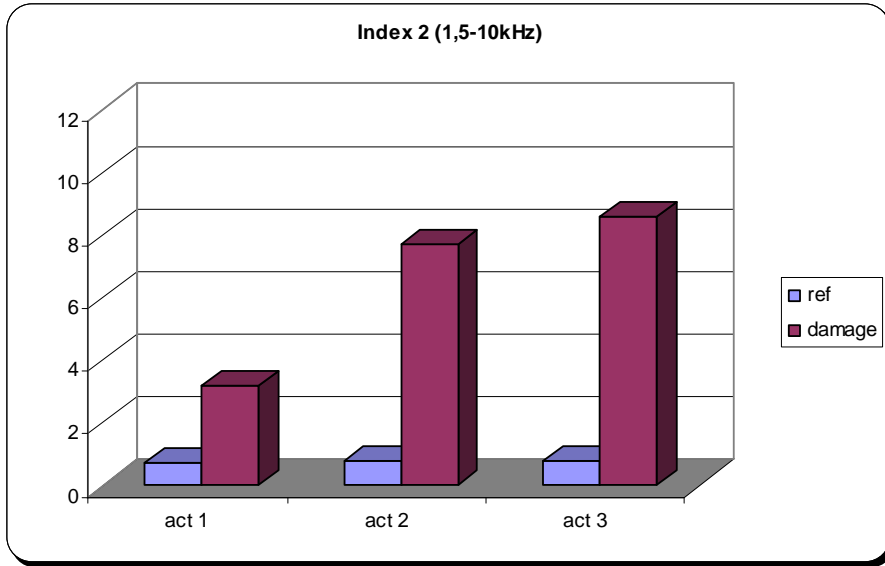


Fig. 5.3.58 – Actuators DI

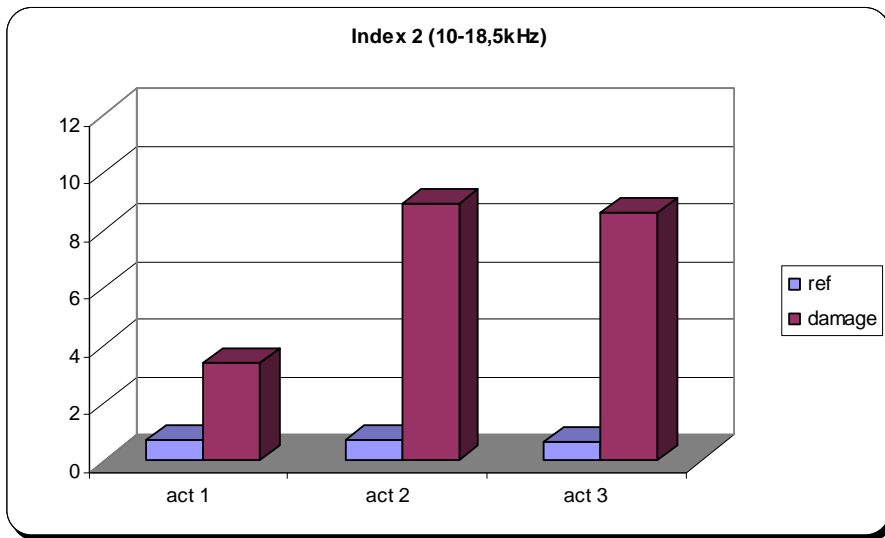


Fig. 5.3.59 – Actuators DI

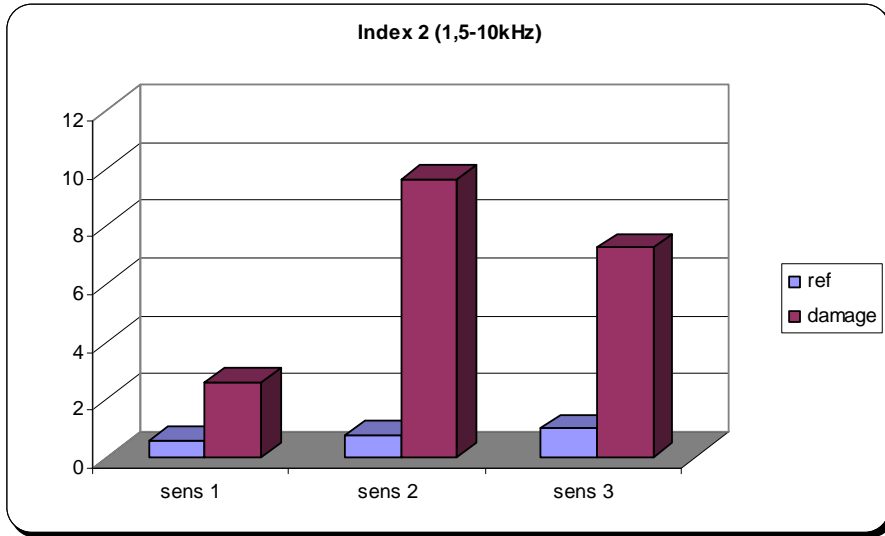


Fig. 5.3.60 – Sensors DI

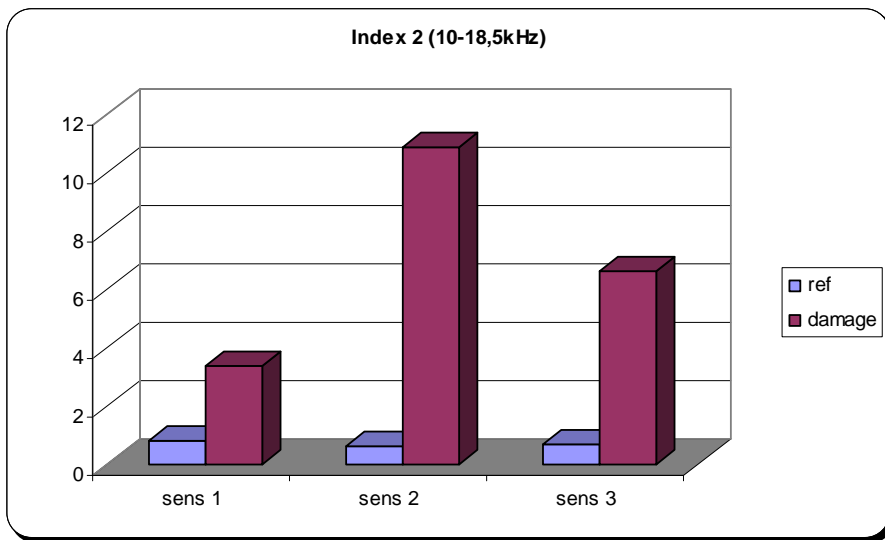


Fig. 5.3.61 – Sensors DI

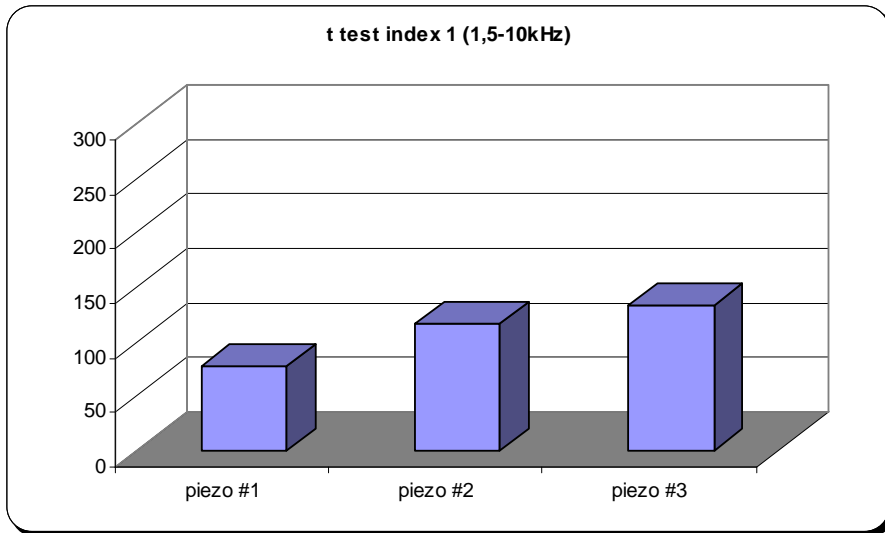


Fig. 5.3.62 – T_test

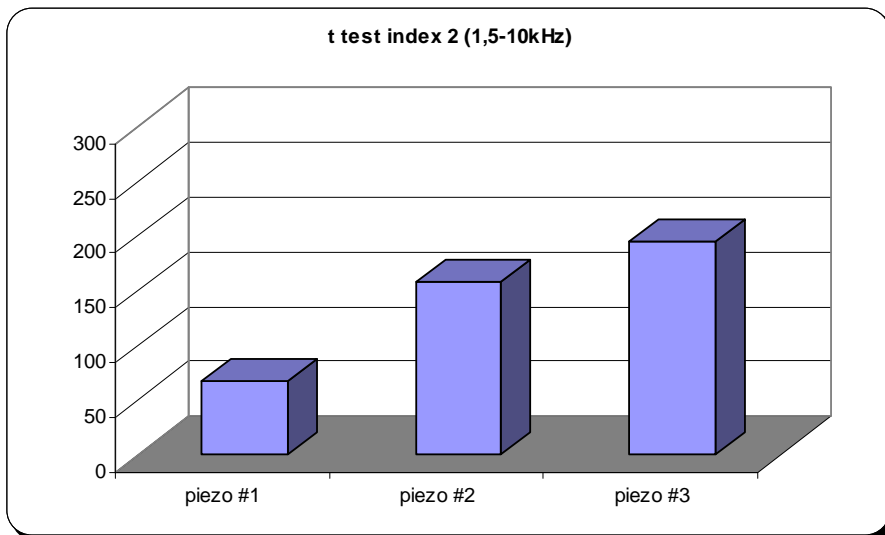


Fig. 5.3.64 – T_test

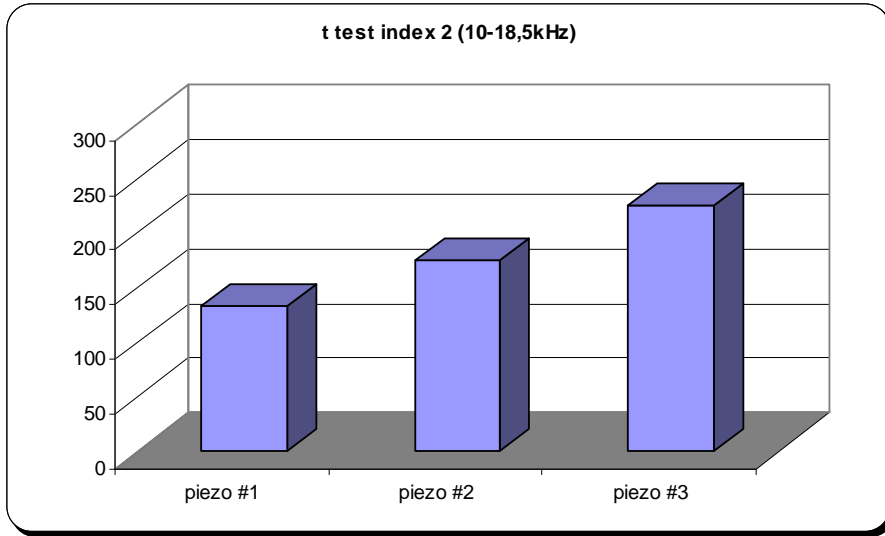


Fig. 5.3.65 – T_test

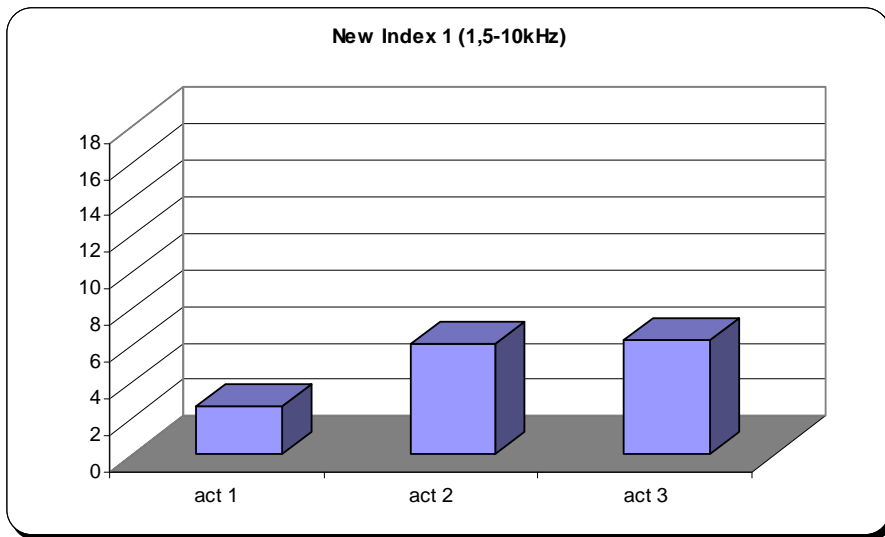


Fig. 5.3.66 – Actuators new DI

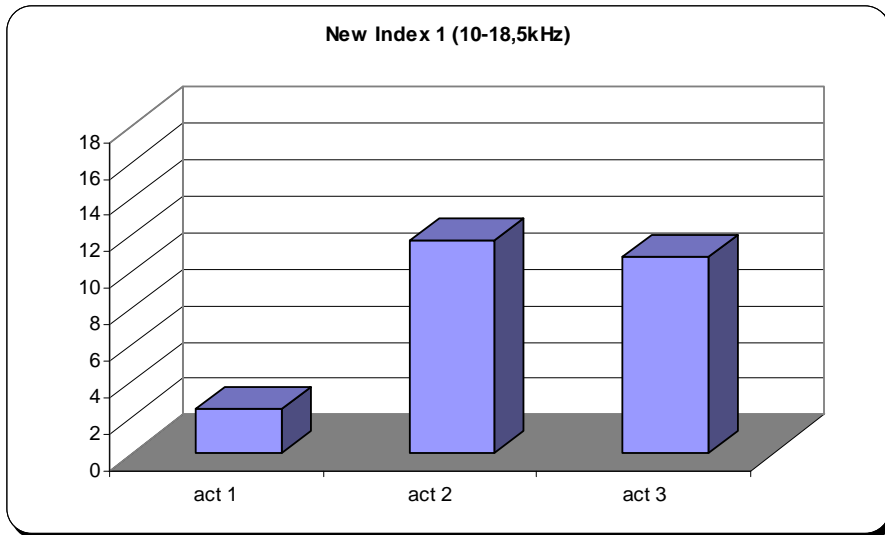


Fig. 5.3.67 – Actuators new DI

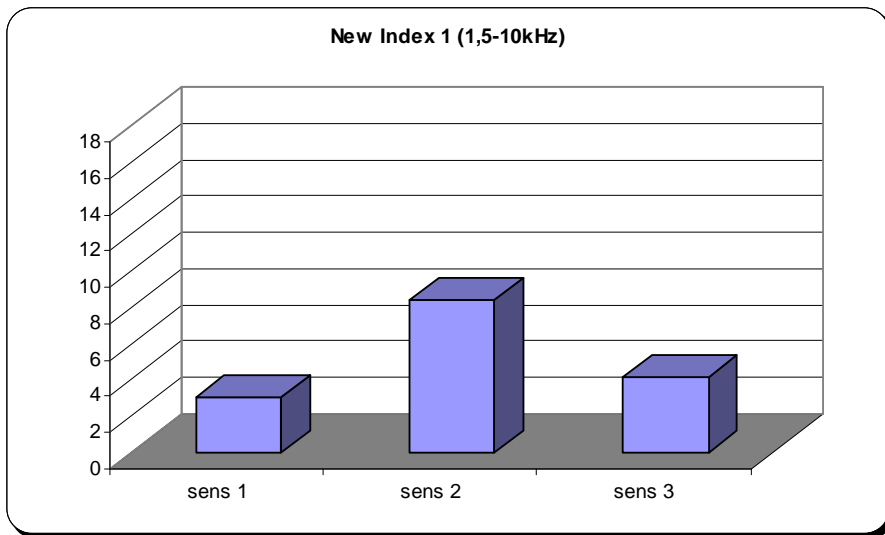


Fig. 5.3.68 – Sensors new DI

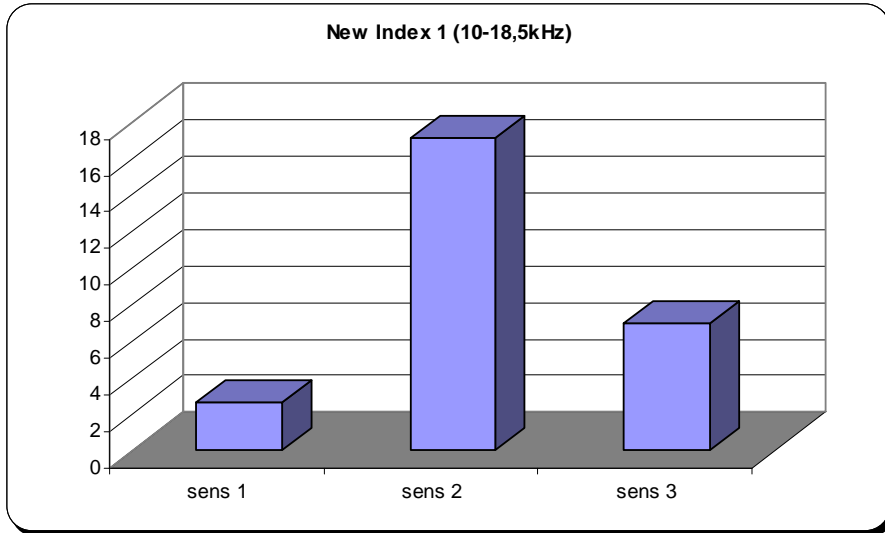


Fig. 5.3.69 – Sensors new DI

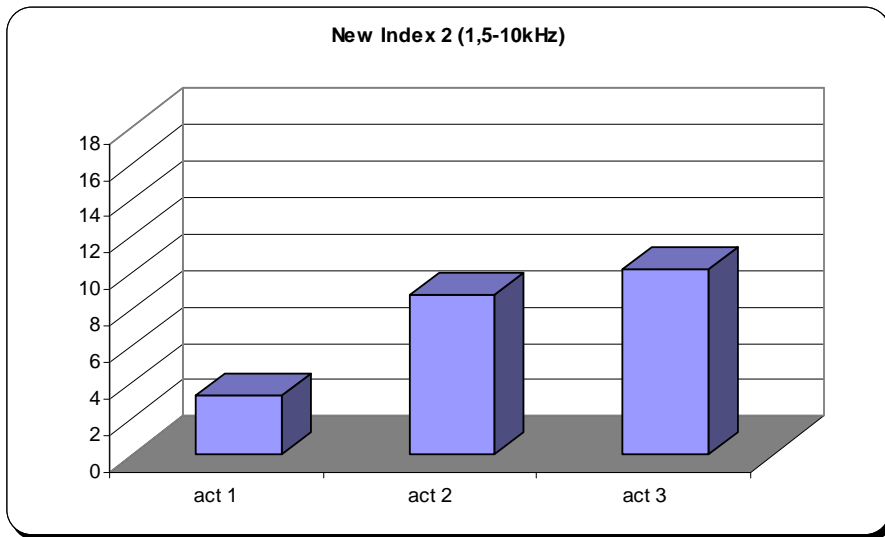


Fig. 5.3.70 – Actuators new DI

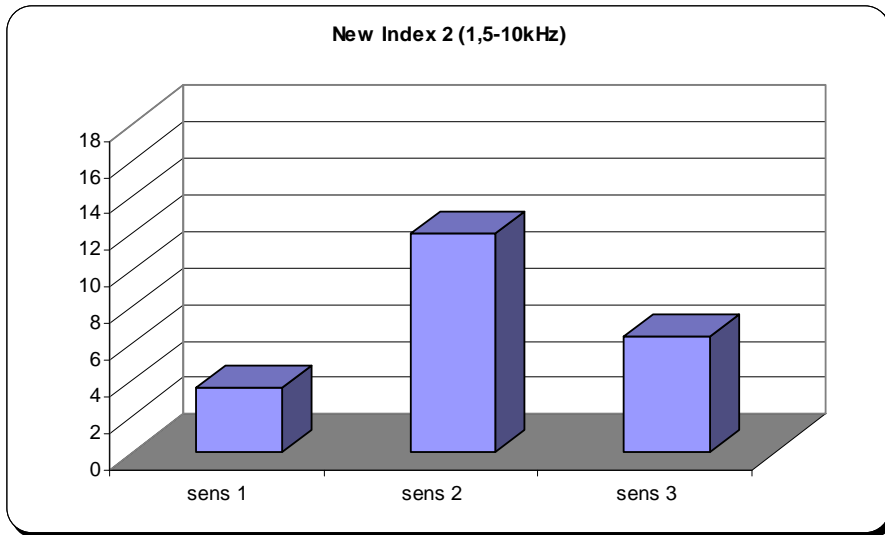


Fig. 5.3.72 – Sensors new DI

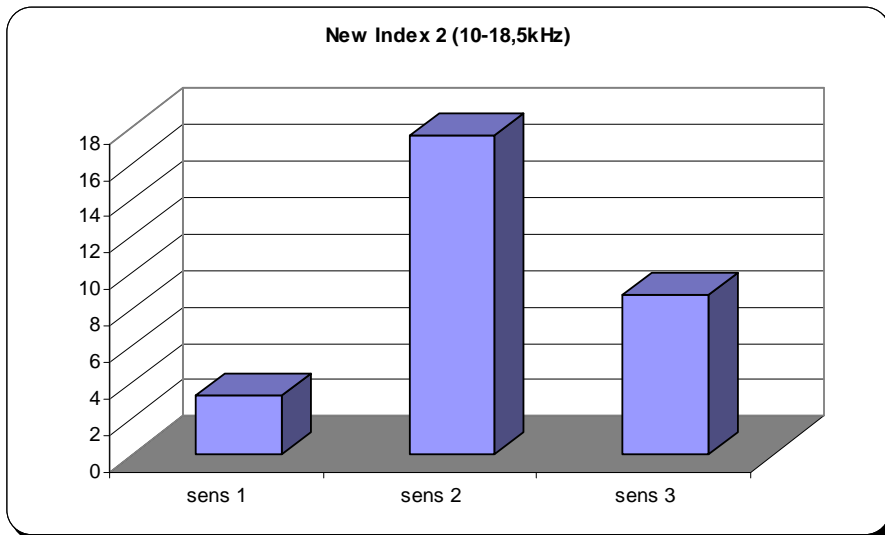


Fig. 5.3.73 – Sensors new DI

A.2 Subparagraph V.3.4

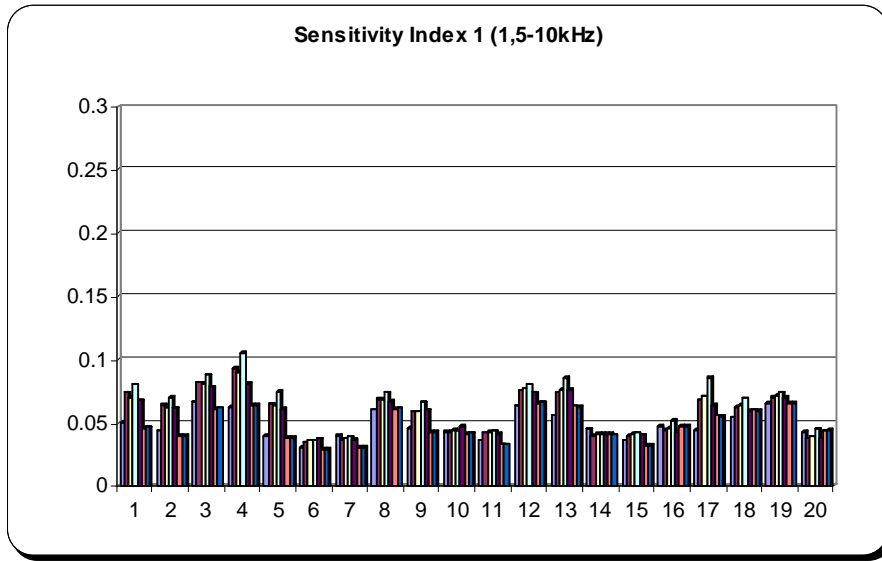


Fig. 5.3.81 – Sensitivity Index

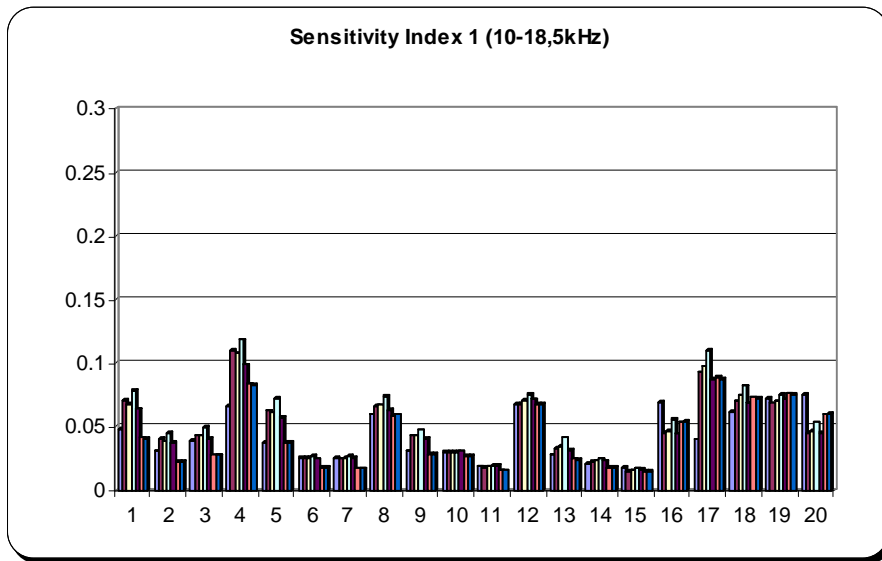


Fig. 5.3.82 – Sensitivity Index

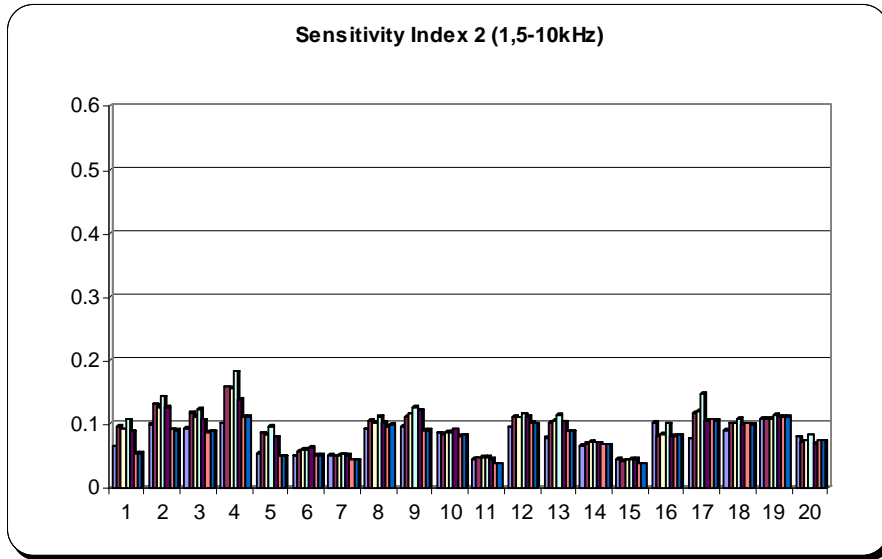


Fig. 5.3.83 – Sensitivity Index

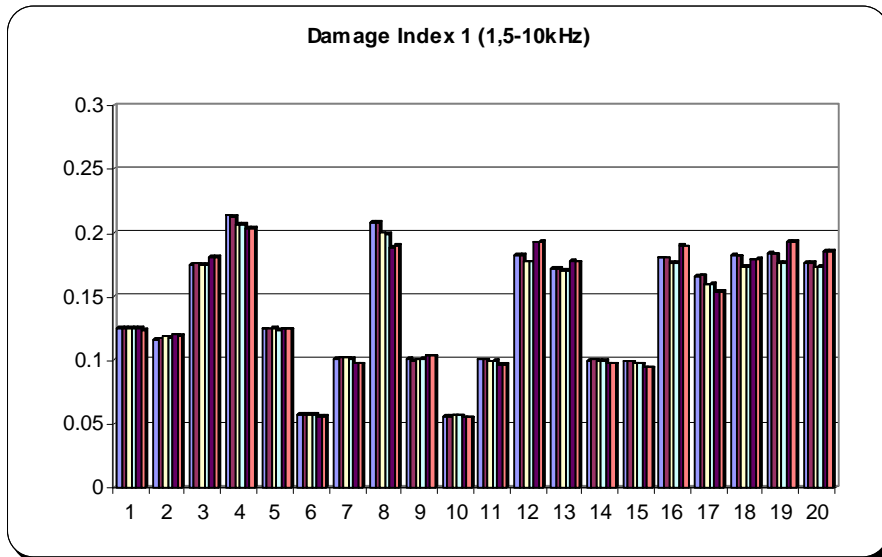


Fig. 5.3.85 – Damage Index

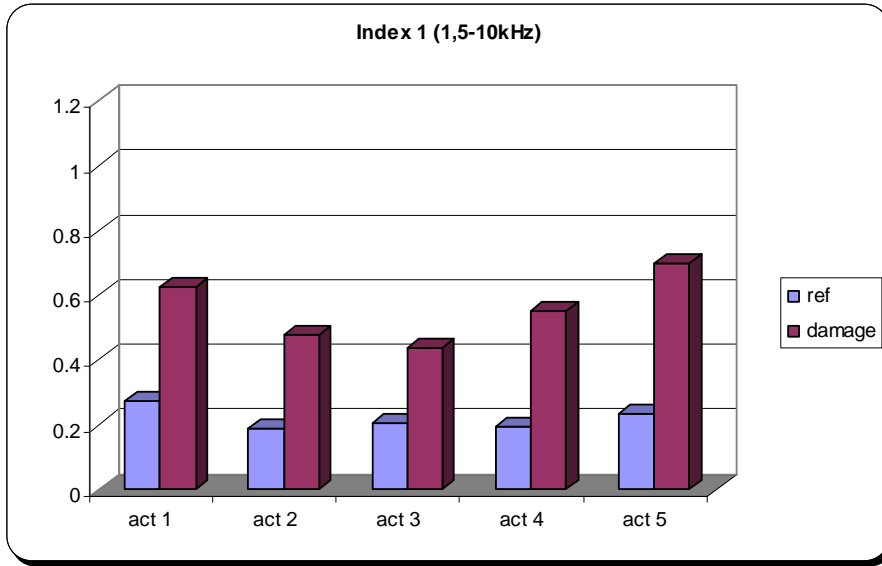


Fig. 5.3.89 – Actuators DI

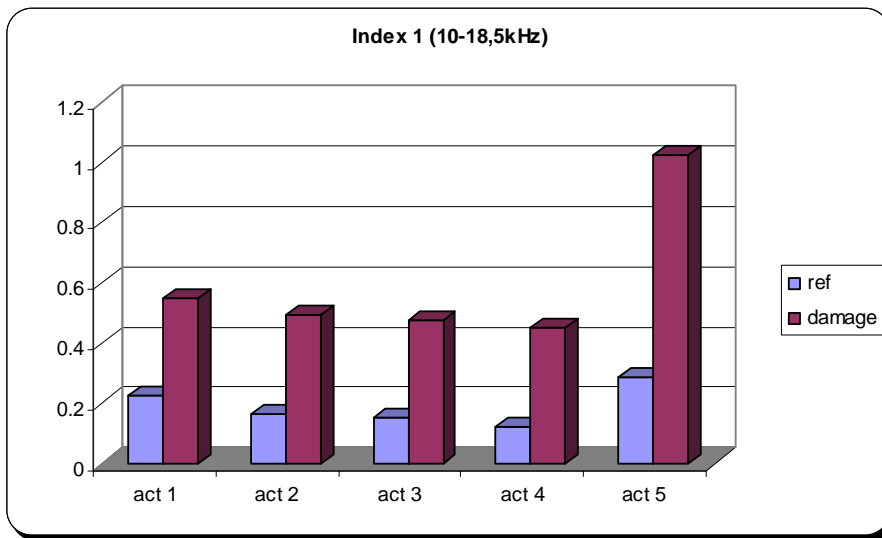


Fig. 5.3.90 – Actuators DI

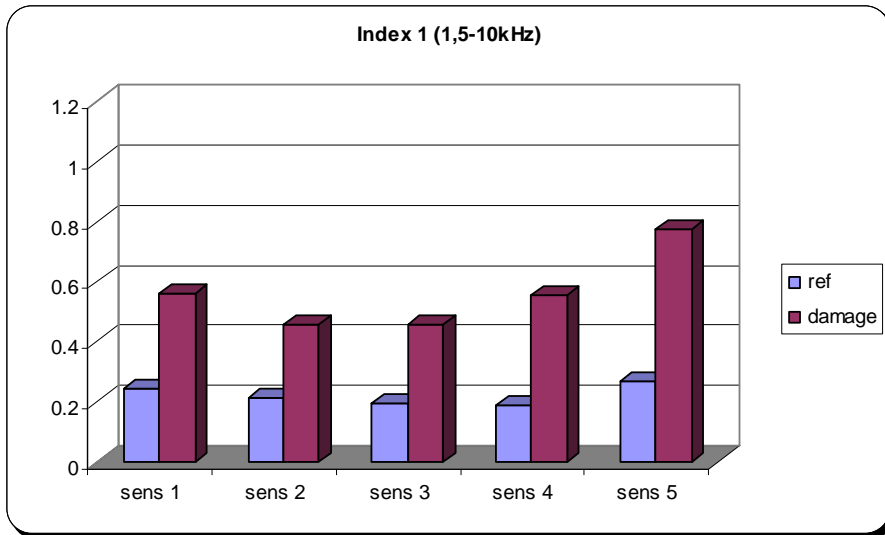


Fig. 5.3.91 – Sensors DI

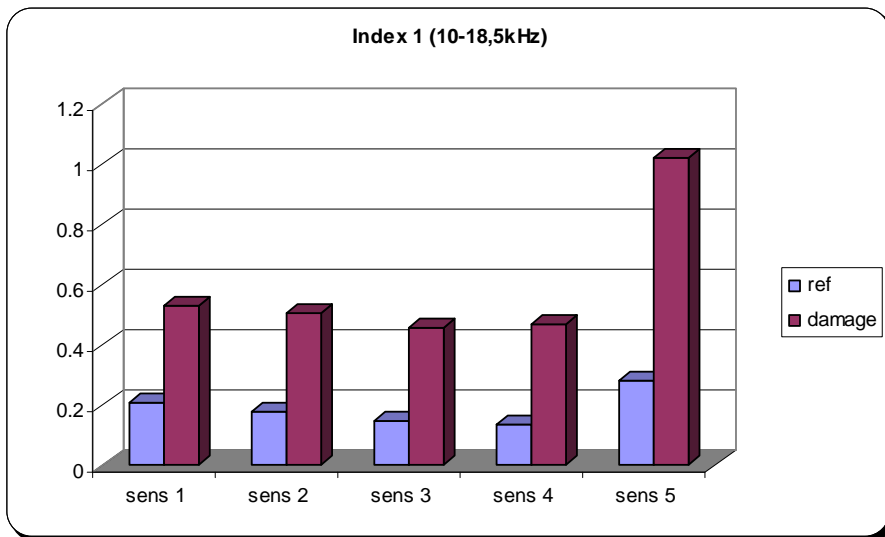


Fig. 5.3.92 – Sensors DI

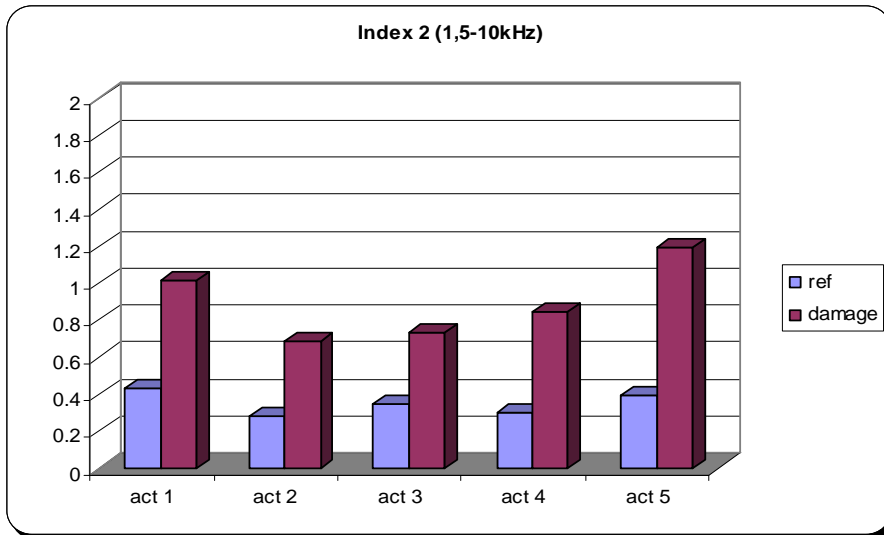


Fig. 5.3.93 – Actuators DI

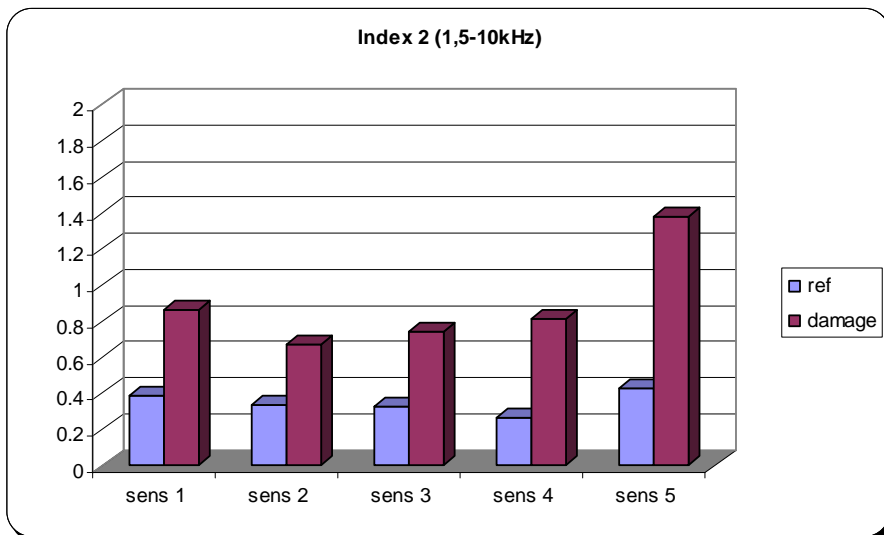


Fig. 5.3.95 – Sensors DI

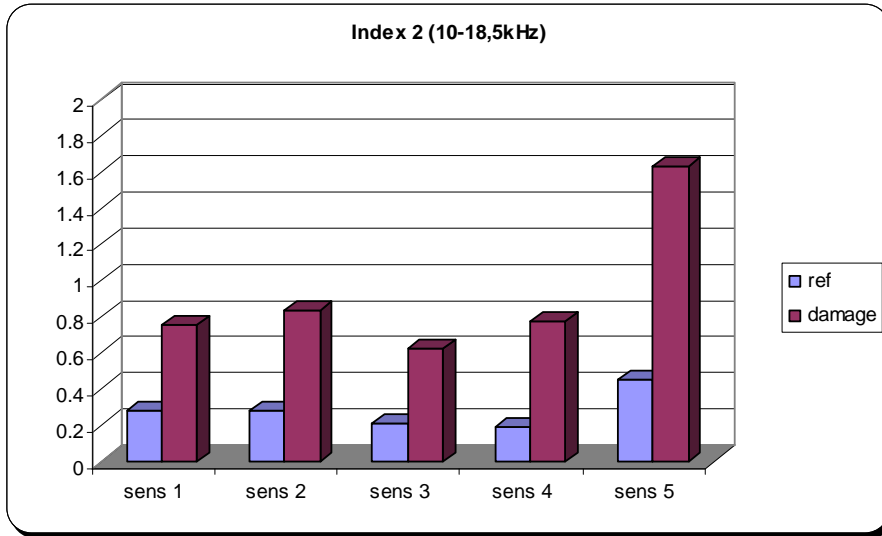


Fig. 5.3.96 – Sensors DI

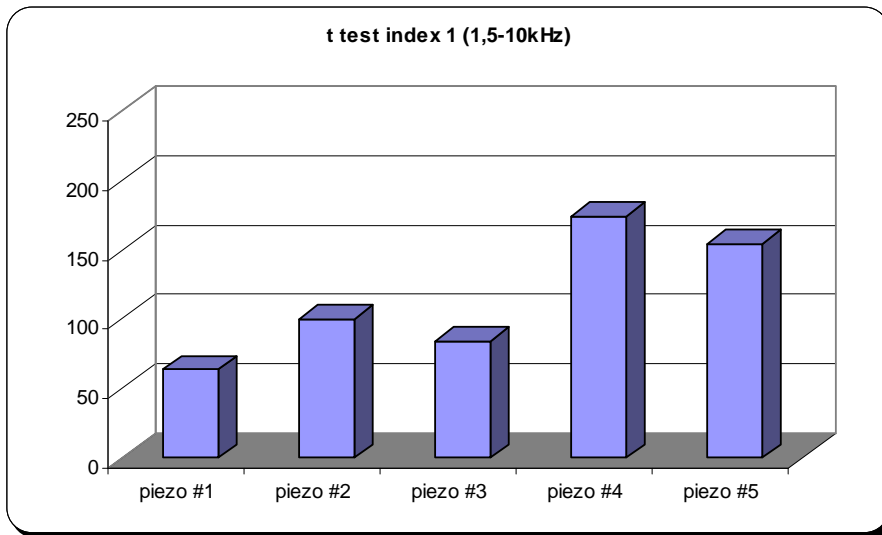


Fig. 5.3.97 – T_test

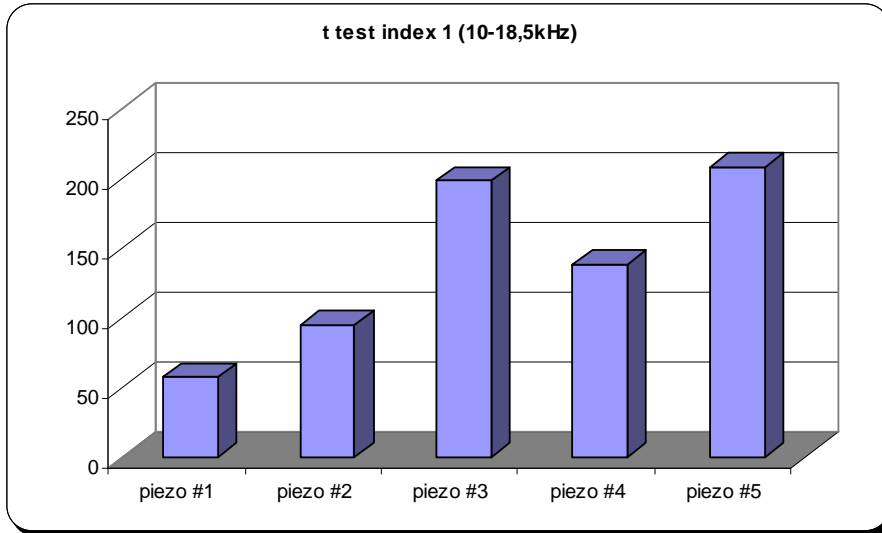


Fig. 5.3.98 – T_test

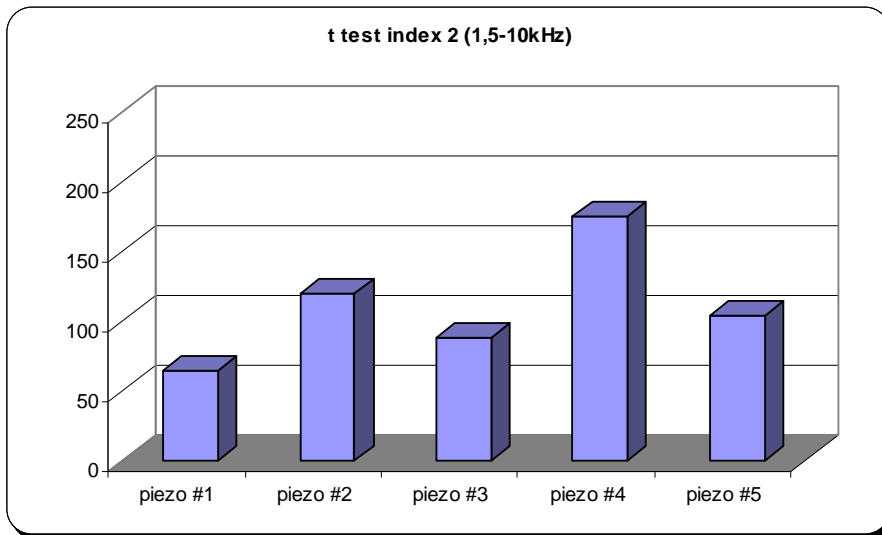


Fig. 5.3.99 – T_test

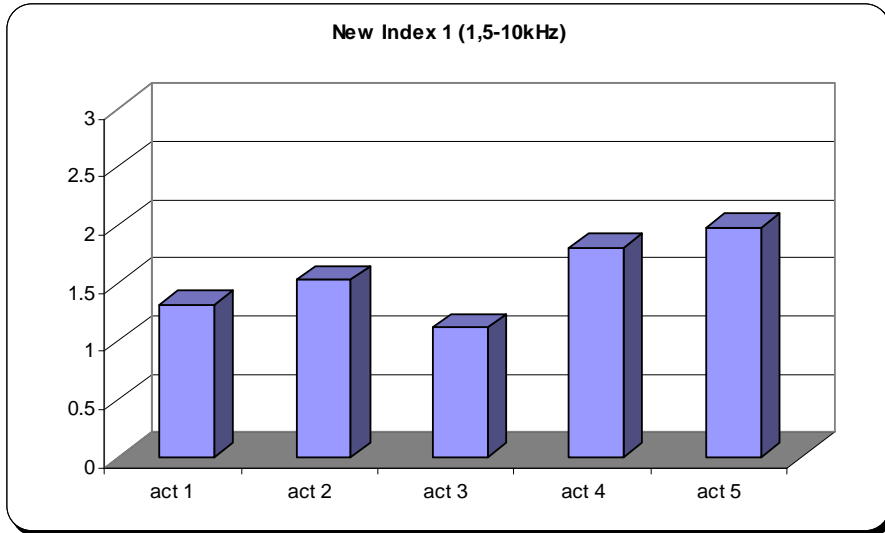


Fig. 5.3.101 – Actuators new DI

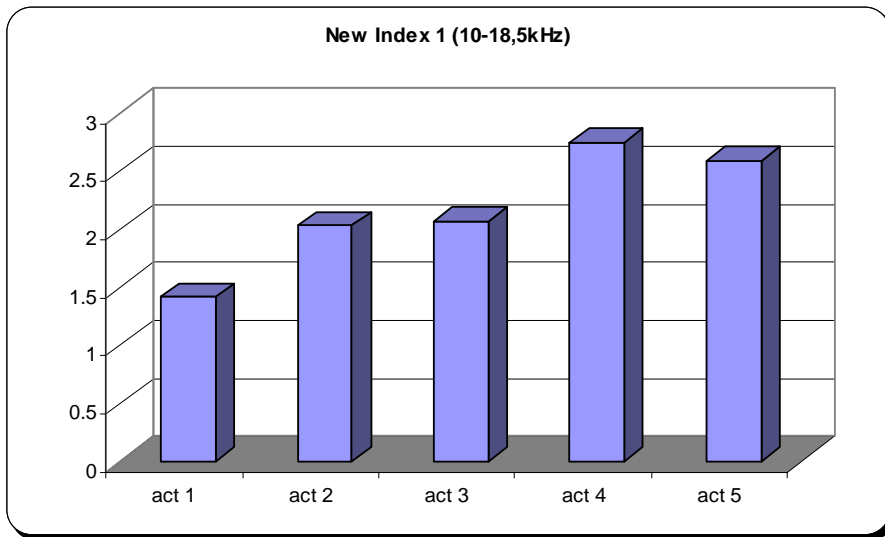


Fig. 5.3.102 – Actuators new DI

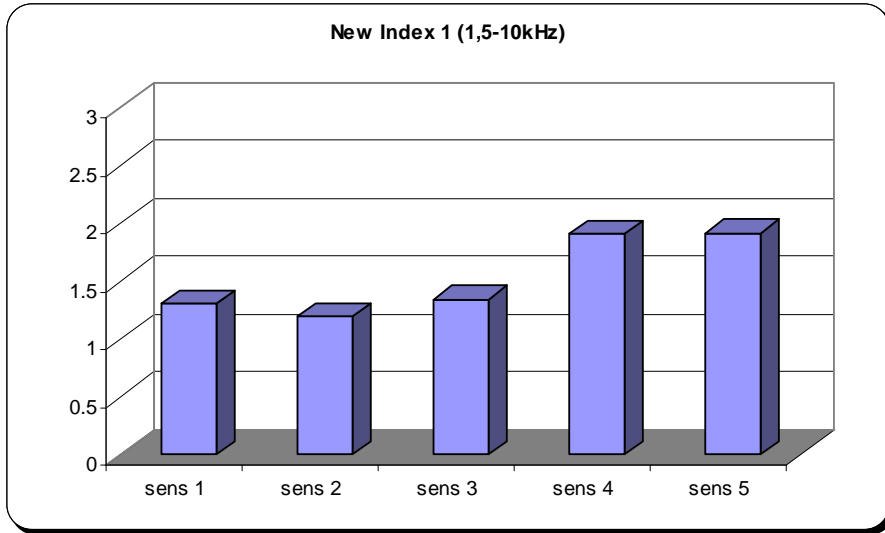


Fig. 5.3.103 – Sensors new DI

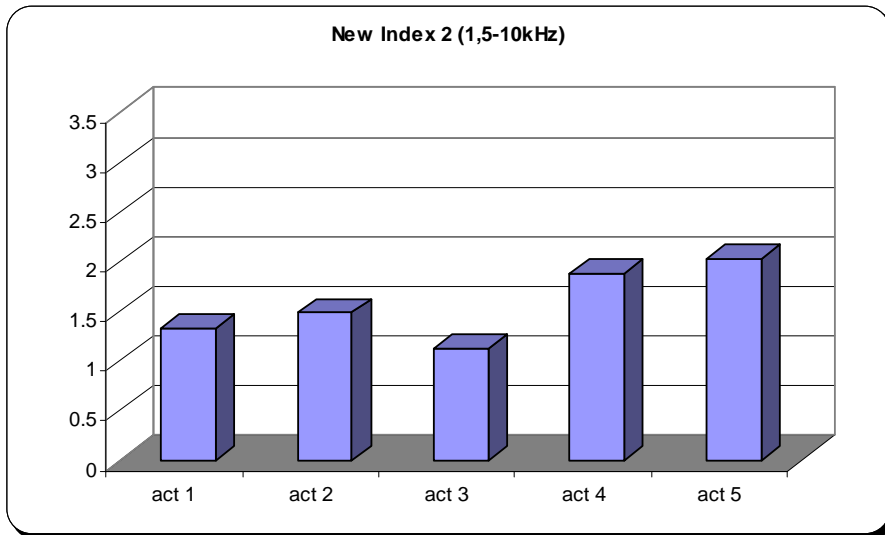


Fig. 5.3.105 – Actuators new DI

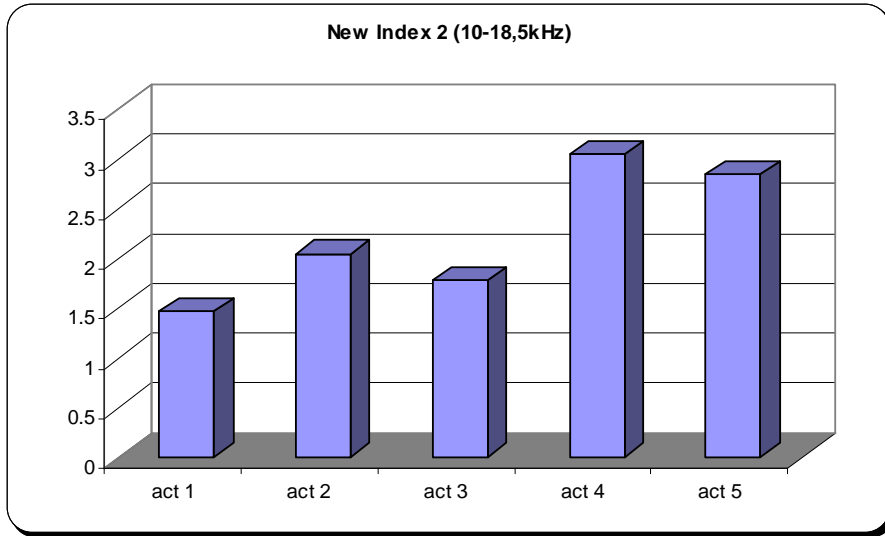


Fig. 5.3.106 – Actuators new DI

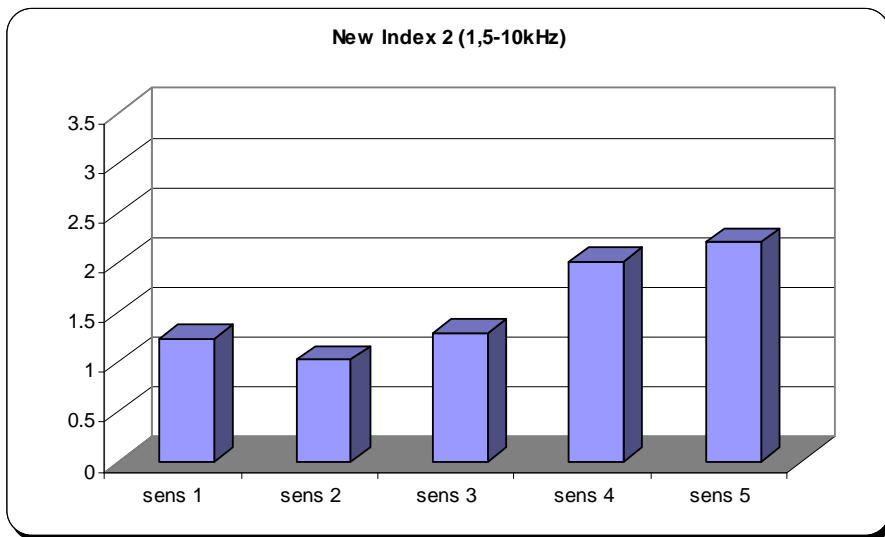


Fig. 5.3.107 – Sensors new DI

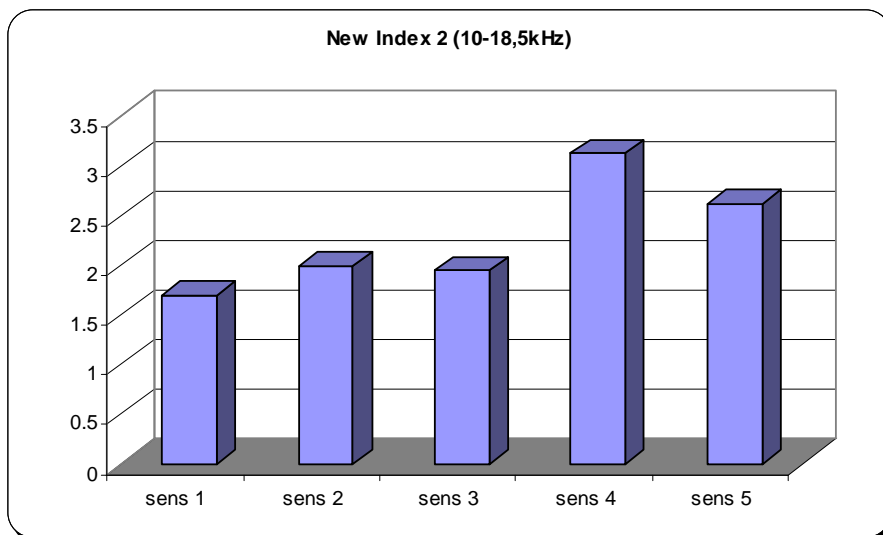


Fig. 5.3.108 – Sensors new DI

A.3 Subparagraph V.3.5

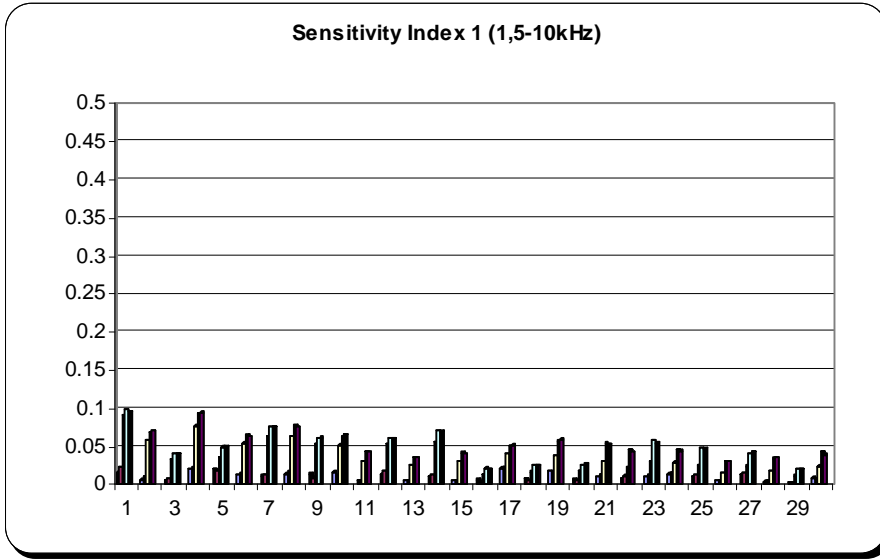


Fig. 5.3.118 – Sensitivity Index

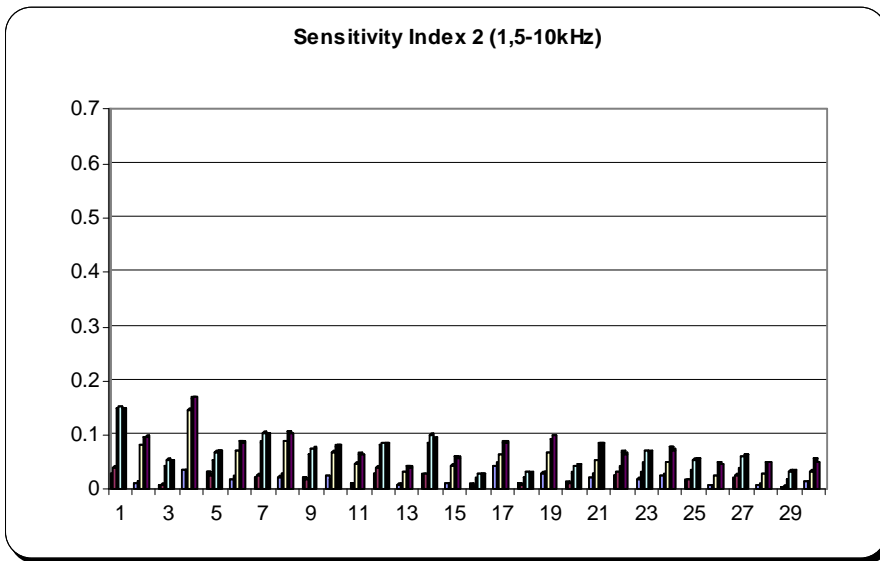


Fig. 5.3.120 – Sensitivity Index

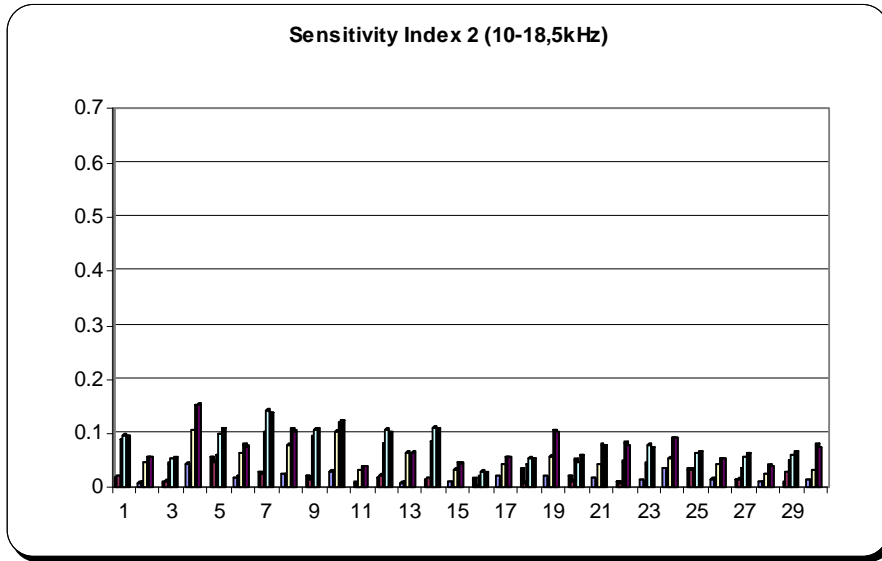


Fig. 5.3.121 – Sensitivity Index

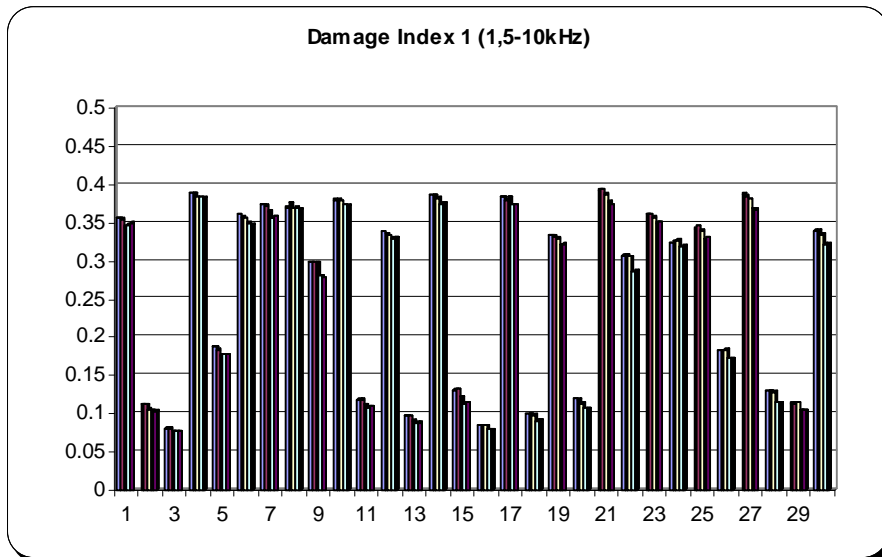


Fig. 5.3.122 – Damage Index

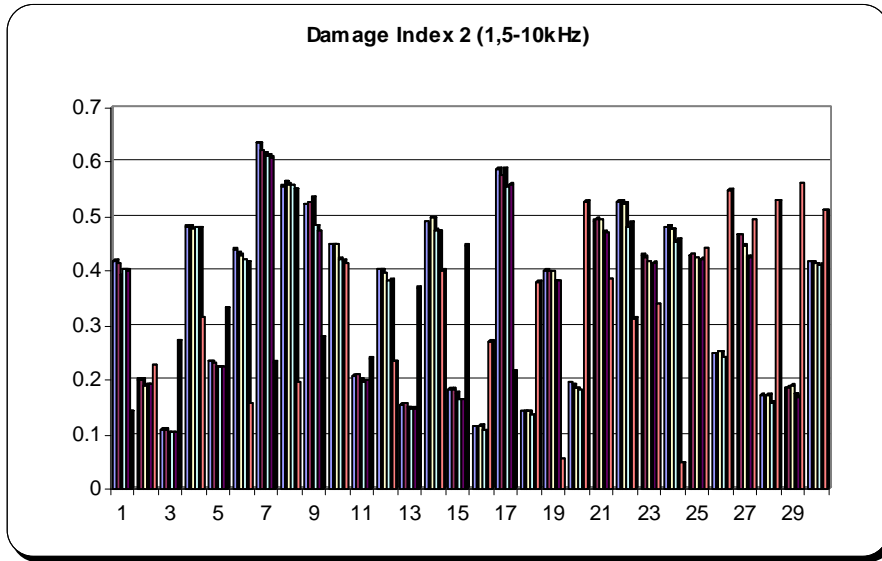


Fig. 5.3.124 – Damage Index

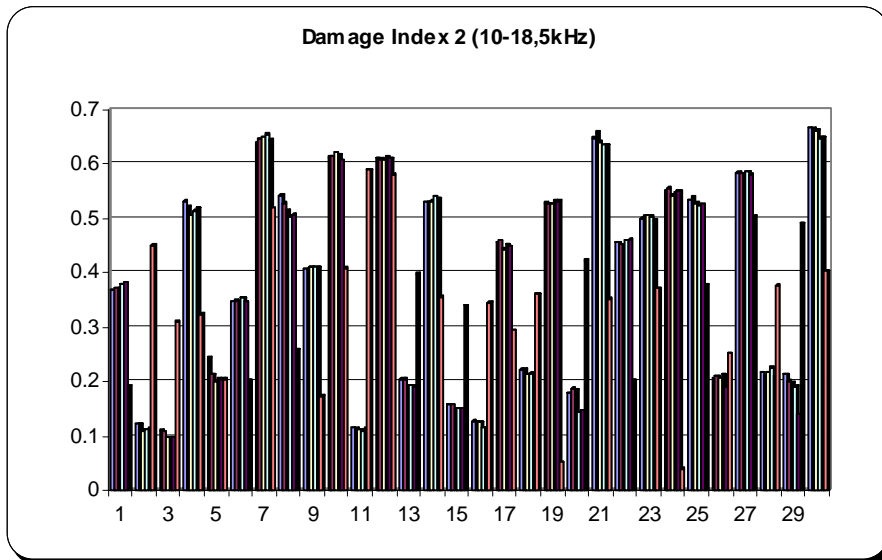


Fig. 5.3.125 – Damage Index

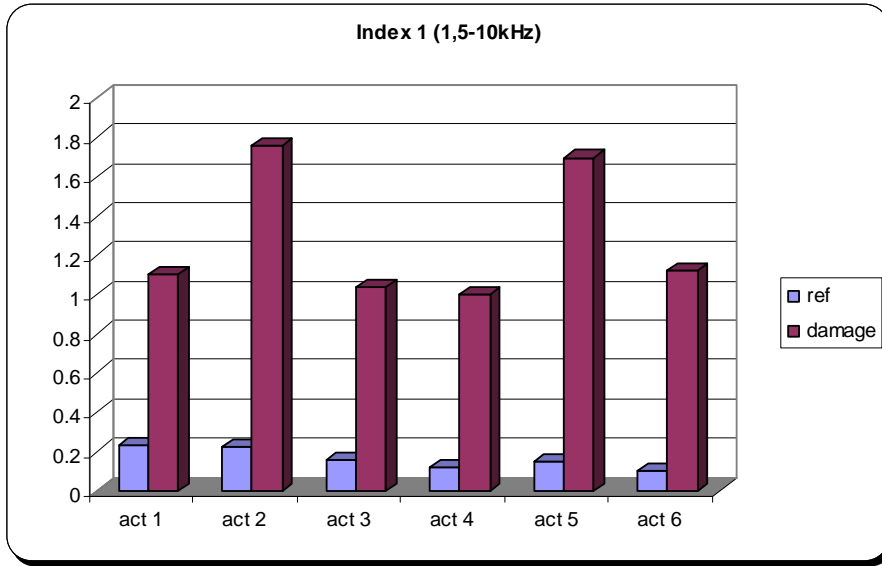


Fig. 5.3.126 – Actuators DI

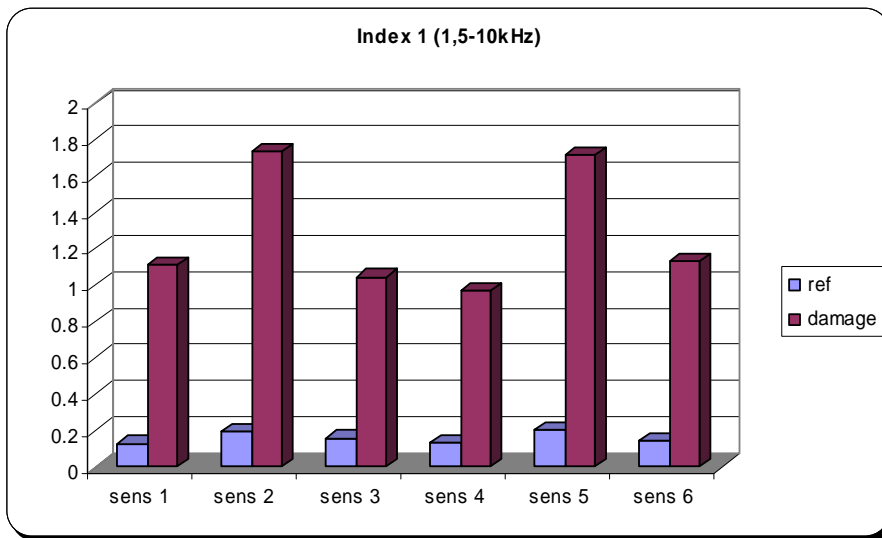


Fig. 5.3.128 – Sensors DI

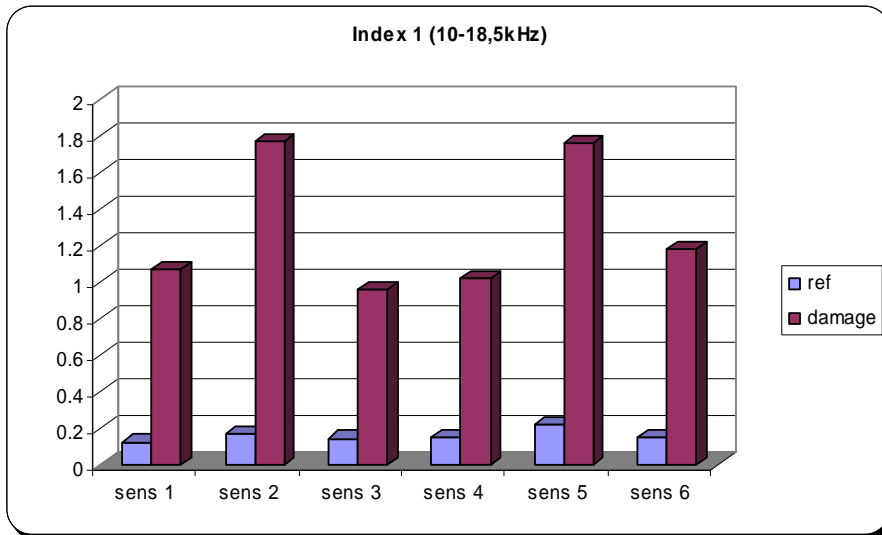


Fig. 5.3.129 – Sensors DI

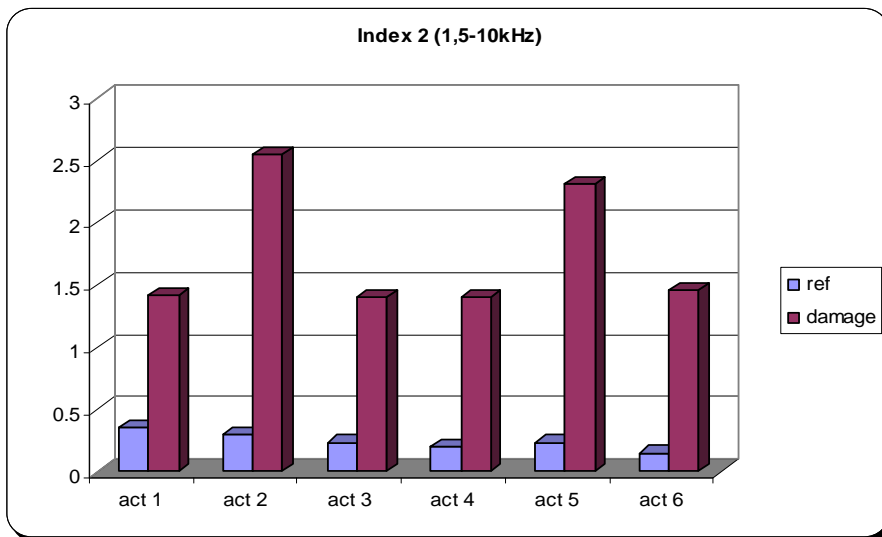


Fig. 5.3.130 – Actuators DI

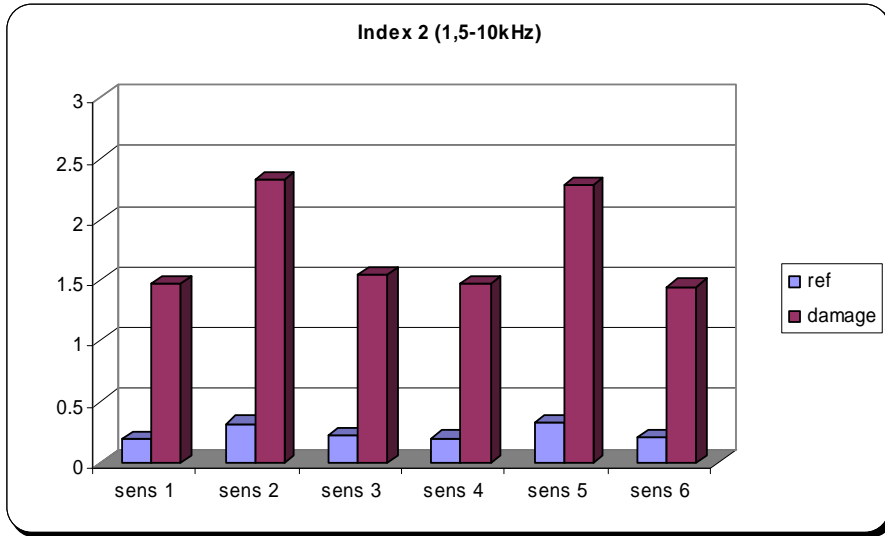


Fig. 5.3.132 – Sensors DI

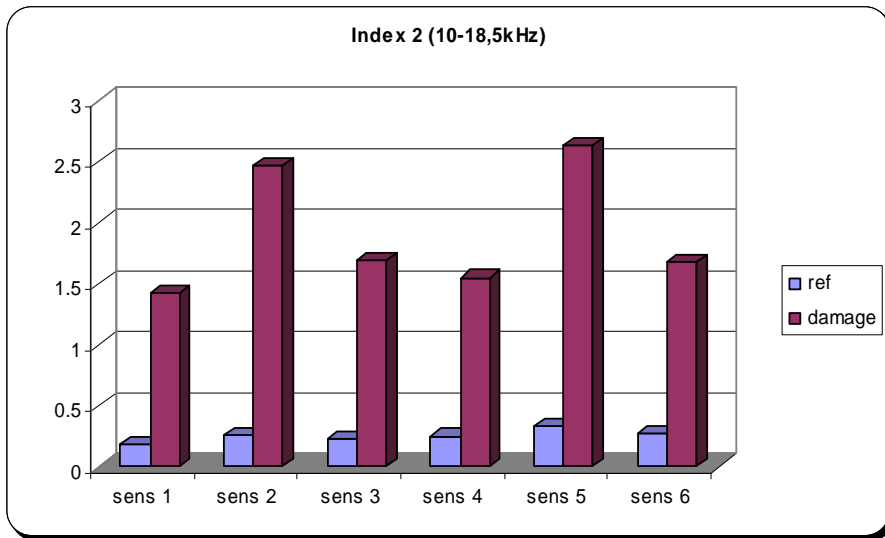


Fig. 5.3.133 – Sensors DI

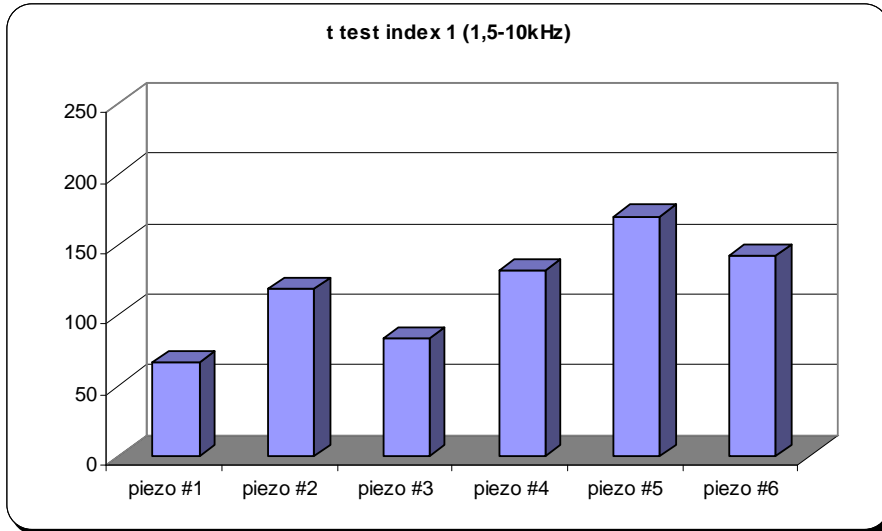


Fig. 5.3.134 – T_test

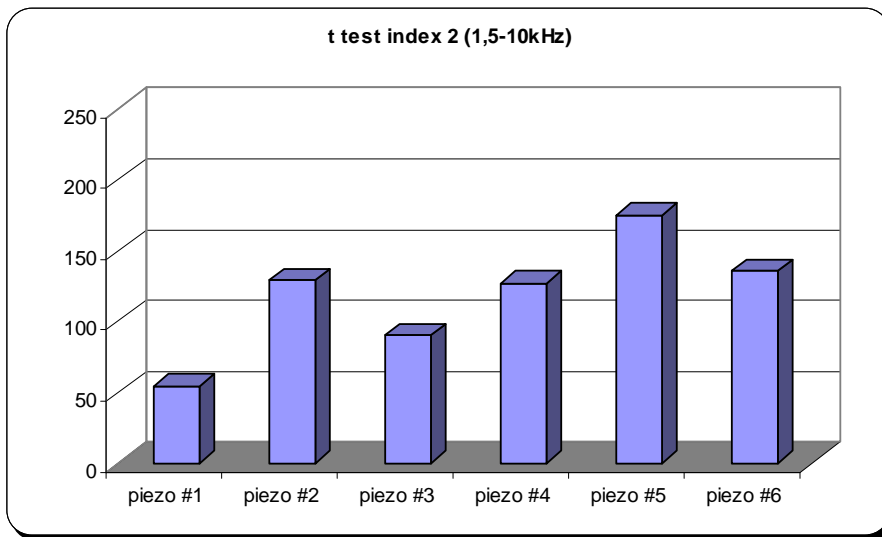


Fig. 5.3.136 – T_test

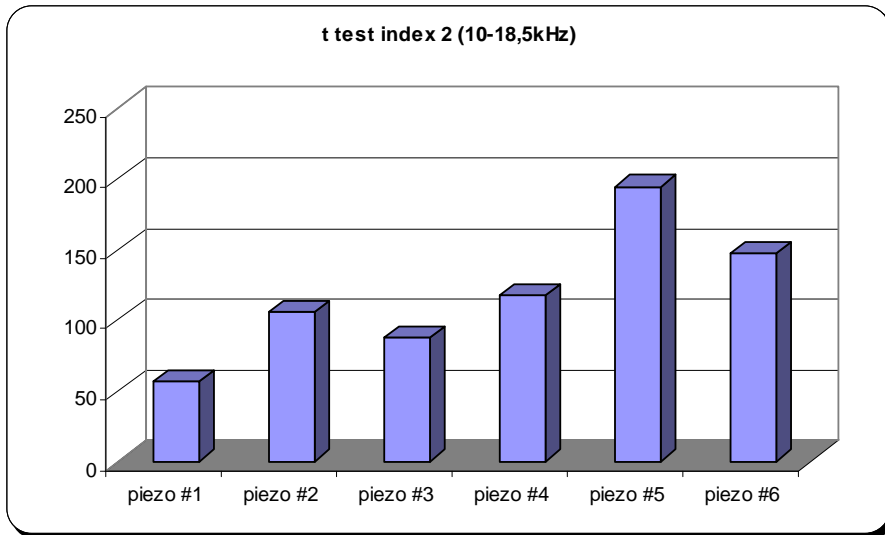


Fig. 5.3.137 – T_test

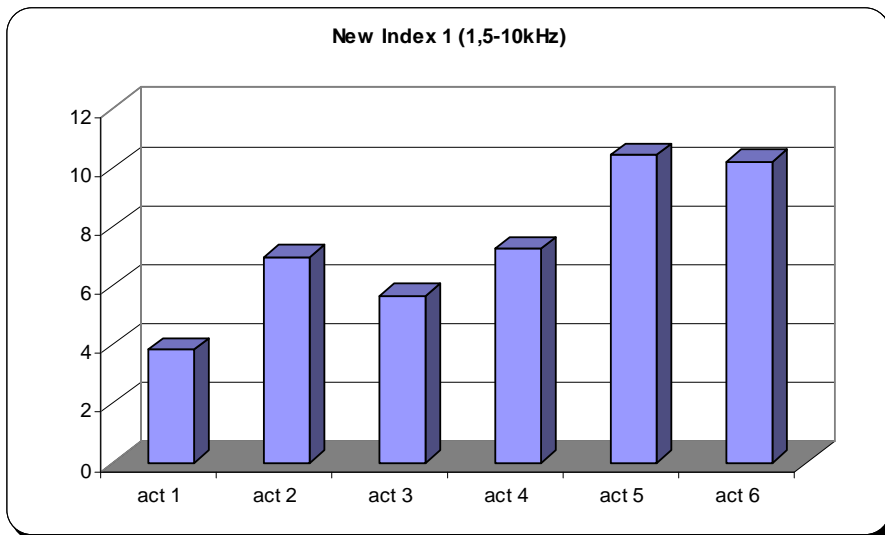


Fig. 5.3.138 – Actuators new DI

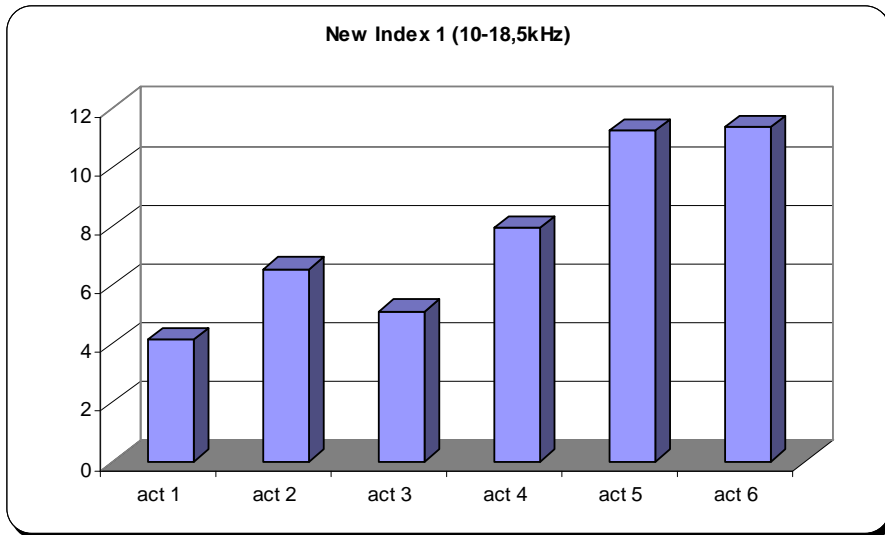


Fig. 5.3.139 – Actuators new DI

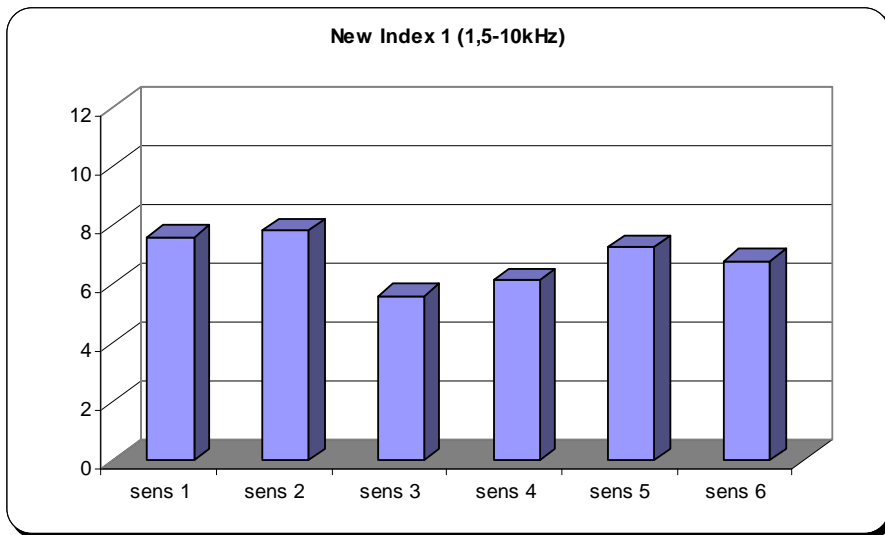


Fig. 5.3.140 – Sensors new DI

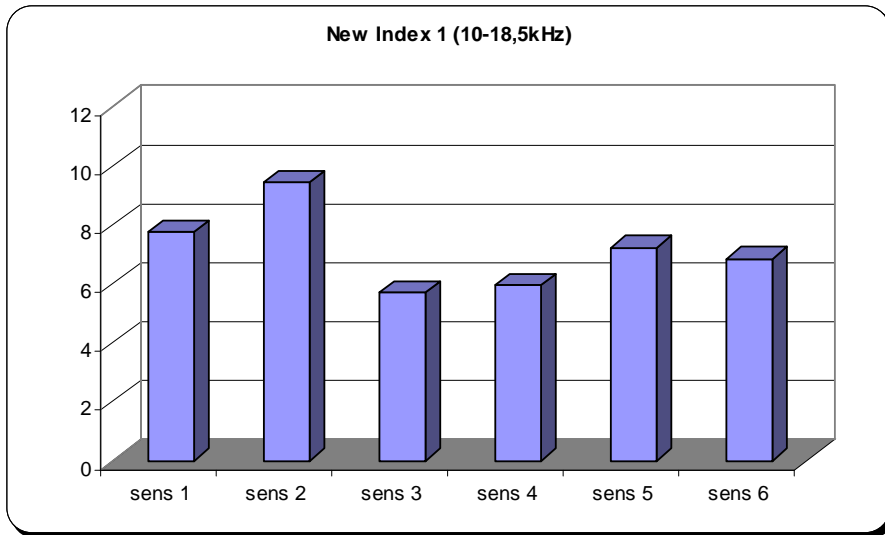


Fig. 5.3.141 – Sensors new DI

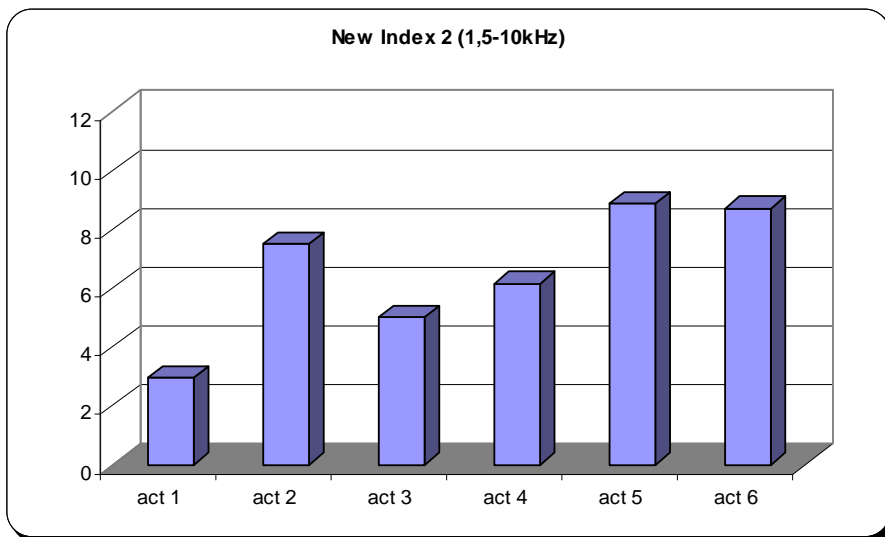


Fig. 5.3.142 – Actuators new DI

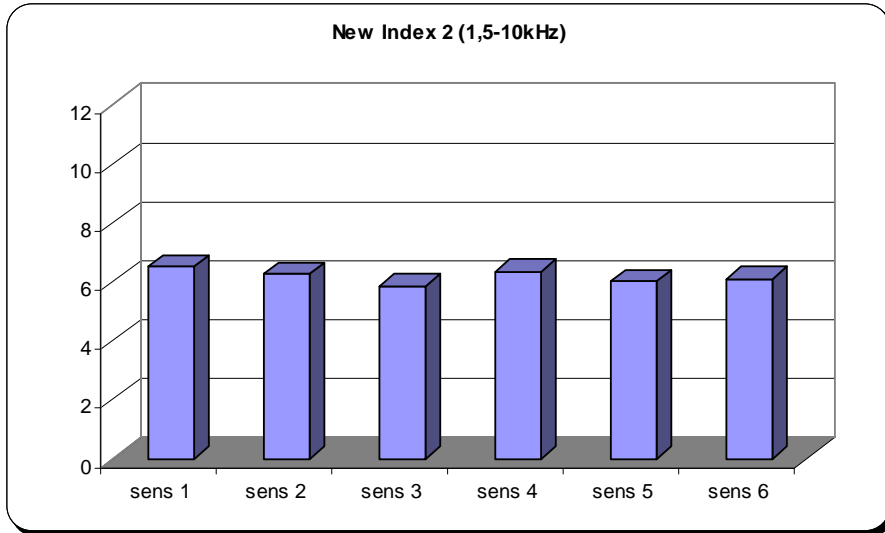


Fig. 5.3.144 – Sensors new DI

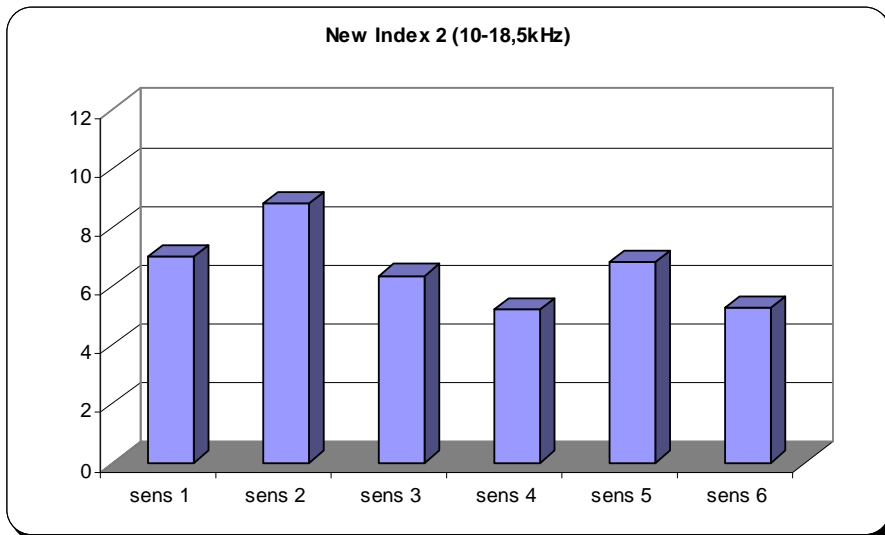


Fig. 5.3.145 – Sensors new DI

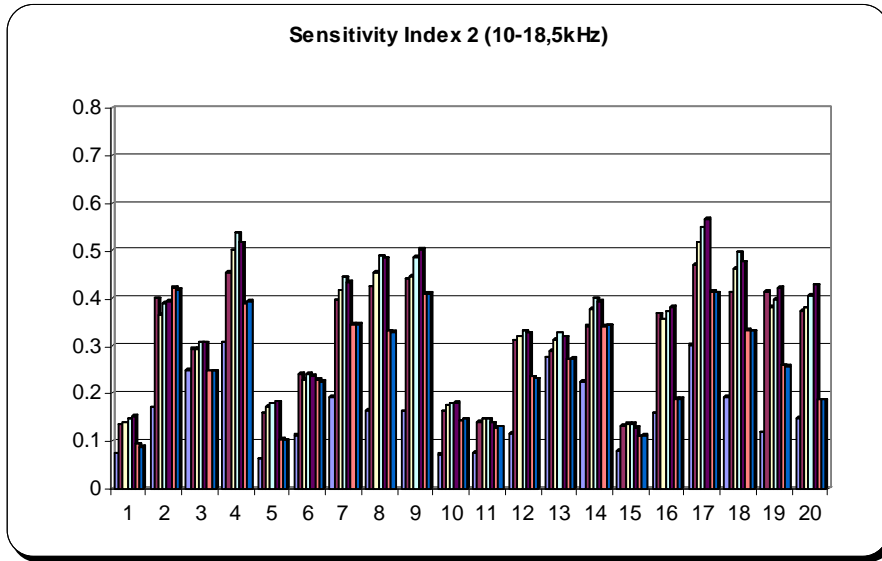


Fig. 5.3.156 – Sensitivity Index

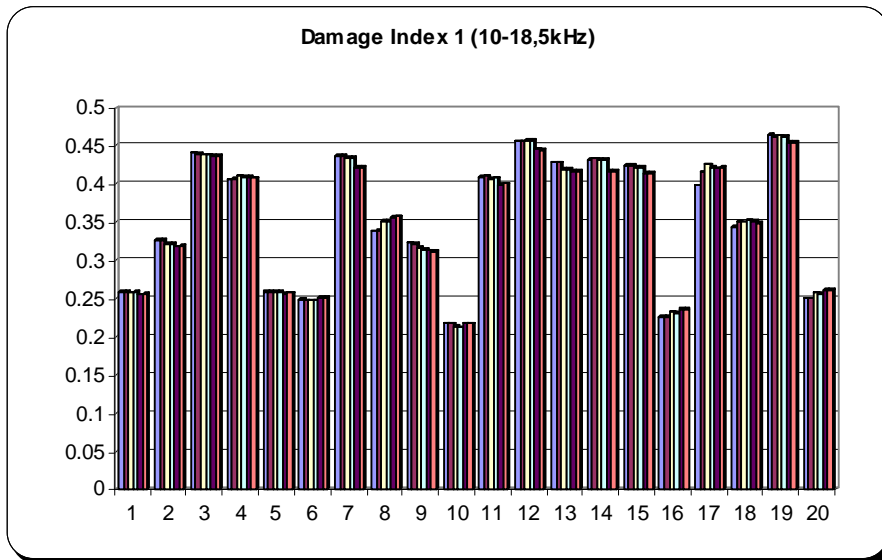


Fig. 5.3.158 – Damage Index

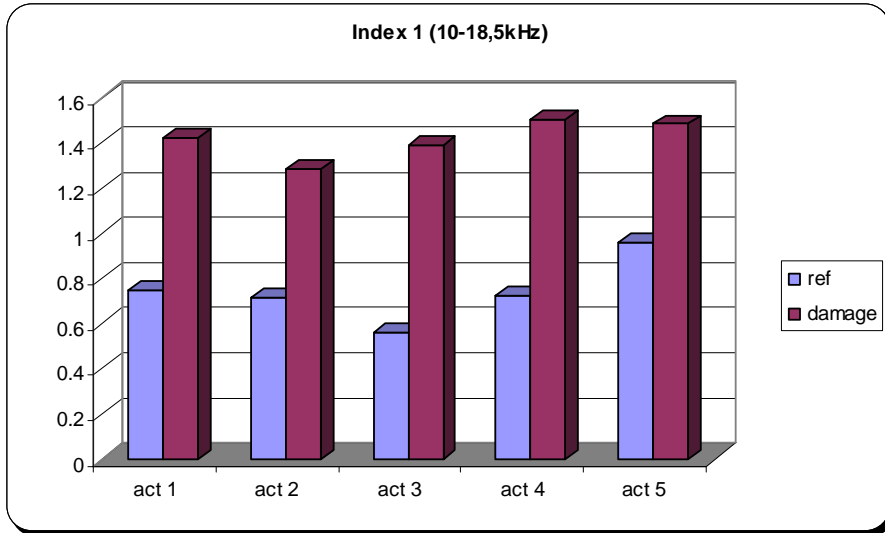


Fig. 5.3.162 – Actuators DI

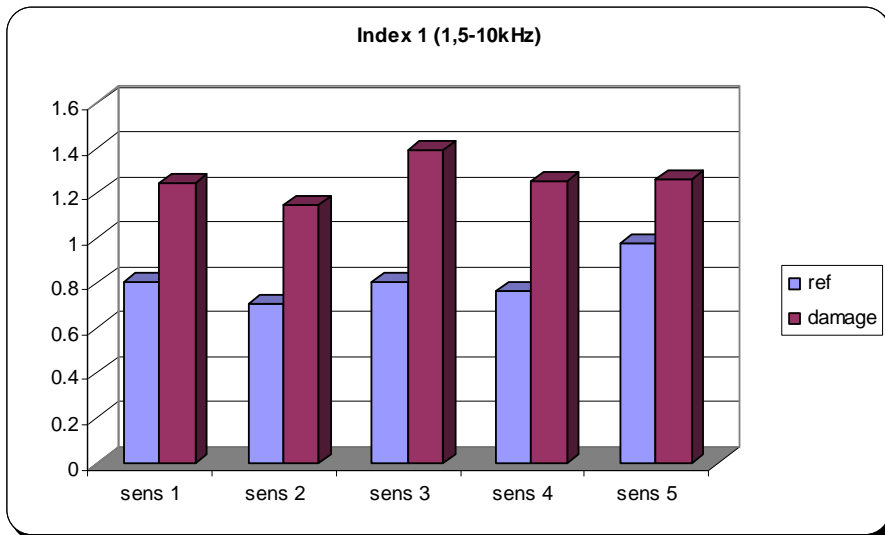


Fig. 5.3.163 – Sensors DI

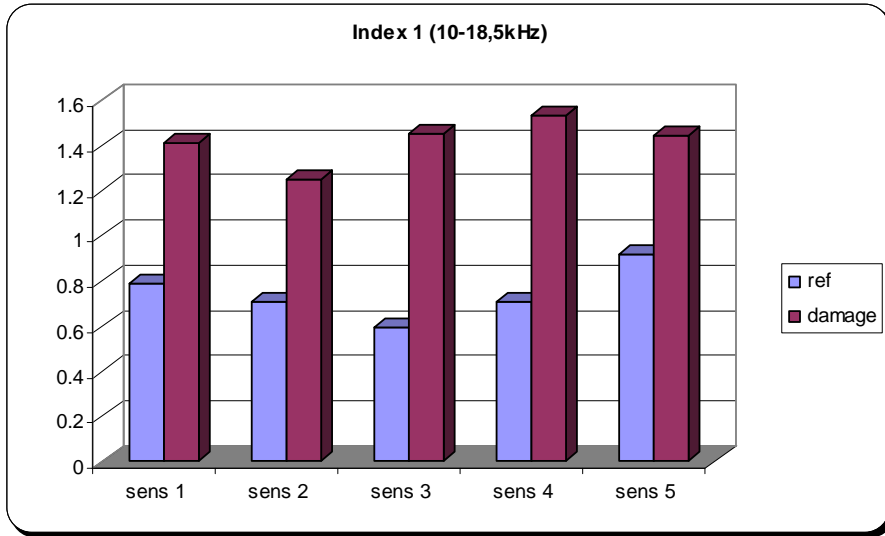


Fig. 5.3.164 – Sensors DI

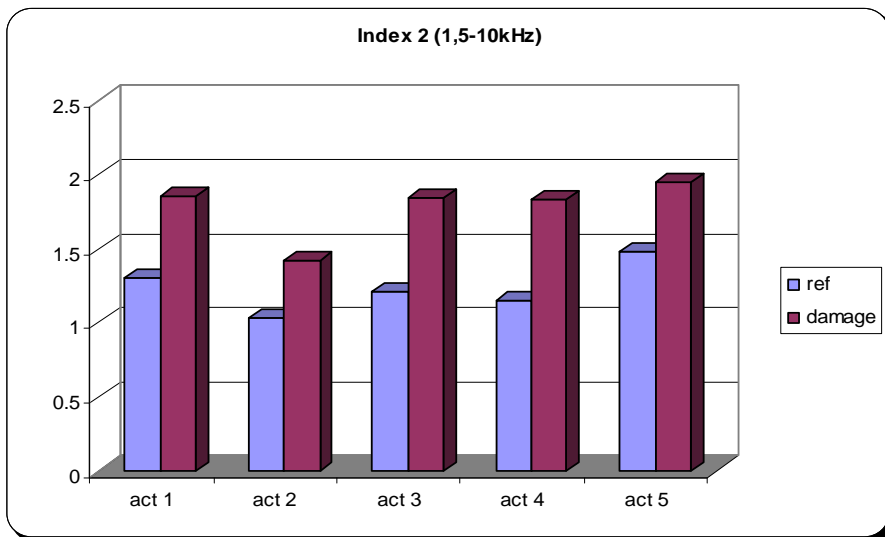


Fig. 5.3.165 – Actuators DI

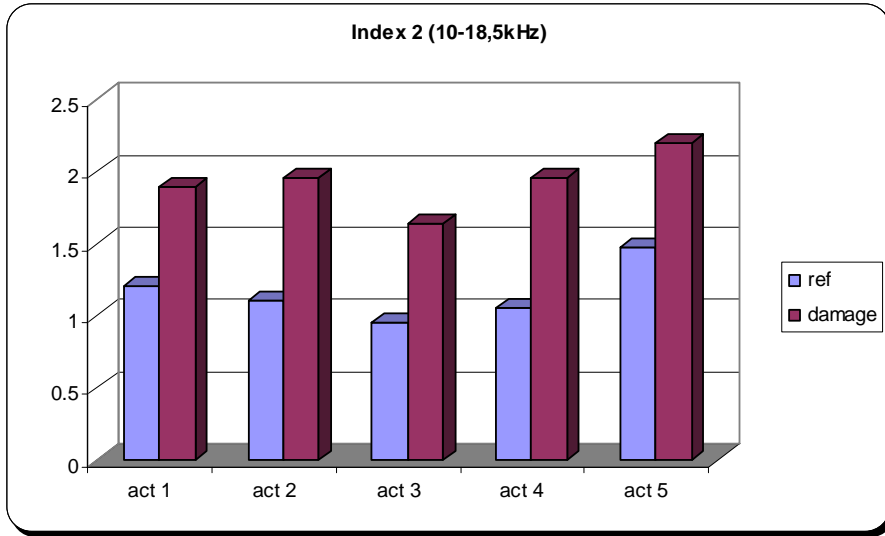


Fig. 5.3.166 – Actuators DI

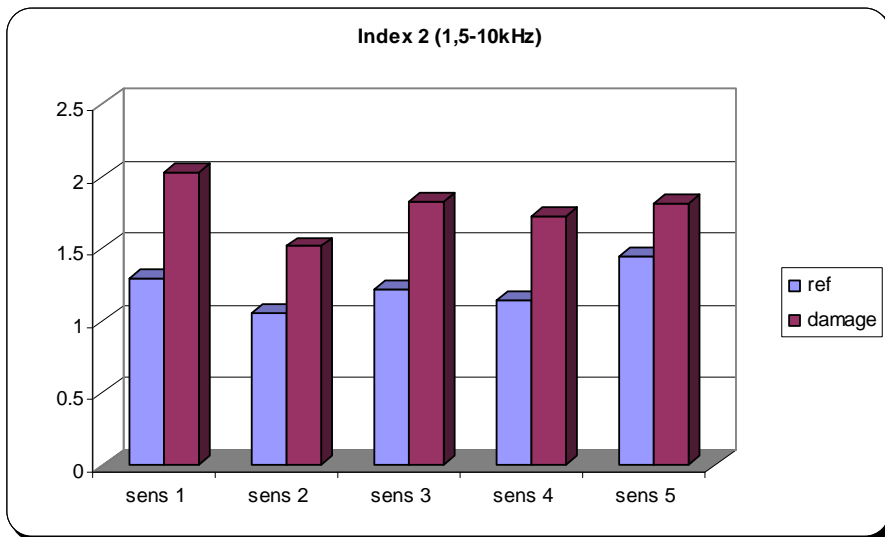


Fig. 5.3.167 – Sensors DI

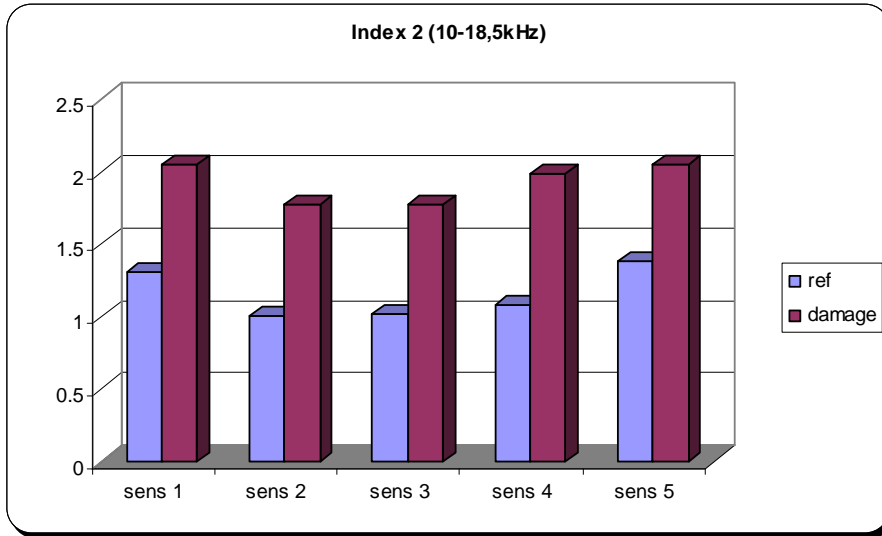


Fig. 5.3.168 – Sensors DI

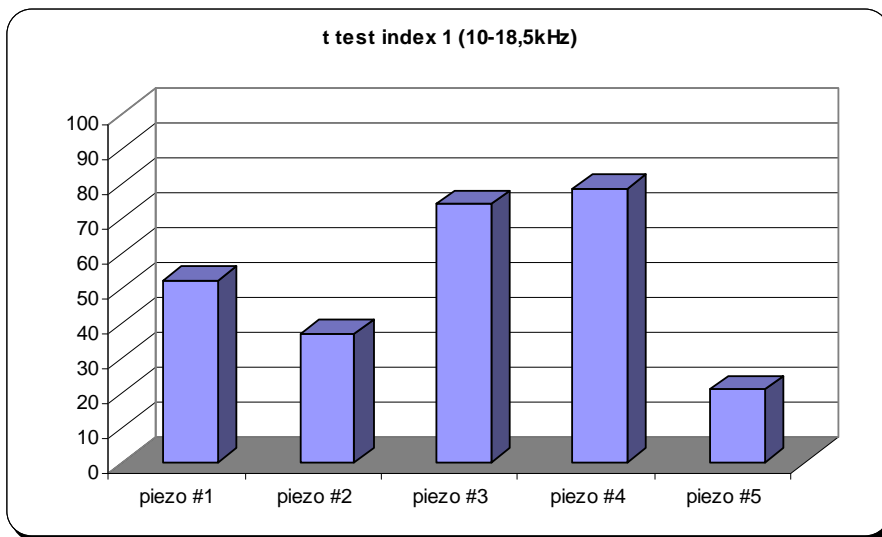


Fig. 5.3.170 – T_test

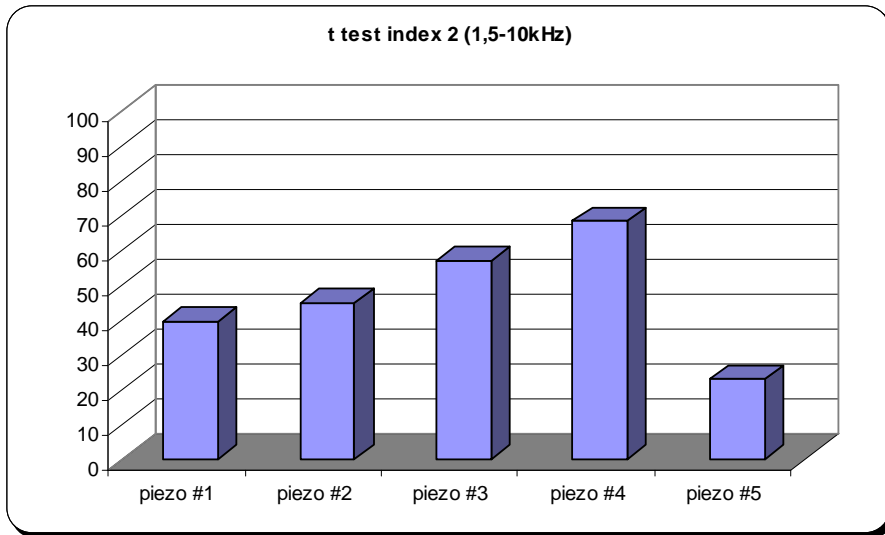


Fig. 5.3.171 – T_test

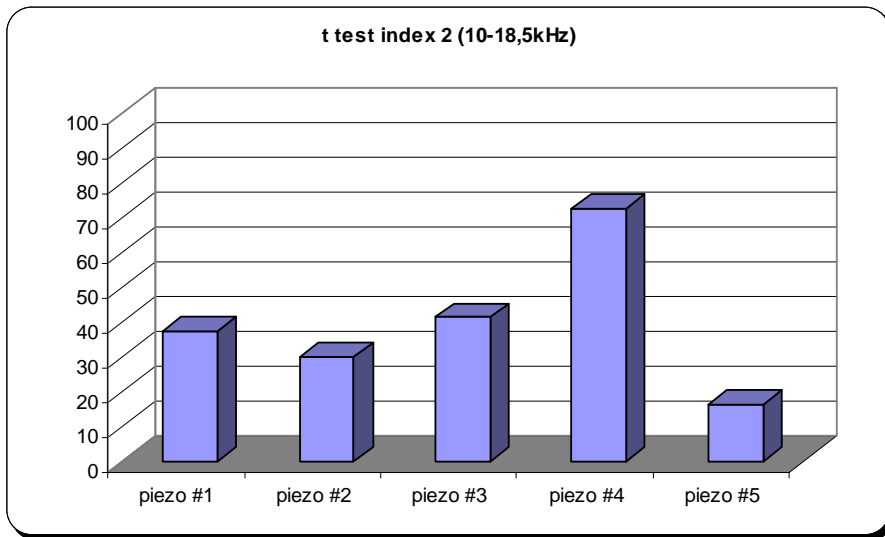


Fig. 5.3.172 – T_test

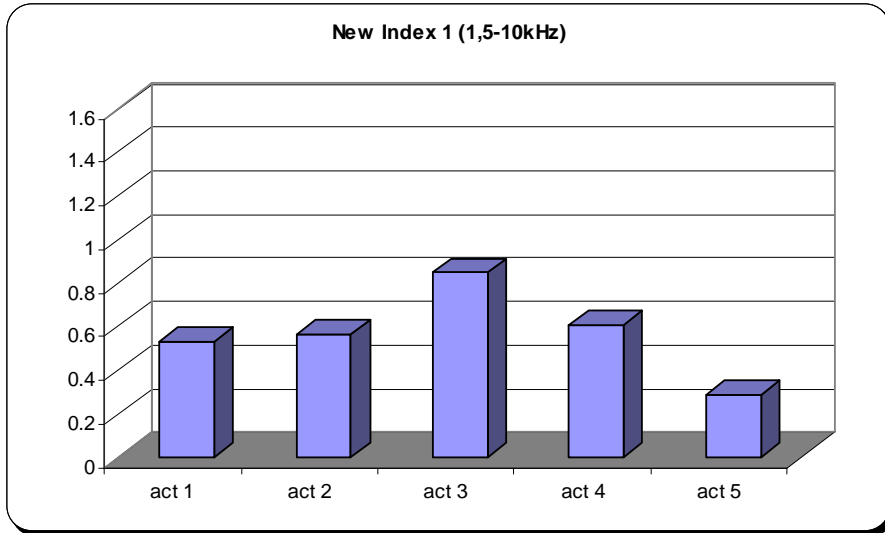


Fig. 5.3.173 – Actuators new DI

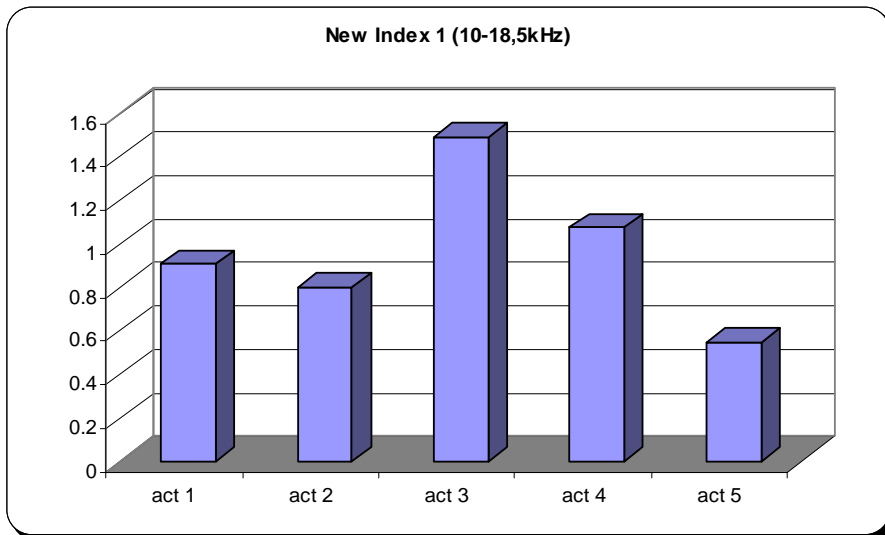


Fig. 5.3.174 – Actuators new DI

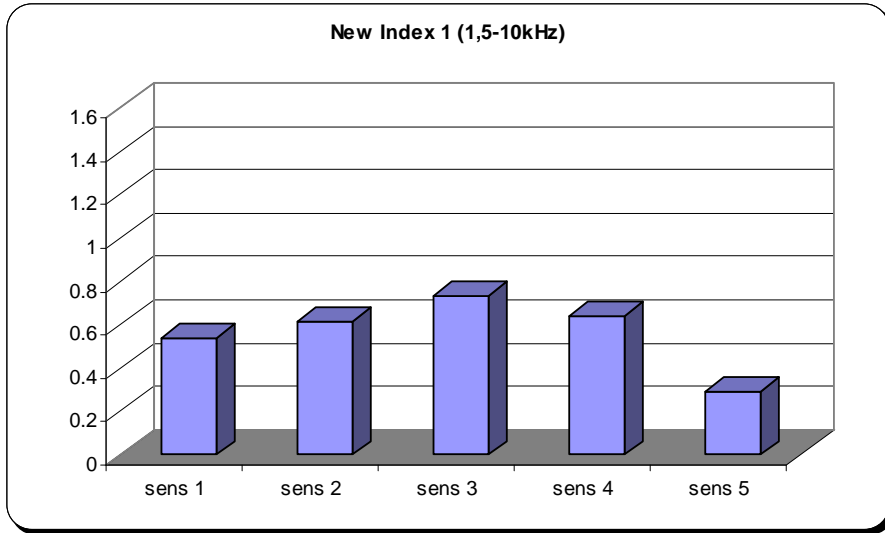


Fig. 5.3.175 – Sensors new DI

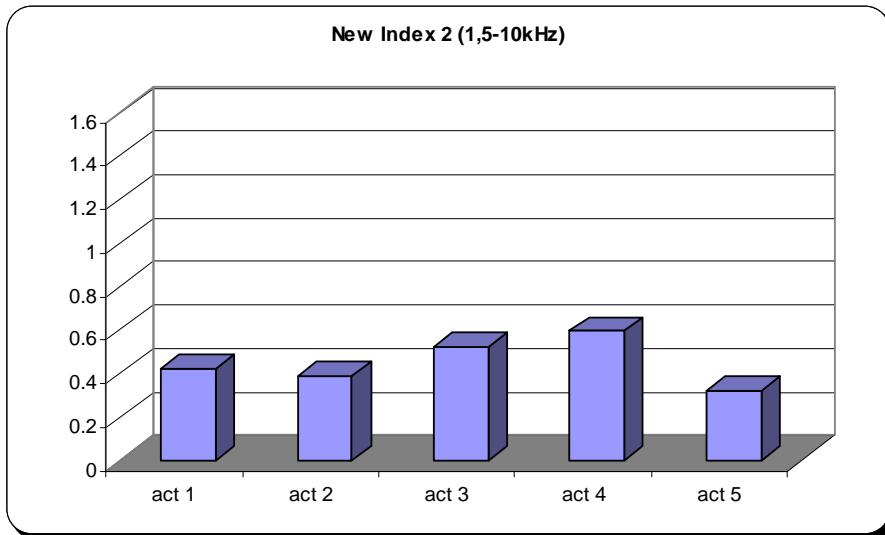


Fig. 5.3.177 – Actuators new DI

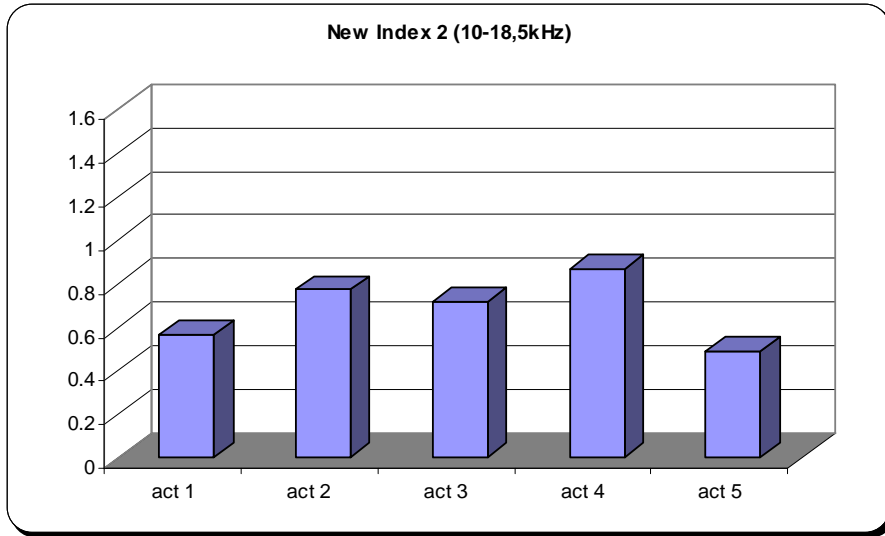


Fig. 5.3.178 – Actuators new DI

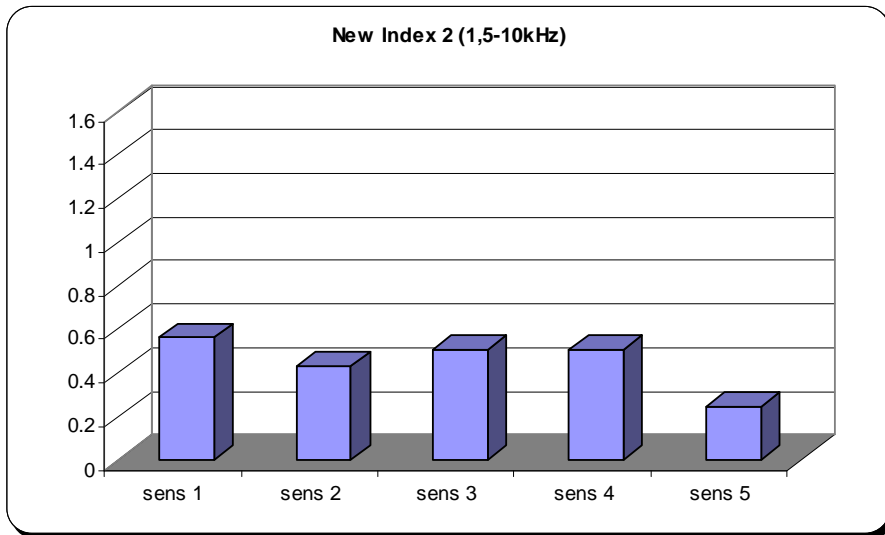


Fig. 5.3.179 – Sensors new DI

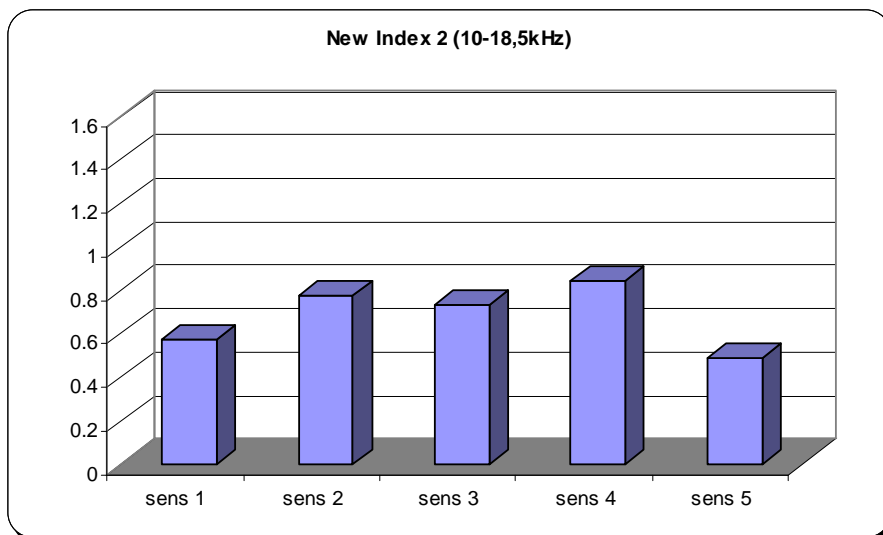


Fig. 5.3.180 – Sensors new DI

Intentionally blank

Conclusions

Purpose of this thesis has been the exposition of the latest results obtained at the Department of Aeronautical Engineering of the University of Naples (Italy) during the last three years, in the Health Monitoring and Non Destructive Test research field. During last years aim of the author has been the development of a NDT strictly responding to most of the mandatory requirements for effective health monitoring systems, simultaneously reducing as much as possible the complexity of the data analysis algorithm and the experimental acquisition equipment; these peculiarities may, in fact, not be neglected for an operative implementation of such a system.

From the algorithm's point of view, the proposed method is based on the acquisition and comparison of Frequency Response Functions (FRFs) of the monitored structure before and after a damage occurred. Structural damage modify, in fact, the dynamical behaviour of the structure and consequently its FRFs making possible to calculate a representative "Damage Index" (DI) and train a Neural Network. These vibration measurements based methods have demonstrated a great ability in identifying a structural damage, localizing its position and quantifying its possible increasing. From an architectural point of view, many different systems have been, during the last years, tested; they mainly differed for the actuators and sensors peculiarities and for the FRF's acquisition technique. On the actuators and sensor field, both piezoceramic patches and magnetostrictive actuators have been tested, as well a scanning laser vibrometer system.

Three structures and several kind of damage have been deeply investigated during these years to assess and compare the approaches. An MD-11 large-scale fuselage reinforced panel, an aeronautical composite panel and a real ATR-72 aircraft have been investigated referring to different typological damages as corrosion, failure of linking rivets, simple cracks, impacts on structure and so on.

All the executed experimental tests have validated both the methods and have permitted to understand the influence of environmental parameters on the Damage Index and Neural Network training capability.

The target of the research presented in this thesis has been achieved. In fact both of the techniques have shown the capability in identifying, localizing and quantifying damage on aeronautical structures. Furthermore, to employ both Health Monitoring methods, a very important point is that:

- ✓ it is not necessary to damage the monitored structure;
- ✓ it is not necessary to use Finite Element Methods;
- ✓ it is not necessary to determine structure's modal free.

Besides, both methods are independent of structure and damage.

Thanks to these new techniques it is possible to carry out a smart Health Monitoring system which is going to lead to the reduction of time and maintenance cost and to the increase of the aeronautical structure safety and reliability.

Bibliography

Chen J. Y., Sharpe Lonnie Jr., Jonkowsky Amy L. - “*An overview of vibrational-based nondestructive evaluation techniques*” - Proceedings of SPIE (Society of Photo-Optical Instrumentation Engineers), Volume 3397 (1998).

Maouk M., Zimmerman D.C. - “*Structural Damage Assessment using a Generalised Minimum Rank Perturbation Theory*” - AIAA Journal, vol.32, No.4, pp. 836-842, April 1994.

S. K. Thyagarayan, M. J. Shulz, P. F. Pai, J. Chung: “*Detecting structural damage using Frequency Response Functions*” – Journal of Sound and Vibration 1998 N. 210.

Fedele P., Cafasso G., Lecce L. - “*A new technique for damage identification and health monitoring of structures using piezoelectric sensors and actuators*” - Proceedings of Seventh International Conference on Adaptive Structures (ICAST), September 1996, Roma (ITALY).

F. P. Sun, Z. Chaundry, C. Liang, C. A. Rogers: “*Truss Structure Integrity Identification Using PZT Sensor-Actuator*” – Journal of Intelligent Material Systems and Structures, Vol. 6, Gennaio 1995.

N. Japkowicz: “*Concept-Learning in the Absence of Counter-Examples: An Autoassociation-Based Approach to Classification*” – Dissertation submitted to the Graduate School-New Brunswick Rutgers, The State University of New Jersey in partial full fillment of the requirements for the degree of Doctor of Philosophy Graduate Program in Computer Science – Ottobre 1999.

Scott W. Doebling, Charles R. Farrar, Michael B. Prime, Daniel W. Shevitz -
“Damage Identification and Health Monitoring of Structural and Mechanical
Systems from Changes in Their Vibration Characteristics: A Literature Review” –
Los Alamos National Laboratory – 1996

T. Petsche, A. Marcantonio, C. Darken, S. J. Hanson, G. M. Kuhn, I. Santoso: “A
neural network autoassociator for induction motor failure prediction” – “Advances
in Neural Information Processing Systems 8.”, MIT, Cambridge, 1996.

D. E. Rumelhart, G. E. Hinton, R. J. Williams: “Learning internal representations
by error propagation” – “Parallel Distributed Processing” MIT Press, Cambridge,
1986.

Bovio I., Monaco E., Arnese M., Lecce L. - “Damage Detection and Health
Monitoring based on vibrations measurements and recognition algorithms on real-
scale aeronautical structural components” – Proceedings of DAMAS 2003, July
2003, Southampton (United Kingdom).

I. Bovio, M. Della Ragione, L. Lecce – “Impiego di tecniche di vibrometria laser nel
campo dell’Health Monitoring con applicazione ad un pannello in materiale
composito” – Proceedings of XII° “Convegno Nazionale A.I.V.E.L.A.”, 2004, Naples
(Italy).

I. Bovio, D. Siano, F.E. Corcione, M. Viscardi – “Identificazione del rumore emesso
da un motore diesel mediante tecniche di vibrometria laser” - Proceedings of XII°
“Convegno Nazionale A.I.V.E.L.A.”, 2004, Naples (Italy).

P. Capoluongo, C. Ambrosino, S. Campopiano, A. Cusano, A. Cutolo, M. Giordano,
I. Bovio, L. Lecce – “Modal analysis and damage detection by Fiber Bragg grating
sensors” Proceedings IEEE Conference on Sensors 2005.

Vandiver, J.K., 1975, "Detection of Structural Failure on Fixed Platforms by Measurement of Dynamic Response," in Proc. of the 7th Annual Offshore Technology Conference, 243–252.

Vandiver, J.K., 1977, "Detection of Structural Failure on Fixed Platforms by Measurement of Dynamic Response," *Journal of Petroleum Technology*, March, 305–310.

Loland, O. and J.C. Dodds, 1976, "Experience in Developing and Operating Integrity Monitoring System in North Sea," in Proc. of the 8th Annual Offshore Technology Conference, 313–319.

Adams, R.D., D. Walton, J.E. Flitcroft, and D. Short, 1975, "Vibration Testing as a Nondestructive Test Tool for Composite Materials," *Composite Reliability, ASTM STP 580*, 159–175.

Adams, R.D., P. Cawley, C.J. Pye and B.J. Stone, 1978, "A Vibration Technique for Non-Destructively Assessing the Integrity of Structures," *Journal of Mechanical Engineering Science*, 20, 93–100.

Worden, K., A. Ball, and G. Tomlinson, 1993, "Neural Networks for Fault Location," in Proc. of the 11th International Modal Analysis Conference, 47–54.

Wang, W. and A. Zhang, 1987, "Sensitivity Analysis in Fault Vibration Diagnosis of Structures," in Proc. of 5th International Modal Analysis Conference, 496–501.

Kam, T.Y. and T.Y. Lee, 1992, "Detection of Cracks in Structures Using Modal Test Data," *Engineering Fracture Mechanics*, 42(2), 381–387.

Salawu, O.S. and C. Williams, 1995, "Bridge Assessment Using Forced-Vibration Testing," *Journal of Structural Engineering*, 121(2), 161–173.

Lam, H.F., J.M. Ko, and C.W. Wong, 1995, "Detection of Damage Location Based on Sensitivity Analysis," in Proc. of the 13th International Modal Analysis Conference, 1499–1505.

Stubbs, N., J.-T. Kim, and K. Topole, 1992, "An Efficient and Robust Algorithm for Damage Localization in Offshore Platforms," in Proc. ASCE Tenth Structures Congress, 543–546.

Manson, G., K. Worden, and G.R. Tomlinson, 1993, "Pseudo-Fault Induction in Engineering Structures," ASME Adaptive Structures and Materials Systems, AD 35, 449–455.

Clark, A. E. Ferromagnetic Materials, vol 1, ed Wolfhart, E.P. (Amsterdam: North-Holland) pp. 531.